TRANSIENT PERFORMANCE EVALUATION OF DIURNAL HEATING AND NOCTURNAL COOLING OF WATER USING A HYBRID FLAT-PLATE SOLAR COLLECTOR/RADIATOR

BY

NWAJI GODSWILL NNABUIHE

(B.Eng., M.Sc.)

REG. No. 20144943278

A Ph.D THESIS SUBMITTED TO THE POSTGRADUATE SCHOOL

FEDERAL UNIVERSITY OF TECHNOLOGY OWERRI

IN PARTIAL FULFILMENT OF THE REQUIRMENTS FOR THE AWARD OF DOCTOR OF PHILOSOPHY (Ph.D) DEGREE IN MECHANICAL ENGINEERING, ENERGY AND POWER ENGINEERING OPTION

FEBRUARY, 2019

CERTIFICATION

This is to certify that this project work, **"TRANSIENT PERFORMANCE EVALUATION OF DIURNAL HEATING AND NOCTURNAL COOLING OF WATER USING A HYBRID FLAT-PLATE SOLAR COLLECTOR/RADIATOR"**, is a research work carried out by Nwaji Godswill Nnabuihe, Reg. No. 20144943278, a postgraduate student in the Department of Mechanical Engineering, Federal University of Technology, Owerri.

Engr Prof., E.E. Anyanwu Principal Supervisor	18/03/2019 Date
Engr Prof., N.V. Ogueke Co-Supervisor	18/3/2019 Date
Engr Dr A.C. Okoronkwo Co-Supervisor	18/03/19 Date
Engr Dr G.O. Osueke Head of Department	18/3/19 Date
Engr Prof., G.I. Nwandikom Dean, School of Engineering	Date
Prof., N.N. Oti Dean, Postgraduate School	Date
Engr Prof. O.V. Ekechukwu External Examiner	Date

DEDICATION

Dedicated to God. To my lovely wife and daughter Phebe Chinaemenma Nwaji.

ACKNOWLEDGEMENTS

My spirit remains humble in appreciating the invaluable time, attention, effort and resources that my Principal Supervisor, Engr Prof. E. E. Anyanwu has put in to ensure that this work has come to completion. People like you are rare. You have aptly demonstrated the real father you are to the younger generation in mentoring them to successful actualization of great dreams. Prof., Sir, I will never forget the time you spent in checking up at every stage of the research to ensure the work is consistent with what prevails in the global community mostly as it regards the use of computational tools for engineering optimization studies. Initially, I was afraid if I would be able to cope with the high demands but through the grace God has given to you, you patiently and painstakingly stood with me. Greater things are ahead of you from the LORD. I am also highly indebted to my co-supervisors, Engr Prof. N.V. Ogueke and Engr Dr C.A. Okoronkwo for their invaluable contributions in painstakingly reading through the drafts.

To my lovely wife, Dr (Mrs) Blessing Chidinma Nwaji and daughter, Phebe Nwaji, I bow in humble appreciation. Thank you for your understanding and support. You are indeed a real blessing! My unalloyed appreciation goes to my beloved parents Mr Christopher Nwaji and Mrs Mary Nwaji for their wonderful prayers and supports from birth till date.

I want to thank my Head of Department Engr Dr G.O. Osueke, Engr Dr. I. Ofong, Engr O.C. Nwufor, Engr C. C. Onwuachu and all the Lecturers and other members of staff at the Department of Mechanical Engineering, Federal University of Technology, Owerri, for their supports and encouragements.

Finally, my sincere appreciations to Mr Marek Nelson of PDE solutions USA, for helping me with the original version of FlexPDE 7.12 used for this work.

Above all, I give thanks to the LORD ALMIGHTY whose inspiration gives wisdom to man's spirit for articulation and will to succeed in life assignments. He has worked in me greatly to be able to carry on till date. I owe Him every allegiance.

TABLE OF CONTENTS

Title page i

Certification ii

Dedication iii

Acknowledgements iv

Abstract v

Table of contents vi

List of tables x

List of figures xi

Nomenclature xv

CHAPTER 1 INTRODUCTION

1.1 Background Information 1

1.2 Problem Statement 6

1.3 Objectives of Study 8

1.4 Justification of study 9

1.5 Scope of Study 10

CHAPTER 2 REVIEW OF THE RELEVANT LITERATURE

2.1 Background Information on Existing Systems 11

2.2 Solar Water Heating Systems 12

2.3 Nocturnal Water Cooling Systems 28

2.4 Hybrid solar water heating and nocturnal water cooling systems 39

2.5 Thermal Stratification in Hot Water and Cold Water Storage Tanks 46

2.6 Summary of findings from literature 51

CHAPTER 3 RESEARCH METHODOLOGY

3.1 The hybrid solar water heating and nocturnal cooling system configuration 54

3.1.1 The Solar Collector/Nocturnal Radiator 55

3.1.2 Mode of Operation 57

3.2 Formulation of system model equations 58

3.2.1 The SCONOR Model 60

3.2.1.1 Simplifying assumptions for model formulation 61

3.2.1.2 Spectral selective surface-coated absorber control volume 62

3.2.1.3 The bond zone 66
3.2.1.4 The Tube Zone Control Volume 68
3.2.1.5 The Fluid Layer 72
3.2.1.6 Heat losses from SCONOR 74
3.2.1.6.1 Top heat losses from the SCONOR surface 74
3.2.1.6.2 The convective heat transfer coefficients 76
3.2.1.6.3 The radiation heat transfer coefficients 78
3.2.1.6.4 Radiopaque-transparent cover radiative and convective heat exchanges 79
3.2.1.6.5 Bottom and edge losses from the SCONOR plate 80
3.2.1.7 The climate model 82
3.2.1.7.1 Models of solar radiation on tilted SCONOR surface 82
3.2.1.7.1.1 Beam radiation on the tilted SCONOR surface 83
3.2.1.7.1.2 Diffuse and reflected solar radiations on the tilted SCONOR surface 85
3.2.1.7.2 The transmittance-absorptance product 88
3.2.1.7.2.1 Formulation of transmittance for beam radiation component 90
3.2.1.7.2.2 Diffuse and ground reflected transmittances due to reflection losses 92
3.2.2 Thermal modeling of the nocturnal cooling process 97
3.2.2.1 The SCONOR model_Nocturnal Phase 98
3.2.2.1.1 The fluid region 100
3.2.2.1.1.1 The tube region 101
3.2.2.1.2 The bond region 102
3.2.2.1.3 The Nocturnal Radiator region 103
3.2.2.1.3.1 Radiator on a horizontal surface 106
3.2.2.1.3.2 Radiator on a tilted surface 107
3.2.3 Thermal stratification in the water storage tanks 108
3.2.3.1 Modelling the hot water storage tank 109
3.2.3.1.1 Differential equation of stratification in the hot water tank 110
3.2.3.2 Modelling the cold water storage tank 117
3.2.3.2.1 Differential equation of stratification in the cold water tank 119
3.2.4 Space conditioning for thermal comfort 122
3.2.4.1 Modelling of comfort cooling 122

3.2.4.1.1 The Room Convector 125
3.2.4.1.2 Heat gain into the room as a result of transmission 127
3.2.4.1.3 Heat gain into the room as a result of infiltration 128
3.2.4.1.4 Heat internally generated in the room 129
3.2.4.1.4.1 Heat generated by people 129
3.2.4.1.4.2 Heat gain in the room by appliances 131
3.2.4.1.4.3 Heat generated from light bulbs 132
3.2.4.2 Modelling of comfort heating 133
3.2.4.2.1 The radiator control volume 136
3.2.4.2.2 Internal heat generation and heat losses by transmission and air renewal 138
3.3 Numerical Implementation 140
3.3.1 Formulation of finite element equations 140
3.3.2 Computational domain 141
3.3.3 Finite element formulation of model equations 142
3.3.3.1 Initial and boundary conditions 145
3.3.3.2 The bond region 148
3.3.3.3 The tube/fluid region 149
3.3.4 Numerical simulations 151
3.3.4.1 FlexPDE scripting procedure 152
3.3.4.2 Grid Independence 154
3.3.4.3 Numerical solution stability 155
3.3.4.4 Convergence Criteria 155
3.3.4.5 Outline of simulations undertaken 156
CHAPTER 4 RESULTS AND DISCUSSIONS
4.1 Results 158
4.1.1 Thermal distribution on the SCONOR 158
4.1.2 Performance predictions using Owerri climatic data 161
4.1.2.1 Solar water heating in the SCONOR 161
4.1.2.2 SCONOR cool-down phase 170
4.1.2.3 Nocturnal water cooling in the SCONOR 176
4.1.3 Performance evaluations during 24-hour period in 5 Nigerian cities 185

4.1.4 Stratification in the storage tanks and space conditioning 187
4.1.4.1 Diurnal stratification and nighttime comfort heating 187
4.1.4.2 Nocturnal stratification and daytime comfort cooling 189
4.1.5 Comparison of model results 190
4.1.6 Parametric analyses 192
4.2 Discussions 197
4.2.1 Thermal energy distribution on the SCONOR 197
4.2.2 Predictions using Owerri climatic data 198
4.2.2.1 Solar water heating in the SCONOR 198
4.2.2.2 The SCONOR cool down phase 206
4.2.2.3 Nocturnal water cooling in the SCONOR 207
4.2.3 Performance evaluation in 5 Nigerian cities 214
4.2.4 Stratification in the storage tanks and comfort conditioning 215
4.2.4.1 Diurnal stratification and nighttime comfort heating 215
4.2.4.2 Nocturnal stratification and daytime comfort cooling 218
4.2.5 Comparison of model results 220
4.2.6 Parametric analyses 222
CHAPTER 5 CONCLUSIONS AND RECOMMENDATIONS
5.1 Conclusions 226
5.2 Recommendations 229
5.3 Contributions to knowledge 230
References 231
Appendix i: Numerical Data for location studies 237
Appendix ii: Numerical Data for surface coatings 242
Appendix iii: Numerical Data for validation studies 243
Appendix iv: Model input parameters 245

LIST OF TABLES

Table	Title	Page
2.1	Comparisons of the characteristics of surfaces and their heating and cooling performances under Hefei, China	42
3.1	Heat generated by people	130
3.2	Cooling Load Factors for people	131
3.3	Heat gain versus nameplate rating from electrical office appliances	132

LIST OF FIGURES

Fig.	Title	Page
1.1	Annual appliance energy usage and their costs	4
1.2	Solar water heater installed capacity per thousand inhabitants	4
1.3	Global installed capacity of solar water	5
2.1	Thermosyphon solar water heating system	13
2.2	Model and experimental geometry of Rostamzadeh system	16
2.3	Existing model and 3-D model of solar water heating system collector	17
2.4	Kian Energy commercial thermosyphon solar water heater	19
2.5	Schematic of natural circulation thermosyphon solar water heater	21
2.6	3-D Mesh of the different configurations of flat plate collector absorber plates	22
2.7	Geometry of the modelled thermo-siphon system	23
2.8	Straight and sine wave configurations of absorber tubes	24
2.9	Modelled geometry of ICS_SWH	25
2.10	Double glazed SWH with three absorber plate geometries	26
2.11	Modelled solar heating system via a low temperature radiator	27
2.12	Setup for the radiative cooling measurement systems-radiator panel with sprayer	28
2.13	Feng's experimental set-up for the radiative cooling measurements	30
2.14	Schematic of thermal model of a night-sky radiation cooling system	31.
2.15	Experimental set-up for the radiative cooling system and recorded parameters	32
2.16	Modelled schematic of radiative water-cooling system	37
2.17	Hybrid nocturnal cooling and cooling coil/direct evaporative cooling unit	39
2.18	Schematic of experimental rig proposed by Balen et al	41
2.19	Schematic of the composite TPET solar heating and radiative cooling system	42
2.20	Hybrid solar collector system with three different storage tanks volume	45
2.21	Model of Torres et al TES system	47
2.22	Modelled geometry of water storage tank of a SWH system	48
2.23	Solar domestic hot water system with thermal stratification in the storage tank	49
3.1	Hybrid solar water heating and nocturnal radiative cooling system	54
3.2	Process line diagram of the thermal model of HSWH-NC system	60
3.3	SCONOR Plate Component Zones	60
3.4	Spectral selective surface-coated absorber and tube	62
3.5	Schematic illustration of contribution to the energy balance for the fin element	63
3.6	The bond control volume	67
3.7	Energy balance for the tube element	69
3.8	Energy balance on the fluid element	72
3.9	Transverse Section of SCONOR (spectral selective absorber) plate	75
3.10	Thermal network for a single windscreen covered collector	75
3.11	Heat exchanges through a spectral selective absorber with a single polyethylene	79
3.12	Beam radiation on horizontal and tilted surfaces	82

3.13	Ray tracing of incident radiation on windscreen panel arrangement	88
3.14	Incident and reflected beams at interfaces of windscreen and air media	90
3.15	Energy Balance on SCONOR_Radiative Process	99
3.16	Energy balance for the fin element of the SCONOR during the nocturnal phase	99
3.17	Energy balance on the stratified hot water storage tank	111
3.18	Elemental volume of the i^{th} fluid zone	111
3.19	Fully stratified cold water storage tank	119
3.20	Energy balance on elemental fluid zone in the cold water tank	120
3.21	Energy balance on the room control volume	123
3.22	Energy balance on the convector control volume	125
3.23	Energy balance on the room control volume (heating)	135
3.24	Energy balance on the radiator control volume	137
3.25	Computational Domain	141
3.26	Quadratic triangular element	150
4.1	Heat flow contour along the SCONOR	158
4.2	Surface plot of temperature along SCONOR x- and y-coordinates	158
4.3	Temperature variation along SCONOR length	159
4.4	Temperature variation along SCONOR centre	159
4.5	Ambient temperature of the test day	160
4.6	Heat flux on the SCONOR plate	160
4.7	Surface plot of heat flux on the SCONOR plate	161
4.8	Predicted ambient temperature in Owerri in January 2017	161
4.9	Predicted Beam, diffuse and total irradiation in January 2017	162
4.10	Predicted thermal energy absorption and losses in January 2017	162
4.11	Predicted SCONOR, bond, tube and water temperatures in January	163
4.12	Predicted ambient Temperature in Owerri in April 2017	163
4.13	Predicted beam, diffuse and total irradiation in April	164
4.14	Predicted thermal energy absorption and losses in April 2017	164
4.15	Predicted SCONOR, bond, tube and water temperatures in April	165
4.16	Predcited ambient Temperature in Owerri in September 2017	165
4.17	Predicted beam, diffuse and total solar irradiation in September 2017	166
4.18	Predicted thermal energy absorption and losses in September 2017	166
4.19	Predicted SCONOR, bond, tube and water temperatures in September 2017	167
4.20	Predicted ambient Temperature in Owerri in November 2017	167
4.21	Predicted beam, diffuse and total solar irradiation in November 2017	168
4.22	Predicted thermal energy absorption and losses in November 2017	168
4.23	Predicted SCONOR, bond, tube and water Temperatures in November 2017	169
4.24	Maximum temperatures of SCONOR plate, tube and bond, and water versus months of the year studied for the diurnal heating phase	169
4.25	Temperature vector during cooldown period in January	170
4.26	Surface plot of Temperature during cooldown period in January	170
4.27	Temperature variation with time during cooldown period in January	171

4.28	Temperature vector during cooldown period in April	171
4.29	Surface plot of Temperature during cooldown period in April	172
4.30	Temperature variation with time during cooldown period in April	172
4.31	Temperature contour during cooldown period in September	173
4.32	Surface plot ot Temperature during cooldown period in September	173
4.33	Temperature variation with time during cooldown period in September	174
4.34	Temperature vector during cooldown period in November	174
4.35	Surface plot of Temperature during cooldown period in November	175
4.36	Temperature variation with time during cooldown period in November	175
4.37	Temperature contour during nocturnal water cooling in January	176
4.38	Temperature vector during nocturnal water cooling in January	176
4.39	Surface plot of Temperature during nocturnal water cooling in January	177
4.40	Predicted SCONOR, bond, tube, water, ambient and sky temperatures during nocturnal water cooling in January	177
4.41	Temperature contour during nocturnal water cooling in April	178
4.42	Temperature vector during nocturnal water cooling in April	178
4.43	Surface plot of temperature during nocturnal water cooling in April	179
4.44	Predicted SCONOR, bond, tube, water, ambient and sky temperatures during nocturnal water cooling in April	179
4.45	Temperature contour during nocturnal water cooling in September	180
4.46	Temperature vector during nocturnal water cooling in September	180
4.47	Surfaace plot of Temperature during nocturnal water cooling in September	181
4.48	Predicted SCONOR, bond, tube, water, ambient and sky temperatures during nocturnal water cooling in September	181
4.49	Temperature contour during nocturnal water cooling in November	182
4.50	Temperature vector during nocturnal water cooling in November	182
4.51	Surface plot of Temperature during nocturnal water cooling in November	183
4.52	Predicted SCONOR, bond, tube, water, ambient and sky temperatures during nocturnal water cooling in November	183
4.53	Minimum temperatures of water, tube and bond and SCONOR versus months of the year studied for the nocturnal cooling phase	184
4.53b	Predicted SCONOR, bond, tube and water temperatures during 24-hour cycle in November in Owerri	184
4.54	Comparison of predicted SCONOR temperatures in 5 Nigerian cities	185
4.55	Comparison of predicted bond temperatures in 5 Nigerian cities	185
4.56	Comparison of predicted tube temperatures in 5 Nigerian cities	186
4.57	Comparison of predicted water temperatures in 5 Nigerian cities	186
4.58	Predicted Temperature stratification inside the hot water storage tank	187
4.59	Top of tank, ambient and Predicted indoor room and radiator outlet Temperatures during comfort heating	187

4.60	Predicted indoor heated and radiator outlet Temperatures	188
4.61	Effect of comfort heating on stratification in the hot water storage tank	188
4.62	Predicted Temperature stratification inside the cold water storage tank	189
4.63	Bottom of tank, ambient and Predicted indoor room and convector outlet Temperatures during comfort cooling	189
4.64	Effect of comfort cooling on stratification in the cold water storage tank	190
4.65	Comparison of predicted SCONOR temperature with Riahi et al (2011) experimental results during diurnal solar heating	190
4.66	Comparison of predicted SCONOR temperature with Mingke et al (2015) experimental results during nocturnal cooling	191
4.67	Comparison of predicted hot storage tank temperature with experimental results carried out in Iran during diurnal solar heating	191
4.68	Comparison of predicted cold storage tank temperature with experimental results carried out in Iran during nocturnal cooling	191
4.69a	Comparison of predicted SCONOR temperature with experimental results carried out in Nigeria during the 24-hour cycle	192
4.69b	Comparison of predicted tube temperature with experimental results carried out in Nigeria during the 24-hour cycle	192
4.70	Effect of 0.1m bond width at varrying thicknesses on the SCONOR performance	192
4.71	Effect of 0.15m bond width at varrying thicknesses on the SCONOR performance	193
4.72	Effect of 0.2m bond width at varrying thicknesses on the SCONOR performance	193
4.73	Effect of 0.25m bond width at varrying thicknesses on the SCONOR performance	193
4.74	Effect of 0.26m bond width at varrying thicknesses on the SCONOR performance	194
4.75	Effect of 0.3m bond width at varrying thicknesses on the SCONOR performance	194
4.76	Effect of bond width and thickness on maximum water temperatures	194
4.77	Effect of riser tube spacing on the SCONOR performance	195
4.78	Effect of number of polyethylene windscreen on the SCONOR performance	195
4.79	Effect of PET coating on carbon steel, aluminium and titanium on the SCONOR temperature	195
4.80	Effect of PET coating on carbon steel, aluminium and titanium on the bond temperature	196
4.81	Effect of PET coating on carbon steel, aluminium and titanium on the tube temperature	196
4.82	Effect of PET coating on carbon steel, aluminium and titanium on the water temperature	196

NOMENCLATURE

Roman alphabets

C_{ID}	Clearness Index
c_p	Specific heat capacity [kJ/kg]
g	Gravitational constant
G_{sc}	Solar constant
h_w	Convective heat transfer coefficient due to wind [W/m^{2}K]
h_f	Fluid heat transfer coefficient [W/m^{2}K]
I	total horizontal solar radiation
I_b	Beam solar radiation
I_d	Diffuse solar radiation
I_{bn}	Beam radiation on horizontal or tilted surface normal to the radiation on the Nth day of the year
I_{bt}	Incident beam radiation on the tilted surface
I_{dt}	Incident diffuse radiation on the tilted surface
I_{gt}	Incident ground reflected radiation on the tilted surface
I_o	Cloudless hourly global irradiation received on the surface
K	Extinction coefficient of polyethylene
k	Thermal conductivity of Collector [W/mK]
Lp	Thickness of polyethylene
L	Collector length
L_{loc}	Location longitude (degrees)
L_{st}	Standard meridian for the local time zone (in degrees),
N	Day number
N_p	Number of people
n_1	Refractive index of Polyethylene
n_2	Refractive index of air
n_{ws}	Number of windscreens
P_r	Prandtl Number
Q_{infil}	Infiltration heat gain in room
Q_{int}	Internal heat source in the room
Q_{solar}	Incident solar energy [W/m^2]
Q_{trans}	Transmission heat gain/loss from cracks and holes in the wall
R_b	Beam radiation tilt factor

R_c Convective resistance

R_r Radiative resistance

R_{ra} The radiator thermal resistance

S Fraction of sunshine hours

T Temperature

T_a Ambient temperature

T_{dry} Dry bulb temperature

T_{dp} Dew point temperature

T_g Ground temperature

t_m Number of hours from midnight in solar time

T_∞ Mean gap temperature

u Wind speed [m/s]

U_L Overall heat transfer coefficient [W/m^{2}K]

W Collector width

Greek alphabets

$\tau\alpha$ Transmittance-absorptance product

τ_a Transmittance of the windscreen due to absorption only

τ_r Transmittance of the windscreen due to reflection only

α_{ss} Absorptivity of Collector plate

ρ_{gr} Ground albedo

ρ_g Ground reflectance

θ_1 Incident angle

θ_2 Refracted angle

θ_{ed} Effective incident angle for sky diffuse radiation

θ_{gr} Effective incidence angle for ground reflected radiation

θ_z Zenith angle of the sun

β' Volumetric coefficient of expansion

η Ratio of refractive indices for the two media forming the interface

ε_{sky} Emittance of the sky

ε_g Emittance of the ground

$\mathcal{R}$ Long-wave radiation incident on the surface of the radiator from the sky

$\mathcal{R}_g$ Ground irradiance

ξ_{ss}^i Selective surface control function

ξ_L^i Load return control function

$\lambda_{s,i}$ Heat conduction coefficient of water in the storage tank

Other Greek symbols

ρ Density [kg/m3]

ε Emissivity

β Collector tilt angle

φ Location latitude

τ Transmissivity

ω Hour angle

γ Solar azimuth angle

σ Stefan-Boltzmann Constant

ξ Control function

Subscripts

a ambient

atm atmospheric

b bond

f fluid

ph plate heating

r room

ss Spectral selective

t tube

ws windscreen

Abbreviations

ACPD	Number of Air Changes in the Room per Day
BDM	Boundary Difference Method
CFD	Computational Fluid Dynamics
CLF	Cooling Load Factor
CSR	Collector Sky Radiator
FEM	Finite Element Method
GWth	Giga Watt Thermal
HSC	Hybrid Solar Collector
H-SWH-NC	Hybrid Solar Water Heating and Nocturnal Cooling
HTF	Heat Transfer Fluid
HVAC	Heating Ventilation Air-conditioning and Cooling
ICS-SWH	Integrated Collector Storage Solar Water Heating
LPD	Litres per day

NCERD	National Centre for Energy Research and Development
NRCS	Nocturnal Radiation Cooling System
PCM	Phase Change Material
PVT	Photovoltaic Thermal
REW	Renewable Energy World
REN	Renewable Energy
SCONOR	Solar Collector/Nocturnal Radiator
SDHW	Solar Domestic Hot Water
SHGPP	Sensible Heat Gain Per Person
SWH	Solar Water Heating
SWHS	Solar Water Heating System
TES	Thermal Energy Storage
TPET	Titanium Polyethylene Terephthalate
T-SWH	Thermosyphon Solar Water Heating

ABSTRACT

Present energy dependence on fossil sources has been identified as the primary cause of the twin menace of global warming and climate change, hence the focus of the ensuing investigation on renewable energy resources to address the current environmental concerns. The transient performance evaluation of a hybrid solar collector/nocturnal radiator (SCONOR) for diurnal water heating and nocturnal water cooling is thus presented. The mathematical models of the physical system are based on the heat transfer mechanism in the SCONOR-bond-tube-water arrangement while for accumulative heating and cooling performances the models were based on lumped energy equations in the SCONOR and multi-zone stratification models in the thermal energy storage tanks. The resulting equations were discretized using finite element numerical scheme for ease of implementation in a digital computer. The transformed equations were solved using a scripted code written with FlexPDE finite element model builder and numerical solver version 7.12. The numerical results obtained from the models were compared with experimental data from literature sourced from three different climatic conditions. In the transient diurnal heating mode, the time of occurrence of SCONOR, bond, tube and water peak temperatures were accurately predicted while a mean deviation of 4-8.6^{o}C was observed between the reported data and numerical predictions. For the transient nocturnal performance evaluation of the SCONOR, the model results closely matched experimental results with a mean deviation of less than 0.2^{o}C, given that the initial conditions varied at about 7^{o}C which was maintained throughout the nocturnal period with minimal fluctuations. The model results from a 24-hour performance cycle covering diurnal heating, cool down and nocturnal cooling of the SCONOR closely matched experimental results for the absorber and radiator functions of the hybrid system with mean deviations of 3-5^{o}C in the diurnal heating mode and 0.2-0.4^{o}C in the nocturnal cooling mode. The accumulated performance results during the diurnal thermal storage and nocturnal thermal storage were also compared with available experimental data from literature, and the results show good agreement with mean deviations of 0.2-5^{o}C and 7^{o}C during heating and cooling respectively. The thermal energy accumulated in the hot tank during diurnal heating maintained the modelled room temperature at approximately 5^{o}C above ambient during the cold harmattan night and that accumulated in the cold storage tank maintained the modelled room temperature at 5.7^{o}C below ambient during the hot day. From parametric analyses, the optimal design parameters are 0.26m, 0.003m, 0.1m, and 1 for the bond width, bond thickness, riser tube spacing and number of windscreen respectively. The overall results show that the developed models are useful design tools for the integrated diurnal water heating-and-nocturnal water cooling.

Keywords: Models, Numerical Simulation, FEM, Hybrid SCONOR, Transient, Diurnal Solar Energy, Nocturnal Radiation, Thermal Storage, Comfort Cooling, Comfort heating.

CHAPTER 1

INTRODUCTION

1.1 Background Information

Global interest is currently increasing on the exploitation of hybrid active heating/passive cooling, low energy water/air heating, and ventilation/air conditioning (comfort cooling) applications. A hybrid system involves the use of a single unit/machine to perform two different functions that otherwise would have been carried out by two independent systems. Several countries are committing a great deal of resources into the research and implementation of such techniques. Both the Evapcool of the European Union Fifth Framework/Energy sub-programme and Solar Heating and Cooling Programme of the International Energy Agency are some of the current collaborative efforts in this area (Balen et al, 2003). Solar energy utilization has been on the increase in recent years due to the declining fossil fuel resources and environmental concerns about global warming and air pollution. Although solar energy is inexpensive relative to conventional sources of energy like natural gas, the overall cost of its exploitation continues to decrease due to advances in technology.

Energy utilization worldwide depends heavily on fossil resources (oil and gas products). Environmental sustainability is highly threatened owing to the pollutant emissions from heavy dependence on these fossil resources (Asere et. al., 2011). Oil prices and energy consumption demand have been on the increase. The finite nature of fossil resources is also a major concern, since studies have revealed that they are tending towards exhaustion (World Energy Council, 2013; Cappellan-Perez et al., 2014; Khan et al., 2015). These have become contending challenges. Consequently, research and technological investments are gaining serious attention in renewable and sustainable energy (Sinan, et. al., 2012; Jung-Sik, et. al., 2010).

Renewable energy technology generates energy by transforming natural phenomena (or natural resources) into useful energy forms and is strongly believed to be one of the promising solutions to the energy challenge. Renewable energy will contribute a great deal in the new millennium in adding the much needed flexibility to the energy mix and decrease dependence on conventional fossil fuels, thus drastic reduction in global warming and climate change. Solar energy is the most sustainable renewable energy source (Eduardo et. al., 2010). The sun is a continuous fusion reactor, turning hydrogen into helium, and producing an effective average body temperature of about 5762K and total output energy of approximately 3.8×10^{20} MW amounting to 63 MW/m^2 of its surface. This energy radiates outwards in all directions and about 1.7×10^{14} kW reaches the earth within 8 minutes 20 seconds after leaving the giant furnace. However, it's been found that harnessing this minute fraction for about 30 minutes is sufficient to meet the world's annual energy demand (Kalogirou, 2004).

Solar thermal energy systems have emerged over the recent decades for several applications in domestic and industrial activities like hot water supply, space heating and cooling, desalination, sterilization, pasteurization, drying, refrigeration, distillation, washing, etc, that can conveniently be carried out within the temperature ranges of 60 to 280^0C (Parimal and Parishwad, 2013). For domestic water heating and cooling applications, flat plat collectors have been extensively used.

Nocturnal cooling concept has many potential applications in the storage of food, seed and medicine, air conditioning of buildings and water desalination (Dobson, et al., 2003). By integration of this concept into the architectural design of building envelopes, thermal comfort can also be provided during hot/dry seasons (summer) with minimum energy utilization, without recourse to the mechanical vapour compression systems extensively used for air conditioning. As global industrialization and standard of living improve, energy consumption related to space

cooling increases and hence associated energy cost. This cooling concept is likely to reduce the energy bills associated with conventional mechanical cooling as well as greenhouse gas emissions.

Thermal water heating dates back a long way, at least as far as Archimedes' use of a concave mirror to heat water in 214 BC (Renewable Energy World, 2004). Solar water heating (SWH) systems harness irradiation from the sun to heat water either for domestic or industrial use. In 1891, Kemp patented the first solar water heating system in the United States. This was essentially boxes that were painted black and filled with water and exposed to the sun to heat up the water. Early 20th century witnessed several efforts to improve the design of the SWH systems (Iordanou, 2009). In Japan, a simple solar water heater was created consisting of a basin with its top covered by glass and by the 1960s more than 100,000 collectors of this type were in use. Australia witnessed an increase in the number of solar water heaters as a result of oil price increases, but the discovery of natural gas in the late 1980s led to a drop in the growing interest in solar water heaters. Levi Yissar, an Israeli engineer pioneered the introduction of solar water heater in Israel around the mid 50s, and by early 1980 about 60% of Israeli population heated their water with energy from the sun. More so, following the drop in oil price in the mid 1980s, Israeli government made it a law, making well above 90% of Israeli households to install solar water heaters today (Iordanou, 2009; REN21, 2017).

According to Veeraboina and Yesuratnam (2014), solar water heating systems can span a period of up to 15 to 20 years and favour regions that have good water quality and are non-hilly. Such systems are available in multiples of 100 LPD (Litres per day) i.e. 100, 200, 300 LPD, etc. Among the common household appliances, solar water heaters consume the highest amount of power on the annual scale and hence constitute the highest source of energy cost for households,

as revealed by the following chart showing the quantity of energy a typical appliance uses annually with a corresponding cost based on national averages, as shown in Fig. 1.1.

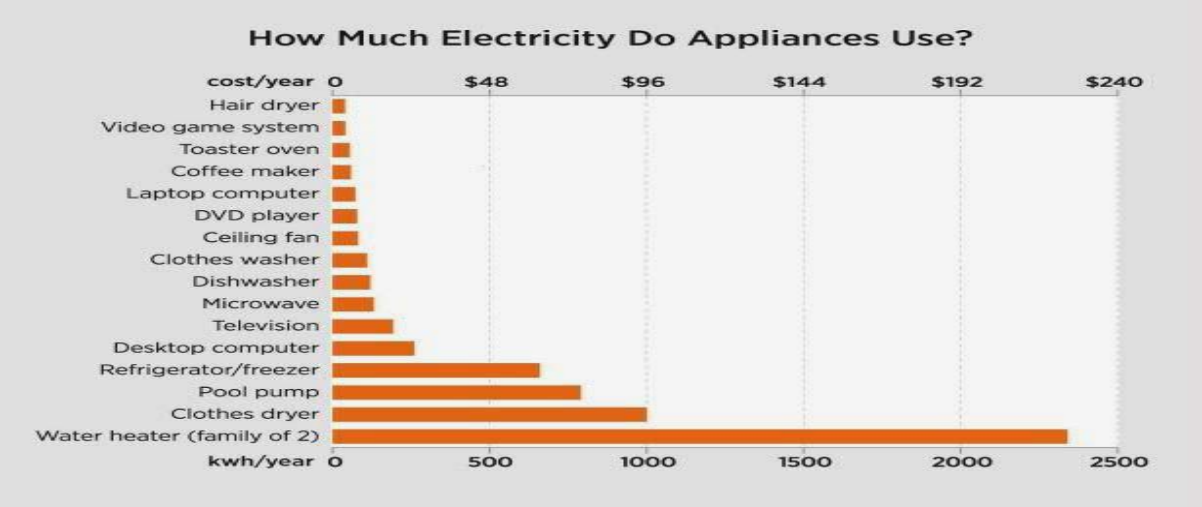

Fig. 1.1 Annual appliance energy usage and their costs (Veeraboina and Yesuratnam, 2014).

Globally, many countries are embracing the solar water heating technology. While countries like Austria, Turkey and Germany have high share of installation of SWH per capita, Israel and Cyprus have almost attained saturation, standing as leaders in world's installed capacity per capita as reflected in figure 1.2 (Leonardo-energy.org; Iordanou, 2009).

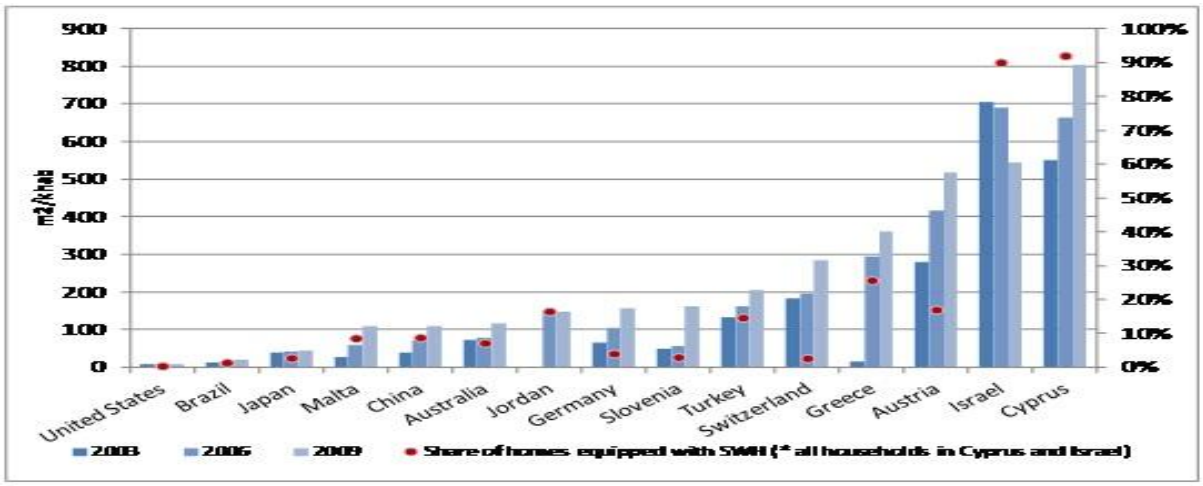

Figure 1.2: Solar water heater installed capacity per thousand inhabitants and share of homes* equipped (source: Enerdata, 2009 as reported in Iordanou, 2009).

China and Brazil are constituents of the emerging markets for solar water heating systems, with China ranking first in terms of installed capacity of about 11 million m², installed up to 2009

(almost 2/3 of the world's capacity). Hence, China has become the leader in solar water heating system additions, surpassing Turkey (380,000 m^2), Austria (about 200,000 m^2) and Portugal (around 88,000 m^2) in that order.

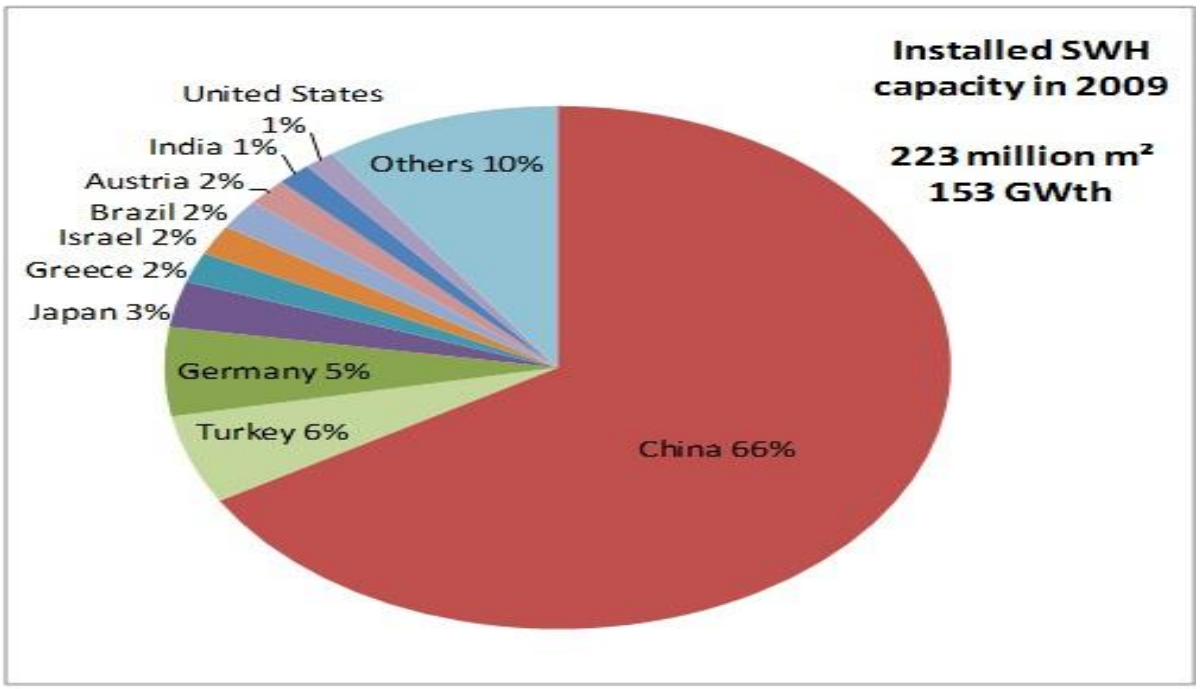

Figure 1.3: Global installed capacity of solar water (source: Enerdata, 2009).

Preliminary estimates indicate that the solar water heater market would have risen to well above 185 GWth in 2010, from 153 GWth estimate of 2009, with China alone contributing about 70% of prospective capacity and only 10% coming from European Union, as shown in Fig. 1.3. The European Union, has included the development of solar water heating (SWH) systems in the National Renewable Energy Action Plans by member states and most of EU countries, therefore, have set targets for solar heat by 2020 (Leonardo-energy.org). According to ECOWAS Centre for Renewable Energy and Energy Efficiency status report (REN21, 2014), solar water heaters are being utilized in West Africa but estimates of the penetration are limited and difficult to assess. Mali has installation of about 1,500 200-litre solar water heaters while mention is made of its use in other countries like Niger, the Gambia, Nigeria, etc. However, Olusola et al (2017) revealed that about 4,000 solar water heating units were installed as at 2015 in Nigeria, with the Nigerian Federal Government setting a target of installations of about 60,000 and 150,000 units in 2020 and 2030 respectively.

1.2 Problem Statement

According to Ogueke et al (2009), hot water demands appear to be highest within the periods of the day when electric energy demand for other purposes is high, usually early in the mornings and late in the evenings. Hot water for domestic activities, industrial process heat, space heating, sterilization in hospitals, bathing at homes, schools and hotels, etc, in Nigeria are currently largely being met by the use of fossil-driven grid electricity and natural gas. These fossil fuel resources, apart from being finite, are reputed to be the sources of the twin menace of global warming and climate change, which have become the two most current contending political issues around the globe today. Global atmospheric temperature is increasing, mostly during dry seasons of the year when ambient temperature is above that needed for human comfort, making comfort cooling inevitable, hence, increased demand on grid electricity to drive the conventional air conditioning systems (Ogueke et al, 2011).

The immediate consequences are progressively increasing cost of energy supply and harmful emissions into the earth environment from conventional energy consumption to meet man's needs. Population is also on the increase, especially in the developing nations, thereby placing a more increased burden on energy demand. Therefore, there is need for nations to develop and provide energy systems commensurate with the growing population but free from adverse environment effects. Another prominent contending issue stifling access to energy in developing nations is the erratic nature of electricity supply, leading to power rationing in most cases. During the periods of highest need for hot water, it is either that the electric power is not available or certain areas are completely shut off due to insufficiency of available grid supply. It is, therefore, foreseeable that removing the energy demand for hot water purposes from electricity is the most seemingly convenient means to eliminate or reduce these problems. Use of the ambient energy is speculated to significantly address the problems.

Solar energy is an immense free energy resource, renewable, free from pollution and capable of meeting the energy needs for hot water during the day, as any object placed on the earth absorbs a great deal of this energy depending on the nature of its surface. Also, the sky during the night, acts as a heat sink as it remains colder that any object placed on the earth's surface. This implies that a surface exposed to the night sky dissipates heat to the environment thereby cooling down. Thus, if the roof of a building is coupled to a thermal storage, nocturnal cooling can be used to keep it cool and provide comfort throughout the day. The urgent need to harness nocturnal cooling resources to supplement our cooling needs cannot be overemphasized.

Accordingly, Nwaigwe et al (2010) documented a comprehensive report of the principles and theories of nocturnal sky radiation cooling and its available systems, including the pertinent experiences of its operations, prospects and technical constraints. Unlike the solar water heating system (SWHS), works in nocturnal radiation cooling systems (NRCS) have remained at the laboratory experimental stage. Independently, each of these systems is quite expensive to produce. This problem can be solved by utilizing a hybrid flat-plate solar collector/radiator to harness solar radiation during the day and night sky radiation during the night. This is integrated into a building envelope and coupled to hot water and cold water storage tanks, room convector and radiator for performing the two different functions that otherwise would have been done by two different independent systems. In which case, diurnal solar water heating and night time or nocturnal radiation water cooling would have been successfully undertaken using a single system. Because the thermal energy supplies for running the heating and cooling phases of this hybrid system are ambient energy, its operations correspond to the natural availability of diurnal (day time) solar energy and nocturnal (nighttime) sky radiation periods respectively. Amraoui

and Aliane (2015) reported that solar energy application is closely related to the performance of the collectors which convert it. This is also true for a nocturnal radiator.

Many objects lack the capability of both absorbing the incoming solar radiation during the day and at the same time radiating heat to the cold sky during the night because their surfaces are non-selective to radiation wavelength within the solar radiation and atmospheric window spectra. Therefore, improvement in their operating condition and geometrical configuration would definitely result in saving conventional fuel and cost.

In synopsis, the demand placed on conventional energy utilization for water heating/cooling and space conditioning can be greatly reduced and hence reduction in energy costs by the effective exploitation of the concepts of diurnal and nocturnal radiant flux interchanges.

1.3 Objectives of Study

The main objective of the present investigation is to carry out a transient performance evaluation of diurnal heating and nocturnal cooling of water using a hybrid flat-plate solar collector/radiator. To achieve the main objective, the specific objectives include, to:

(i) Develop a 2-D dynamic thermal model that will enable comprehensive overview of the effects of thermo-physical and material properties as well as weather conditions on the performance of the H-SWH-NC system.

(ii) Determine the mean diurnal heating and nocturnal cooling outputs of the collector-radiator surface under some selected locations in Nigeria.

(iii) Study the effect of stratification in the storage tanks on the performance of the hybrid collector/radiator for diurnal and nocturnal thermal energy storage and thus the possibility of comfort heating and cooling.

(iv) Carry out parametric analyses to ascertain the effects of riser tube spacing, optimum configuration of the bond region, insolation intensity and surface spectral properties on the dynamic and thermal behaviour of the hybrid SCONOR, to enable further improvements on the H-SWH-NC system.

1.4 Justification of study

The advent of hardware-in-the-loop technology or virtual prototyping brought a revolution in engineering products/systems development. Engineering today has shifted greatly from the traditional method that dominated the period of early development of the field. Nowadays, prototypes can be modelled and tested in the virtual environment to ascertain its functionality before finally building the physical prototype. Virtual prototyping and high speed digital computers coupled with available and powerful numerical solvers have made this possible. This has led to considerable conservation of time, material and money and other resources that go into product and systems development. Also, there are parameters that are difficult to measure experimentally due to either the complexity of the system or expensive nature of transducers to carry out such measurements. Modelling and simulation will provide comprehensive insight into the nature of the parameter and how it affects the system performance and can therefore help in system optimization studies.

Water heating forms significant part of energy consumption of many countries and has been accomplished greatly using electricity and natural gas. Where consumption data are available, for instance, in the United States, Europe and Japan, statistics show that water heating alone represents about 15% of households' energy use in Europe, 20% in the United States and as much as 30% in Japan. Hence, switching from electricity and gas to solar water heating could

strongly reduce fossil fuel consumption and CO_2 emissions (Leonardo-energy, n.d). Also, available statistical data for building energy consumption show that the heating, ventilation and air conditioning (HVAC) component, primarily provided by the mechanical vapour compression systems accounts for as much as 70% of the total energy consumption (Martin, 2000). Modelling the exploitation of space heating and passive cooling techniques using solar water heating and nocturnal cooling concepts cannot only reduce the costs involved in experimentation of the innovative system but would also enable recommendations to be made about the concepts economic importance in achieving drastic reductions in household energy consumption.

1.5 Scope of Study

This investigation is limited to numerical analyses of hybrid solar water heating and cooling, both for production of hot water for domestic use and cool water for space conditioning. This involves the development of a 2-D dynamic thermal model for comprehensive evaluation of the effects of thermo-physical properties and weather conditions on the performance of the hybrid solar water heating and nocturnal cooling system. It is also intended to examine the performance of the system in some selected Nigerian locations as well as the effects of stratification in the cold and hot water storage tanks on the overall performance. Moreso, it will encompass a parametric analyses to ascertain optimum design parameters that would aid prototype development. It is an integrated sustainable energy system that uses a solar thermal panel for hot and cold water production plus space ventilation system with air-heating/cooling by means of a water coil for the supply of air conditioning, mostly during the periods of adverse climatic conditions during the year, for the Nigerian climate, through sufficient preparation of cold water.

CHAPTER 2

REVIEW OF THE RELEVANT LITERATURE

2.1 Background Information on Existing Systems

There is an increasing demand for hot water for domestic activities in homes and hotels, sterilization of medical instruments in hospitals and many other industrial activities, as well as space heating in cold climates. Trailing behind this, is the demand for energy efficient cooling (air conditioning) systems to ameliorate local and global energy consumptions during the warmest (summer and dry) seasons of the year. These have constituted important issues for researchers, thus, leading to extensive research in the solar water heating and radiative cooling systems' modelling and performance predictions.

While there exists two broad categories of solar water heating systems, namely, the active and passive solar water heating systems (Ogueke et al., 2009; Sumathy et al., 2013), nocturnal or radiative cooling systems can be viewed also under two broad classifications, namely, direct (or passive) and mixed (hybrid) radiative cooling systems (Okoronkwo, 2011). The active solar water heating systems rely on pumps to move the liquid between the collector and the storage tank, while passive solar water heating systems rely on gravity and buoyancy effects to naturally circulate water between the collector and storage tank as it is heated. While the active system ensures constant flow rate, and could be achieved using concentrated collectors, evacuated tube collectors and flat plate collectors, it uses a conventional energy to drive the pump and hence, not completely an environmentally friendly system. Passive systems include the integrated collector storage solar water heating (ICS-SWH) system and the thermosyphon solar water heating (T-SWH) system. While the integrated collector storage solar water heating (ICS-SWH) systems employ a tank that acts as both a storage and solar collector device (Garnier, 2009), the thermosyphon solar water heating systems comprise the solar collector, the water storage tank

and the connecting pipes; and simply circulate water or a heat transfer fluid by natural convection between a collector and an elevated storage tank, normally placed above the collector (Ogueke et al., 2009; Sumathy et al, 2013). The integrated collector storage system is not very common but the thermosyphon systems are more common (Garnier, 2009).

The direct radiative cooling involves exposing the building envelope directly to the sky where it radiates heat to the sky and cools and by so doing evacuates heat from the interior of the building to the outer atmosphere, whereas the hybrid (mixed) radiative cooling entails incorporating a metallic radiator on the roof of the building and air or water is made to pass through the radiator where it is cooled and thereafter channelled to the building for cooling purposes using the slab or ceiling cooling (Okoronkwo, 2011).

Hybrid solar water heating and cooling systems comprise both the hot water production for domestic and other uses as well as space heating, and chilled water production for space conditioning in a single unit. According to Pierrick et al (2015), hybrid systems have become the subject of renewed interest in recent years, more especially with the advent of low or positive energy buildings, requiring all the multifunctional envelopes to meet the energy needs.

The subsequent sections centre on the exploration of comprehensive literature on the previous work done on solar water heating, nocturnal or radiation cooling and hybrid systems.

2.2 Solar Water Heating Systems

The thermosyphon solar water system has gained popularity in developing countries with acute power issues as well as in countries with well developed technologies and conducive climates. In this investigation, a more detailed picture of the thermosyphon system is of interest and is explored in the subsequent sections. Wealth of literature abounds on the thermal performance of

the thermosyphon solar water heating (SWH) system, in natural and forced circulation modes. The performance of the thermosyphon system depends on the collector thermal capacity, size and capacity of the storage tank, and the connecting pipes including fluid flow and on the pattern of hot water use (Riahi and Taherian, 2011). A modelling, simulation and validation of a natural circulation closed thermosyphon glass solar tube collector water heater has been reported by Samuel et al. (2016) as shown in figure 2.1.

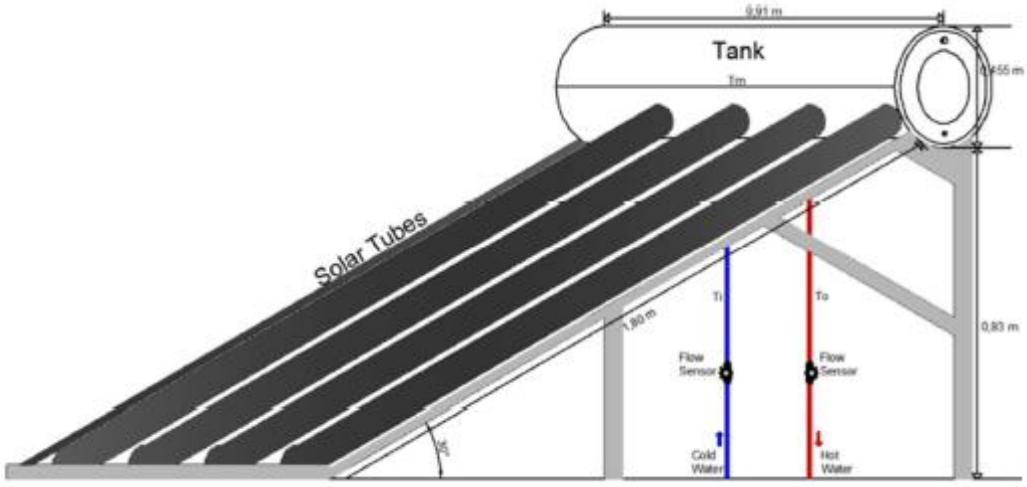

Figure 2.1: Thermosyphon solar water heating system (source: Samuel et al., 2016)

They used 10 borosilicate glass tubes (58mm outer diameter; 47mm inner diameter; 1800mm length), 150 litres storage tank and control valves. For the purpose of validating the model, the cold water temperature, working fluid temperature, collector temperature, storage tank temperature, insolation levels, hot water temperature, relative humidity, wind velocity and ambient temperature, were recorded at thirty minutes intervals. Energy conservation equations were written for heat transfer and fluid flow in finite-difference form, integrated and solved to yield the behaviour of the thermosyphon system at different insolation levels and water mass flow rate conditions as well as water storage tank temperatures. It was shown that higher solar

radiation enhances the solar collector energy conversion efficiency. Also they reported a very high water temperature in the storage tank, owing to efficient design of the system, which was attributed to less heat losses from the storage tank in the course of the water heating. The proposed model predicted fairly the evacuation storage tank time-temperature variation at various initial conditions of the water at the storage tank and solar radiations (Samuel et al., 2016). The major issue with the solar water heating system is excessive heat loss as a result of very high storage tank temperature.

The efficiency of solar water heating system is dependent on the effectiveness of the collector. It provides an overview of the size of the system and the interconnection between the collector area and the volume of water being heated. Three parameters are very important in determining the flat plate collector efficiency, namely, the gross area (total width by the total height), the aperture area (total glazing area exposed to sunlight) and absorber area (area of absorber exposed to sunlight). Ijemaru et al., (2014), adopted the gross area technique in predicting the solar collector efficiency in a thermosyphon solar water heating system and computed the effect on volumetric flow rate. The study showed that the efficiency and area of solar collector affect the time it would take to heat water for an average of $20.05^{o}C$ temperature difference. Hence, the larger the amount of water to be heated, the more the time needed to accomplish the heating.

Naveena and Sharath (2014) have numerically studied heat transfer enhancement to water from the flat plate solar collector absorber plate in a forced circulation mode by employing finned circular tubes and rectangular tubes with and without fins. They carried out the CFD analysis using FLUENT. The work also captured the potential of cost reduction for unglazed solar domestic water heating (SDWH) over the glazed collectors. The validation results show close

agreement. However, it is common knowledge that the solar thermal systems such as flat plate solar collectors experience the problem of lower efficiency level and energy losses by re-radiation and convection.

Rostamzadeh et al. (2011) carried out a numerical and experimental investigation of the flow and temperature distribution in a forced circulation solar water heater. They preferred forced circulation mode for the simple reason of achieving constant rate of mass flow in the system. The tests of experiments were performed under the outdoor clear sky climatic conditions of Tabriz, Iran with an ambient temperature of 31^{o}C, relative humidity of 57%, wind speed of 3 km/h and insolation of 1168 W/m^{2}. For the experiment, the collector comprised a total absorber area of 1.82m^{2}; 12 tubes of 1.5cm diameter and 194cm long each; 60-litres storage tank at a higher elevation to the rest of the system, with a 3mm sheet glass collector glazing; the mass flow rate was 0.005 kg/s while the inlet and outlet temperatures were put at 298 K and 358.3 K respectively. The flat plate collector was placed facing the equator at a tilt angle of 53.7^{o}N (latitude of Tabriz, 38.7^{o}N +15^{o}). A finite volume methodology was employed for the numerical descretization of the model equations developed for the simulation of the solar water heating system. They presented temperature contours, Nusselt number and temperature distribution in the tubes conveying the fluid. Numerical analysis showed a maximum outlet water temperature of 360 K. They investigated both elliptical and circular tubes and reported almost identical thermal characteristics for both tube configurations. They also investigated cases of parallel and series connections of the solar water heaters (SWHs) and reported that parallel coupling favours high mass flow rate while series connection best suits high outlet temperatures. An identifiable constraint in this system is the low mass flow rate reported. The model geometry and experimental configuration of Rostamzadeh et al (2011) is as shown in figure 2.2.

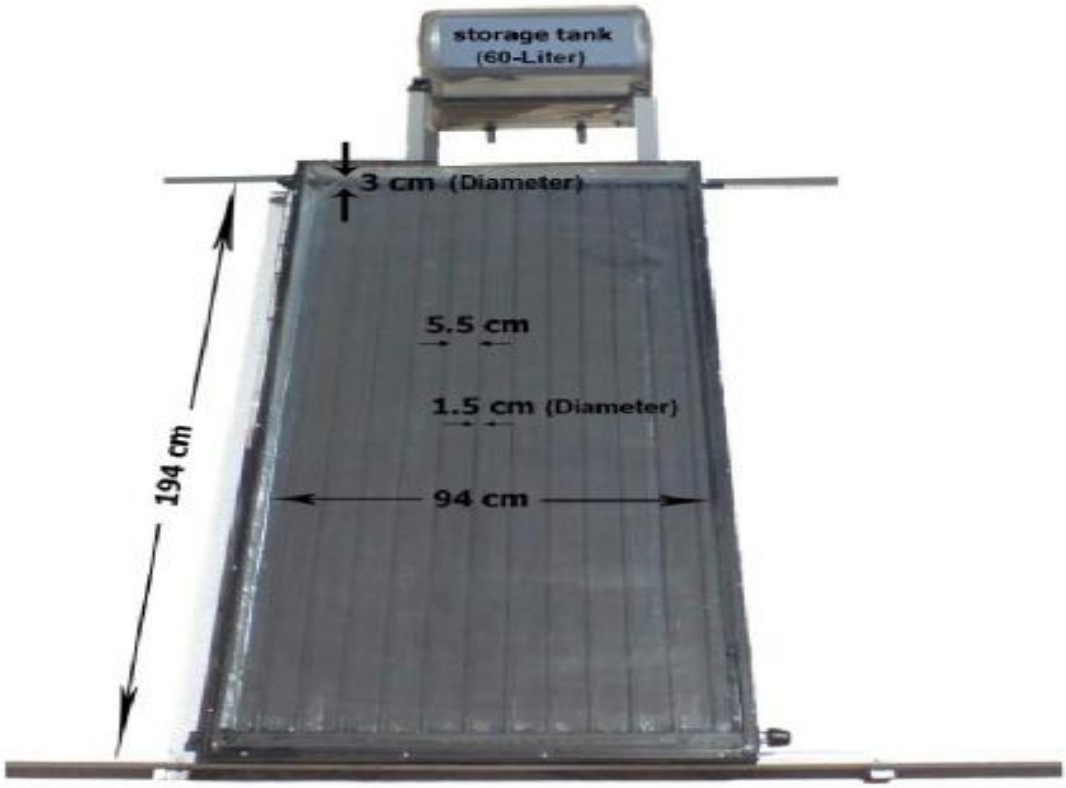

Figure 2.2: Model and experimental geometry of Rostamzadeh system (Source: Rostamzadeh et al., 2011)

Eswaran et al (2014) carried out a CFD investigation of an existing solar water heating system in order to improve its operating condition and geometry (figure 2.3). They concentrated on developing a model that would validate the reported mass flow rate of the said existing model which was experimentally given as 0.1 kg/s. They employed Solidworks and ANSYS FLUENT software for the numerical analysis and reported a maximum mass flow rate in the collector tube as 0.6 kg/s (a value well above the experimental value). They have identified a reduction in the overall thermal performance of the base system owing to non-uniform flow in the riser tubes. Hence, variable header system would ensure uniform flow velocity and improve overall thermal performance.

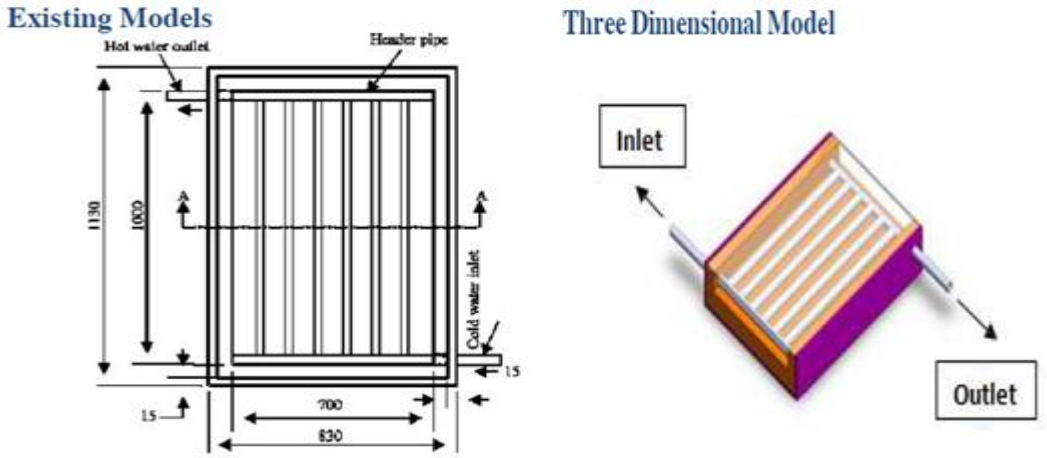

Figure 2.3: Existing model and 3-D model of solar water heating system collector Eswaran et al (2014)

Yarshi and Benny (2015) investigated the heat transfer performance of flat plate solar collector for solar water heating application using CFD. The focus of the analysis was to ascertain the effects of varying the shapes of the tubes, and such parameters as mass flow rate and absorber material on the flat plate performance. The lack of information on the various geometrical and operating parameters on the overall collector performance informed the study. They employed commercial ANSYS FLUENT software for the numerical computation and validated their numerical results with Ranjitha's experimental data.

They used a collector tube 0.8 m long, 0.012 m inner diameter, 0.10 m distance between pipes, with header pipes at both inlet and outlet of 0.24 m diameter and 0.8 m long. The collector overall dimension is 1.0*0.5*0.1 and the effective glazing area is 0.5 m^2, with a mass rate of flow given as 0.025kg/s in the system. The model assumptions included treatment of water as a continuum, incompressible, steady laminar flow and thermo-physical properties of absorber plate, water, absorber tube are all independent of temperature.

It was shown that increase in flow rate increases the collector efficiency, the outlet temperature increased with heat flux more in semi-circular riser tube than in circular (due to increasing absorbing area of tube which reduced the resistance resulting from the bonding material between

the plate and the tube, and the resistance due to the wall thickness of the tube) and the efficiency of the absorber increased with increase in absorber conductivities, making the absorber plate made of copper to have higher efficiency, followed by aluminium and finally steel.

Agbo (2011) in his work 'analysis of the performance profile of the NCERD thermosyphon solar water heater' modelled and simulated the performance of a thermosyphon solar water heater, which would help in developing and optimizing performance parameters for the SWHS designs, developed by the National Centre for Energy Research and Development (NCERD) at the University of Nigeria, Nsukka. The focus of the investigation was the effect of the number of glazing covers, glazing cover thickness, tube spacing and the nature of absorber plate material on the overall system performance. A maximum average daily collector efficiency of 65.8% and a mean temperature of 81^{o}C were reported. The collector efficiency varied with the seasons, dropping to an average of about 54%. The tube spacing for optimum system performance was found to be 0.1m irrespective of the nature of the absorber plate material. It was also found that the system top-loss coefficient is influenced greatly by the number of glazings, depending on the type of absorber plate used. For low temperature applications, multiple glazing is not attractive. Finally, it was also observed that the thickness of the glazing material has no significant effect on the system performance.

According to Riahi and Taherian (2011), the study of the entire thermosyphon solar water heating system performance is possible. They posited that under the climatic conditions of the South Caspian Sea, existing studies on thermosyphon SWH system either focus on the performance of the collector or the water storage tank. Therefore, they proposed and investigated the performance of the entire SWH system. To overcome one of the challenges of the thermosyphon solar water heating system, which is alteration of actual system performance in

the event of any flow obstructions, a non-intrusive method was used to measure the flow rate. In the work, the length of time delays in the collector and tank, as well as the level of thermal stratification in the horizontal tank was shown.

Their experimental set-up is as shown in figure 2.4, which is a Kian Energy commercial thermosyphon solar water heater installed at the Faculty of Mechanical Engineering, University of Mazandaran, Babol city (36E, 52N) and mounted facing south at a tilt angle of 45^{o} to the horizontal which is the appropriate tilt angle corresponding to the location latitude. The system incorporates two flat plate collectors, a horizontal storage tank (equipped with mantle heat exchanger), an up-riser and a down-comer pipe (3/4" diameter). Collectors were of single glazed aluminium flat-plate absorber type formed from 7 copper finned tubes, with each riser having an inside diameter of 12 mm and a 140 mm centre-to-centre spacing.

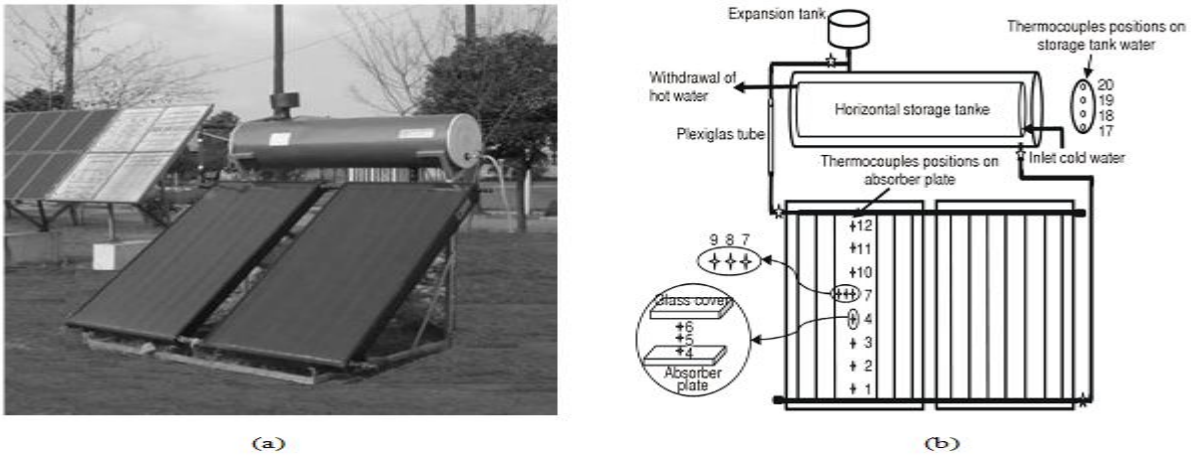

Figure 2.4: Kian Energy commercial thermosyphon solar water heater (a) Prototype (b) location of sensors for measurement (Source: Riahi and Taherian, 2011)

The system was equipped with several thermocouples to measure and collect data via a data logger. The collector temperature reached 90 °C at about an hour after the maximum solar insolation point. Their experimental investigations focused on the time variations of such parameters as absorber plate temperatures, storage tank temperature, temperature in the air gap between absorber and glazing, absorber plate temperature along fin width, mass flow rate, input

and output temperature, collector temperature, ambient temperature on a sunny day; time variations of absorber plate temperatures and storage tank temperatures on a cloudy day, and the variation of storage tank temperature with time at night; as well as the variations of absorber plate temperature along the height of plate and that of storage tank with height of tank. It was shown that the storage tank achieved a satisfactory thermal stratification, with a water top layer temperature reaching about 72^{o}C on a sunny day. The system worked well under the considered climate even in cloudy days and findings were congruent with that reported by other researcher.

One of the major issues with performance studies of thermosyphon solar water heating system is flow rate measurement. The measurement of flow rate poses a great difficulty because conventional flow measurement methods like the Venturi metre, Orifice metre and turbine metre are difficult to apply. Hence, recourse is made to such advanced techniques as Dye injection, Thermal tracing, Laser-Doppler Anemometry, Self-heated Thermistor and hydrogen bubble method, as revealed in few investigations.

Hammadi (2008) presented a theoretical study of the performance of natural circulation thermosyphon solar water heater under the climatic condition of Basrah city, South of Iraq, with latitude (30.4 N). The main study objective was to theoretically analyse the effect of collector geometry, orientation (tilt angle) and insolation on the performance of the solar water heating system, as depicted in figure 2.5 below. Water thermo-physical properties were considered as functions of temperature. Basrah city has an average temperature in the range 7-17^{o}C and the wind velocity ranges from 2.0-7.0 m/s. The performance of the solar water heating system is strongly dependent on such parameters as the collector location, collector tilt, wind velocity, and the solar time. Also solar intensity and water outlet temperature at the collector exit were found

to be dependent on the tilt angle. Moreover, the larger the tank volume, the lower the temperature of the water therein and the higher the time needed to heat it up.

From the investigation, it could be found that there was a strong connection between the area of the collector, the heat capacity of the collector and the wind velocity in a given climate. The larger the collector area and the higher the wind velocity, the higher the rate of heat losses from the collector and the decrease in water temperature. Hence, there is need for further investigation to ascertain the optimum collector area for optimal water temperature.

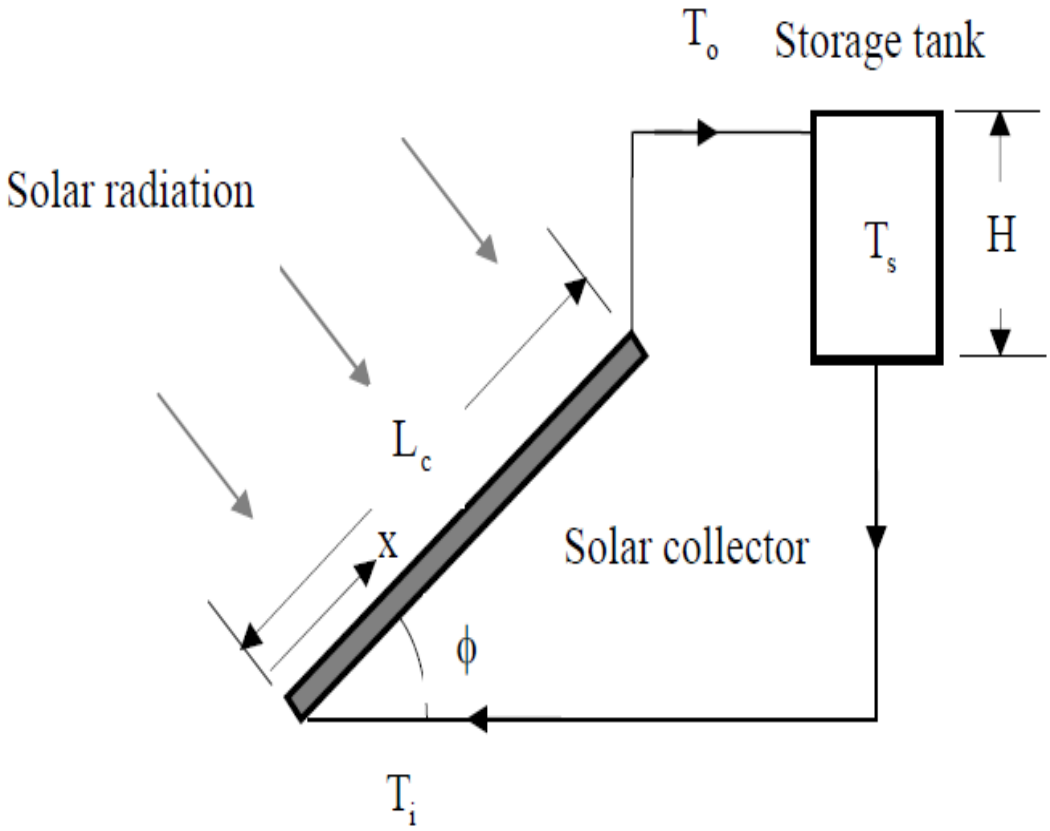

Figure 2.5: Schematic of natural circulation thermosyphon solar water heater (Source: Hammadi, 2008)

Kumavat (2016) carried out a numerical simulation of four different configurations of solar flat plate collector (types A, B, C and D) to ascertain the best configuration that would ensure optimum performance or efficiency and thereafter designed and fabricated same for experimental validation of simulation results, as shown in figure 2.6. The overall dimension for the solar

collector is 1882×960×93 mm^3 with 3 mm thick glass plate which was placed at 25mm above the absorber plate of thickness 2 mm. The collector inlet was of circular cross section with diameter 50 mm and the collector also has two outlets with circular cross sections having diameters 40 mm. The numerical results varied significantly with the experimental as would be expected due to local material characteristics as posited by the researcher. From the numerical results, type D design was recommended for fabrication and experimentation.

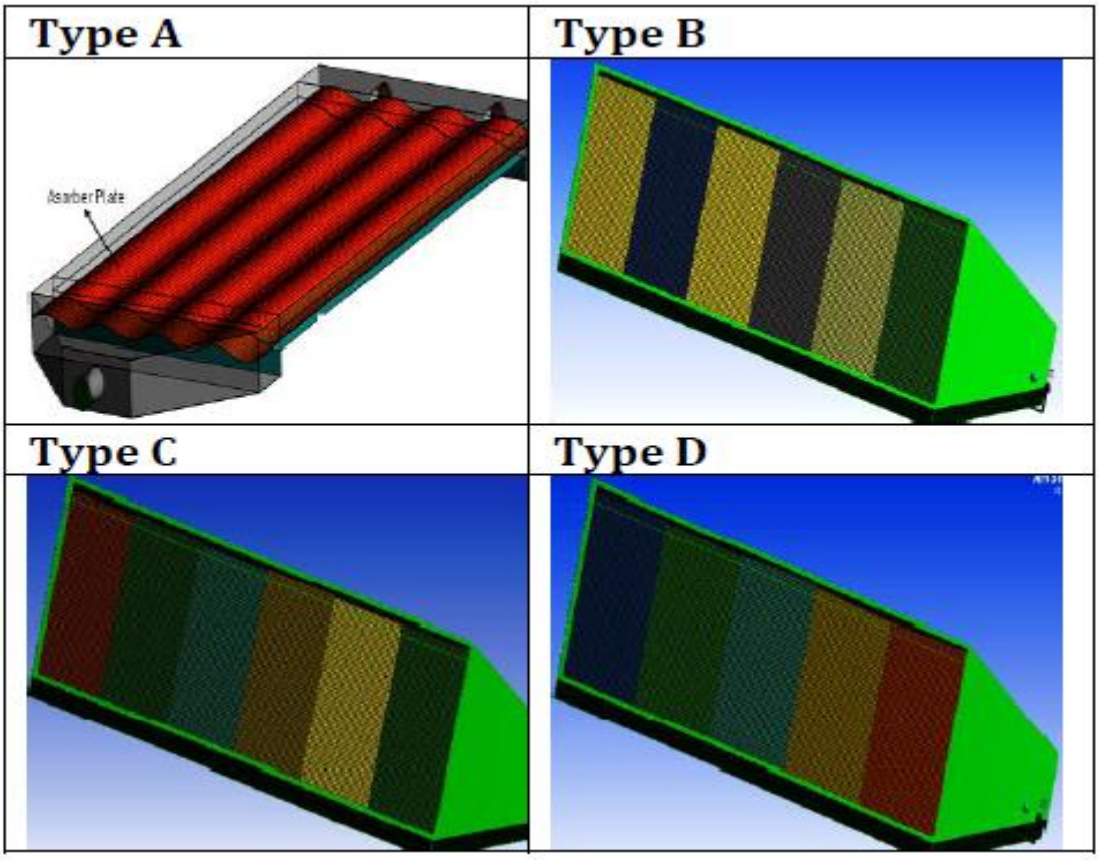

Figure 2.6: 3-D Mesh of the different configurations of flat plate collector absorber plates.

Freegah et al (2013) developed an insight into the understanding of the flow structure within a closed loop thermo-siphon solar water heating system by analysing the natural convection phenomenon using Computational Fluid Dynamics techniques. They created a virtual domain of the working fluid within the thermo-siphon system, operating under no-load condition and

investigated the effects of geometric parameters (the length to diameter ratio of the pipes connecting the condenser and the evaporator, number of connecting pipes, angle of inclination of the thermo-siphon) and the heat flux from the solar rays to the working fluid, on the performance of the thermo-siphon system. The results depicted that the heat flux and the length to diameter ratio of the pipes have significant effects on the performance of a thermo-siphon system. It was reported that angle of inclination has no pronounced effect the thermal system performance. Furthermore, an increase in the number of connecting pipes increases the temperature of the working fluid by absorbing more solar energy. In the main, they set out to show that CFD can be a useful tool to design, evaluate and optimise the performance of a thermo-siphon solar water system with reasonable accuracy. The geometry of the modelled system is as shown in figure 2.7.

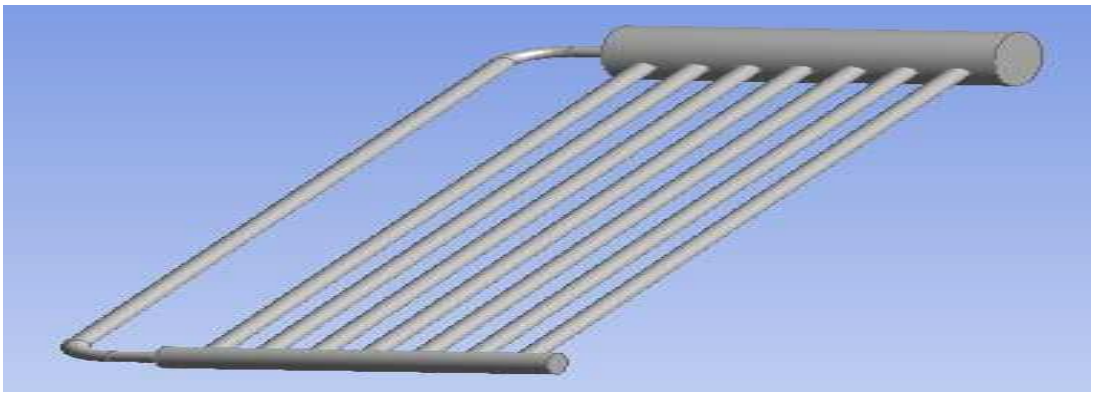

Fig. 2.7: Geometry of the modelled thermo-siphon system.

The numerical model of the thermo-siphon system was created with varying geometrical parameters while the working fluid (water), diameter (0.025m) and thickness of connecting pipes (2mm) were kept constant. They used a recirculating pipe of the same diameter with the connecting pipes to complete the loop. They modelled only the part with the working fluid since the system was under no load. The model was tested against length to diameter (L/d) ratios of 50 and 100, and fluxes of 250W/m^2 and 500W/m^2. The whole model was inclined by 30º and 60º for

clear visualisation of the natural convection phenomena occurring in the thermo-siphon. The observed outputs of the numerical investigation include the natural convection phenomena and the distribution of temperature, velocity and pressure of the working fluid within the model.

Vasudeva et al (2015) carried out numerical and experimental study of a solar water heater for enhancement in thermal performance using computational fluid dynamics. The analysis was majorly concentrated on the analysis of the solar water heater involving conduction and convection due to radiation heat on the sine wave absorber tube using CFD (since it is generally understood that sinusoidal flow passage tends to increase turbulence which in turn increases convective heat transfer) and the determination of the more optimal performance of the straight and sinusoidal absorber tube configurations. The modelled configurations of the flat plate collectors with straight and sinusoidal absorbers are as shown in figure 2.8.

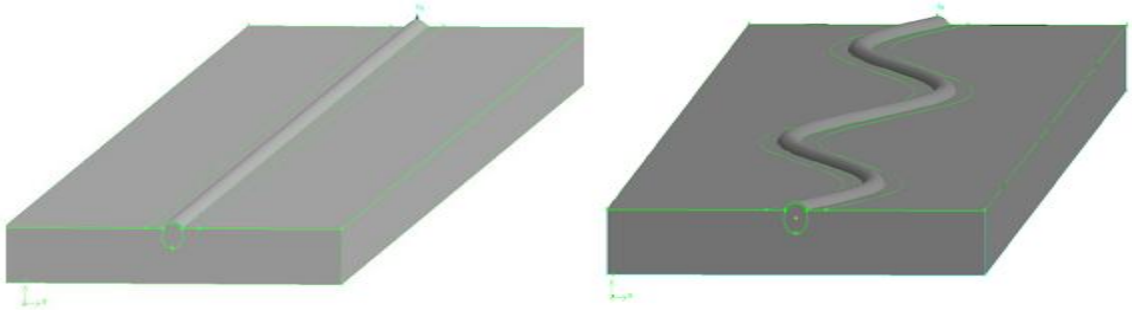

Figure 2.8: Straight and sine wave configurations of absorber tubes (Vasudeva et al., 2015).

The flow domain comprises absorber plates of 1.2 m length, 195 mm wide and 0.5 mm thickness. Absorber tube of 12.5 mm diameter and 0.65 mm thickness is attached below the absorber plate. The tube is centrally attached to the plate with a small angle of lap and both insulated with glass wool of 25 mm thickness. The sinusoidal geometry has a wavelength of 0.6 m and amplitude of 30 mm. For all the test conditions, it was found that the Nusselt number and convective heat transfer coefficients were higher for straight absorber tube than the sinusoidal

under same boundary conditions and mass flow rates. Hence, straight absorber performed more optimally than the sinusoidal.

Chaabane et al (2010) numerically investigated an integrated collector storage solar water heater (ICS-SWH) using FLUENT based on a finite volume methodology. The effect of storage tank position on the system performance was studied while the collector area and the storage volume were kept constant. The mean water temperature profile over time was investigated to highlight this position change's effect on water heating process. Streamlines and temperature contours were also investigated for a cross section of the solar water heater. The modelled geometry is as shown in figure 2.9 below.

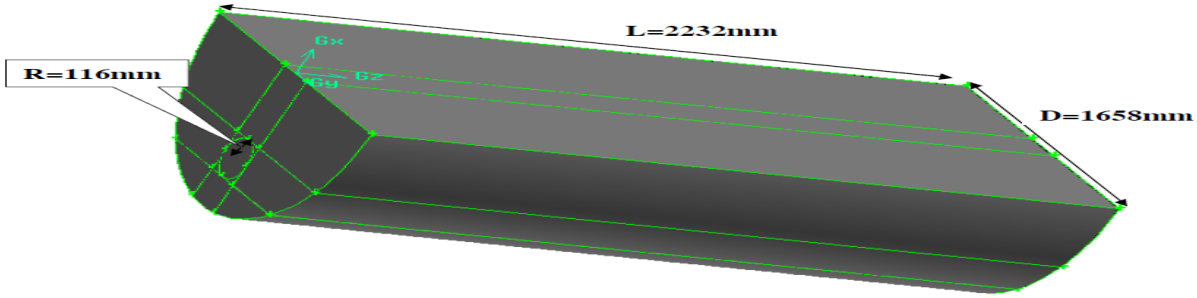

Figure 2.9: Modelled geometry of ICS_SWH (Chaabane et al, 2010).

The k-ε turbulence model was used to simulate the flow and the S2S radiation model was considered to introduce the radiative term in the energy equation. Validation studies revealed that reasonable agreement with model results in the case of unsteady simulation of the solar water heater. The change in tank position led to improvement in efficiency of the system by raising the water temperature in the tank.

Manikandan and Sivaraman (2016) experimentally assessed the performance of double glazed solar flat plate water heater incorporated with three different geometries of absorber plates, namely, flat plate, v-grooved and square pulse and varying mass flow rates (0.0041, 0.0083, 0.0125 kg/s). They employed mild steel plate of 1.42 x 0.7 m^2 size as absorber plates with two

glazing materials made of glass to protect the absorber plate from heat loss to atmosphere. It was reported that the thermal efficiency for the flat plate absorber was higher than those of the other two geometries. The configuration is as shown in figure 2.10.

Fig. 2.10: Double glazed SWH with three absorber plate geometries

The experimental setup consisted of mild steel absorber plates of 1.4 x 0.7 m^2, with different shapes of absorber tubes. Two glass plates of similar size were used to protect the absorber plate from heat loss to atmosphere. A gap of 2 cm was maintained in between top glass cover and the bottom glass cover. The bottom of the collector was covered with heat resisting material to minimize heat loss to the surroundings. An Agilent data logger (34970A) was used to acquire all the data at one minute interval while T-type copper constantan thermocouples were used to measure the inlet, outlet, absorber plate, glass plate, and ambient temperatures. Global Pyranometer mounted on a surface parallel to the collector surface was used to measure the global solar irradiance. The experiment was subjected to a uniform mass flow rate in all the three absorber geometries studied and it was found that the flat plate geometry outperformed the others.

Zeghib and Chaker (2015) carried out a modelling and simulation of a solar thermal system for domestic space heating to ascertain the thermal behaviour of a solar heating system at a low

temperature (50/45^{o}C), in the climatic conditions of Adrar, Algeria. They substituted a storage tank heated by a set of flat plate solar collectors for a conventional fluid heating boiler system as shown in Fig 2.11. The model evaluated the thermal (temperature) changes of each part of the system, namely, energy collection (via the collector), storage (in the tank), distribution and room indoor air. This aptly demonstrated that the hot water can be employed for home heating using low temperature radiators as against high temperature radiators provided by conventional boilers. The economic and environmental impact of the solar system carried out showed that the system did not only minimize energy consumption by 20% but also resulted in drastic decrease in carbon emissions and energy costs. Water was used as storage medium. This thermal model was a zero dimensional model based on the energy balance equations of the different components and concentrated only on the temperature variations in one direction in the system from inlet to outlet, both in the flat plate collector and storage tank.

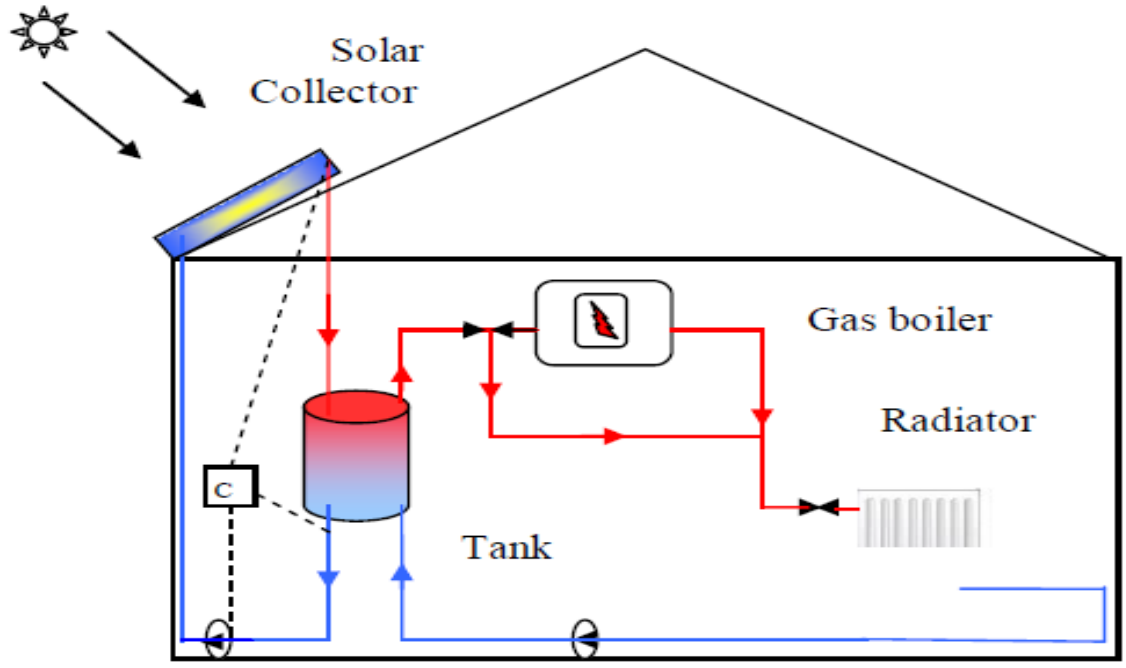

Fig. 2.11: Modelled solar heating system via a low temperature radiator (Zeghib & Chaker, 2015)

2.3 Nocturnal Water Cooling Systems

Nocturnal radiative cooling with night sky radiation phenomena could be considered as attractive technology with capability to be a passive alternative to the conventional air conditioning system (Ahmed and John, 2014). Several researchers have explored the different nocturnal cooling systems and applications for cooling of fluids by means of heat rejection by radiation to the sky at night.

A detailed study on the design and mathematical modelling of water chilling production system was carried out by employing the combined effects of evaporation and night sky radiation, using a panel capable of deducing separate effects of evaporative cooling and night sky radiative cooling from recorded data, under the climatic conditions of Sydney and Alice Springs. The radiator panel constitutes a sprayer as shown in figure 2.12.

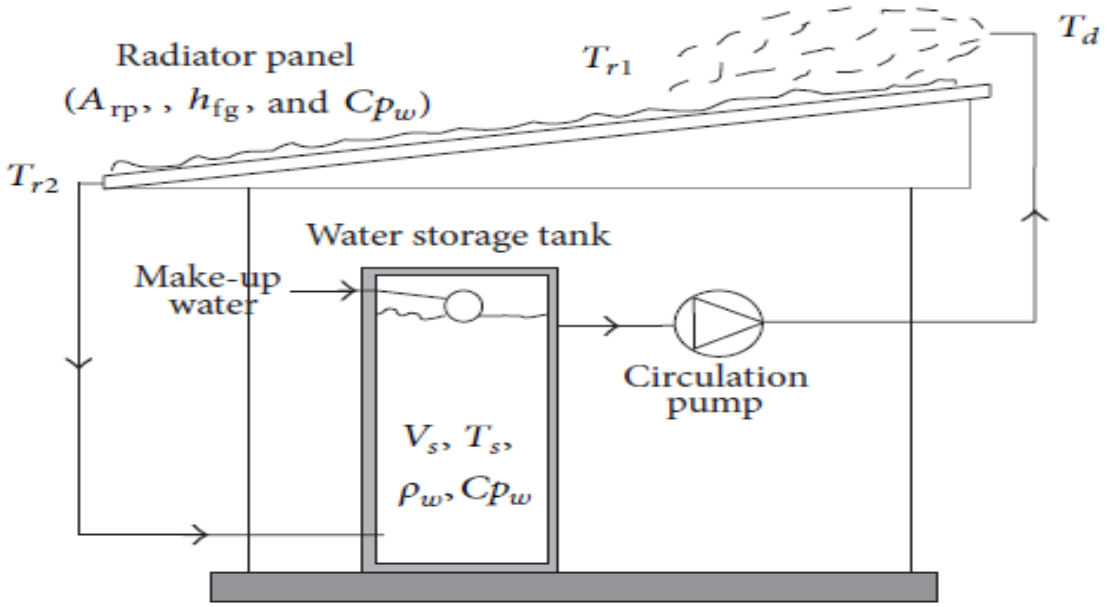

Figure 2.12: Experimental setup for the radiative cooling measurement systems-radiator panel with sprayer (Source: Ahmed and John, 2014).

The system comprises a radiator panel with a well-insulated back, storage tank and pump for circulation of water from the tank to the panel. Mass loss by evaporation occurs as water comes

into contact with air. There is make-up water to the tank at different temperature from the storage tank water temperature. Emphasis was laid on the tank, spray nozzle inlet, water pond inlet and outlet temperatures. They performed the simulation using the Transient System Simulation (TRNSYS) software to analyse the results in order to optimize the design parameters and investigate the contribution of the three heat transfer phenomena which occur in different nocturnal cooling applications. From the simulation results, a 260 litre volume of water, initially at 25^{o}C was cooled to as low as 13^{o}C using the net long wave radiation to a clear sky during summer night in Sydney and Alice Springs, being typical Australian climate. The simulation results were not validated.

Feng et al (2015) carried out experimental and theoretical performance evaluation of a flat-plate collector for radiative cooling purposes, using a cooling loop comprising a radiator, storage tank, pump, radiant floor and connecting pipes, under the climatic conditions of Beijing, China. They considered a closed system with the radiators mounted as integrated modules on the roof of a building, under a small tilt angle of 32^{o}C, which replaced conventional roof cover materials. The storage tank capacity was 300 litres and 10mm outer diameter copper tubes place 2-3cm apart were installed atop the unglazed collector. The pump in the upper part of the radiator lifted the heat carrier. Driven by the force of gravity the liquid trickles through the radiator intrinsic channels, releases heat and returns to the reservoir. The system is a drain-back system and the store represents the drain-back reservoir for the heat carrier when the system is not operative. The heat carrier circulates freely between the radiator loop and the storage tank without intermediate heat exchangers, as shown in figure 2.13. During the night, the water drawn from the top layer of the storage tank was circulated through the copper tubes and delivered to the

bottom of the storage tank, after being cooled, by exchange of heat with the low-temperature sky by convection and radiation.

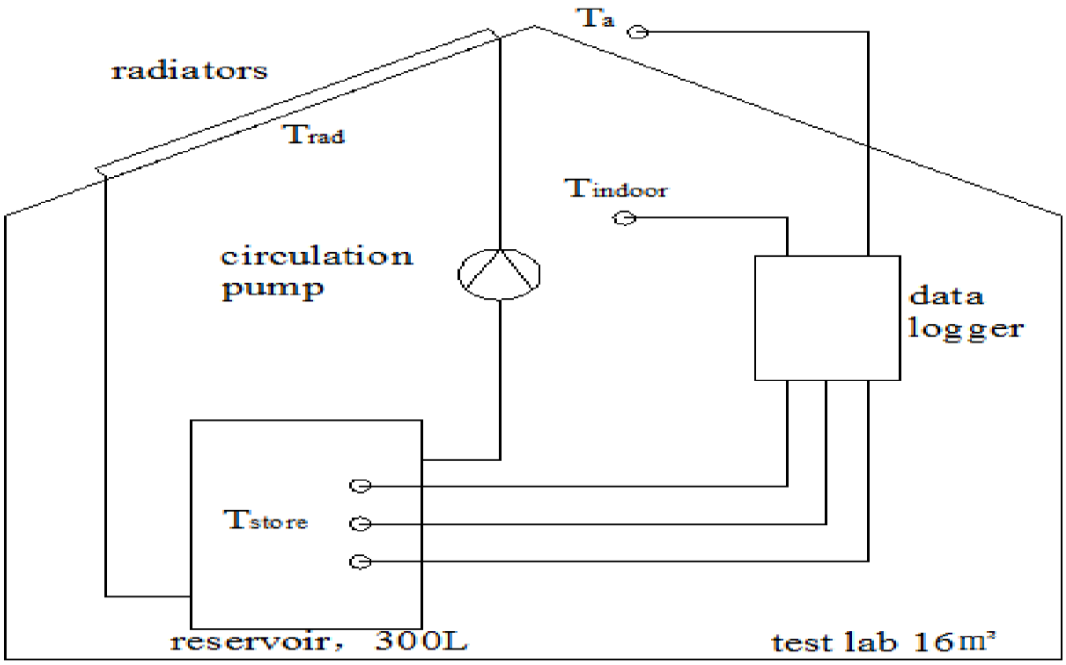

Figure 2.13: Fang et al. (2015) experimental set-up for the radiative cooling measurements

They analysed the heat loss of an unglazed night-sky radiator in line with radiation and convection theory, by circulating water through a $2m^2$ flat plate radiator at night. Cooling was by convection and radiation to night sky only. It was found that the vertical temperature field is uniform while the minimum floor surface temperature was 19.5^oC, with an average net cooling of about 26W/m2, with no condensation occurring. From the investigation of the effect of the design and operating characteristics of the night radiator on the system efficiency, it is possible to increase the total cooling capacity while maintaining a low pressure drop. This work has amply demonstrated the feasibility of cooling using fluid medium through nocturnal radiation.

Dobson (2005) of the Department of Mechanical Engineering, University of Stellenbosch, carried out a thermal modelling of a night sky radiation cooling system to ascertain the suitability

or otherwise, of the model as design tool for sizing of night sky radiation cooling systems. This was done in a room situated in the Namib Desert at Gobabeb, Namibia. The modelled system comprises radiator panels, a single water storage tank, room air-to-water natural convection heat exchangers or convectors, circulating pump(s), interconnecting pipe work and temperature sensors and controls, as shown in figure 2.14.

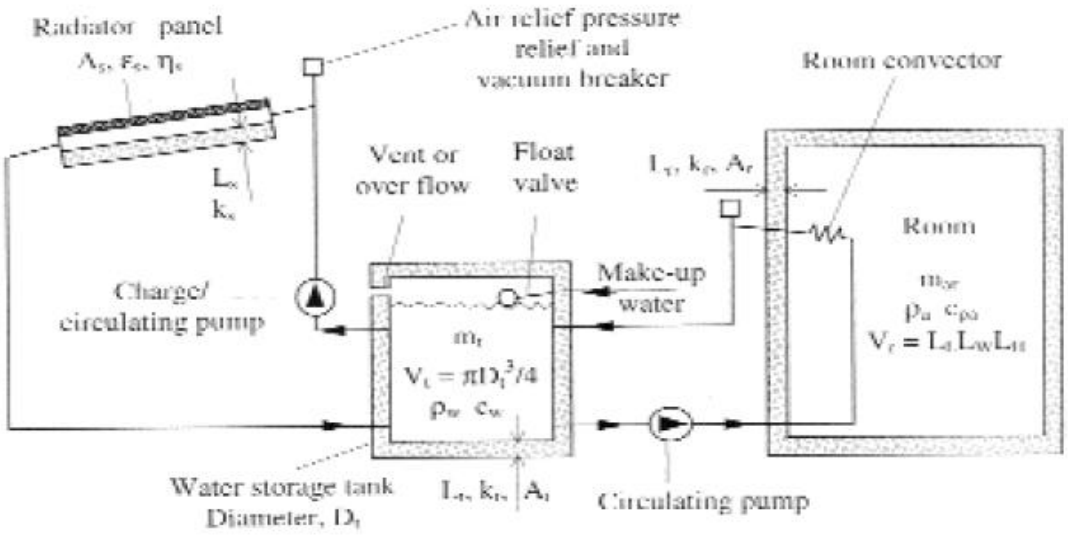

Figure 2.14: Schematic of thermal model of a night-sky radiation cooling system (Source: Dobson, 2005).

During night time, water from the storage tank is circulated through the radiator panel, where it is cooled by virtue of temperature differential between the radiator and the night sky. The cooled water drifts into the storage tank under gravity, from where it is circulated by the pump through convector to cool the room. The effective and efficient functioning of the cooling system much depends on the rational design and sizing of the different subsystems. It was found that the 48 m^2 radiator panel surface area was able to remove 84 MJ of heat energy from the water in the storage tank, corresponding to an average heat removal rate of 60.8 W/m^2. Because this value compares favourably with previously reported data, the researcher concluded that the thermal model can be confidently used as a design tool for the sizing of night sky radiation cooling

systems. Panels of high surface emissivity, specially coated with polyethylene cover sheet to reduce the convective heat transfer coefficient, were recommended for further improvements.

An experimental and numerical investigation of a nocturnal cooling system comprising unglazed flat plate collectors made of low cost Polyphenylenoxide resin and PC twin-wall sheets has been carried out under Oslo climatic conditions (Meir et al., 2003). The system comprises a radiator roof, a storage tank, connecting pipes, a pump and control unit and employs water as heat carrier, as shown in figure 2.15.

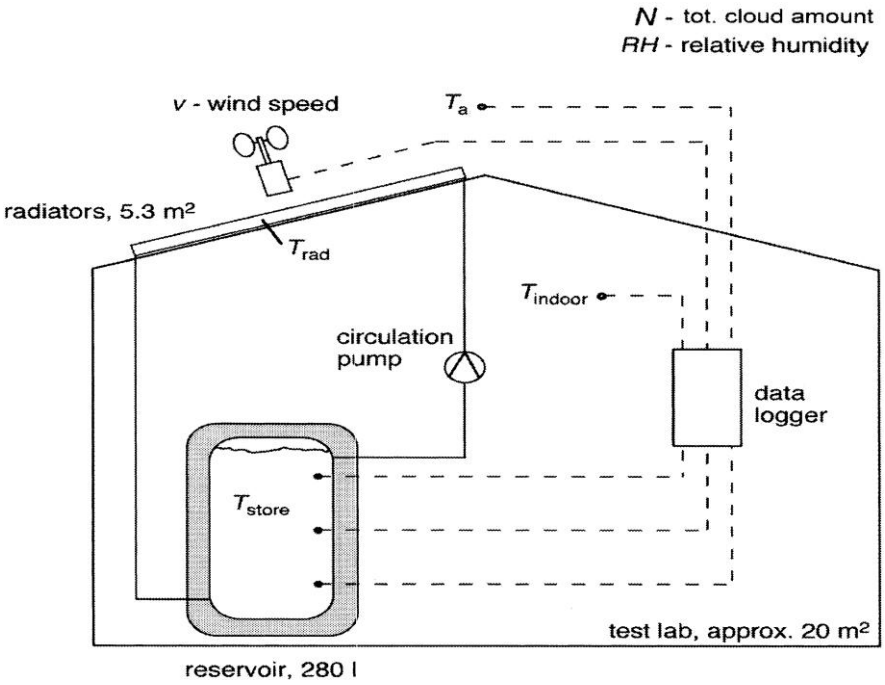

Figure 2.15: Experimental set-up for the radiative cooling system and recorded parameters

The radiators have overall aperture area of 5.3m and formed roof integrated modules while a 280 litres storage tank served as the water reservoir. The researchers applied a parameterization for a tilted radiator cooling performance on clear and cloudy skies to model the experimental results and investigated the impact of the angle of tilt, aperture area and storage tank volume on the cooling effectiveness and efficiency of the simulated system. The overall aim of the work was to determine the cooling power of the radiators. The analysis was simplified by avoiding a

simultaneous load while the radiative cooling system is in operation. And they proposed hydronic radiant distribution systems like ceilings or floors for conveying the cooling energy from the reservoir to the building. It was shown that even under unfavourable conditions; the system has the capacity to cover a significant fraction of the cooling demand. Also the simulation results show that sufficient radiative cooling much below 20^{o}C is obtained during modest air humidity and ambient night temperatures (Meir et al., 2003). They however, recommended simulation of the system covering a longer period of time to enable full and more elaborate evaluation as well as realizing employing the design for a cooling system in climates with significant cooling demands.

Thibault et al (2016) investigated the dependency of nocturnal radiative cooling technology on weather conditions, by developing a computational model of unglazed and photovoltaic/thermal (PV/T) collectors. The parametric study was carried out under the climatic conditions of Kgs, Lyngby, Denmark, based on the influence of such parameters as relative humidity, ambient temperature, cloud cover, cloud base height and wind speed on the radiative cooling output. One 2.4 m^2 unglazed collector of 2.4 and three series mounted PV/T panels (each 1.3 m^2) were modelled using TRNSYS commercial software. The simulation was validated with experimental results carried out previously and there was good agreement with little error margin. The results show that nocturnal radiative cooling highly depends on weather conditions. The cooling output depends heavily on the ambient air temperature, which impacts both the radiative and convective heat losses. In one night, a temperature drop of 9^{o}C resulted in cooling energy decreasing by 75% and an increase in temperature of 9^{o}C resulted in an increase in cooling energy of above 65%. There were also significant influences of cloudiness, wind speed and relative humidity on

the cooling output. The study revealed that unglazed collectors are slightly more efficient for cooling operations than PV/Ts, mostly when the cooling power peaks (above 100 W/m^2), due largely to the panel compositions (PV/Ts are covered by glazing panes that reduce heat losses while the unglazed collectors inherently loose more heat. Weather-dependent studies are very relevant to ascertain the most important parameter (s) that influence a particular renewable energy source so as to ensure a minimum production of energy, for any kind of weather conditions encountered. The researchers concluded that climates with lower temperatures at night, clear skies, relatively dry weather and windy would favour exploitation of nocturnal radiative cooling. The major constraint to the reliability of this model is that the difficulty associated with measuring cloudiness with the use of complex and expensive sensors, thus, making the cloud cover data for most locations unavailable. In this study, the cloud cover data used in the simulations was retrieved from a weather station located 10 km away from the experiment location, on hourly basis whereas the simulation was done in a minute time step. The presence of cloud as well as cloud altitude affects cooling energy output.

Nwaigwe et al., (2012) carried out transient analysis and performance prediction of passive cooling of a building in Owerri using long wave nocturnal radiation. They modelled a nocturnal water cooling system whereby they obtained cool water during the night, using a nocturnal radiator and used same for cooling of a room during the day via a heat exchanger. They developed a mathematical model based on the thermal radiation properties of the local atmosphere, the physics of heat exchange in the panel during the night and the physics of the relevant heat transfers of the space to be conditioned during the day. The developed model was solved using explicit finite difference scheme and implemented on MATLAB software. The

model sought to quantify the rate of heat removal from the storage tank through the radiator, the temperature depression between the ambient and room, and the total heat gained by the water in the tank from the conditioned space via the convector. Conclusively, the model result showed a radiator heat flux of 57.6W/m^2, temperature depression in the range 1-1.5^oC and the heat flux into the storage water was reported to be about 60W/m^2.

An experimental study of passive cooling of building using long-wave night sky radiation was carried out by Okoronkwo (2011) in the city of Owerri, Nigeria. This was a complementary validation study of the work reported by Nwaigwe (2011) in Owerri. The experimental rig was built using a flat plate sky radiator, heat exchanger, storage tank, water pump and pipes, incorporated in a rectangular room. The room housed two windows located east and south of the building with a door opposite the south window and the roof pitched at 12^o for cooling potential maximization. During the night, water passed through the radiator to be cooled and was channelled to the storage tank from where it was channelled to the room to be conditioned via convective heat exchange in the room convector during the day. He conducted series of tests under the meteorological condition of the Federal University of Technology Owerri, covering the major climatic seasons of Nigeria. He reported a minimum water temperature in the range of 21^{o}C-23^{o}C through night sky cooling and a maximum temperature depression of 3.5^{o}C below the average room temperature of 28^{o}C. A higher cooling power of 52.5W/m^2 was reported during the dry season as against 37W/m^2 during the wet season. The coefficient of performance of the system was relatively low (0.01-0.09), a situation attributed to the low relative humidity of the study location. The major foreseeable constraint revealed in this study is the need for more cooling energy for effective space conditioning in the tropics with high ambient temperatures

comparable to colder climate in the temperate region. Hence, much is needed to be done in terms of radiator property and material enhancement to further improve heat depression from the ambient conditions. Among other things, he suggested the use of highly selective surface coatings, porous medium in place of plastic tank, porous bricks lining sandwiched between the inner wall surfaces as evaporative cooling technique, to reduce wall thermal mass.

Balen and Vladimir (2005) mathematically modelled the dynamic thermal performance of a radiative cooling system to enable the design of a test rig for the system experimental analysis; using a high emitting surface flat plate radiator panel to cool water by means of nocturnal radiation towards the sky and convection to outside air during night time, with an integrated space-ventilation for air-cooling with cold water via cold-water coil. The panel was used to prepare cold water during the night by nocturnal radiative cooling and during the day, the collected cold water was used for cooling of the air in a room. They developed a simulation model for parametric analysis of the system as well as the influence of its components on the operation of the system and the control of the control of the system's operation, which prevented water circulation in the periods without cooling contributions. The simulation results were obtained for a small cooling system with a total aperture area of $6m^2$ and storage tank volume of 300L and tested under the Irish and Continental Croatian climatic conditions. The results showed that the radiative cooling system is more efficient in maritime than in moderate continental climatic conditions during summer. The aim of the research was to predict the system behaviour in order to enable sizing and design of the test rig that was to be built for validation studies.

The modelled system comprised a flat plate solar radiator, a water storage tank, a pump and controls, heat exchanger and an axial fan as shown in Fig 2.16.

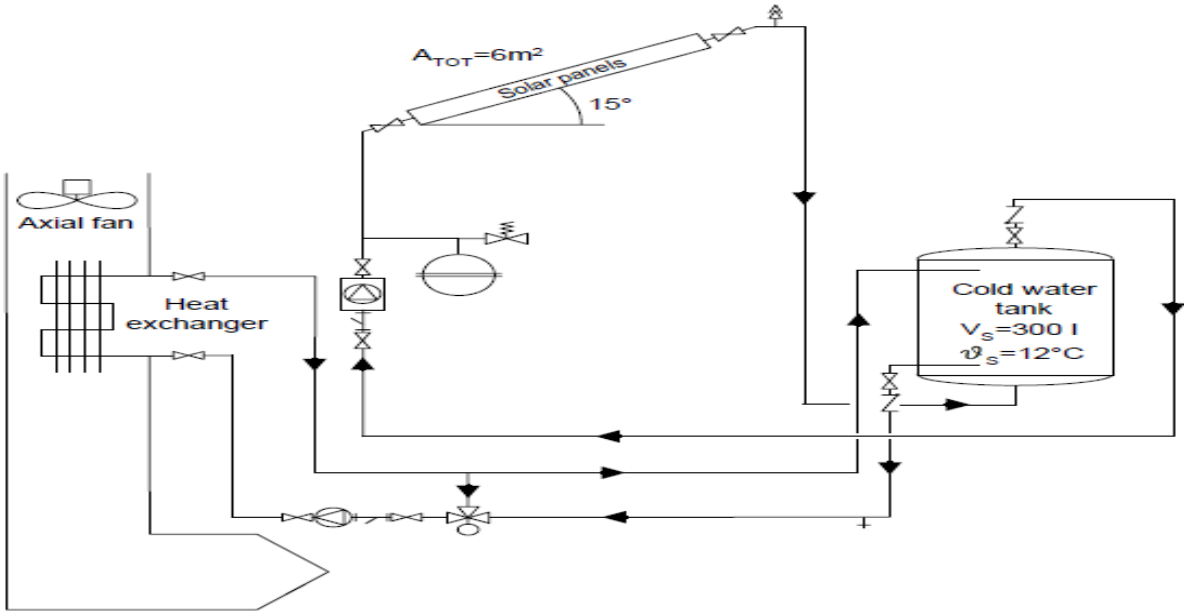

Fig. 2.16: Modelled schematic of radiative water-cooling system (Igor and Vladimir, 2005)

Partridge and Coulstock (2003) investigated solar heating and cooling potentials across a range of building types and climates, in conjunction with the Australian Greenhouse Office, using APACHE V4.02 software. They carried out numerical modelling of five buildings incorporating a conventional air conditioning system, an absorption air conditioning system and a desiccant dryer to treat outdoor air. The purpose of the design guide was to assist building owners, developers and designers during the early stages of a project in determining whether solar cooling or heating is likely to be viable. The design guide provides a graphical matrix of energy performances comparing cooling and heating system type with building type and Australian capital city location. The model results provided an indication of the relative benefits or otherwise of different solar cooling strategies in the specific buildings modelled as part of the overall research objectives. It is worthy of note that not all buildings are the same and variant parameters influence a final design solution. Consequently, the cooling trend developed for the

different buildings studied were considered far more important than the results for the type of research presented.

Ghassem et al (2010) presented numerical investigation of a hybrid nocturnal cooling and cooling coil/direct evaporative cooling unit under Tehran climatic conditions, as shown in figure 2.17. The behaviours of the hybrid system of the nocturnal radiative cooling, cooling coil, and direct evaporative cooling were investigated during 8 hours in Tehran. The nocturnal radiative cooling, during the night, provided the required chilled water used in the cooling unit. This was done by circulating water in a storage tank through a flat-plate radiator throughout the night. During the eight hours of the next day, spanning the period of office hours, the temperature of hot outdoor air was decreased (i.e. pre-cooled) using the cold water from the storage tank in a cooling coil unit. The pre-cooled air with lower wet bulb temperature passed through a direct evaporative cooling unit as shown in the figure. The pre-cooling of the hot outdoor air through the cooling coil unit augmented the efficacy of the entire cooling system. They investigated the temperature variations of the conditioned air. The results showed that Tehran has the capability of providing cold water at night during summer. Also, whereas direct evaporative coolers lonely cannot provide comfort conditions, the hybrid system has high potential to provide comfort conditions. In addition, the effectiveness of the hybrid system is considerably higher than stand-alone direct evaporative cooling. Taking advantage of sky as a renewable source of passive cooling, the hybrid cooling system can be considered as an environmentally clean and energy efficient system. Thus, this system can be used as a replacement for mechanical vapour compression systems, leading to decrease in electrical energy consumption.

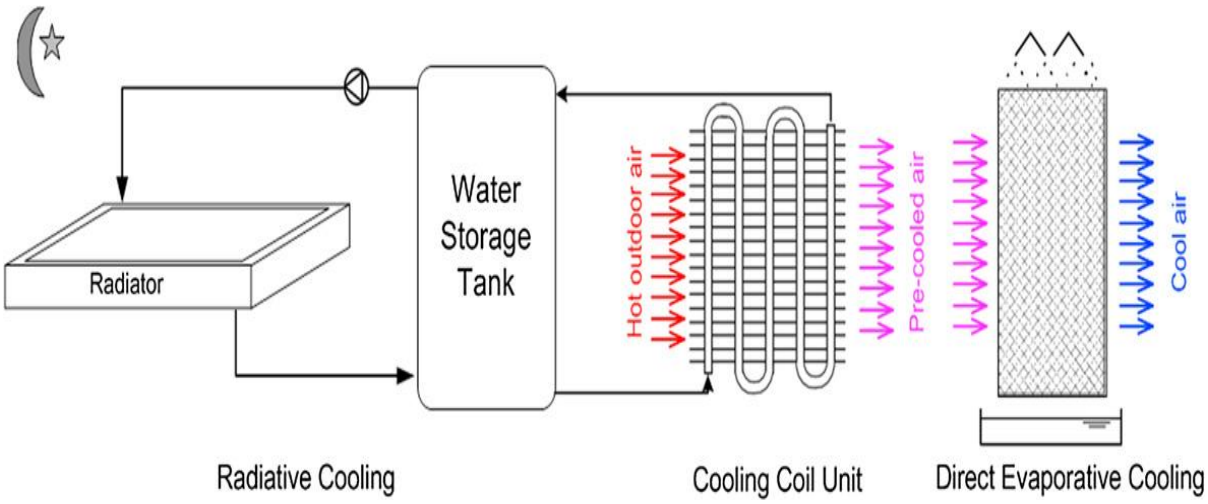

Fig. 2.17: Hybrid nocturnal cooling and cooling coil/direct evaporative cooling unit

2.4 Hybrid solar water heating and nocturnal water cooling systems

Balen et al (2003) carried out an extensive investigation on the development and design of a system utilizing solar energy to supply air-conditioning on an annual scale by the use of a single flat-plate both as a collector and radiator for both water heating during the day and water cooling at night respectively, under Irish maritime climatic conditions. The system designed was to prepare sufficient quantity of cold water using the night sky radiative principle and store in a cold water tank form where it would be used to accomplish air-cooling during day time. To do that, the panels were integrated in the space ventilation system with air-cooling by means of a cold-water coil. By small modification during daytime, the same solar panels can be turned into solar collectors and used to produce hot water, collected in a separate tank. They have developed a simulation model of the system in summer operating conditions and analysed the influence of its components on the operation of the system. The model includes the control of the system's operation, which prevents water circulation in the periods without cooling/heating contributions. The research objectives include analysis of solar system performance in cooling and heating operating mode. Hence, thermal analysis of cooling and heating of water, including weather data

analysis (temperatures, wind velocities, solar irradiation), together with design of the experimental rig were performed. The purpose of the research was to predict the system behaviour in order to size and design the test rig needed for experimental validation as part of a large research project. From the simulation results, it could be seen that significant hot water requirements could be met during the day time with a small modifications to the physical set-up. The proposed system experimental design is as shown in figure 2.18. Their design focussed on completely satisfying the cooling energy requirements by using a solar radiator and partly satisfying the heating energy requirements by modifying the same radiator to act as a collector, because heating demands are significantly larger than cooling demands in their absolute values.

The major constraint in this work is the difficulty in achieving good performance of a single flat-plate collector in both heat collection and heat dissipation modes since the requirements on collectors and radiators operation are opposite to each other. Thus, for small to moderate panel areas, system efficiency would be enhanced by using flat plate solar collectors for solar heat collection and modified swimming pool absorbers for nocturnal radiative water cooling. A single collector best suits large area requirements in order to offset costs and the flat plate can be adjusted by replacing its glazing with high-radiative cover for radiative cooling.

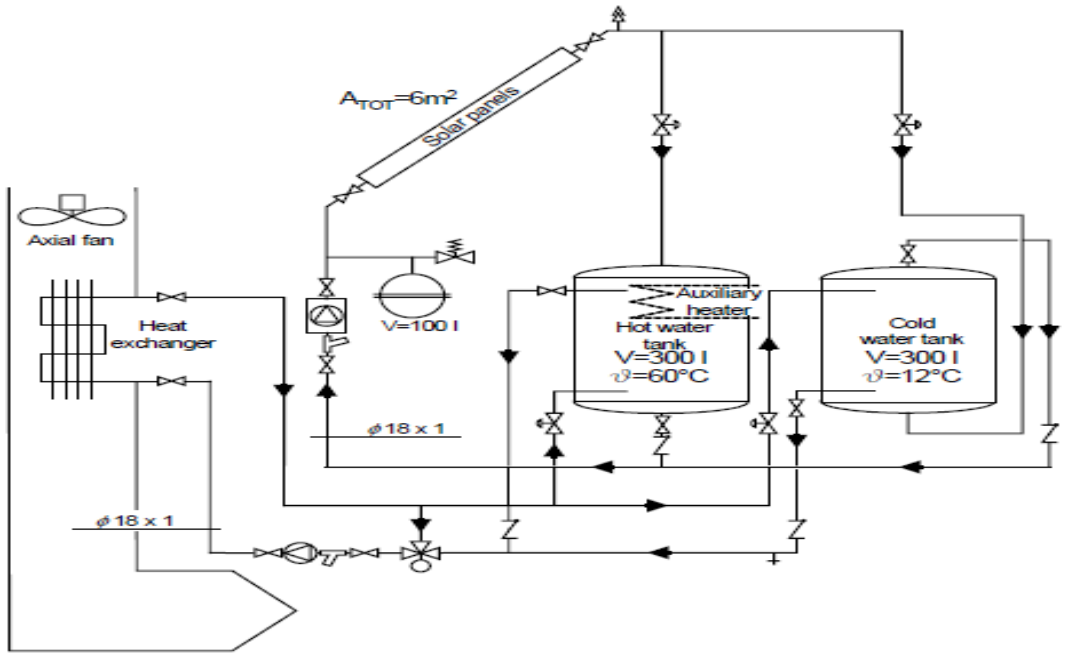

Figure 2.18: Schematic of experimental rig proposed by Balen et al (Source: Balen et al, 2003)

Mingke et al (2015) reported a composite spectrally selective surface, referred to as titanium polyethylene terephthalate (TPET), and manufactured same by the combination of titanium-based solar selective absorbing coating with polyethylene terephthalate, for both solar heating and radiative cooling, based on properties and limitations of solar collectors and nocturnal radiators. The panel combines the properties of high spectral absorptivity (approximately 0.92 and hence the ability to absorb enormous diurnal solar radiation) and emissivity (approximately 0.8 and hence the ability to obtain a large cooling power by radiating heat to the cold outer space at night) in the solar radiation and atmospheric window bands (i.e., 0.2~3 μm and 8~13 μm) respectively; and low absorptivity and emissivity of 0.55 in other bands outside the solar radiation and atmospheric window wavelengths (i.e., 3~8 μm or above 13 μm), and hence the ability to decrease diurnal radiant heating loss and radiant cooling loss during night time.

Polyethylene film has a high spectral transmittance in the entire 0.2~25 μm region, which indicates that it is a favourable windscreen for both solar heating and radiative cooling. This

novel panel has been employed in carrying out simple tests at the University of Science and Technology of China, Hefei, China ($31^{o}51'N$, $117^{o}17'E$) with ambient temperature of $35^{o}C$ and solar irradiation of $800W/m^2$ during daytime, and $30^{o}C$ during night time, to ascertain the extent of spectral selectivity in the spectra of both solar heating and nocturnal radiative cooling wavelengths. They tested both the diurnal and night equilibrium temperatures of the proposed surface (TPET) under varying sky conditions and different angles of inclination and found out that radiative cooling was better at zero inclination while heating was optimum at 32^{o} inclination, which is the latitude of the test location.

They also numerically investigated the solar heating and radiative cooling performance of the TPET surface and compared with three typical surfaces, namely, solar selective absorbing coating surface (conventional solar heating surface), polyvinyl-fluoride film coating with a sheet of evaporated aluminium (conventional radiative cooling surface), and ideal solar heating and radiative cooling composite surface (ideal composite surface), according to their spectral properties. The proposed TPET composite surface is as depicted in figure 2.19.

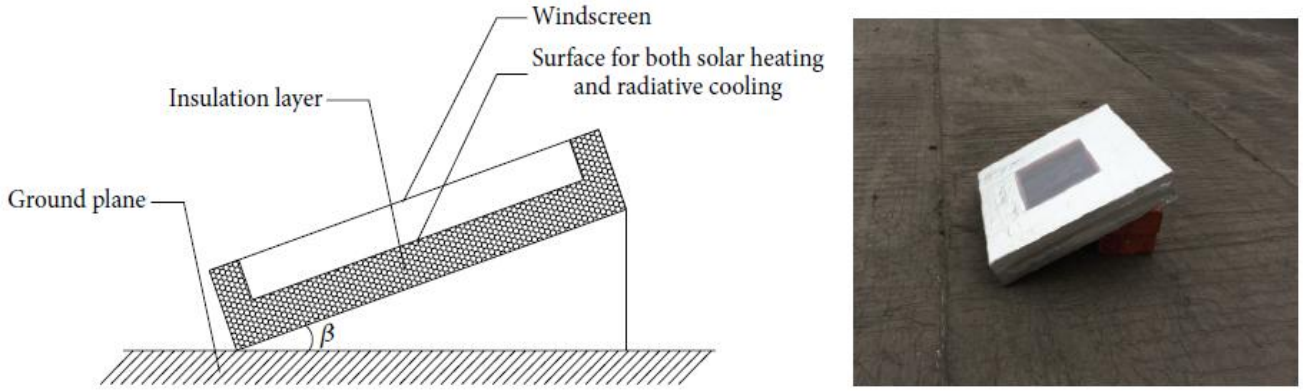

Figure 2.19: Schematic diagram and physical picture of the composite TPET solar heating and radiative cooling system.

The comparative results of a sample calculation performed by setting the temperature of each surface at $50^{o}C$ during the day and $25^{o}C$ at night are as shown in Table 2.1.

Table 2.1: Comparisons of the characteristics of surfaces and their heating and cooling performances under Hefei, China climatic conditions (Mingke et al, 2015)

	Function	$\alpha_{0.2-3\,\mu m}$	$\varepsilon_{8-13\,\mu m}$	$\alpha/\varepsilon_{3-8\,\mu m \text{ and } 13-25\,\mu m}$	η_1/%	η_2/%	T_r °C	q W·m^{-2}
Conventional solar heating surface	Heating	0.93	0.05	0.05	100	≈0	29.2	≈0
Conventional radiative cooling surface	Cooling	0.12	0.74	0.32	≈0	100	10.8	36.1
TPET composite surface	Heating and cooling	0.92	0.80	0.55	76.8	75.0	15.6	35.6
Ideal composite surface	Heating and cooling	1.00	1.00	0	80.6	166	−1.89	47.2

*T_r and q are equilibrium temperature and radiative cooling power of each surface, respectively.

The results showed that while the conventional heating surface has the highest efficiency in the heating mode, the conventional radiative cooling surface has the highest efficiency in the cooling mode. The TPET composite surface has a relatively efficiency of 76.8% in the heating mode and 75% in the cooling mode respectively. It was, however, shown that the cooling power was a little different. Even though the researchers have claimed that the TPET composite collector can address the shortcomings of conventional collectors and nocturnal radiators and shortens the initial payback period, research is ongoing on reducing the spectral absorptivity (emissivity) of the TPET composite or finding alternative materials with closer spectral properties to the ideal solar heating and radiators.

Alomer and Kiss (1988) designed a computerized method for predicting the heating and cooling performance of roof collectors based on a dual network model comprising the collector part model and thermal model of the storage tank. The collector part model (hydrodynamical model) is a mass flow network model which captured the modelling of the executional functions of the control system and determination of branch mass flows, while thermal part model captured the

temperature variations of the flowing medium and built from the heat flow network model of the storage, heat exchanger and consumption. They presented mathematical expressions, namely, a nodal type non-linear heat balance equation by lumping the collector into discrete parts along the flow direction and the heat balance equation for a partially stratified storage tank. No simulation was done and so no results were presented.

Matsuta et al (1987) constructed and investigated the performance of a selective type solar collector-sky radiator (SCR) that heated fluid to a higher temperature at daytime and cooled to a lower temperature at night. The collective-radiative surface was made of black copper plate with an effective dimension 1 by 2 m^2 coated with 9 μm thick polyvinyl-diflouride film (KF-Film). It has high absorptance within the visible and near-infrared band ($\lambda < 2$ μm) and atmospheric window band ($8<\lambda<13$ μm) and high reflectance for ($\lambda < 2$ μm), excluding the ($8<\lambda<13$ μm) band. They discovered in the course of the radiative cooling experiments, that a specular aluminium plate coated with 9 μm thick KF-Film reached lower equilibrium temperatures than the reference "black" radiator surface. Copper tubes of 10 mm diameter were attached to the collector for the flow of water and the collector-radiative surface was recessed 10 cm into a 30 mm thick glass wool box, covered with a 30 μm thick clear polyethylene film to prevent the convective heat transfer between the surface and ambient atmosphere.

Adnan et al (2015) developed and solved a numerical model using MATLAB to analyze the performance of a hybrid solar collector for water and air heating with different mass flow rates, using different shapes of the air channel and three volumes of the storage tank which was used to store (accumulate) the thermal energy gained from the sun by the collectors. The numerical

simulation was done using typical Romanian climatic conditions. They established that the efficiency of thermosyphon solar water heating (SWH) system can be increased by using a smaller collector area or larger hot water storage tank. This hybrid solar collector is working with water and air simultaneously. They adopted a sensible energy storage system to investigate the effect of the size of the storage tank volume on the accumulated energy, the collector and heat exchanger efficiency. The main components of the studied thermal heating system include a hybrid solar collector, three insulated fully mixed storage tanks and a pump, as shown below in figure 2.20. The research findings show that the Hybrid Solar Collector (HSC) system can raise the water temperature inside the storage tank to 30º C on a clear sky day, the efficiency of an HSC system can be increased by increasing the volume of the water storage tank and the HSC system permits storage of maximum thermal energy in the storage during the day than at night. The hybrid system did not consider solar cooling during the night which could be an improved means of energy storage gain at night.

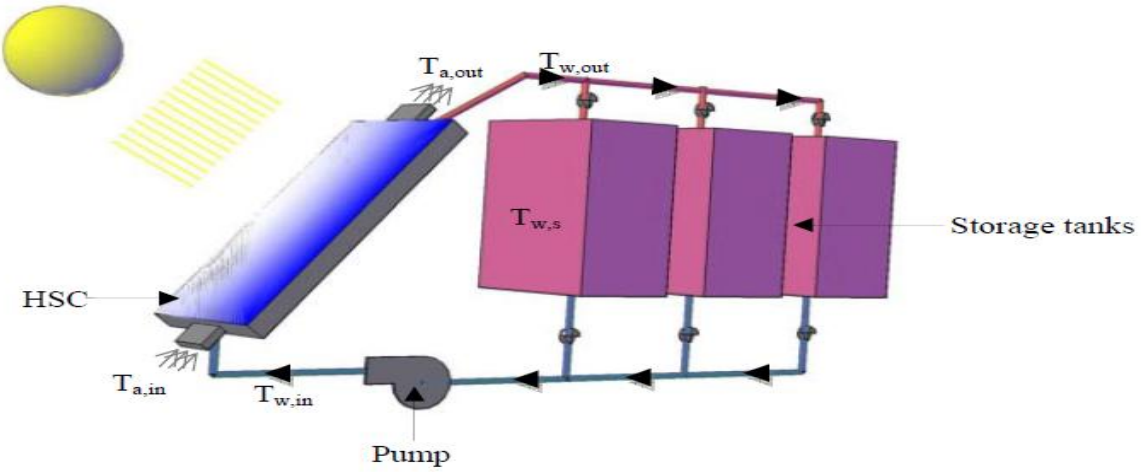

Figure 2.20: Hybrid solar collector (HSC) system with three different storage tanks volume

2.5 Thermal Stratification in Hot Water and Cold Water Storage Tanks

Stratification improves the overall performance of the systems by increasing the efficiency of solar collectors (i.e. reducing the average collector absorber plate temperature), making its investigation a necessary step towards overall system optimization. It is, therefore, important to understand the temperature distribution in hot water tanks in order to identify the factors which ameliorate or decline stratification in the storage tank (Ivette, 2006; Ayoola, 2014). Several factors have been identified to weaken temperature stratification in storage tanks, namely, the mixing produced by the inlet streams during the charge and discharge phases, convective heat losses to the environment from the tank envelope, conduction between hot and cold layers, thermal bridges along the tank walls, the volume of the tank, etc. These associated issues have made thermal stratification studies subject of many researches both experimentally and theoretically. Thermal stratification can enhance hot water availability during peak periods (mornings and evenings) with low or non existence solar irradiation. According to Ayoola (2014), the storage tank needs to be correctly-sized to ensure an optimum performance of a hot water solar heating system.

Torres et al (2013) numerically investigated the thermal energy storage (TES) system in domestic hot water (DHW) application in houses in South Spain, in order to create a simple tool that enables simulation of working cycle of solar TES systems incorporating encapsulated phase change material (PCM). TES systems utilization needs careful analysis, which depends on the climate zone and the local weather conditions. The working cycle of solar TES systems was simulated by applying finite volume discretization and enthalpy method for the phase change phenomena. The model was validated with available experimental results and a good agreement was obtained. They assumed perfect insulation for all the component systems (pipes, tank),

constant mass flow rate, and laminar, axial and incompressible flow, constant fluid velocity in the tank. The TES system combined with solar collectors is modelled as shown below in figure 2.21.

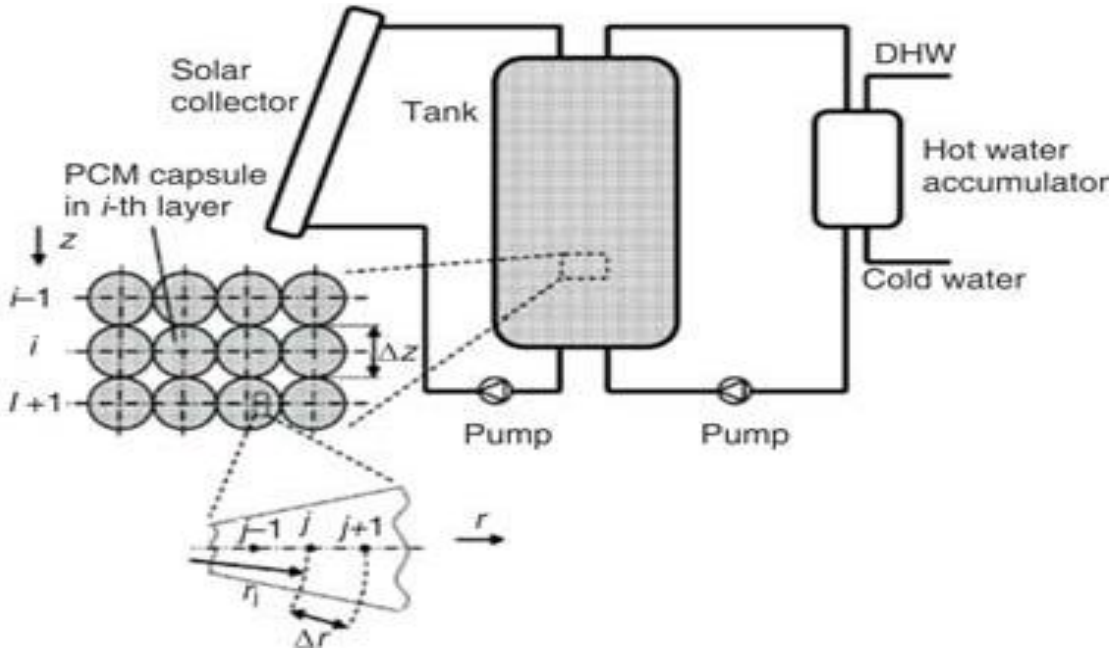

Figure 2.21: Model of Torres et al TES system

They assumed a spherical coordinate and developed the energy equation for the encapsulated PCM and the heat transfer fluid (HTF) in the axisymmetric co-ordinate system based on laminar, incompressible, constant velocity, negligible convection in PCM as well as temperature-independent HTF and PCM thermo-physical properties.

Wenfeng et al (2011) investigated the mixing characteristics of hot water inside a storage tank with different inlet velocities of the supply cold water by using three-dimensional CFD numerical modelling techniques, in order to provide viable insights for solar engineers to improve the design of solar water heating systems and develop a more accurate standard for testing the systems. The flow was considered transient buoyancy driven and hence a pressure

based approach with the energy equation was employed in the analysis. The geometry (physical model) of the hot water tank investigated in the work is as shown in figure 2.22.

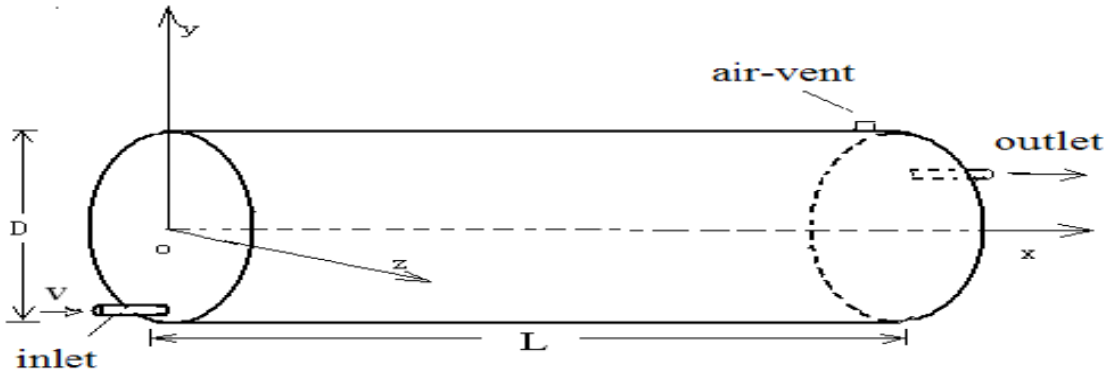

Figure 2.22: Modelled geometry of water storage tank of a SWH system

The geometry of the model is a typical cylindrical hot water storage tank most widely used in solar water heaters, with 1000 mm in length, 540 mm in diameter, and 15mm in diameter for inlet and outlet openings. An entrainment factor was introduced for quantitative determination of water mixing in the tank since mixing of hot with cold (makeup) water in the tank is related to the to the inlet velocity, temperature of the cold water, temperature of the hot water and the tank geometry. It was also revealed that significant turbulence can be found near the tank inlet/outlet interface, even for the case of very low cold water charging rate. While the effort concentrated on investigating the effect of inlet velocity of cold water on the entrainment factor and water mixing, the temperature and geometry were left out. With the increase in inlet velocity, the heat discharging efficiency decreases and the mixing of hot water and cold water in the tank becomes more significant.

Ivette (2006) investigated numerically the unsteady laminar convection in cylindrical domains and its application to the study of heat transfer and fluid flow phenomena occurring in stratified storage tanks. Thermal stratification occurs in water storage tanks as a result of the mixing due to

the inlet streams during load and unload (inlet and outlet), heat losses to the environment, etc and the degree of stratification determines the amount of energy stored. The focus was using virtual prototyping concept to study the behaviour of the fluid under different working conditions and tank configurations leading to the proposition of a non dimensional exergy-based parameter as a tool for assessing and comparing storage tanks as well as determining the quality of stored energy. He also analysed the thermal behaviour of the storage tank during the static mode of operation in the light of heat losses to the ambient to develop an understanding of water cool down in the storage tank for solar thermal systems in the low-to-medium temperature range. The configuration is as shown in figure 2.23.

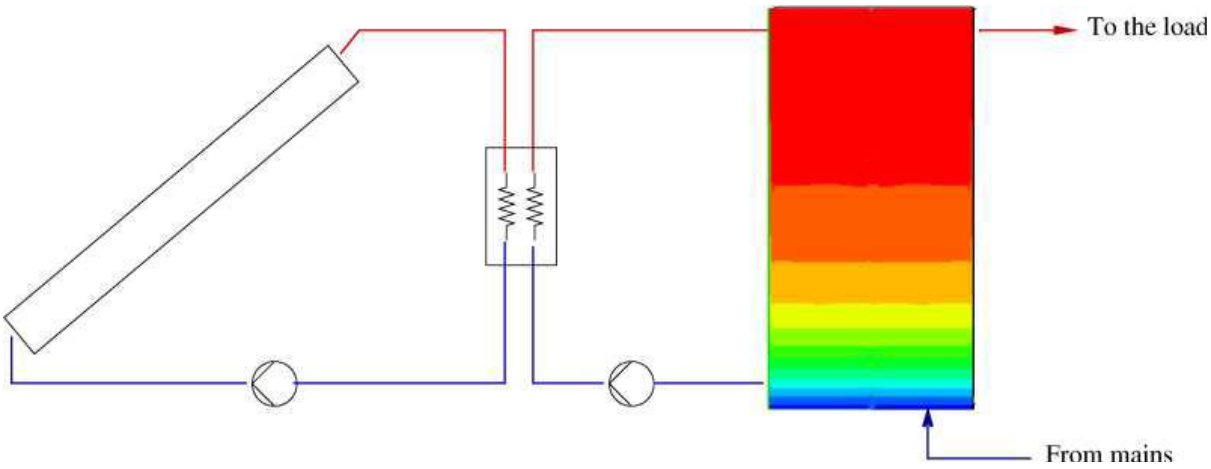

Figure 2.23: Studied solar domestic hot water system with thermal stratification in the storage tank.

Temperature gradient in the tank sets up corresponding density gradient. At the inlet to the tank (from the collector) occurs a mixing fluid region which is gradually pushed down with more fluid entering the tank. This creates a region with steep temperature gradient known as the thermocline. The continuation of the charging process causes the thermocline region to travel down, limiting the mixing between the cold and hot regions. In the main, the thickness of the

thermocline is useful in optimizing the functioning of stratified tanks. The higher the mixing at the inlet, the thicker the thermocline zone.

Water is the most attractive choice of fluid as storage medium, mostly, in the low-to-medium temperature due largely to its abundance, low cost and good thermal properties such as high specific heat capacity and density. In sensible heat storage cases, the heat capacity of the storage medium forms the major parameter. In majority of the solar thermal energy systems, water is heated during the day, stored for use during the day time or night time while in nocturnal cooling systems, water is cooled during the night and stored for use in space conditioning during the day. The main objective of the storing process is to maintain the thermodynamic availability of the stored energy to allow its extraction at the same temperature level at which it was stored. The storage capacity in low-to-medium solar energy systems is constrained by the moderate range of working temperature, hence, requiring relatively large tanks in order to store large amounts of energy. To optimize the cost of solar energy systems, stratification is the best option. This study was undertaken with the assumption that the flow is laminar and incompressible, without any participating radiating medium.

2.6 Summary of findings from literature

The foregoing review has extensively explored the existing works on solar heating and nocturnal cooling of water as independent systems, as well as the existing works on combined solar heating and cooling as single units. It is pertinent to note that the initial capital outlay of the hybrid solar heating and nocturnal cooling projects is quite enormous and would increase significantly if the development of the prototype would commence without optimal sizing of the components of the system. One of the cardinal objectives of the literature review was to ascertain the coverage of the hitherto undertaken investigations, establish research gap(s) and then devise a most suitable means of filling the identified knowledge gap(s). Trailing behind this, is the effort to explore the modelling approaches so far adopted in studying solar water heating and cooling systems, and their capabilities. While lots of work have been done on solar water heating and nocturnal cooling as independent units, only a few investigations have attempted to look at solar water heating and nocturnal radiation cooling as a hybrid unit, such as the works of Balen et al (2003) and Mingke et al (2015).

Literature shows that modelling and simulation of solar water heating and cooling either as a single or hybrid system, is location specific because of varying climatic conditions. As a result of this, model input parameters vary and hence the system output. Therefore, it becomes a sine qua non to make parameterisation of numerical codes location specific in order to fully optimize the system. Currently, all the models developed and their parametric studies are based on temperate climatic conditions. There is the need, therefore, to provide data base of the behavioural characteristics of such systems under tropical conditions.

The existing works reveal that full systems description and optimization are strongly dependent on thorough understanding of both their dynamic and thermal behaviours. Despite this, almost all

the works hitherto carried out concentrated on the study of their thermal behaviour based on energy balance equations, which only simulate temporal variations of thermo-physical properties at different climatic conditions. This modelling approach is more or less a one or zero dimensional modelling approach and leaves much to be desired because it only fully captures the inlet and outlet conditions of the systems and lacks the capability to provide the fundamental parameters needed for system optimization. For example, because measurement of fluid mass flow rate is always a challenging task in such systems, these studies assume a constant fluid mass flow rate which is a limitation in dynamic systems. These are mostly analytical studies requiring expensive experimental trial and error analysis using physical prototypes to supply the necessary information such as convective heat transfer and pressure loss coefficients, mixing parameters, etc, for the models in question.

Since the collector serves as a heater in the day and a radiator in the night, the thermal and dynamic behaviours during the diurnal and nocturnal operating modes need to be investigated using the transient full three dimensional heat transfer and fluid dynamic nature of the flow field in the collector and piping networks. The transient three-dimensional fluid dynamics within the thermal storage tanks is one of the critical factors affecting the thermal efficiency of a heating system under a dynamical load situation, and is crucial for the improvement of the performance of solar water heaters and utilization efficiency under the dynamic load situation. There is no evidence of work done on the dynamic behaviour of the hybrid diurnal solar water heating and nocturnal water cooling system. Therefore, both the thermal and dynamic behaviours of this system are still open areas of research.

Some of the inherent difficulties in solar water heating and cooling systems include integration to building envelopes, adaptation to varying climatic conditions, flow rate measurements,

development of spectrally selective surfaces that can serve both as a diurnal collector and nocturnal radiator. Despite the fact that Mingke et al (2015) reported a composite spectral selective surface, titanium polyethylene terephthalate (TPET), that is both highly spectrally absorptive and emissive in the solar radiation and atmospheric window bands, as well as lowly absorptive and emissive outside the radiation and atmospheric window bands, studies to ascertain optimum spectral selective surface through combination of different materials are necessarily required. Furthermore, the design and optimisation of thermal collectors and stratified storage tanks require a profound knowledge of the thermal and fluid dynamic phenomena involved.

Modelling has become imperative to fully address these difficulties, mostly as virtual prototyping has become a ready, viable and available engineering optimization tool for thermal systems, allowing a drastic reduction in costs and time. This reduces the efforts made to embark on expensive experimentations and provide a technology that enables prediction of parameters that are intricate to measure experimentally, such as the mass flow rates. Therefore, the current investigation is premised on the fact that, to the best of the knowledge of the researcher, there is no study at present that has taken care of a comprehensive numerical investigation of both the dynamic and thermal behaviours of hybrid solar water heating and nocturnal cooling system under either temperate or tropical climatic conditions.

CHAPTER 3

RESEARCH METHODOLOGY

3.1 The hybrid solar water heating and nocturnal cooling system configuration

The configuration of the hybrid solar water heating and nocturnal cooling system modelled is illustrated in Fig. 3.1. It comprises a single spectral selective surface-coated absorber/radiator, for both water heating and cooling, otherwise known as the Solar Collector-Nocturnal Radiator (SCONOR) panel; hot water storage tank (Reservoir A); cold water storage tank (Reservoir B); a room convector (for space cooling); a room radiator (for space heating); pump A (for water circulation from the tanks to the plate); pump B (for cold water circulation from the cold water reservoir through the room convector for cooling the room during hot ambient day or hot water circulation from the hot water reservoir through the room radiator for heating the room during moderate to high cold ambient periods); valves, connectors, pipe network and temperature sensors.

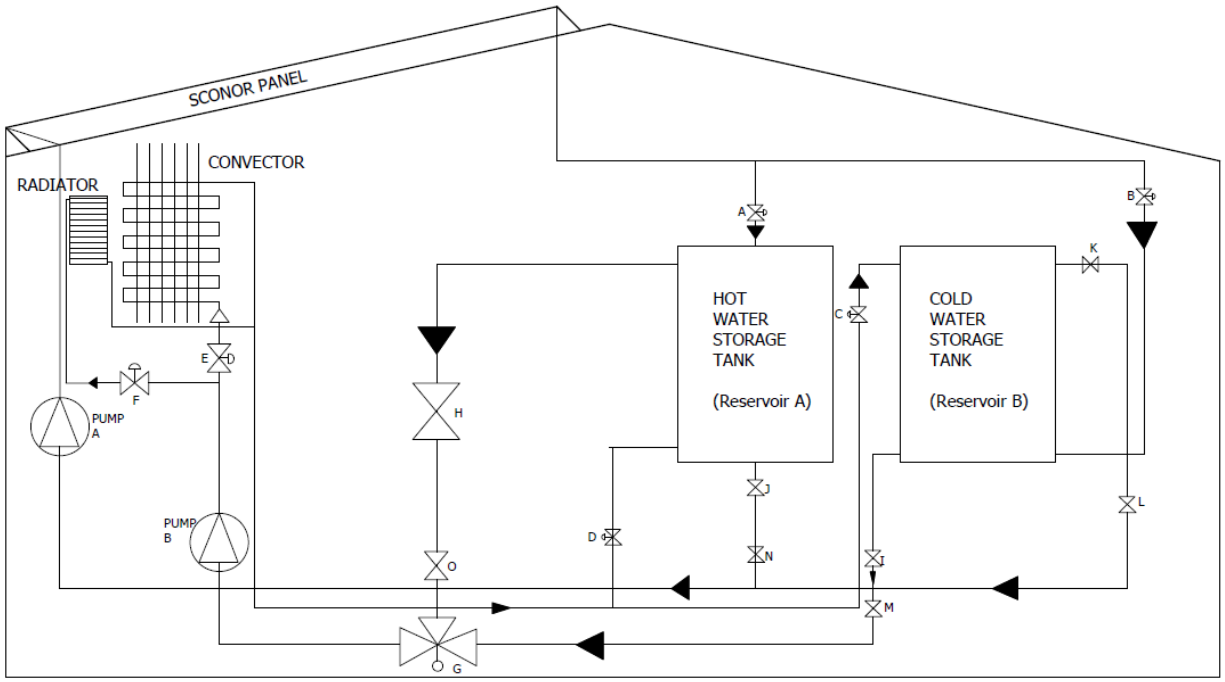

Fig. 3.1: Hybrid solar water heating and nocturnal radiative cooling system in a building envelope

3.1.1 The Solar Collector/Nocturnal Radiator

The hybrid flat plate solar collector/nocturnal radiator functions as the heart of this type of system. It collects insolation for heating water during daytime and dissipates heat to the environment thereby cooling water during the nighttime. Thus, if SCONOR is coupled to thermal storage, its hot water can be harnessed during the day and the nocturnal cooling can be used to keep a space cool throughout the day. The SCONOR comprises a flat-plate Titanium based absorber coated with a Polyethylene Terephthalate Powder, which is a special purpose spectral selective surface in both the solar radiation and atmospheric window bands. Its special surface coating derives from the fact that conventional solar collectors cannot function as nocturnal radiators during nighttimes while nocturnal radiators cannot function as solar collectors during daytimes. This is because conventional collectors have extremely low spectral emissivity in the atmospheric window spectrum ($8 \sim 13 \mu m$) while conventional nocturnal radiators (radiative cooling devices) have very low spectral absorptivity in the solar radiation spectrum ($0.2 \sim 3 \mu m$). The efficiency of a collector (in the heating operation) depends on its spectral absorptivity within the solar radiation wavelength (which must be very high in this band) and heating losses (which must be as low as possible in this band) while that of a radiator depends on spectral emissivity (which must be very high within the atmospheric window wavelength) and low heat gains from the surrounding. Therefore, the selective treatment on the absorber surface enables the SCONOR plate to switch between diurnal and nocturnal operations.

There are SCONOR tubes of copper material bonded onto the underside of its plate at specified intervals. The tubes are fixed to common inlet and outlet headers with the aid of fittings. Water flows through the copper tubes to be heated or cooled during the day or night, respectively. The

plate together with the tubes is placed on insulation inside a box made of 16G galvanized steel sheets.

It also incorporates a polyethylene film, referred to as a windscreen (Mingke et al., 2015), which serves to reduce wind effects and convection losses from the top of the absorber. The polyethylene film is also highly transparent, allowing passage of long wavelength and short wavelength radiations, hence, helps the SCONOR function as a solar collector during the day and a nocturnal radiator during the night. In order for the SCONOR to function effectively, both the surface and windscreen would allow exchange of radiation within the entire $0.2{\sim}25\mu m$ wavelength window, covering both the solar radiation spectrum of $0.2{\sim}3\mu m$ and atmospheric window spectrum of $8{\sim}13\mu m$. Thus, the optical properties of the windscreen depend on the period of the day; the windscreen being characterised by high transmittance in the wavelength range of $8{\sim}13\mu m$ (Mingke et al, 2015).

At present, such compounds as silicon oxide, magnesium oxide, Lithium Ferride, Polyethylene Terephthalate and Zinc Sulphide have been used as radiators with only Polyethylene Terephthalate achieving up to 11^{o} equilibrium temperature lower than the ambient. Though Zinc Sulphide is very close to Polyethylene, it is reportedly extremely expensive. A radiopaque Titanium solar selective absorber coated with Polyethylene Terephthalate film as a composite solar absorber/radiator surface, with Polyethylene film as a convection cover (or windscreen) to reduce losses due to convection has been reported (Mingke et al, 2015). They found out that Polyethylene film has high spectral transmittance in the entire $0.2{\sim}25\mu m$ spectrum while the titanium-base selective absorber/radiator has spectral absorptivity of about 0.92 within $0.2{\sim}3\mu m$

wavelength and spectral emissivity of 0.80 within $8\sim13\mu m$ wavelength and 0.55 outside the solar radiation and atmospheric window (i.e. $3\sim8\mu m$ and $13\sim25\mu m$) spectra respectively.

3.1.2 Mode of Operation

The hybrid solar water heating and nocturnal cooling (HSWH-NC) system operates for 24 hours of the day, capturing both the diurnal and nocturnal characteristics of the collector/radiator with the prevailing climatic conditions. During the day, water at room temperature from the hot water storage tank (Reservoir A) is circulated by pump A through the SCONOR plate which at this time acts like a solar collector. The water is, thus, heated and returned to Reservoir A where it is stored for later use. As the hot water is being drawn from Reservoir A, make-up water from the mains or any other source is used to replace it. The process continues throughout the sunshine duration of about 08:00-16:00 hours. During the night at about 22:00 hours, the SCONOR surface automatically becomes a thermal radiator, thus emitting heat to the night sky. Therefore, water in Reservoir B which requires cooling is circulated through it. By operating within the atmospheric window (8~13 μm), the SCONOR extracts heat from the water from Reservoir B, flowing through the bonded tubes underneath it and radiates same to the ambient sky thus cooling the water. The cooled water is stored in Reservoir B. This process continues throughout the night period (i.e. nocturnal duration of about 22:00-06:00 hours). The special spectral properties of the selective surface coating of the SCONOR enable it to work in both the heating and cooling modes. During the day (08:00-16:00 hours), the cooled water obtained from the radiative cooling operation could be used to condition any space of interest (living room, office space, etc), making it thermally comfortable, by circulating it using pump B through the convector where it exchanges heat with the higher temperature air in the conditioned space. Also, during moderate to extreme cold ambient periods, the hot water is circulated via pump B to heat

the room space to make it thermally comfortable for the occupants. Valves I, M, H, O, C, D, E, F and G enable this to be achieved. This way, the system functions to provide both hot water for space heating, domestic and other uses and cold water for space cooling and other purposes, at the appropriate periods.

3.2 Formulation of system model equations

This involves the development of the mathematical model for the transient analysis and optimization of the hybrid solar water heating and nocturnal radiative cooling system. The model comprises five major sections, namely, solar water heating; meteorological data; nocturnal radiative cooling; tank stratification; and space conditioning. In the solar water heating section (which occurs at about 08:00 to 16:00 hours and 0.2-3μm wavelength), the differential equations for the spectral selective surface-coated absorber are developed. The meteorological section takes cognizance of the system location input parameters for the numerical simulation of the model equations during the heating phase. This serves as a source term for the model. In the nocturnal radiative cooling mode or solar water cooling section (which occurs at about 22:00-06:00 hours and 8-13μm wavelength), appropriate differential equations for nocturnal cooling are developed using the same spectral selective surface-coated absorber while in the tanks stratification section, the stratification in the storage tanks are modelled. Finally, in the space conditioning section, the differential equations describing space heating (in periods of moderate to high cold ambient periods) using the hot water stored during the diurnal operation, and space cooling (in periods of moderate to high hot ambient periods) using the cold water stored during the nocturnal operation, are developed.

Numerical study provides a detailed insight into the complex heat transfer and fluid flow phenomena occurring in the hybrid solar water heating and cooling system, and helps in quantifying the thermal performance of the system. Some parameters that are difficult (or expensive) to measure experimentally such as the mass flow rates and small differences in temperature outputs can conveniently be predicted by numerical simulations. Solar water heating and cooling systems performance predictions are always formidable tasks, considering the inherent challenges with location changes and configuration modifications. To understand the evolution of fluid flow, heat transfer, temperature and storage tank stratification in the hybrid solar water heating and cooling system, numerical modelling is significantly useful.

This numerical study involves a comprehensive dynamic thermal macro-model of the overall system developed from first principle using known physical laws and dynamic micro-model (computational fluid dynamic -CFD analysis) of the hybrid SCONOR, built using standard CFD software, to serve as a virtual test bench to capture real flow variations.

The system consists of five major parts (i) the SCONOR (Solar Collector/Nocturnal Radiator), (ii) the Hot Water Storage Tank (HWST), (iii) the Cold Water Storage Tank (CWST), (iv) the Room Convector (RC) and (v) the Room Radiator (RR), as shown in the process line diagram of Fig.3.2. The physics of solar radiation and basic principles of heat and mass transfer are employed in the formulations and modelling of each subcomponent as described in the following subsections. The thermal energy models, in simple terms, detail the heat fluxes and temperature differentials in the subcomponents to predict water temperature in the system and hence serve as a useful tool to allow any user to predict its performance given the location and orientation.

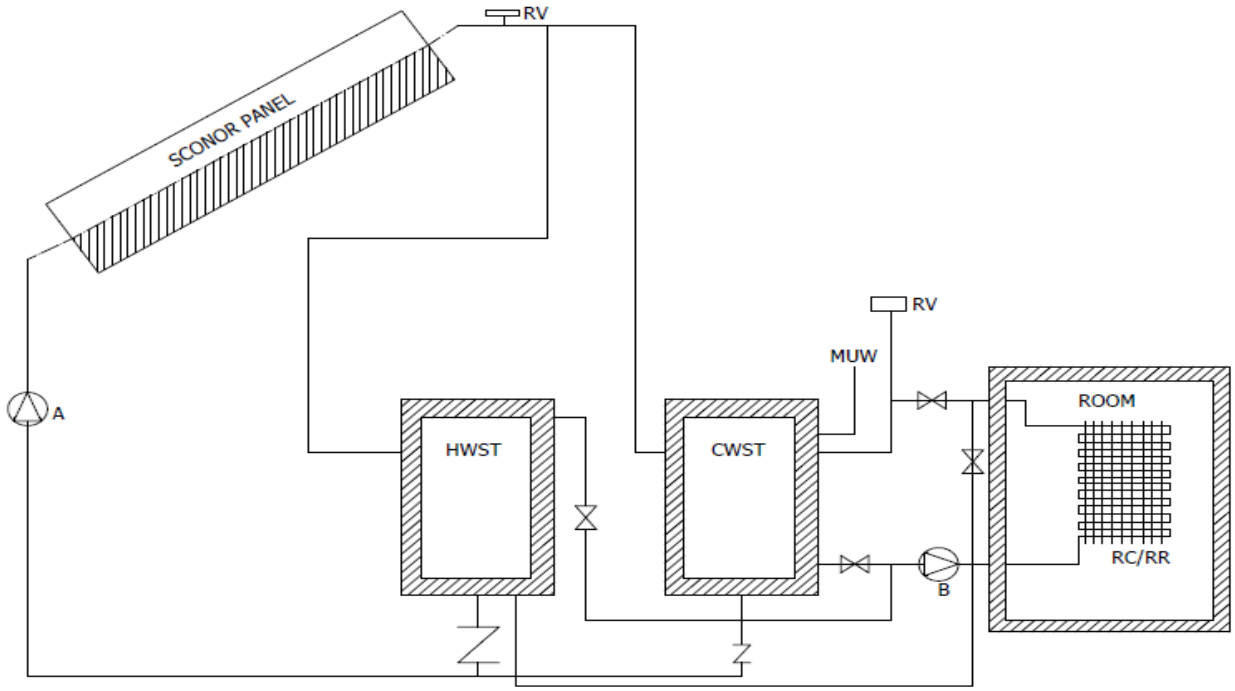

Figure 3.2: Process line diagram of the thermal model of HSWH-NC system

3.2.1 The SCONOR Model

Fig. 3.3 illustrates a transverse section of the plate. It is subdivided into six zones, namely, the windscreen (polyethylene film), radiopaque spectral selective surface (Titanium-base Polyethylene Terephthalate) absorber, bond, tube, fluid and insulation.

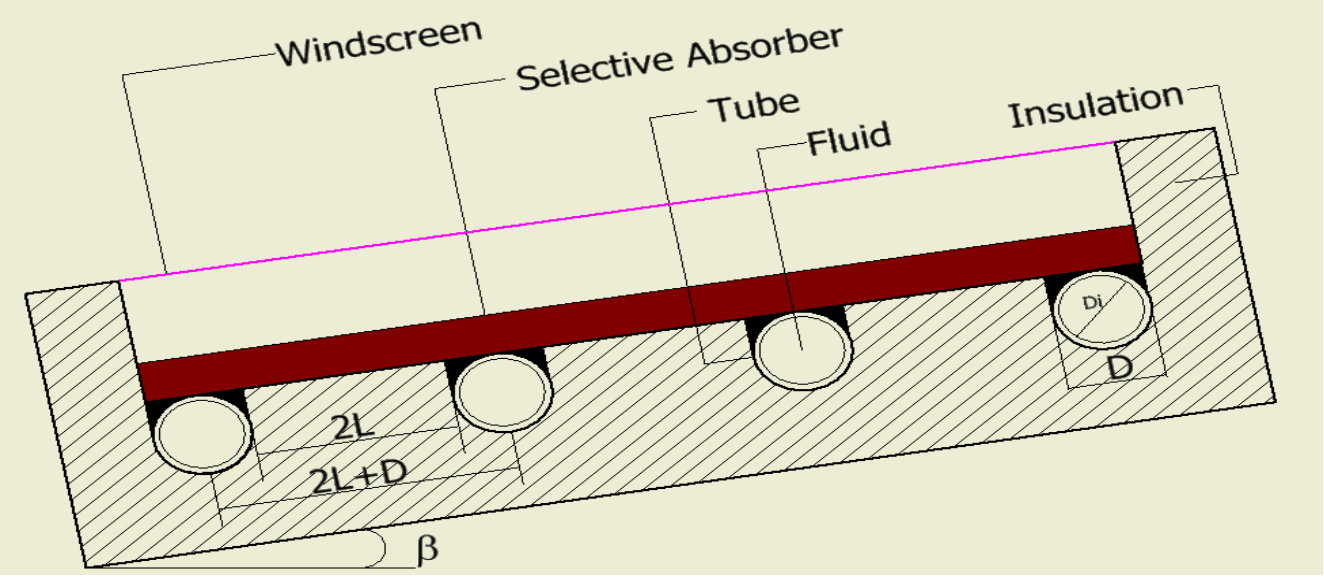

Fig. 3.3 SCONOR Plate Component Zones

3.2.1.1 Simplifying assumptions for model formulation

The following assumptions are adopted in the formulation of the differential equations governing the transient operation of the system.

(i) The selective surface-coated absorber plate is treated as a two dimensional (2-D) rectangular fin. Considering the absorber plate thickness of about 0.001030m, and its material high thermal conductivity, it is plausible to assume negligible temperature gradients across its thickness. This implies that heat flow in the plate is only by conduction along its width and length.

(ii) The spectral properties of the selective surface-coated absorber plate and windscreen are dependent on wavelength. The optical properties are also dependent on the optical characteristics of the materials. However, each of them is considered homogeneous and their thermal properties are the same and independent of temperature at all points.

(iii) There is no internal heat generation in the selective surface coated absorber plate, tube, bond and fluid.

(iv) Only the spectral selective surface-coated absorber plate is exposed to solar radiation, since it is the component that intercepts the incoming solar radiation, from where it is transferred to the bond and tube.

(v) Energy transfer from the absorber to tube occurs only by conduction through the bond which is used to join the tube to the absorber.

(vi) Bonding of tubes to the SCONOR plate is achieved using a material of known thermal conductivity.

(vii) The selective surface-coated plate, bond, tube, fluid and windscreen are treated independently.

(viii) Heat transfer at the tube-fluid interface occurs only by convection.

(ix) The plate is perfectly insulated underneath, such that no heat transfer by conduction occurs between the plate and insulation layer, as stipulated by Nwosu and Onyegegbu (2012).

(x) Heat losses to the ambient are by radiation and convection from the selective surface-coated absorber. Edge effects are considered.

3.2.1.2 Spectral selective surface-coated absorber control volume

The governing differential equations for the heat flow processes in the different zones are derived by applying the general energy balance for each of the zones in the SCONOR shown in Fig. 3.3. In order to determine the heat gain by the fluid from the spectral selective surface-coated absorber and tube, an energy balance is done at the region between the SCONOR centreline and tubes as shown in Fig. 3.4. Fig.3.5 illustrates the absorber, viewed as a fin with various contributions to the energy balance.

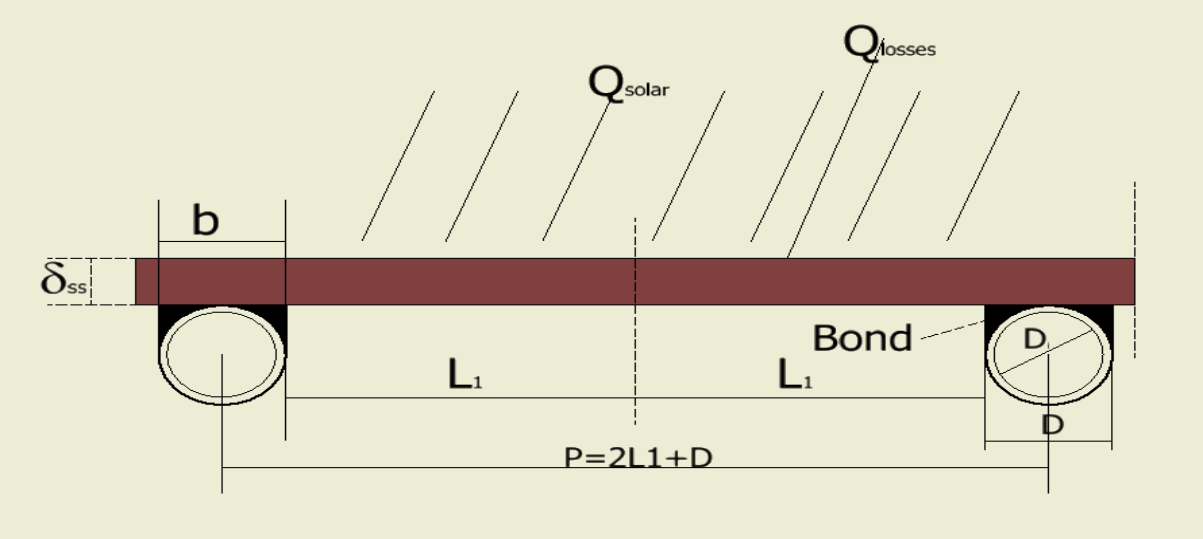

Fig. 3.4 Spectral selective surface-coated absorber and tube

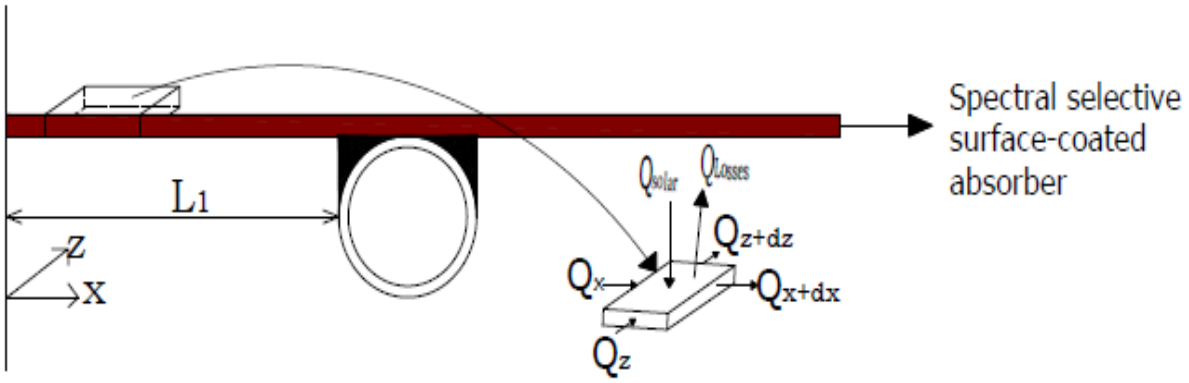

Fig 3.5 Schematic illustration of contribution to the energy balance for the fin element

The general energy balance equation for a control volume is expressed as:

$$\begin{aligned} &Energy\ Inflow\ into\ the\ control\ volume \\ &\quad + \ Internal\ Heat\ Generation\ in\ the\ control\ volume \\ &\quad = \ Energy\ Outflow\ from\ the\ control\ volume \\ &\quad + \ Rate\ of\ increase\ in\ Internal\ Energy\ of\ the\ control\ volume \end{aligned} \qquad 3.1$$

Equation 3.1 may be written in mathematical terms as:

$$Q_{in} + Q_{i,gen} = Q_{out} + \dot{Q}_{int} \qquad 3.2$$

During the water heating mode, equation 3.2 can be written for the SCONOR plate as:

$$Q_{in-h} + Q_{i,gen-h} = Q_{out-h} + \dot{Q}_{int-h} \qquad 3.3$$

From Fig.3.5, the energy inflow into the control volume, Q_{in-h}, is given by:

$$\begin{aligned} &Q_{in-h} = \\ &Heat\ flow\ into\ the\ control\ volume\ in\ the\ x-direction + \\ &Heat\ flow\ into\ the\ control\ volume\ in\ the\ z-direction + Incident\ Solar\ radiation \end{aligned} \qquad 3.4$$

Equation 3.4 is stated mathematically as given in equation 3.5

$$Q_{in-h} = Q_x + Q_z + Q_{solar} \quad 3.5$$

Q_x is the heat flow into the control volume in the x-direction, and from Fourier's Law (Kreith and Bohn, 2000):

$$Q_x = -k_x A \frac{\partial T_{ph}}{\partial x} \quad 3.6$$

From Fig.3.5,

$$Q_x = -k_x dydz \frac{\partial T_{ph}}{\partial x} \quad 3.7$$

Similar analysis yields the heat flow into the control volume in the z-direction as:

$$Q_z = -k_z dxdy \frac{\partial T_{ph}}{\partial z} \quad 3.8$$

Therefore, the total heat flow into the control volume is obtained by substituting equations 3.7 and 3.8 into equation 3.5, to yield:

$$Q_{in-ss} = -k_x dydz \frac{\partial T_{ph}}{\partial x} - k_z dxdy \frac{\partial T_{ph}}{\partial z} + Q_{solar} dxdz \quad 3.9$$

Considering assumption (iii), of subsection 3.2.1.1, we have that $Q_{i,gen} = 0$.

The energy outflow from the control volume, Q_{out-h}, is given as:

$$Q_{out-h} =$$
$$Heat\ conducted\ out\ of\ the\ fin\ element\ in\ the\ x-direction +$$
$$Heat\ conducted\ out\ of\ the\ fin\ element\ in\ the\ z-direction + Total\ Heat\ losses \quad 3.10$$

This implies that:

$$Q_{out-h} = Q_{x+dx} + Q_{z+dz} + Q_{losses} \quad 3.11$$

The heat flow out of the control volume in the x-direction, Q_{x+dx}, expanded using the Taylor series expansion (), is given as:

$$Q_{x+dx} = Q_x + \frac{\partial Q_x}{\partial x} dx = -k_x dydz \frac{\partial T_{ph}}{\partial x} + \frac{\partial}{\partial x}\left(-k_x dydz \frac{\partial T_{ph}}{\partial x}\right) dx \quad 3.12$$

$$Q_{x+dx} = -k_x dydz \frac{\partial T_{ph}}{\partial x} - k_x dxdydz \frac{\partial^2 T_{ph}}{\partial x^2} \quad 3.13$$

Similarly,

$$Q_{z+dz} = Q_z + \frac{\partial Q_z}{\partial z} dz = -k_z dxdy \frac{\partial T_{ph}}{\partial z} + \frac{\partial}{\partial z}\left(-k_z dxdy \frac{\partial T_{ph}}{\partial z}\right) dz \quad 3.14$$

$$Q_{z+dz} = -k_z dxdy \frac{\partial T_{ph}}{\partial z} - k_z dxdydz \frac{\partial^2 T_{ph}}{\partial z^2} \quad 3.15$$

The total heat losses from the element, Q_{losses}, is expressed as:

$$Q_{losses} = U_L\left(T_{ph} - T_a\right)dxdz \quad 3.16$$

Therefore, the energy flow out of the fin element control volume can be obtained by substituting equations 3.13, 3.15 and 3.16 into equation 3.11. Hence,

$$Q_{out-h} = -k_x dydz \frac{\partial T_{ph}}{\partial x} - k_x dxdydz \frac{\partial^2 T_{ph}}{\partial x^2} - k_z dxdy \frac{\partial T_{ph}}{\partial z} - k_z dxdydz \frac{\partial^2 T_{ph}}{\partial z^2} + U_L\left(T_{ph} - T_a\right)dxdz \quad 3.17$$

The net heat flow into the fin element control volume and the absorbed solar energy result in increase in the thermal energy of the control volume, given by the time rate of change in the heat capacity of the control volume, expressed as:

$$\dot{Q}_{int-h} = \rho_{ss} c_{p_{ss}} dxdydz \frac{\partial T_{ph}}{\partial t} \quad 3.18$$

Finally, the energy balance of the fin element control volume is obtained by substituting equations 3.9, 3.17 and 3.18 respectively into the general equation 3.3, resulting in:

$$-k_x dydz\frac{\partial T_{ph}}{\partial x} - k_z dxdy\frac{\partial T_{ph}}{\partial z} + Q_{solar}dxdz + 0 = -k_x dydz\frac{\partial T_{ph}}{\partial x} - k_x dxdydz\frac{\partial^2 T_{ph}}{\partial x^2} - k_z dxdy\frac{\partial T_{ph}}{\partial z} - k_z dxdydz\frac{\partial^2 T_{ph}}{\partial z^2} + U_L\left(T_{ph} - T_a\right)dxdz + \rho_{ss}c_{p_{ss}}dxdydz\frac{\partial T_{ph}}{\partial t} \quad 3.19$$

Simplifying and rearranging,

$$\rho_{ss}c_{p_{ss}}dxdydz\frac{\partial T_{ph}}{\partial t} = -k_x dydz\frac{\partial T_{ph}}{\partial x} - k_z dxdy\frac{\partial T_{ph}}{\partial z} + Q_{solar}dxdz + k_x dydz\frac{\partial T_{ph}}{\partial x} + k_x dxdydz\frac{\partial^2 T_{ph}}{\partial x^2} + k_z dxdy\frac{\partial T_{ph}}{\partial z} + k_z dxdydz\frac{\partial^2 T_{ph}}{\partial z^2} - U_L\left(T_{ph} - T_a\right)dxdz \quad 3.20$$

$$\rho_{ss}c_{p_{ss}}dxdydz\frac{\partial T_{ph}}{\partial t} = Q_{solar}dxdz + k_x dxdydz\frac{\partial^2 T_{ph}}{\partial x^2} + k_z dxdydz\frac{\partial^2 T_{ph}}{\partial z^2} - U_L\left(T_{ph} - T_a\right)dxdz \quad 3.21$$

Dividing through by $dxdz$,

$$\rho_{ss}c_{p_{ss}}dy\frac{\partial T_{ph}}{\partial t} = Q_{solar} + k_x dy\frac{\partial^2 T_{ph}}{\partial x^2} + k_z dy\frac{\partial^2 T_{ph}}{\partial z^2} - U_L\left(T_{ph} - T_a\right) \quad 3.22$$

From Fig.3.5, dy is the thickness of the absorber and can be designated as δ_{ss}, hence, substituting δ_{ss} for dy in equation 3.22, the resulting expression becomes:

$$\rho_{ss}c_{p_{ss}}\delta_{ss}\frac{\partial T_{ph}}{\partial t} = Q_{solar} + k_x\delta_{ss}\frac{\partial^2 T_{ph}}{\partial x^2} + k_z\delta_{ss}\frac{\partial^2 T_{ph}}{\partial z^2} - U_L\left(T_{ph} - T_a\right) \quad 3.23$$

Since the material of the spectral selective surface-coated absorber is homogeneous (assumption ii), equation 3.23 becomes:

$$\rho_{ss}c_{p_{ss}}\delta_{ss}\frac{\partial T_{ph}}{\partial t} = Q_{solar} + k\delta_{ss}\left(\frac{\partial^2 T_{ph}}{\partial x^2} + \frac{\partial^2 T_{ph}}{\partial z^2}\right) - U_L\left(T_{ph} - T_a\right) \quad 3.24$$

3.2.1.3 The bond zone

The energy gained by the spectral selective surface-coated absorber is transferred to the bond through heat conduction mechanism. The bond makes contact with the tube all through the entire tube length and the segment defining the contact area is same throughout this length.

Accordingly, it can be assumed that along the tube, across this segment of contact, the same amount of heat is transferred from the bond. Hence, negligible temperature gradient may be assumed along the length. Thus, it can be modelled as a rectangular domain receiving heat from the surface in contact with the absorber and conducting same to the tube in one dimension only. From Fig.3.5, this heat transfer path from the absorber via the bond to the tube corresponds to the y-axis, as illustrated in Fig.3.6.

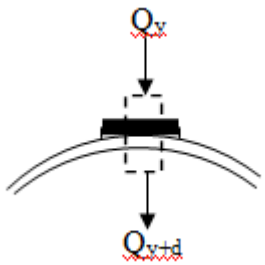

Fig.3.6 The bond control volume

Employing equation 3.1, the energy balance for the bond zone becomes:

$$Q_{in-b} + Q_{i,gen-b} = Q_{out-b} + \dot{Q}_{int-b} \qquad 3.25$$

From Fig.3.6, the energy inflow from the underside of the plate into the bond in contact with it,Q_{in-b}, is equal to Q_y, given as:

$$Q_y = -k_b dx dz \frac{\partial T_b}{\partial y} \qquad 3.26$$

From assumption (iii) of subsection 3.2.1.1, we have that $Q_{i,gen-b} = 0$.

The energy outflow from the bond into the tube outer surface, Q_{out-b}, is equal to Q_{y+dy}, which from Taylor series expansion, gives:

$$Q_{y+dy} = Q_y + \frac{\partial Q_y}{\partial y} dy \qquad 3.27$$

Substituting for Q_y into equation 3.27,

$$Q_{y+dy} = -k_b dxdz\frac{\partial T_b}{\partial y} + \frac{\partial}{\partial y}\left(-k_b dxdz\frac{\partial T_b}{\partial y}\right)dy \quad 3.28$$

$$Q_{y+dy} = -k_b dxdz\frac{\partial T_b}{\partial y} - k_b dxdydz\frac{\partial^2 T_b}{\partial y^2} \quad 3.29$$

The rate of change in the internal energy of the bond, $\dot{Q}_{int-b}$, is expressed as:

$$\dot{Q}_{int-b} = \rho_b c_{p_b} dxdydz\frac{\partial T_b}{\partial t} \quad 3.30$$

The energy balance for the bond, therefore, is obtained by substituting equations 3.26, 3.29 and 3.30 into 3.25, resulting in the following expression:

$$-k_b dxdz\frac{\partial T_b}{\partial y} + 0 = -k_b dxdz\frac{\partial T_b}{\partial y} - k_b dxdydz\frac{\partial^2 T_b}{\partial y^2} + \rho_b c_{p_b} dxdydz\frac{\partial T_b}{\partial t} \quad 3.31$$

$$\rho_b c_{p_b} dxdydz\frac{\partial T_b}{\partial t} = -k_b dxdz\frac{\partial T_b}{\partial y} + k_b dxdz\frac{\partial T_b}{\partial y} + k_b dxdydz\frac{\partial^2 T_b}{\partial y^2} \quad 3.32$$

$$\rho_b c_{p_b}\frac{\partial T_b}{\partial t} = k_b\frac{\partial^2 T_b}{\partial y^2} \quad 3.33$$

3.2.1.4 The Tube Zone Control Volume

The energy gained by the bond is transferred to the tube at the region of contact with the tube. At this region, energy flows into the tube by conduction only (see section 3.2.1.1 v). Although the tube configuration as shown in Fig.3.7(a) is a three dimensional domain and temperature is a function of the three coordinates, as shown in Fig.3.7(b), the tube receives energy from the bond at a point on its circumference (azimuth) and transfers same to the fluid zone radially and circumferentially, hence, it can be conveniently treated as a two dimensional heat transfer in radial and circumferential directions, assuming the temperature gradient in the axial direction is

negligible, since the tube and bond are in thermal contact over this segment all along the entire tube length.

It follows that the energy balance for the tube element control volume shown in Fig.3.7(c) does not consider the axial flow in the tube.

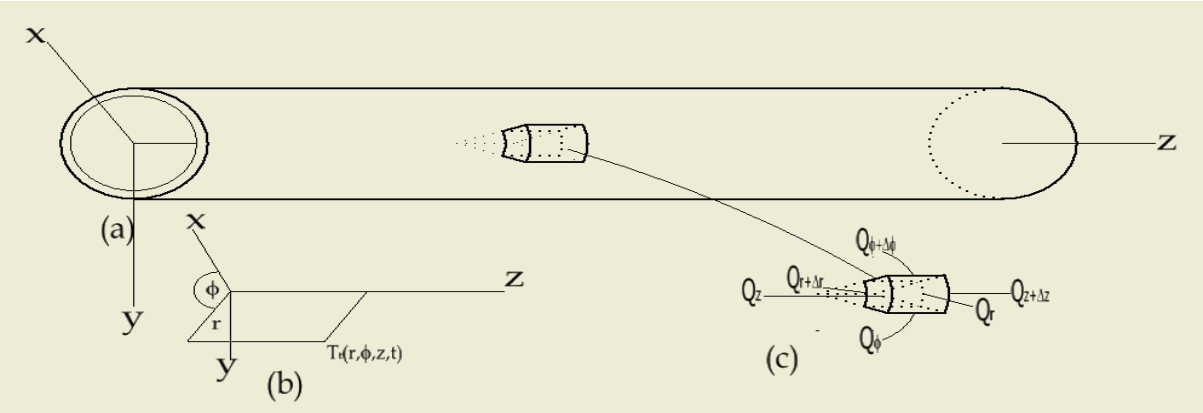

Fig. 3.7 (a) Tube configuration (b) $r, \emptyset, z-$ coordinates and (c) energy balance for the tube element

Therefore, from Fig.3.7(c), the two dimensional (2-D) energy balance around the tube element control volume comprises the heat flows in the radial direction ($x-\emptyset$ *plane*) and that around the azimuthal direction ($r-z$ *plane*). Hence, applying equation 3.1 to the tube element control volume, it can be written as:

$$Q_{in-t} + Q_{i,gen-t} = Q_{out-t} + \dot{Q}_{int-t} \qquad 3.34$$

From Fig.3.7(c), the energy flow into the tube element control volume, Q_{in-t}, is equal to the energy flow into the control volume in the radial direction, Q_r plus the energy flow into the control volume in the azimuthal direction, $Q_\emptyset$. It is given as:

$$Q_{in-t} = Q_r + Q_\emptyset \qquad 3.35$$

The energy flow into the tube element in the radial direction, Q_r, is obtained by applying the Fourier equation to the control volume. It is given by,

$$Q_r = -k(rd\emptyset dz)\frac{\partial T_t}{\partial r} \quad 3.36$$

The energy flow into the tube element in the azimuthal direction, $Q_\emptyset$, is also given by,

$$Q_\emptyset = -k(drdz)\frac{\partial T_t}{r\partial \emptyset} \quad 3.37$$

Therefore,

$$Q_{in-t} = -k(rd\emptyset dz)\frac{\partial T_t}{\partial r} - k(drdz)\frac{\partial T_t}{r\partial \emptyset} \quad 3.38$$

The internal heat generation, $Q_{i,gen-t}$, in the tube is zero according to assumption (iii).

The energy flow out of the tube element control volume, Q_{out-t}, as shown in Fig.3.7(c), is equal to the energy flow out of the control volume in the radial direction, Q_{r+dr}, plus the energy flow out of the control volume in the azimuthal direction, $Q_{\emptyset+d\emptyset}$. It is expressed as:

$$Q_{out-t} = Q_{r+dr} + Q_{\emptyset+d\emptyset} \quad 3.39$$

Heat flow out of the element at $r + dr$, is given as:

$$Q_{r+dr} = Q_r + \frac{\partial}{\partial r}(Q_r)dr = -k(rd\emptyset dz)\frac{\partial T_t}{\partial r} + \frac{\partial}{\partial r}\left(-k(rd\emptyset dz)\frac{\partial T_t}{\partial r}\right)dr \quad 3.40$$

Heat leaving the element at $\emptyset + d\emptyset$ is also given as:

$$Q_{\emptyset+d\emptyset} = Q_\emptyset + \frac{\partial}{r\partial \emptyset}(Q_\emptyset)rd\emptyset = -k(drdz)\frac{\partial T_t}{r\partial \emptyset} + \frac{\partial}{r\partial \emptyset}\left(-k(drdz)\frac{\partial T_t}{r\partial \emptyset}\right)rd\emptyset \quad 3.41$$

Hence, the total heat out of the tube control volume is obtained by substituting equations 3.40 and 3.41 into 3.39, and the resulting expression is as follows:

$$Q_{out-t} = -k(rd\emptyset dz)\frac{\partial T_t}{\partial r} + \frac{\partial}{\partial r}\left(-k(rd\emptyset dz)\frac{\partial T_t}{\partial r}\right)dr - k(drdz)\frac{\partial T_t}{r\partial \emptyset} + \frac{\partial}{r\partial \emptyset}\left(-k(drdz)\frac{\partial T_t}{r\partial \emptyset}\right)rd\emptyset \quad 3.42$$

The resultant increase in the internal energy of the control volume, $\dot{Q}_{int-t}$, given by the time rate of change of its heat capacity, can be written as,

$$\dot{Q}_{int-t} = \rho_t c_{p_t} dV \frac{\partial T_t}{\partial t} \quad 3.43$$

Where,

$$dV = rd\emptyset.dr.dz \quad 3.44$$

Hence, by substituting for dV in equation 3.43, the rate of change of energy in the tube control volume becomes:

$$\dot{Q}_{int-t} = \rho_t c_{p_t}(rd\emptyset.dr.dz)\ \frac{\partial T_t}{\partial t} \quad 3.45$$

Finally, the energy balance of the tube element control volume is obtained by substituting equations 3.38, 3.42 and 3.45 respectively into equation 3.34, resulting in:

$$-k(rd\emptyset dz)\frac{\partial T_t}{\partial r} - k(drdz)\frac{\partial T_t}{r\partial \emptyset} + 0 =$$
$$-k(rd\emptyset dz)\frac{\partial T_t}{\partial r} + \frac{\partial}{\partial r}\left(-k(rd\emptyset dz)\frac{\partial T_t}{\partial r}\right)dr - k(drdz)\frac{\partial T_t}{r\partial \emptyset} + \frac{\partial}{r\partial \emptyset}\left(-k(drdz)\frac{\partial T_t}{r\partial \emptyset}\right)rd\emptyset +$$
$$\rho_t c_{p_t}(rd\emptyset.dr.dz)\ \frac{\partial T_t}{\partial t} \quad 3.46$$

Rearranging, equation 3.46 becomes:

$$\rho_t c_{p_t}(rd\emptyset.dr.dz)\ \frac{\partial T_t}{\partial t} =$$
$$-k(rd\emptyset dz)\frac{\partial T_t}{\partial r} - k(drdz)\frac{\partial T_t}{r\partial \emptyset} + k(rd\emptyset dz)\frac{\partial T_t}{\partial r} + \frac{\partial}{\partial r}\left(k(rd\emptyset dz)\frac{\partial T_t}{\partial r}\right)dr + k(drdz)\frac{\partial T_t}{r\partial \emptyset} +$$
$$\frac{\partial}{r\partial \emptyset}\left(k(drdz)\frac{\partial T_t}{r\partial \emptyset}\right)rd\emptyset \quad 3.47$$

The common terms cancel out and equation 3.47 reduces to:

$$\rho_t c_{p_t}(rd\emptyset.dr.dz)\ \frac{\partial T_t}{\partial t} = \frac{\partial}{\partial r}\left(k(rd\emptyset dz)\frac{\partial T_t}{\partial r}\right)dr + \frac{\partial}{r\partial\emptyset}\left(k(drdz)\frac{\partial T_t}{r\partial\emptyset}\right)rd\emptyset \qquad 3.48$$

Simplifying equation 3.48 and noting that thermal conductivity is constant, gives:

$$\rho_t c_{p_t}\ \frac{\partial T_t}{\partial t} = k_t\left[\frac{\partial^2 T_t}{\partial r^2} + \frac{1}{r}\frac{\partial T_t}{\partial r} + \frac{1}{r^2}\frac{\partial^2 T_t}{\partial \emptyset^2}\right] \qquad 3.49$$

3.2.1.5 The Fluid Layer

Considering Fig. 3.8, the energy of the working fluid entering the tube at a distance z plus the energy gain from the tube will equal to the energy gained by convection at a distance $z + \Delta z$.

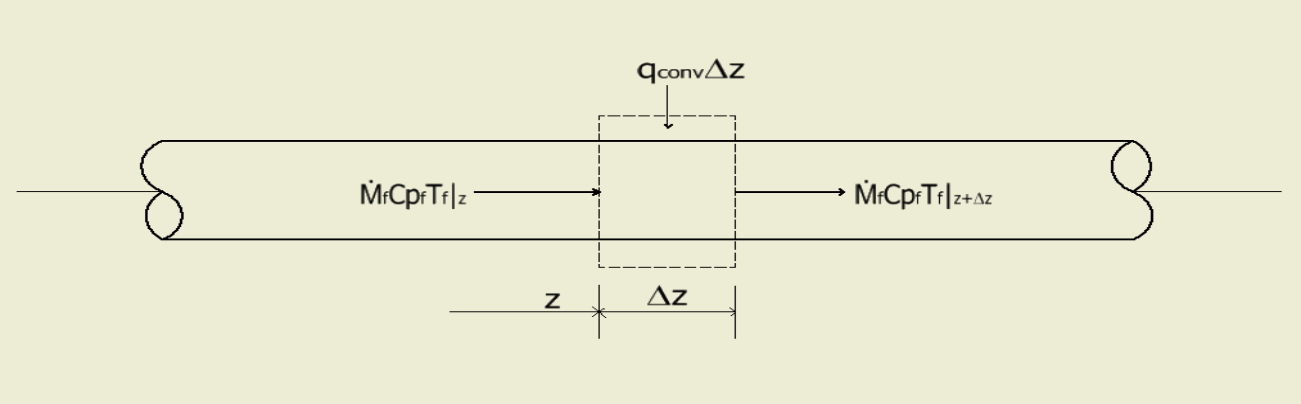

Fig. 3.8 Energy balance on the fluid element

Employing equation 3.2, the energy balance for the fluid zone becomes:

$$Q_{in-fluid\ layer} + Q_{i,gen-fluid\ layer} = Q_{out-fluid\ layer} + \dot{Q}_{int-fluid\ layer} \qquad 3.50$$

Considering Fig. 3.8 and applying assumption (iii) in subsection 3.2.1.1, the general energy equation for the fluid element can be written as:

$$\dot{m}_f c_{p_f} T_f|_z + q_{conv}\Delta z = \dot{m}_f c_{p_f} T_f|_{z+\Delta z} + \rho_f c_{p_f} dV \frac{dT_f}{dt} \qquad 3.51$$

On rearranging,

$$\rho_f c_{p_f} dV \frac{dT_f}{\partial t} = \dot{m}_f c_{p_f} T_f|_z + q_{conv}\Delta z - \dot{m}_f c_{p_f} T_f|_{z+\Delta z} \qquad 3.52$$

Since the fluid gains energy by convective heat exchange with the tube inner wall,

$$\rho_f c_{p_f} dV \frac{dT_f}{\partial t} = \pi D_i h_{f_i} (T_t - T_f)\Delta z + \dot{m}_f c_{p_f} T_f|_z - \dot{m}_f c_{p_f} T_f|_{z+\Delta z} \quad 3.53$$

If there are n tubes welded to the absorber (Kalogirou, 2009), equation 3.53 is reformulated for a single tube to reflect the mass flow into one tube as follows:

$$\rho_f c_{p_f} \frac{dV}{n} \frac{dT_f}{\partial t} = \pi D_i h_{f_i} (T_t - T_f)\Delta z + \left(\frac{\dot{m}_f}{n}\right) c_{p_f} T_f|_z - \left(\frac{\dot{m}_f}{n}\right) c_{p_f} T_f|_{z+\Delta z} \quad 3.54$$

Taking n as a common factor, equation 3.54 can be written as,

$$\rho_f c_{p_f} dV \frac{dT_f}{\partial t} = \pi D_i h_{f_i} n(T_t - T_f)\Delta z + \dot{m}_f c_{p_f} T_f|_z - \dot{m}_f c_{p_f} T_f|_{z+\Delta z} \quad 3.55$$

$$\rho_f c_{p_f} dV \frac{dT_f}{\partial t} = \pi D_i h_{f_i} (T_t - T_f) n\Delta z + \dot{m}_f c_{p_f} T_f|_z - \dot{m}_f c_{p_f} \left(T_f + \frac{dT_f}{dz}\Delta z\right) \quad 3.56$$

$$\rho_f c_{p_f} dV \frac{dT_f}{\partial t} = \pi D_i h_{f_i} (T_t - T_f) n\Delta z - \dot{m}_f c_{p_f} \frac{dT_f}{dz}\Delta z \quad 3.57$$

Dividing all elements of equation 3.57 by Δz, the following equation is obtained:

$$\rho_f c_{p_f} \frac{dV}{\Delta z} \frac{dT_f}{\partial t} = \pi D_i h_{f_i} (T_t - T_f) n - \dot{m}_f c_{p_f} \frac{dT_f}{dz} \quad 3.58$$

Considering the domain of fluid flow, as shown in Fig.3.8, neglecting the bond area, $\frac{dV}{\Delta z}$, can be approximated as the cross-sectional area of the tube A_t, hence, equation 3.58 can be written as:

$$\rho_f c_{p_f} A_t \frac{dT_f}{dt} = \pi D_i h_{f_i} (T_t - T_f) n - \dot{m}_f c_{p_f} \frac{dT_f}{dz} \quad 3.59$$

This is a simplified fluid model, having been developed without recourse to the mass and momentum conservation of the fluid flowing in the pipe. Since the major consideration in the thermal macro-model is the temporal temperature behaviour of the fluid in the flow direction, the foregoing concept is valid and does not impose any constraint on the model.

3.2.1.6 Heat losses from SCONOR

During the heating operation, part of the energy absorbed by the absorber yields useful energy gain while the rest is lost to the environment through the top, bottom and edges of the SCONOR assembly. The total heat loss from the surface during the diurnal heating operation comprises the top heat losses through the windscreen, bottom heat losses through the bottom (or under-insulation) and edge heat losses through the edge insulation. Hence, the overall heat loss from the surface is given by the third term in the RHS of equation 3.24 expressed as:

$$Q_{losses} = U_L(T_{ph} - T_a) \quad 3.60$$

Where U_L is the overall heat loss coefficient of the surface given by:

$$U_L = U_{L-t} + U_{L-b} + U_{L-e} \quad 3.61$$

And U_{L-t} is the overall top loss heat transfer coefficient, U_{L-b} is the overall bottom loss heat transfer coefficient and U_{L-e} is the overall edge loss heat transfer coefficient. According to Nwosu and Onyegegbu (2012), the edge loss is affected by such factors as thermo-physical properties of the insulation material, draft condition in the ambient air as well as the functionality of the active components. They opined that for miniature absorbers, this loss can be neglected without significant effect on the performance of solar absorbers. However, it is not so for sizeable absorbers as the performance of such absorbers greatly depend on proper evaluation of edge losses.

3.2.1.6.1 Top heat losses from the SCONOR surface

The energy losses through the top comprise convection and radiation from the surface via the windscreen to the ambient sky. Fig. 3.9 shows a transverse cross-section of the selective absorber configuration.

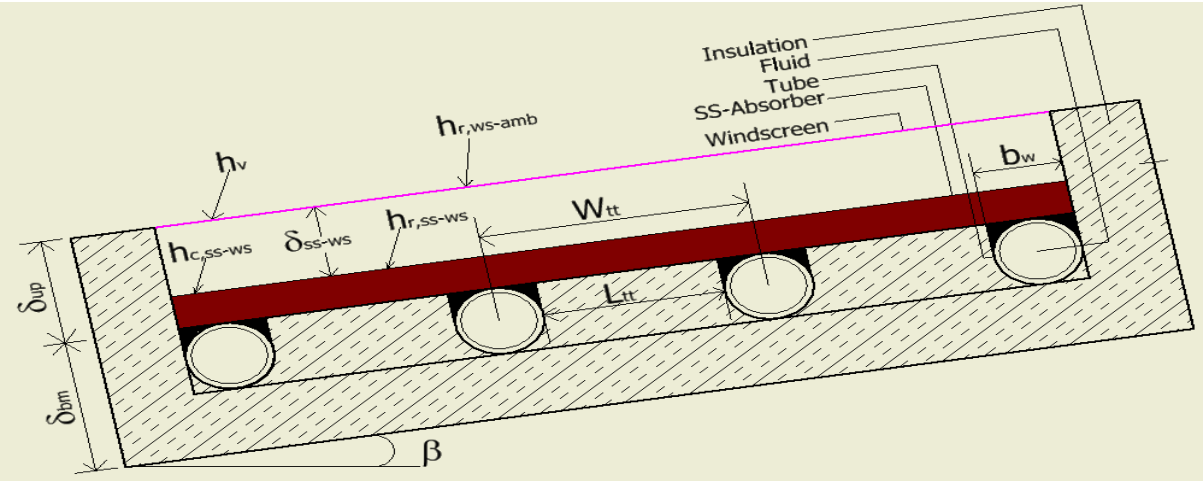

Fig. 3.9 Transverse Section of SCONOR (spectral selective absorber) plate

For a flat-plate collector with a single transparent cover (windscreen), as shown in Fig. 3.9, the thermal network in terms of conduction, convection and radiation is as shown in Fig. 3.10.

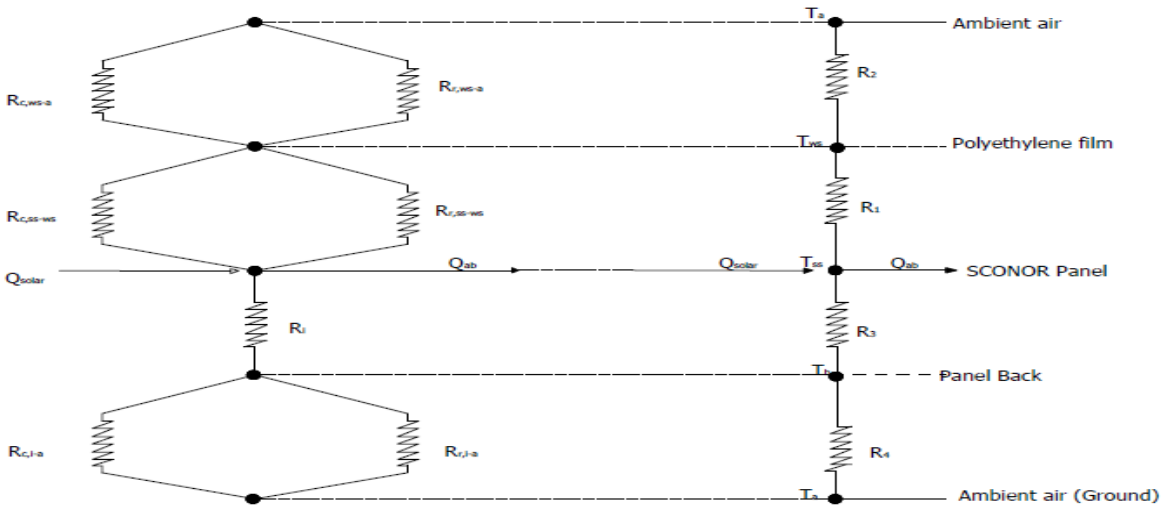

Fig. 3.10 Thermal network for a single windscreen covered collector

Considering the thermal network of Fig. 3.10, the resistances R_1 and R_2 can be defined respectively as,

$$R_1 = R_{c,ss-ws} + R_{r,ss-ws} \quad 3.62$$

$$R_2 = R_{c,ws-a} + R_{r,ws-a} \quad 3.63$$

Where,

$$R_{c,ss-ws} = \frac{1}{h_{c,ss-ws} * A_{ss}} \quad 3.64$$

$$R_{r,ss-ws} = \frac{1}{h_{r,ss-ws} * A_{ss}} \quad 3.65$$

$$R_{c,ws-a} = \frac{1}{h_{c,ws-a} * A_{ss}} \quad 3.66$$

$$R_{r,ws-a} = \frac{1}{h_{r,ws-a} * A_{ss}} \quad 3.67$$

For a series resistance shown in Fig.3.10, the total resistance is $R_1 + R_2$ given by,

$$R_T = R_1 + R_2 = \frac{1}{h_{c,ss-ws} * A_{ss} + h_{r,ss-ws} * A_{ss}} + \frac{1}{h_{c,ws-a} * A_{ss} + h_{r,ws-a} * A_{ss}} \quad 3.68$$

The top loss coefficient (U_{L-t}) per unit area of absorber plate is given by the expression,

$$U_{L-t} = \frac{1}{R_t} = \frac{1}{R_1 + R_2} \quad 3.69$$

Therefore,

$$U_{L-t} = \left[\frac{1}{h_{c,ss-ws} + h_{r,ss-ws}} + \frac{1}{h_{c,ws-a} + h_{r,ws-a}}\right]^{-1} \quad 3.70$$

3.2.1.6.2 The convective heat transfer coefficients ($h_{c,ss-ws}$ and $h_{c,ws-a}$)

For optimal performance of collectors, they are given a tilt of equal magnitude with the location latitude. The relationship between Nusselt Number and Rayleigh Number for tilt angles from 0-75^o is expressed as (Kalogirou, 2009 and Iordanou, 2009):

$$N_u = 1 + 1.446\left[1 - \frac{1708}{R_a Cos\beta}\right]^+ \left\{1 - \frac{1708 Sin(1.8\beta)^{1.6}}{R_a Cos\beta}\right\} + \left\{\left(\frac{R_a Cos\beta}{5830}\right)^{\frac{1}{3}} - 1\right\}^+ \quad 3.71$$

The plus signs mean positive values only while β is the plate tilt angle (as shown in Fig. 3.9). Kreith and Bohn (1993) defined Nusselt Number as:

$$N_u = \frac{hL}{K} \tag{3.72}$$

Therefore, for the distance between the selective surface and windscreen under consideration, δ_{ss-ws}, the Nusselt Number is be defined as:

$$N_u = \frac{h_{c,ss-ws}\delta_{ss-ws}}{K_{air}} \tag{3.73}$$

Then, transforming equation 3.73 to obtain a formula for the convection coefficient for the convective exchange between the spectral surface and windscreen, the resulting expression for the convective coefficient becomes:

$$h_{c,ss-ws} = \frac{N_u K_{air}}{\delta_{ss-ws}} \tag{3.74}$$

According to Kalogirou (2009), the Rayleigh Number is given by,

$$R_a = \frac{g\beta' P_r}{v^2}\left(T_{ph} - T_{ws}\right)(\delta_{ss-ws})^3 \tag{3.75}$$

Where g is the gravitational constant; and β' is the volumetric coefficient of expansion with P_r the Prandtl Number given respectively as:

$$\beta' = \frac{1}{T_\infty} \tag{3.76}$$

$$P_r = \frac{v}{\alpha} \tag{3.77}$$

Where v is the kinematic viscosity of the air within the gap, α is the thermal diffusivity of air and δ_{ss-ws} is the absorber-to-windscreen distance, since air occupies the space between the absorber surface and windscreen.

The fluid (air) properties are evaluated at the mean gap temperature given as:

$$T_{\infty} = \frac{T_{ph} + T_{ws}}{2} \tag{3.78}$$

3.2.1.6.3 The radiation heat transfer coefficients ($h_{r,ss-ws}$ and $h_{r,ws-a}$)

The radiation heat transfer coefficient from the selective absorber to the inner side of the windscreen and that from the windscreen to the ambient are respectively given as (Duffie and Beckman, 2006),

$$h_{r,ss-ws} = \frac{\sigma\left(T_{ph} + T_{ws}\right)\left({T_{ph}}^2 + {T_{ws}}^2\right)}{\frac{1}{\varepsilon_{ss}} + \frac{1}{\varepsilon_{ws}} - 1} \tag{3.79a}$$

$$h_{r,ws-a} = \varepsilon_{ws}\sigma(T_{ws} + T_a)\left({T_{ws}}^2 + {T_a}^2\right) \tag{3.79b}$$

It is worthy of note that since the sky temperature does not affect the results much during the diurnal heating operations, the ambient temperature, T_a, is used for convenience. According to Mirzabozorg et al (2014), the ambient temperature can be correlated with reasonable accuracy using the sinusoidal function given in equation 3.80a.

$$T_a(t) = \bar{A}Sin\left(\frac{2\pi(t-\vartheta)}{P}\right) + \bar{B} \tag{3.80a}$$

$\bar{A}$ is the amplitude of the sine function, given as:

$$\bar{A} = \frac{1}{2}\left(|T_{max} - T_{mean}| + |T_{min} - T_{mean}|\right) \tag{3.80b}$$

Where $\bar{B}$ is the daily mean temperature, t is any given time in the day, ϑ is time in the day when $T_a(\vartheta) = \bar{B}$, and P is the period of the sine function which is 24 hours.

3.2.1.6.4 Radiopaque-transparent cover radiative and convective heat exchanges

The radiation and convection heat exchange between a radiopaque absorber and a plastic transparent cover is as illustrated in Fig.3.11:

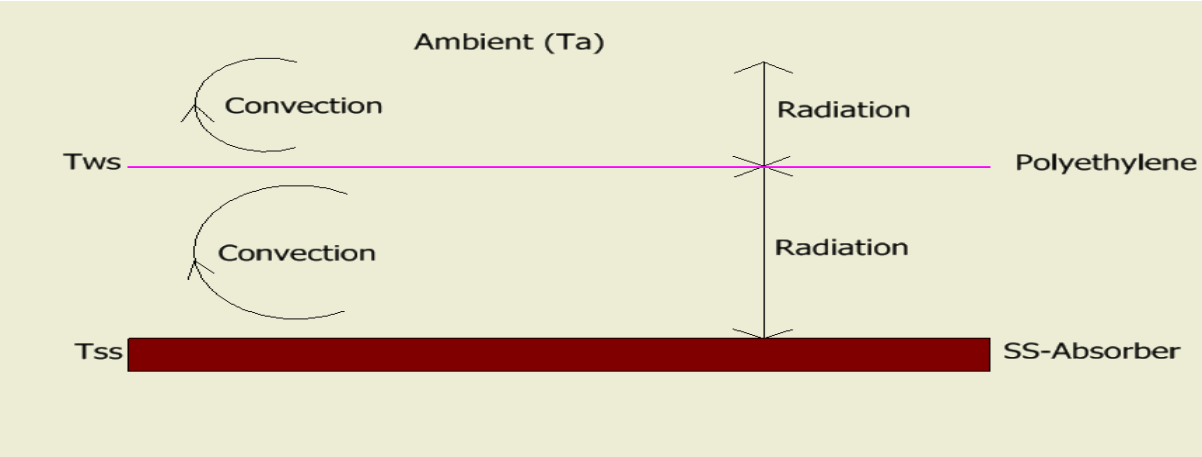

Fig. 3.11 Heat exchanges through a spectral selective absorber with a single polyethylene windscreen

The foregoing analyses as presented in sections 3.2.1.6.2 and 3.2.1.6.3 require iterative solution for the windscreen temperature in estimating the top loss coefficient. This demands increased computer power, simulation time and cost in handling the tedious iterative procedure. Hence, it is customary to resort to Klein's correlation for the evaluation of top loss coefficient, which has been shown to reasonably predict the top loss to within ±3W/m^{2}K for flat plate collectors (Duffie and Beckman, 2006; Kalogirou, 2009). The Klein's correlation, applied to the selective absorber and windscreen in place of plate and glass cover respectively, is given by (Kalogirou, 2009) as:

$$U_{L-t} = \left[\frac{N_{ws}}{\frac{C}{T_{ph}}\left[\frac{T_{ph}-T_a}{N_{ws}+f}\right]^{0.33}}\right]^{-1} + \frac{\sigma\left(T_{ph}{}^2 + T_a{}^2\right)\left(T_{ph}+T_a\right)}{\frac{1}{\varepsilon_{ss}+0.05N_{ss}(1-\varepsilon_{ss})} + \frac{2N_{ss}+f-1}{\varepsilon_{ws}} - N_{ws}} \quad 3.81$$

Where,

$$f = \left(1 - 0.04h_w + 0.0005{h_w}^2\right)(1 + 0.091N_{ws}) \quad 3.82$$

$$C = 365.9(1 - 0.00883\beta + 0.0001298\beta^2) \quad 3.83$$

For a SCONOR covered with a single polyethylene film windscreen, the convective heat transfer coefficient due to wind given by Mingke et al (2015) as in equation 3.84 is used.

$$h_w = h_{c,ws-a} = 0.5 + 1.2u^{0.5} \quad 3.84$$

Where u is the prevailing wind speed of the location in question.

Anyanwu and Iwuagwu (1995) provided the average wind speed for this study location Owerri, Nigeria as $2.80 \pm 0.81\ m/s$.

3.2.1.6.5 Bottom and edge losses from the SCONOR plate

From Fig. 3.10, the insulation will pose a resistance to the flow of heat from the SCONOR plate, given by the resistance R3 and also the resistance from the SCONOR plate bottom housing to the ambient environment is given by R4. This energy loss is transferred to the ambient environment in the underside of the housing by combined convection and infrared radiation. The magnitudes of R3 and R4 are such that it is usually possible to neglect R4 and all resistance to heat flow is now due to insulation (Duffie and Beckman, 2006; Nwosu and Onyegegbu, 2012). Therefore, the bottom energy loss conductance is given by the approximation,

$$U_{L-b} = \left[\frac{\delta_{ins}}{k_{ins}}\right]^{-1} \quad 3.85$$

Finally, the edge loss heat transfer coefficient from the plate edges is estimated assuming one-dimensional sideways heat flow around the perimeter of the collector system. Nwosu and

Onyegegbu (2012) recommended an area multiplier $\frac{A_e}{A_c}$ in estimating accurately the edge losses.

These losses are referenced to the collector area and obtained by:

$$U_{L-e} = \frac{\frac{\delta_{ins}}{k_{ins}} A_e}{A_c} \quad 3.86$$

$$\mathrm{A_e} = \text{Collector Thickness} * \text{Perimeter of Collector} \quad 3.87$$

The overall heat transfer coefficient U_L is therefore obtained by substituting equations 3.81, 3.85 and 3.86 into 3.61 and the resulting expression is:

$$U_L = \left[\frac{N_{ws}}{\frac{C}{T_{ph}}\left[\frac{T_{ph}-T_a}{N_{ws}+f}\right]^{0.33}}\right]^{-1} + \frac{\sigma\left({T_{ph}}^2 + {T_a}^2\right)\left(T_{ph}+T_a\right)}{\frac{1}{\varepsilon_{ss}+0.05N_{ss}(1-\varepsilon_{ss})} + \frac{2N_{ss}+f-1}{\varepsilon_{ws}} - N_{ws}} + \left[\frac{\delta_{ins}}{k_{ins}}\right]^{-1} + \frac{\frac{\delta_{ins}}{k_{ins}} A_e}{A_c} \quad 3.88$$

And the total heat loss from the surface is obtained by substituting equation 3.88 into equation 3.60 to yield:

$$Q_{loss} = \left\{\left[\frac{N_{ws}}{\frac{C}{T_{ph}}\left[\frac{T_{ph}-T_a}{N_{ws}+f}\right]^{0.33}}\right]^{-1} + \frac{\sigma\left({T_{ph}}^2 + {T_a}^2\right)\left(T_{ph}+T_a\right)}{\frac{1}{\varepsilon_{ss}+0.05N_{ss}(1-\varepsilon_{ss})} + \frac{2N_{ss}+f-1}{\varepsilon_{ws}} - N_{ws}} + \left[\frac{\delta_{ins}}{k_{ins}}\right]^{-1} + \frac{\frac{\delta_{ins}}{k_{ins}} A_e}{A_c}\right\}\left(T_{ph}-T_a\right) \quad 3.89$$

3.2.1.7 The climate model

The incident solar radiation (flux) comprises direct (or beam) radiation and diffuse radiation. Flat-plate collectors are known to collect both beam and diffuse components of the incident radiation (Sen, 2008; Kalogirou, 2009). The hybrid surface has different optical properties such as transmittance, absorptance and reflectance when solar radiation is incident it. While beam radiation increases with the clearness of the sky, the diffuse component decreases with sky clearness and it is largely dependent on the proportion of the sky viewed by the surface (Amos, 2009). The short wavelength radiation reaching any horizontal surface on the earth may be direct or diffuse. Usually, for optimal yield (i.e. optimal collection of solar radiation) and reduction of reflection and cosine losses, solar collectors are not installed horizontally but given an inclination that is dependent on the latitude of the location of installation.

3.2.1.7.1 Models of solar radiation on tilted SCONOR surface

The SCONOR flat surface on a horizontal and inclined surface is as shown in Fig. 3.12.

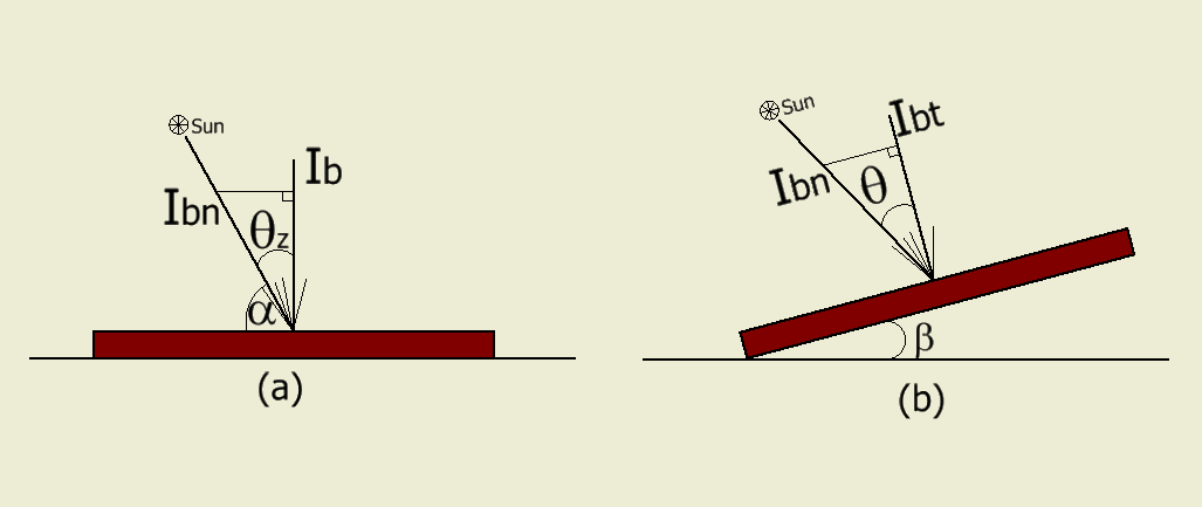

Fig. 3.12 Beam radiation on horizontal and tilted surfaces

The total amount of radiation on the tilted surface is given as the sum of a set of radiation streams, comprising the beam radiation, the three components of diffuse radiation (isotropic,

circumsolar and horizontal brightening) and ground reflected radiation. Mathematically, it is given as:

$$I_{t,T} = I_{bt} + I_{dt} + I_{gt} \quad 3.90$$

Where, I_{bt} is the incident beam radiation on the tilted surface; I_{dt} is the incident diffuse radiation on the tilted surface and I_{gt} is the incident ground reflected radiation on the tilted surface.

3.2.1.7.1.1 Beam radiation on the tilted SCONOR surface

From the tilted surface of Fig. 3.12b, the incident beam radiation on the tilted surface can be expressed as,

$$I_{bt} = I_{bn} Cos\theta \quad 3.91$$

Similarly, from the horizontal surface of Fig. 3.12a,

$$I_b = I_{bn} Cos\theta_z \quad 3.92$$

Where θ is the incident angle of the beam radiation, θ_z is the zenith angle of the sun while I_b is the theoretical amount of solar energy incident on a horizontal SCONOR surface.

The ratio of the incident solar flux on the tilted surface to that on the horizontal, defines a new parameter, which is referred to as the beam radiation tilt factor, R_b, given by,

$$R_b = \frac{I_{bt}}{I_b} = \frac{I_{bn} Cos\theta}{I_{bn} Cos\theta_z} = \frac{Cos\theta}{Cos\theta_z} \quad 3.93$$

The incident angle of beam radiation (θ) and the zenith angle (θ_z) can be computed from equations 3.94 and 3.95 (Duffie and Beckmann 2006; Kalogirou 2009).

$$Cos\theta = Sin\delta Sin\emptyset Cos\beta - Sin\delta Cos\emptyset Sin\beta Cos\gamma + Cos\delta Cos\emptyset Cos\beta Cos\omega + Cos\delta Sin\emptyset Sin\beta Cos\gamma Cos\omega + Cos\delta Sin\beta Sin\gamma Sin\omega$$ 3.94

$$Cos\theta_z = Cos\emptyset Cos\delta Cos\omega + Sin\emptyset Sin\delta$$ 3.95

Where, β is the angle of tilt of the surface (β = 0 for a horizontal surface; β = 90 for a vertical surface), γ is the surface azimuth angle, $\emptyset$ is the location latitude, and δ is the declination angle.

For solar water heating applications, optimal heating occurs at tilt angles equal to either location latitude or latitude+15^o or in the range between latitude + 15^{o}C (Rostamzadeh et al., 2011).

The angle of declination is expressed as (Kalogirou, 2009):

$$\delta = 23.45Sin\left[\frac{360\,(284+N)}{365}\right]$$ 3.96

N is day number and it is in the range $1 \leq N \leq 365$.

ω is the hour angle given by the expression,

$$\omega = 15^o\,(Solar\ Time - 12)$$ 3.97

Solar time is the time based on the apparent angular motion of the sun across the sky. This time does not overlap with local clock time (otherwise known as standard time). It is the time used in all the sun-angle relations. It can be estimated by (Kalogirou, 2009),

$$Solar\ Time = Standard\ Time + 4(L_{st} - L_{loc}) + E\ (\text{min})$$ 3.98

Where, L_{st} is the standard meridian for the local time zone (in degrees), L_{loc} is the longitude of the location in question (in degrees) and E is the equation of time (in minutes).

The equation of time is obtained from (Kalogirou, 2009):

$$E = 229.2(0.000075 + 0.001868CosB - 0.032077SinB - 0.014615Cos2B - 0.04089Sin2B) \quad 399$$

Where B is given by the expression (Kalogirou, 2009),

$$B = \frac{360(N-1)}{365} \quad 3.100$$

From equation 3.93, the beam radiation component on the tilted surface can, therefore, be expressed as,

$$I_{bt} = I_b R_b \quad 3.101$$

3.2.1.7.1.2 Diffuse and reflected solar radiations on the tilted SCONOR surface

Many models have been proposed for estimating the solar radiation on tilted surfaces. The models are isotropic model and Hay, Davies, Klucker and Reindel model. Each of the models considers the three components of diffuse radiation (i.e. isotropic, circumsolar and horizontal brightening), as well as ground reflection differently. The isotropic sky model, proposed by Liu and Jordan in 1963, assumes that all diffuse radiations are uniformly distributed over the sky dome and ground reflection is also diffuse (Kalogirou, 2009). This model, though easiest to use, gives reasonably accurate result for use in most solar energy studies. According to Kalogirou (2009), using the isotropic sky model, the diffuse component of the radiation on the tilted surface is given by,

$$I_{dt} = I_d\left(\frac{1+Cos\beta}{2}\right) \quad 3.102$$

While the ground reflected radiation on a tilted surface is given by,

$$I_{gt} = \rho_{gr}(I_b + I_d)\left[\frac{1-Cos\beta}{2}\right] \quad 3.103$$

Substituting equations 3.101, 3.102 and 3.103 into equation 3.90 gives the total radiation on the tilted SCONOR surface as:

$$I_{t_T} = I_b R_b + I_d \left(\frac{1+Cos\beta}{2}\right) + \rho_{gr}(I_b + I_d)\left[\frac{1-Cos\beta}{2}\right] \quad 3.104$$

The terms $\left(\frac{1+Cos\beta}{2}\right)$ and $\left[\frac{1-Cos\beta}{2}\right]$ represent the view factors of the collector to the sky and the collector to the ground, respectively.

The diffuse radiation received by a tilted surface strongly depends on the clearness index of the atmosphere. The clearness index is the ratio of a particular day's radiation to the extraterrestrial radiation for that day (Duffie and Beckmann, 2006). It is a very important parameter for any solar simulation and strongly varies from location to location, and is expressed by (Farschad and Mohammad, 2014) as:

$$C_{ID} = 0.8417S + 0.02332T - 0.03184ST \quad 3.105$$

Where C_{ID} is the clearness index, T is the atmospheric temperature and S is the fraction of sunshine hours

The total hourly horizontal solar radiation at the SCONOR surface I is related to the clearness index according to the following expression:

$$C_{ID} = \frac{I}{I_o} \quad 3.106$$

Where I_o is the cloudless hourly global irradiation received on the SCONOR surface, given as (Kalogirou, 2009):

$$I_o = \frac{12*3600G_{sc}}{\pi}\left[1 + 0.033Cos\left(\frac{360N}{365}\right)\right] * \left\{Cos\emptyset Cos\delta Sin(\omega_2 - \omega_1) + \left[\frac{\pi(\omega_2 - \omega_1)}{180}\right] Sin\emptyset Sin\delta\right\} \quad 3.107$$

Where G_{sc} is the solar constant given as 1367W/m^2.

However, data on beam solar radiation, I_b, and diffuse solar radiation, I_d, are not available. Therefore, a correlation between horizontal diffuse, I_d, and total horizontal solar radiation, I, is required. The diffuse flux to horizontal solar radiation is related by the following correlations (Farschad and Mohammad, 2014):

$$I_d = \begin{cases} I(1 - 0.249C_{ID}) & C_{ID} < 0.35 \\ I(1.557 - 1.84C_{ID}) & 0.35 < C_{ID} < 0.75 \\ 0.177I & C_{ID} > 0.75 \end{cases} \quad 3.108$$

Care must be taken in the use of equation 3.93 for the computation of beam radiation tilt factor on tilted surfaces at times near sunrise and sunset (Duffie and Beckman, 2006). This is because in situations where sunrise or sunset occurs at the midpoint of the hour, the cosine of the zenith angle is zero and R_b calculated with equation 3.101 at that condition is infinite (extremely large). Therefore, its effect on any measured or computed beam radiation exceeds the solar constant, a situation which must be avoided. Hence, it is more convenient to evaluate R_b using an average parameter defined as (Duffie and Beckman, 2006):

$$R_{b\,ave} = \frac{\int_{\omega_1}^{\omega_2} \mathrm{Cos}\theta \mathrm{d}\omega}{\int_{\omega_1}^{\omega_2} \mathrm{Cos}\theta_z \mathrm{d}\omega} \quad 3.109$$

Where ω_1 and ω_2 are hour angles which could be two adjacent hours in a day away from sunrise or sunset (in which case $R_{b\,ave} \approx R_b$) or sunrise and sunset (in which case the unit integration holds). Solution of equation 3.109 yields:

$$R_{b\,ave} = \frac{a^*}{b^*} \quad 3.110$$

Where a^* and b^* are expressed respectively as:

$$a^* = \frac{\pi(\omega_2-\omega_1)}{180}(Sin\delta Sin\emptyset Cos\beta - Sin\delta Cos\emptyset Sin\beta Cos\gamma) + (Sin\omega_2 - Sin\omega_1)[Cos\delta Cos\emptyset Cos\beta + Cos\delta Sin\emptyset Sin\beta Cos\gamma] - (Cos\omega_2 - Cos\omega_1)[Cos\delta Sin\beta Siny\gamma] \quad 3.111$$

$$b^* = (Sin\omega_2 - Sin\omega_1)[Cos\emptyset Cos\delta] + \frac{\pi(\omega_2-\omega_1)}{180}[Sin\emptyset Sin\delta] \quad 3.112$$

3.2.1.7.2 The transmittance-absorptance product

This represents fraction of the incident beam or diffuse radiation absorbed by the panel. The value of this product is a function of the windscreen transmittance and panel absorptance for solar radiation. The transmittance-absorptance product is established for the windscreen and absorber plate by adopting the ray tracing approach shown in Fig. 3.13.

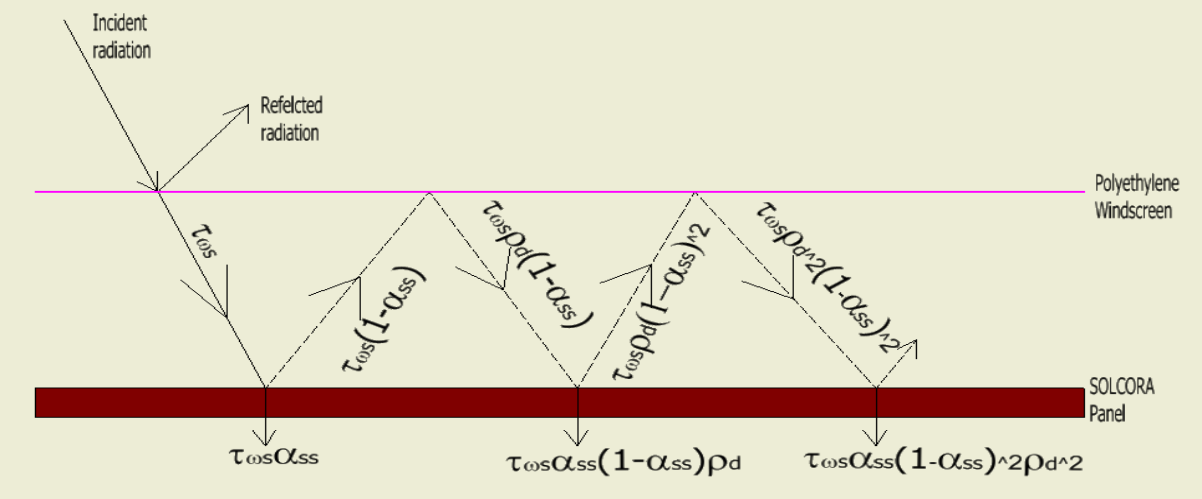

Fig. 3.13 Ray tracing of incident radiation on windscreen panel arrangement

Considering Fig. 3.13 and assuming no absorption of energy by the cover, part of the incident energy is transmitted through the polyethylene windscreen (cover) while part is reflected back to the atmosphere. Since polyethylene is highly transparent to solar radiation, significant amount of short wavelength solar radiation passes through it during the solar heating phase. As shown in Fig.3.13, the SCONOR plate absorbs $\tau_{ws}\alpha_{ss}$ and

$\tau_{ws}(1-\alpha_{ss})$ is reflected back to the windscreen, and the process continues. According to Kalogirou (2009), the fraction of the incident solar energy that is finally absorbed is given by,

$$(\tau\alpha) = \tau_{ws}\alpha_{ss}\sum_{n=1}^{\infty}[(1-\alpha_{ss})\rho_d]^n = \frac{\tau_{ws}\alpha_{ss}}{1-(1-\alpha_{ss})\rho_d} \quad 3.113$$

For most practical collectors, a reasonable approximation of equation 3.113 is given by equation 3.114:

$$(\tau\alpha) \cong 1.01\tau_{ws}\alpha_{ss} \quad 3.114$$

Solar radiation absorbed by the plate is therefore obtained by multiplying equation 3.104 by the transmittance-absorptance product$(\tau\alpha)$. This is shown as equation 3.115.

$$I_{t_T} = (\tau\alpha)_b I_b R_b + (\tau\alpha)_d I_d \left(\frac{1+Cos\beta}{2}\right) + (\tau\alpha)_{gr}\rho_{gr}(I_b + I_d)\left[\frac{1-Cos\beta}{2}\right] \quad 3.115$$

The subscripts b, d and gr attached to $(\tau\alpha)$ represent the $(\tau\alpha)$ for beam, diffuse and ground reflected radiation, respectively.

The transmittance of a single windscreen cover can be approximated mathematically as (Duffie and Beckmann, 2006):

$$\tau_{ws} \cong \tau_a\tau_r \quad 3.116$$

Where τ_a is the transmittance of the windscreen due to absorption only and τ_r is the transmittance of the windscreen due to reflection only. Therefore, the beam component of the windscreen transmittance can be represented in accordance with equation 3.116.

$$\tau_{ws_b} \cong \tau_{a_b}\tau_{r_b} \quad 3.117$$

3.2.1.7.2.1 Formulation of transmittance for beam radiation component

Schematic representation of the polyethylene (plastic) film is shown in Fig. 3.14. When a beam radiation strikes its surface at an incidence angle of θ_1, part is reflected while the remainder is refracted through a refraction angle θ_2, as it crosses the interface.

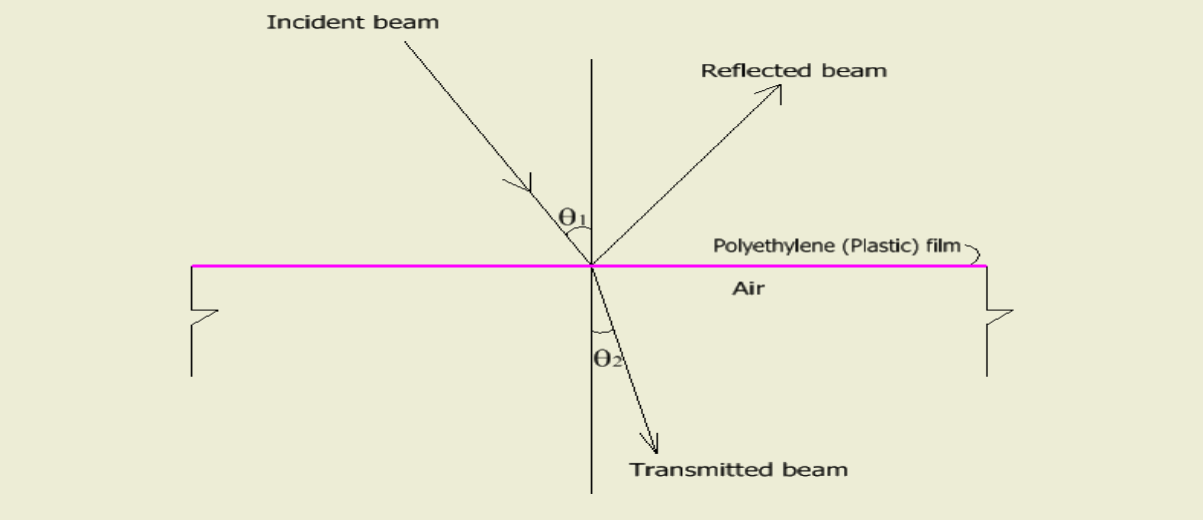

Fig. 3.14 Incident and reflected beams at interfaces of windscreen and air media

The transmitted beam bends towards the perpendicular to the surface of higher density (plastic denser than air) as a result of refraction. Snell's Law relates the angle of incidence θ_1, to the angle of refraction θ_2, according to the following expression,

$$\frac{Sin\theta_1}{Sin\theta_2} = \frac{n_2}{n_1} = \eta \qquad 3.118$$

n_1 is the refractive index of Polyethylene (plastic), n_2 is the refractive index of air and η is the ratio of refractive indices for the two media forming the interface.

According to Fresnel, the perpendicular and parallel components (i.e. plane defined by the incident beam and surface normal) of radiation for smooth surfaces are given as (Kalogirou, 2009):

$$r_{\perp} = \frac{Sin^2(\theta_2 - \theta_1)}{Sin^2(\theta_2 + \theta_1)} \quad 3.119$$

$$r_{\parallel} = \frac{tan^2(\theta_2 - \theta_1)}{tan^2(\theta_2 + \theta_1)} \quad 3.120$$

The perpendicular and parallel components of radiation as shown in equations 3.119 and 3.120 are unpolarized and hence properties are evaluated at the average of the two equations, given as,

$$\zeta = \frac{1}{2}[r_{\perp} + r_{\parallel}] = \frac{1}{2}\left[\frac{Sin^2(\theta_2 - \theta_1)}{Sin^2(\theta_2 + \theta_1)} + \frac{tan^2(\theta_2 - \theta_1)}{tan^2(\theta_2 + \theta_1)}\right] \quad 3.121$$

Since transmission of solar radiation is usually through a slab or film of material, reflection losses occur across two interfaces per cover material (Duffie and Beckman, 2006). The transmitted and reflected radiations become partially polarized at off-normal incidence and as a result, each component of polarization can be treated separately. Thus, the transmittance for the perpendicular component of polarization is expressed as (Duffie and Beckman, 2006):

$$\tau_{\perp} = (1 - r_{\perp})^2 \sum_{n=0}^{\infty} {r_{\perp}}^{2n} = \frac{(1 - r_{\perp})^2}{1 - {r_{\perp}}^2} = \frac{1 - r_{\perp}}{1 + r_{\perp}} \quad 3.122$$

Similarly, the transmittance for the parallel component of polarization is given as,

$$\tau_{\parallel} = (1 - r_{\parallel})^2 \sum_{n=0}^{\infty} {r_{\parallel}}^{2n} = \frac{(1 - r_{\parallel})^2}{1 - {r_{\parallel}}^2} = \frac{1 - r_{\parallel}}{1 + r_{\parallel}} \quad 3.123$$

Except at normal incidence, $r_{\perp}$ and $r_{\parallel}$ are not equal. Hence, the beam transmittance due to reflection only (of the initially unpolarized radiation) becomes the average transmittance of the perpendicular and parallel components (equations 3.119 and 3.120) given by,

$$\tau_{r_b} = \frac{1}{2}[\tau_{\perp} + \tau_{\parallel}] \quad 3.124$$

Substituting for $\tau_{\perp}$ and $\tau_{\parallel}$ from equations 3.122 and 3.123 into equation 3.124, the beam transmittance due to reflection only becomes:

$$\tau_{r_b} = \frac{1}{2}\left[\frac{1-r_\perp}{1+r_\perp} + \frac{1-r_\parallel}{1+r_\parallel}\right] \quad 3.125$$

If a system of n-windscreens of the same material is considered, the resulting expression for the beam radiation transmittance due to reflection (i.e. reflection losses) only is given by,

$$\tau_{r_b} = \frac{1}{2}\left[\frac{1-r_\perp}{1+(2n_{ws}-1)r_\perp} + \frac{1-r_\parallel}{1+(2n_{ws}-1)r_\parallel}\right] \quad 3.126$$

Hence, the equivalence reflectance for diffuse radiation becomes,

$$\rho_d = 1 - \tau_{r_b} \quad 3.127$$

The beam radiation transmittance of the windscreen due to absorption only is given by (Ogueke, 2005; Duffie and Beckmann 2006; Kalogirou, 2009) as,

$$\tau_{\alpha_b} = e^{\left(-\frac{KL}{Cos\theta_2}\right)} \quad 3.128$$

Where K is the extinction coefficient for the windscreen (plastic) and L is the thickness of the windscreen.

However, one of the simplifying assumptions is that there is no internal absorption in the polyethylene windscreen since the plastic film is infinitesimally thin (≈20μm) for appreciable absorption to occur, the transmission of the plastic cover can be considered with treatment of reflection losses only and equation 3.116 approximates to:

$$\tau_{ws} \cong \tau_{r_b} \quad 3.129$$

3.2.1.7.2.2 Diffuse and ground reflected transmittances due to reflection losses only

Brandemuehl and Beckman computed the transmittances of glazing systems by treating both sky diffuse radiation and ground-reflected radiation as isotropic (Duffie and Beckman, 2006;

Kalogirou, 2009). They presented their results in terms of effective incidence angles θ_{e_d} and $\theta_{e_{gr}}$ expressed as functions of the plate tilt angle β:

$$\theta_{e_d} = 59.7 - 0.1388\beta + 0.001497\beta^2 \quad 3.130$$

$$\theta_{e_{gr}} = 90 - 0.5788\beta + 0.002693\beta^2 \quad 3.131$$

Where θ_{e_d} and $\theta_{e_{gr}}$ are effective incidence angles for sky diffuse and ground reflected radiation, respectively.

The angle of incidence (θ_1) for beam radiation is determined using equation 3.94 while the angle of refraction for the polyethylene (θ_2) is obtained from equation 3.118 using refractive indices n_1 and n_2 for the polyethylene and air, respectively. The components of polarized radiation are computed from equations 3.122 and 3.123, and the transmittance due to reflection only is evaluated using equation 3.125.

By substituting equation 3.129 into equation 3.114, the transmittance-absorptance product for beam radiation component becomes:

$$(\tau\alpha)_b = 1.01\tau_{r_b}\alpha_{ss} \quad 3.132$$

Also, substituting equation 3.125 into 3.132, the transmittance-absorptance product for the beam radiation becomes:

$$(\tau\alpha)_b = \frac{1.01}{2}\left[\frac{1-r_\perp}{1+r_\perp} + \frac{1-r_\parallel}{1+r_\parallel}\right]\alpha_{ss} \quad 3.133$$

This product can also be computed using the resulting expression when equation 3.129 for the transmittance due to reflection only and equation 3.127 for equivalent reflectance for diffuse radiation are substituted into equation 3.113 as follows:

$$(\tau\alpha)_b = \frac{\tau_{rb}\alpha_{ss}}{1-(1-\alpha_{ss})(1-\tau_{rb})} \qquad 3.134$$

Substituting equation 3.125 into equation 3.134, the transmittance-absorptance product for beam radiation due to reflection losses becomes:

$$(\tau\alpha)_b = \frac{\frac{\alpha_{ss}}{2}\left[\frac{1-r_\perp}{1+r_\perp}+\frac{1-r_\parallel}{1+r_\parallel}\right]}{1-(1-\alpha_{ss})\left(1-\left[\frac{1-r_\perp}{1+r_\perp}+\frac{1-r_\parallel}{1+r_\parallel}\right]\right)} \qquad 3.135$$

Similarly, using equation 3.130, the effective incidence angle for all diffuse radiations θ_{e_d}, can be evaluated and applying Snell's relation (equation 3.118), the refraction angle for the diffuse component can be evaluated as:

$$\theta_{2_d} = Sin^{-1}\left[\frac{n_1 Sin\theta_{e_d}}{n_2}\right] \qquad 3.136$$

From Fresnel's relations (equations 3.119 and 3.120), the polarized perpendicular and parallel radiation components ($r_{\perp_d} and\ r_{\parallel_d}$) can be evaluated for the diffuse component of radiation as:

$$r_{\perp_d} = \frac{Sin^2(\theta_{2_d}-\theta_{e_d})}{Sin^2(\theta_{2_d}+\theta_{e_d})} \qquad 3.137$$

$$r_{\parallel_d} = \frac{tan^2(\theta_{2_d}-\theta_{e_d})}{tan^2(\theta_{2_d}+\theta_{e_d})} \qquad 3.138$$

The transmittance for the perpendicular component of polarization for the diffuse radiation is expressed as:

$$\tau_{\perp_d} = \frac{1-r_{\perp_d}}{1+r_{\perp_d}} \qquad 3.139$$

While the transmittance for the parallel component of polarization is expressed as:

$$\tau_{\parallel_d} = \frac{1 - r_{\parallel_d}}{1 + r_{\parallel_d}} \qquad 3.140$$

Hence, the diffuse radiation transmittance due to reflectance (i.e. reflection losses) only is obtained by combining equations 3.139 and 3.140. This gives:

$$\tau_{r_d} = \frac{1}{2}\left[\frac{1-r_{\perp_d}}{1+r_{\perp_d}} + \frac{1-r_{\parallel_d}}{1+r_{\parallel_d}}\right] \qquad 3.141$$

Substituting τ_{r_d} for τ_{ws} and equation 3.127 for ρ_d in equation 3.113, the transmittance-absorptance product for diffuse radiation component becomes:

$$(\tau\alpha)_d = \frac{\tau_{r_d}\alpha_{ss}}{1-(1-\alpha_{ss})(1-\tau_{r_b})} \qquad 3.142$$

Also, from equation 3.131, the effective incidence angle for all ground-reflected radiations $\theta_{e_{gr}}$ can be evaluated and applying Snell's relation, the refraction angle for the ground-reflected component becomes:

$$\theta_{2_{gr}} = Sin^{-1}\left[\frac{n_1 Sin\theta_{e\,gr}}{n_2}\right] \qquad 3.143$$

From Fresnel's relations (equations 3.119 and 3.120), the polarized perpendicular and parallel radiation components ($r_{\perp_{gr}} and\ r_{\parallel_{gr}}$) can be evaluated for the ground reflected component of radiation as:

$$r_{\perp_{gr}} = \frac{Sin^2\left(\theta_{2\,gr} - \theta_{e\,gr}\right)}{Sin^2\left(\theta_{2\,gr} + \theta_{e\,gr}\right)} \qquad 3.144$$

$$r_{\parallel_{gr}} = \frac{tan^2\left(\theta_{2\,gr} - \theta_{e\,gr}\right)}{tan^2\left(\theta_{2\,gr} + \theta_{e\,gr}\right)} \qquad 3.145$$

The transmittance for the perpendicular component of polarization for ground reflected radiation is expressed as:

$$\tau_{\perp_{gr}} = \frac{1-r_{\perp_{gr}}}{1+r_{\perp_{gr}}} \quad 3.146$$

And the transmittance for the ground reflected parallel component of polarization is expressed as:

$$\tau_{\parallel_{gr}} = \frac{1-r_{\parallel_{gr}}}{1+r_{\parallel_{gr}}} \quad 3.147$$

Hence, the ground reflected radiation transmittance due to reflectance (i.e. reflection losses) only is given by the combination of equations 3.146 and 3.147 to give:

$$\tau_{r_{gr}} = \frac{1}{2}\left[\frac{1-r_{\perp_{gr}}}{1+r_{\perp_{gr}}} + \frac{1-r_{\parallel_{gr}}}{1+r_{\parallel_{gr}}}\right] \quad 3.148$$

Therefore, substituting $\tau_{r_{gr}}$ for τ_{ws} and equation 3.127 for ρ_d into equation 3.113, the transmittance-absorptance product for ground reflected radiation component becomes:

$$(\tau\alpha)_{gr} = \frac{\tau_{r_{gr}}\alpha_{ss}}{1-(1-\alpha_{ss})(1-\tau_{r_b})} \quad 3.149$$

Finally, the net radiation absorbed by the SCONOR plate during the diurnal exposure to thermal radiation from the sun, in an hourly basis, is obtained by substituting the beam, diffuse and ground-reflected components of the transmittance-absorptance products as given in equations 3.135, 3.142, and 3.149 into equation 3.115. The resulting expression becomes:

$$I_{t_T} =$$

$$I_b R_b \left\{ \frac{\frac{\alpha_{ss}}{2}\left[\frac{1-r_\perp}{1+r_\perp}+\frac{1-r_\parallel}{1+r_\parallel}\right]}{1-(1-\alpha_{ss})\left(1-\left[\frac{1-r_\perp}{1+r_\perp}+\frac{1-r_\parallel}{1+r_\parallel}\right]\right)} \right\} + I_d \left\{ \frac{\tau_{r_d}\alpha_{ss}}{1-(1-\alpha_{ss})(1-\tau_{r_b})} \right\} \left(\frac{1+Cos\beta}{2}\right) +$$

$$\rho_{gr}(I_b + I_d) \left\{ \frac{\tau_{r_{gr}}\alpha_{ss}}{1-(1-\alpha_{ss})(1-\tau_{r_b})} \right\} \left[\frac{1-Cos\beta}{2}\right]$$

3.150

Equation 3.150 is the Q_{solar} term of equation 3.24.

Dust and shading factors, when considered, account for reduction of about 2% and 3% of the total absorbed radiation respectively (Ogueke, 2005). Therefore, equation 3.150 becomes:

$$I_{t_T} =$$

$$\left\{ I_b R_b \left\{ \frac{\frac{\alpha_{ss}}{2}\left[\frac{1-r_\perp}{1+r_\perp}+\frac{1-r_\parallel}{1+r_\parallel}\right]}{1-(1-\alpha_{ss})\left(1-\left[\frac{1-r_\perp}{1+r_\perp}+\frac{1-r_\parallel}{1+r_\parallel}\right]\right)} \right\} + I_d \left\{ \frac{\tau_{r_d}\alpha_{ss}}{1-(1-\alpha_{ss})(1-\tau_{r_b})} \right\} \left(\frac{1+Cos\beta}{2}\right) + \right.$$

$$\left. \rho_{gr}(I_b + I_d) \left\{ \frac{\tau_{r_{gr}}\alpha_{ss}}{1-(1-\alpha_{ss})(1-\tau_{r_b})} \right\} \left[\frac{1-Cos\beta}{2}\right] \right\} * 0.98 * 0.97$$

3.151

3.2.2 Thermal Modelling of the Nocturnal Cooling Process

During the night, at about 20:00 hours, when there is no solar radiation and the sky temperature is low, the SCONOR plate automatically functions as a thermal radiator due to its spectral properties, thus dissipating infrared radiation to the night sky. It cools water flowing through the pipe welded to the panel underneath, which is stored in the cold water tank (Reservoir B) that would be used to provide cooling in a room the following day. The lower the ambient temperature and clearer the sky conditions the more efficient the performance of the radiative cooling system. During the nocturnal cooling process, the transparent polyethylene cover acts to reduce thermal convective gain from the surroundings without preventing the long wave radiation losses to the sky (Aelenei et al., n.d.).

Dobson (2005), Nwaigwe et al (2011) and Mingke et al (2015) adopted the lumped parameter approach in the analysis of heat flow in nocturnal radiators using the assumptions that the temperature is uniform everywhere on the radiator surface at any given time and also that the water is in direct contact with the radiator on its underside. Dobson stated that when such approach is adopted in the radiator analysis, the efficiency is considered unity (Dobson, 2005). However, in most cases, as is the case in this analysis, water flows beneath the radiator in pipes bonded to it and so the efficiency is practically less than unity and the best approach is the fin theory approach as is generally applicable in diurnal heating, in order to correctly evaluate the radiator performance (Mills, 2000).

3.2.2.1 The SCONOR model_Nocturnal Phase

Fig.3.15 illustrates the energy balance on the solar collector/nocturnal radiator (SCONOR) taken at the region between the centrelines and a tube. Water enters into the tube from the top and leaves the tube through the downside into the cold water reservoir B. There is an exchange of energy between the water and the tube inner walls and the energy lost from the water is transferred to the tube through convection, from where it is conducted via the bond to the nocturnal radiator. When the radiator receives the energy at the point of contact with the bond, it conducts the energy axially along the x- and y-axes of the plate to the edges where it is eventually lost by convection. Also, the radiator is losing energy by radiative exchange with the night-sky.

The thermal model of the nocturnal radiator is established based on the following assumptions:

i. The SCO**NOR** plate retains its material properties, being made of Titaniun Polyethylene Terephthalate as the selective radiator surface with a constant emissivity of 0.8.
ii. There is no internal heat generation in the nocturnal radiator.

iii. The back of the panel is perfectly insulated underneath to eliminate convection gain from the ambient through the back of the radiator.

iv. The computation is taken only for a clear sky condition.

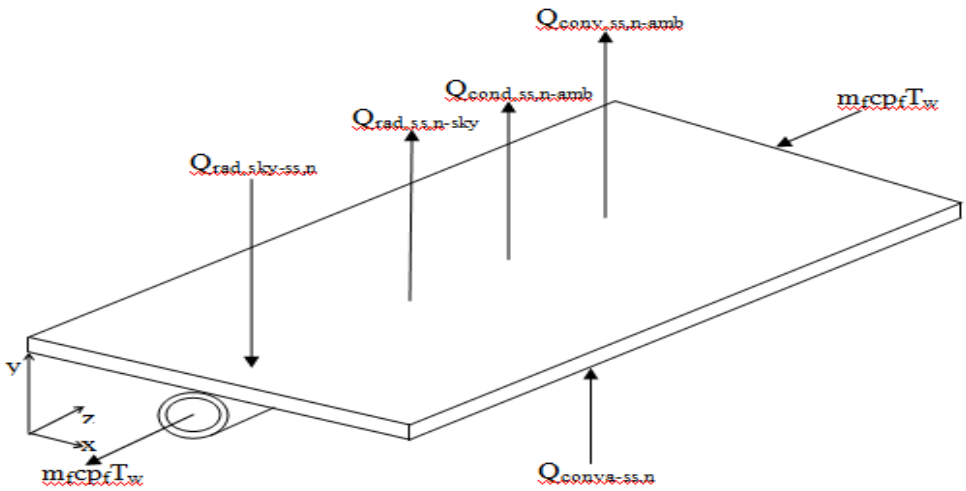

Fig. 3.15 Energy Balance on SCONOR_Radiative Process

Fig 3.16 illustrates the radiator as a fin with various contributions to the energy balance.

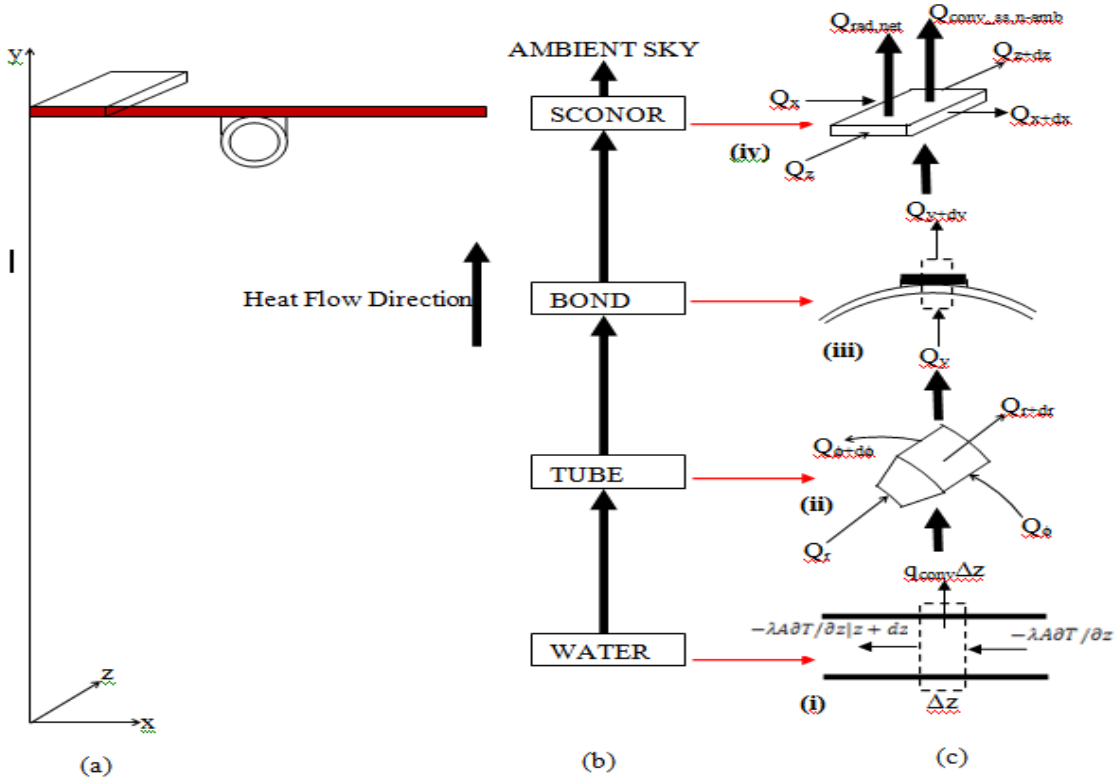

Fig. 3.16 Energy balance for the fin element of the SCONOR during the nocturnal phase

Fig. 3.16 shows the SCONOR represented as a fin, following the same treatment for the diurnal heating phase but with a reversal of both the fluid and heat flow processes. Water enters into the tube from the top and heat flows from the water in the tube to the tube inner surface by convection and the heat received by the tube is conducted to the SCONOR via the bond and from the SCONOR it is lost to the ambient sky as shown in Fig. 3.16 (b). Fig. 3.16 (ci-iv) illustrates the differential control volumes for the water, tube, bond, and SCONOR. These are employed in deriving the governing differential equations of the heat flow process in the system.

3.2.2.1.1 The fluid region

At about 20:00 hours, reservoir B is opened and water inside it flows into the SCONOR through the tubes bonded underneath. Energy transfer begins from the water. The differential control volume of the fluid element in the tube can be represented as shown in Fig. 3.16 c(i). Conducting an energy balance about the elemental volume of the fluid element, equation 3.2 is employed:

$$\dot{Q}_{in_w} + Q_{i,gen_w} = Q_{out_w} + \dot{Q}_{int,w} \qquad 3.152$$

Since there is no internal energy generation in the fluid region according to assumption (ii), Q_{i,gen_w} equals zero.

The net increase in the thermal energy of the fluid in the control volume is given by the time rate of change of the heat capacity of the element and can be written as:

$$\dot{Q}_{int,w} = \rho_w c_{p_w} dV \frac{\partial T_w}{\partial t} \qquad 3.153$$

Therefore, the energy balance for the fluid zone becomes:

$$-k_w \mathrm{A} \frac{\partial \mathrm{T_w}}{\partial \mathrm{z}} = -k_w \mathrm{A} \frac{\partial \mathrm{T_w}}{\partial \mathrm{z}}|_{\mathrm{z+dz}} + \mathrm{q_{conv}} \Delta \mathrm{z} + \mathrm{m_w} c_{p_w} \frac{\partial T_w}{dt} \qquad 3.154$$

This implies that,

$$\mathrm{m_w} c_{p_w} \frac{\partial T_w}{dt} = -k_w \mathrm{A} \frac{\partial \mathrm{T_w}}{\partial \mathrm{z}} + k_w \mathrm{A} \frac{\partial \mathrm{T_w}}{\partial \mathrm{z}}|_{\mathrm{z+dz}} - \mathrm{q_{conv}} \Delta \mathrm{z} \qquad 3.155$$

$$\mathrm{m_w} c_{p_w} \frac{\partial T_w}{dt} = -k_w \mathrm{A} \frac{\partial \mathrm{T_w}}{\partial \mathrm{z}} + k_w \mathrm{A} \frac{\partial}{\partial \mathrm{z}} \left[\mathrm{T_w} + \frac{\partial \mathrm{T_w}}{\partial \mathrm{z}} \Delta \mathrm{z} \right] - \pi \mathrm{D ih_{wi}} (\mathrm{T_w} - \mathrm{T_t}) \Delta \mathrm{z} \qquad 3.156$$

Equation 3.156 simplifies to:

$$\mathrm{m_w} c_{p_w} \frac{\partial T_w}{dt} = k_w \mathrm{A} \frac{\partial}{\partial \mathrm{z}} \left[\frac{\partial \mathrm{T_w}}{\partial \mathrm{z}} \Delta \mathrm{z} \right] - \pi \mathrm{D ih_{wi}} (\mathrm{T_w} - \mathrm{T_t}) \Delta \mathrm{z} \qquad 3.157$$

3.2.2.1.1.1 The tube region

The energy received by the tube from the water is transferred by conduction radially and azimuthally from the inner walls to the outer surface of the tubes where the SCONOR plate is bonded to them. The elemental control volume of the tube element is as shown in Fig. 3.16c (ii). Applying equation 3.1 to the tube control volume,

Energy into the tube control volume + Internal energy generation within the control volume = energy out of the control + rate of change of internal change of the control volume.

$$Q_r + Q_{\emptyset} + Q_{i,gen} = Q_{r+dr} + Q_{\emptyset+d\emptyset} + Q_{int} \qquad 3.158$$

The energy flow into the tube element in the radial and azimuthal directions are given as:

$$\left.\begin{aligned} Q_r &= -k_t (r d\emptyset dz) \frac{\partial T_{tn}}{\partial r} \\ Q_{\emptyset} &= -k_t (r dr dz) \frac{\partial T_{tn}}{r \partial \emptyset} \end{aligned}\right\} \qquad 3.159$$

The energy flow out of the tube control volume in the radial and azimuthal directions can also be given as:

$$\left.\begin{aligned} Q_{r+dr} &= -k_t (r d\emptyset dz) \frac{\partial T_{tn}}{\partial r} + \frac{\partial}{\partial r} \left(-k_t (r d\emptyset dz) \frac{\partial T_{tn}}{\partial r} \right) dr \\ Q_{\emptyset+d\emptyset} &= -k_t (dr dz) \frac{\partial T_{tn}}{r \partial \emptyset} + \frac{\partial}{r \partial \emptyset} \left(-k_t (dr dz) \frac{\partial T_{tn}}{r \partial \emptyset} \right) r d\emptyset \end{aligned}\right\} \qquad 3.160$$

The rate of change in the internal energy of the tube is given as:

$$Q_{int} = \rho_t c_{p_t} r d\emptyset dr dz \frac{\partial T_{tn}}{\partial t} \qquad 3.161$$

Since there is no internal energy generation in the tube during the nocturnal phase, the energy balance for the tube element control volume can be written by substituting equations 3.159, 3.160 and 3.161 into equation 3.158 to yield:

$$-k_t(rd\emptyset dz)\frac{\partial T_{tn}}{\partial r} - k_t(rdrdz)\frac{\partial T_{tn}}{r\partial\emptyset} = -k_t(rd\emptyset dz)\frac{\partial T_{tn}}{\partial r} + \frac{\partial}{\partial r}\left(-k_t(rd\emptyset dz)\frac{\partial T_{tn}}{\partial r}\right)dr - k_t(drdz)\frac{\partial T_{tn}}{r\partial\emptyset} + \frac{\partial}{r\partial\emptyset}\left(-k_t(drdz)\frac{\partial T_{tn}}{r\partial\emptyset}\right)rd\emptyset + \rho_t c_{p_t} rd\emptyset drdz\frac{\partial T_{tn}}{\partial t} \quad 3.162$$

On simplification and taking cognizance of the fact that the heat is being conducted out of the tube, equation 3.162 becomes:

$$\rho_t c_{p_t}\delta_t\frac{\partial T_{tn}}{\partial t} = -k_t\delta_t\left[\frac{\partial^2 T_{tn}}{\partial r^2} + \frac{1}{r}\frac{\partial T_{tn}}{\partial r} + \frac{1}{r^2}\frac{\partial^2 T_{tn}}{\partial\emptyset^2}\right] \quad 3.163$$

3.2.2.1.2 The bond region

Assuming perfect thermal contact exists between the tube and bond, the energy lost by the tube is gained by the bond by conduction along the y-axis only since the bond span the entire tube length. Thus, the bond is conveniently treated as a one dimensional zone as shown in Fig. 3.16c (iii). Applying equation 3.1 to the bond control volume:

$$Q_y + Q_{i,gen} = Q_{y+dy} + Q_{int} \quad 3.163$$

The energy inflow from the tube outer surface at the point of contact with the bond region into the bond control volume can be expressed as:

$$Q_y = -k_b dxdz\frac{\partial T_{bn}}{\partial y} \quad 3.164$$

And the energy outflow from the bond control volume across the differential element is given as:

$$Q_{y+dy} = -k_b dxdz\frac{\partial T_{bn}}{\partial y} + \frac{\partial}{\partial y}\left(-k_b dxdz\frac{\partial T_{bn}}{\partial y}\right)dy \quad 3.165$$

Since there is no volumetric heat generation in the bond region, the energy balance around the bond becomes:

$$-k_b dxdz\frac{\partial T_{bn}}{\partial y} = -k_b dxdz\frac{\partial T_{bn}}{\partial y} + \frac{\partial}{\partial y}\left(-k_b dxdz\frac{\partial T_{bn}}{\partial y}\right)dy + \rho_b c_{p_b} dxdydz\frac{\partial T_{bn}}{\partial t} \quad 3.166$$

This equation simplifies to:

$$\rho_b c_{p_b} dy\frac{\partial T_{bn}}{\partial t} = k_b dy\frac{\partial}{\partial y}\left(\frac{\partial T_{bn}}{\partial y}\right) \quad 3.167$$

3.2.2.1.3 The Nocturnal Radiator (SCONOR) region

Assuming perfect thermal contact between the bond and radiator, the energy lost by the bond is received by conduction by the nocturnal radiator from where part of it is lost to the ambient sky through radiation and convection from the top of the SCONOR. The remaining part of this energy is conducted along the SCONOR to the edges from where it is lost by convection. The radiator control volume is as shown in Fig. 3.16c (iv).

Employing equation 3.1, the general energy balance for the SCONOR functioning as a nocturnal radiator can be mathematically expressed as:

$$\dot{Q}_{in} + \dot{Q}_{i,gen} = \dot{Q}_{out} + \dot{Q}_{int} \quad 3.168$$

From Fig. 3.16d (iv),

$$\dot{Q}_{in} = \dot{Q}_x + \dot{Q}_z \quad 3.169$$

The energy inflows in the x- and z-directions into the nocturnal radiator, Q_x and Q_z are given as:

$$\dot{Q}_x = -k_{ss} dydz\frac{\partial T_{ssn}}{\partial x}$$

$$\dot{Q}_z = -k_{ss} dxdy \frac{\partial T_{ssn}}{\partial z} \quad 3.170$$

Therefore,

$$\dot{Q}_{in} = -k_{ss} dydz \frac{\partial T_{ssn}}{\partial x} - k_{ss} dxdy \frac{\partial T_{ssn}}{\partial z} \quad 3.171$$

From Fig. 3.16d (iv), the energy outflow from the NOR control volume can be given as:

$$\dot{Q}_{out} = \dot{Q}_{x+dx} + \dot{Q}_{z+dz} + \dot{Q}_{rad,net} + \dot{Q}_{conv_{ss},n\_amb} \quad 3.172$$

The energy outflows from the NOR control volume in the x- and z-directions is respectively:

$$\dot{Q}_{x+dx} = -k_{ss} dydz \frac{\partial T_{ssn}}{\partial x} + \frac{\partial}{\partial x}\left(-k_{ss} dydz \frac{\partial T_{ssn}}{\partial x}\right) dx$$

$$\dot{Q}_{z+dz} = -k_{ss} dxdy \frac{\partial T_{ssn}}{\partial z} + \frac{\partial}{\partial z}\left(-k_{ss} dxdy \frac{\partial T_{ssn}}{\partial z}\right) dz \quad 3.173$$

Therefore the energy being conducted away from the NOR control volume in the x- and z-directions become:

$$\dot{Q}_{x+dx} + \dot{Q}_{z+dz} = -k_{ss} dydz \frac{\partial T_{ssn}}{\partial x} + \frac{\partial}{\partial x}\left(-k_{ss} dydz \frac{\partial T_{ssn}}{\partial x}\right) dx - k_{ss} dxdy \frac{\partial T_{ssn}}{\partial z} + \frac{\partial}{\partial z}\left(-k_{ss} dxdy \frac{\partial T_{ssn}}{\partial z}\right) dz \quad 3.174$$

Substituting equation 3.174 into equation 3.172, the energy leaving the control volume by conduction, radiation and convection can be expressed as:

$$\dot{Q}_{out} = -k_{ss} dydz \frac{\partial T_{ssn}}{\partial x} + \frac{\partial}{\partial x}\left(-k_{ss} dydz \frac{\partial T_{ssn}}{\partial x}\right) dx - k_{ss} dxdy \frac{\partial T_{ssn}}{\partial z} + \frac{\partial}{\partial z}\left(-k_{ss} dxdy \frac{\partial T_{ssn}}{\partial z}\right) dz + \dot{Q}_{rad,net} dxdz + \dot{Q}_{conv_{ss},n\_amb} dxdz \quad 3.175$$

The time rate of change of the heat capacity of the control volume, Q_{int} can be expressed as:

$$\dot{Q}_{int} = \rho_{ss} c_{p_{ss}} dxdydz \frac{\partial T_{ssn}}{\partial t} \quad 3.176$$

The net energy leaving the nocturnal radiator is obtained by substituting equations 3.171, 3.175 and 3.176 into equation 3.168, resulting in:

$$k_{ss}dydz\frac{\partial T_{ssn}}{\partial x} - k_{ss}dxdy\frac{\partial T_{ssn}}{\partial z} = -k_{ss}dydz\frac{\partial T_{ssn}}{\partial x} + \frac{\partial}{\partial x}\left(-k_{ss}dydz\frac{\partial T_{ssn}}{\partial x}\right)dx - k_{ss}dxdy\frac{\partial T_{ssn}}{\partial z} + \frac{\partial}{\partial z}\left(-k_{ss}dxdy\frac{\partial T_{ssn}}{\partial z}\right)dz + \dot{Q}_{rad,net}dxdz + \dot{Q}_{conv_{ss},n\_amb}dxdz + \rho_{ss}c_{p_{ss}}dxdydz\frac{\partial T_{ssn}}{\partial t}$$

3.177

Simplifying and rearranging equation 3.177 would lead to:

$$\rho_{ss}c_{p_{ss}}dxdydz\frac{\partial T_{ssn}}{\partial t} = \frac{\partial}{\partial x}\left(-k_{ss}dydz\frac{\partial T_{ssn}}{\partial x}\right)dx + \frac{\partial}{\partial z}\left(-k_{ss}dxdy\frac{\partial T_{ssn}}{\partial z}\right)dz + \dot{Q}_{rad,net}dxdz + \dot{Q}_{conv_{ss},n\_amb}dxdz$$

3.178

Dividing through by $dxdz$,

$$\rho_{ss}c_{p_{ss}}dy\frac{\partial T_{ssn}}{\partial t} = -\frac{\partial}{\partial x}\left(k_{ss}dy\frac{\partial T_{ssn}}{\partial x}\right) - \frac{\partial}{\partial z}\left(k_{ss}dy\frac{\partial T_{ssn}}{\partial z}\right) + \dot{Q}_{rad,net} + \dot{Q}_{conv_{ss},n\_amb} \quad 3.179$$

The net long-wave radiation exchange between the SCONOR and the night-sky, $\dot{Q}_{rad,net}$ is given as (Meir et al., 2003):

$$\dot{Q}_{rad,net} = A_{ss}\varepsilon_{ss,n}\left(\sigma {T_{ss,n}}^4 - \mathcal{R}\right) \quad 3.180$$

Where $\mathcal{R}$ is the long-wave radiation incident on the surface of the radiator from the night-sky which is dependent on the surface orientation. While equation 3.157 representing the energy which is being lost from fluid is given in watts because of the surface (area) term appearing in it, equations 3.163, 3.167 and 3.179 for the tube, bond and nocturnal radiator respectively are given in watts per unit area because the surface terms are not represented. For homogeneity, during implementation, equations 3.163, 3.167 and 3.179 should be multiplied by the surface areas of the tube, bond and NOR respectively.

3.2.2.1.3.1 Radiator on a horizontal surface

For a radiator on a horizontal surface, the radiation from the night-sky to the radiator takes place within a few hundred meters thick atmospheric layer near the ground, where the ambient temperature fairly approximates the sky temperature (Meir et al., 2003; Duffie and Beckman, 2006). The radiant heat transfer from the atmosphere to the horizontal surface on the earth $\mathcal{R}$, is therefore given as:

$$\mathcal{R}_A = \sigma {T_{sky}}^4 \quad 3.181$$

Therefore, the net radiant exchange between the radiator and the night-sky is given by:

$$\dot{Q}_{rad,net} = A_{ss}\varepsilon_{ss,n}\sigma\left({T_{ss,n}}^4 - {T_{sky}}^4\right) \quad 3.182$$

According to Meir et al (2003) and Rupinder et al (2015), the sky temperature is related to the ambient temperature by equation 3.183.

$$T_{sky} = {\varepsilon_{sky}}^{0.25} T_a \quad 3.183$$

The emittance of the night-sky ε_{sky} is a function of temperature and relative humidity of the air and has been correlated by Berdahl and Martin (Meir et al., 2003; Rupinder et al., 2015) as:

$$\varepsilon_{sky} = 0.711 + 0.0056T_{dp} + 0.000073{T_{dp}}^2 + 0.013Cos\frac{2\pi t_m}{24} \quad 3.184$$

Where t_m is the number of hours from midnight in solar time, T_{dp} is the dew point temperature (^{o}C) given as (Rupinder et al., 2015; Meir et al., 2003):

$$T_{dp} = \frac{\varrho_3[ln(RH)+\varrho_1]}{\varrho_2-[ln(RH)+\varrho_1]} \quad 3.185$$

And ϱ_1 is expressed as:

$$\varrho_1 = \frac{\varrho_2 T_{dry}}{\varrho_3+T_{dry}} \quad 3.186$$

ϱ_2 and ϱ_3 are constants given as 17.08085 and 234.175 respectively while the dry bulb temperature T_{dry} is equal to the ambient temperature T_a.

3.2.2.1.3.2 Radiator on a tilted surface

When the radiator is inclined to the horizontal with a tilt angle β, the long-wave radiation incident on the surface $\mathcal{R}$ is expressed as function of β, and is given by Meir et al. (2003) as:

$$\mathcal{R}(\beta) = \mathcal{R}_A(\beta) + \mathcal{R}_g(\beta) \quad 3.187$$

$\mathcal{R}_A(\beta)$ is the atmospheric irradiance expressed as:

$$\mathcal{R}_A(\beta) = \mathcal{R}_A Cos^2\left(\frac{\beta}{2}\right) + bI_7\sigma {T_a}^4 = \sigma {T_{sky}}^4 Cos^2\left(\frac{\beta}{2}\right) + bI_7\sigma {T_a}^4 \quad 3.188$$

Where b is a constant in the range $0.07 \ll b \ll 0.14$; I_7 is dependent on the tilt angle β. For a tilt angle of 39^o, $I_7 \approx 0.2$.

And $\mathcal{R}_g$ is the ground irradiance expressed as:

$$\mathcal{R}_g(\beta) = Sin^2\left(\frac{\beta}{2}\right)\left(\varepsilon_g\sigma T_g^4 + \rho_g\mathcal{R}_A\right) = Sin^2\left(\frac{\beta}{2}\right)\left(\varepsilon_g\sigma T_g^4 + \rho_g\sigma {T_{sky}}^4\right) \quad 3.189$$

While ε_g is the emittance of the ground; T_g and ρ_g are ground temperature and reflectance respectively.

Therefore, the radiant heat transfer from the atmospheric to the tilted radiator becomes:

$$\mathcal{R}(\beta) = \sigma {T_{sky}}^4 Cos^2\left(\frac{\beta}{2}\right) + bI_7\sigma {T_a}^4 + Sin^2\left(\frac{\beta}{2}\right)\left(\varepsilon_g\sigma T_g^4 + \rho_g\sigma {T_{sky}}^4\right) \quad 3.190$$

And the net radiant exchange between the radiator and the night-sky is given by:

$$\dot{Q}_{rad,net}(\beta) = A_{ss}\varepsilon_{ss,n}\left(\sigma {T_{ss,n}}^4 - \left[\sigma {T_{sky}}^4 Cos^2\left(\frac{\beta}{2}\right) + bI_7\sigma {T_a}^4 + Sin^2\left(\frac{\beta}{2}\right)\left(\varepsilon_g\sigma T_g^4 + \rho_g\sigma {T_{sky}}^4\right)\right]\right) \quad 3.191$$

The convection heat losses from the SCONOR surface to the ambient $\dot{Q}_{conv_{ss,n-a}}$ can be expressed as:

$$\dot{Q}_{conv_{ss,n-a}} = h_{conv_{ss,n-a}}A_{ss}\left(T_{ss,n} - T_a\right) \quad 3.192$$

For a radiator with a single polyethylene windscreen, the convection heat transfer coefficient due to wind is given by Mingke et al. (2015) as presented in equation 3.84. Therefore,

$$h_{conv_{ss,n-a}} = h_{c,ws-a} = 0.5 + 1.2u^{0.5} \quad 3.193$$

3.2.3 Thermal stratification in the water storage tanks

The high specific heat capacity and density of water make it extremely attractive as a storage medium, mostly in low-to-medium temperature applications. This is because in sensible heat storage, the heat capacity is the major parameter. In the hybrid water heating/cooling system, water is heated during the day and stored for use at later times (domestic use, space heating, etc); and water is cooled during the night and stored for use at later times (for storage of agricultural products especially vegetable, space cooling). The main objective of the storing process is to maintain the thermodynamic availability of the stored energy to allow its extraction at the same temperature level at which it was stored. Because relatively large tanks are required to store substantial amount of energy in the low-to-medium temperature solar energy systems owing to their moderate range of working temperature, stratification therefore is the best option in order to optimize the cost of the systems. The amount of stored energy as well as the water cool down pattern in the tanks much depends on the degree of stratification achieved. Thermal stratification

investigation is a necessary step towards the overall hybrid water heating/cooling system optimization since it improves the overall system performance by increasing the efficiency of the SCONOR plate and enhance hot water availability during peak periods (mornings and evenings) with low or non availability of solar irradiation, and cold water availability during the day after it has gone through the nocturnal process.

3.2.3.1 Modelling the hot water storage tank

During the diurnal operation, heated water from the selective absorber is let into the hot water tank (from the top) where it is stored. Cold water flows from the tank bottom into the selective absorber where it absorbs energy, raising its temperature and finally flows back into the tank through the top. Mixing of hot and cold water occurs in the tank, resulting in a thermocline, which is a region of steep temperature gradient, the thickness of which is useful in optimizing the functioning of stratified tanks. The temperature gradient in the tank also results in density gradient as hotter water would become less dense and moves up while the colder region would settle towards the bottom of the tank. The thermocline region is as a result of mixing which occurs at the inlet to the tank from the collector. This region gradually travels down as more water enters the tank thus limiting the mixing between the cold and hot regions in the tank. The process continues until an equilibrium temperature is achieved and the charging and mixing stop. Hot water can then be drawn from the tank at any time for domestic use or space heating (to provide thermal comfort) in extremely cold weather.

In order to formulate the differential equation governing the transient behaviour of the hot water storage tank as the tank is being charged and discharged, the following assumptions are made:

i. The storage tank is vertically positioned and cylindrical in shape.

ii. Temperature stratification occurs in the tank in the axial direction only, which takes the y-coordinate in the Cartesian plane and hence it is regarded as a Y-cylinder.

iii. The entire tank volume is divided into N-horizontal zones of equal height and uniform temperature, numbered from top to bottom.

iv. Internal heat generation occurs in the tank as result of the fluid flowing to and from the neighbouring fluid zones.

v. The tank is completely mixed and filled, and the fluid velocity in the tank is constant.

vi. The mass flow rates into the tank from the selective collector and to the load are constant.

vii. Water leaves the tank through the bottom (last zone) to the collector and hot water leaves the tank through the top (first zone) to the load.

viii. The water from the collector enters the tank through a fluid zone with temperature close to but less than the outlet collector temperature while water from load enters the tank through a fluid zone with temperature close to but greater than the load return temperature, where its density closely matches that of the water in the tank.

3.2.3.1.1 Differential equation of stratification in the hot water tank

The energy balance in the tank takes cognizance of the gain in energy from the SCONOR during the day, losses to the surroundings and the energy utilized by the load. Fig 3.17 is a vertically positioned tank of length L and diameter D, divided into N-horizontal zones, from zone 1 at the top to zone N at the bottom. Water enters the tank from the SCONOR at the top and leaves the tank through zone N back to the SCONOR plate. It also leaves the tank from zone 1 at the top to load and returns to the tank according to assumption (viii). The energy balance on the i^{th} fluid element in the tank is given as shown in Fig. 3.18.

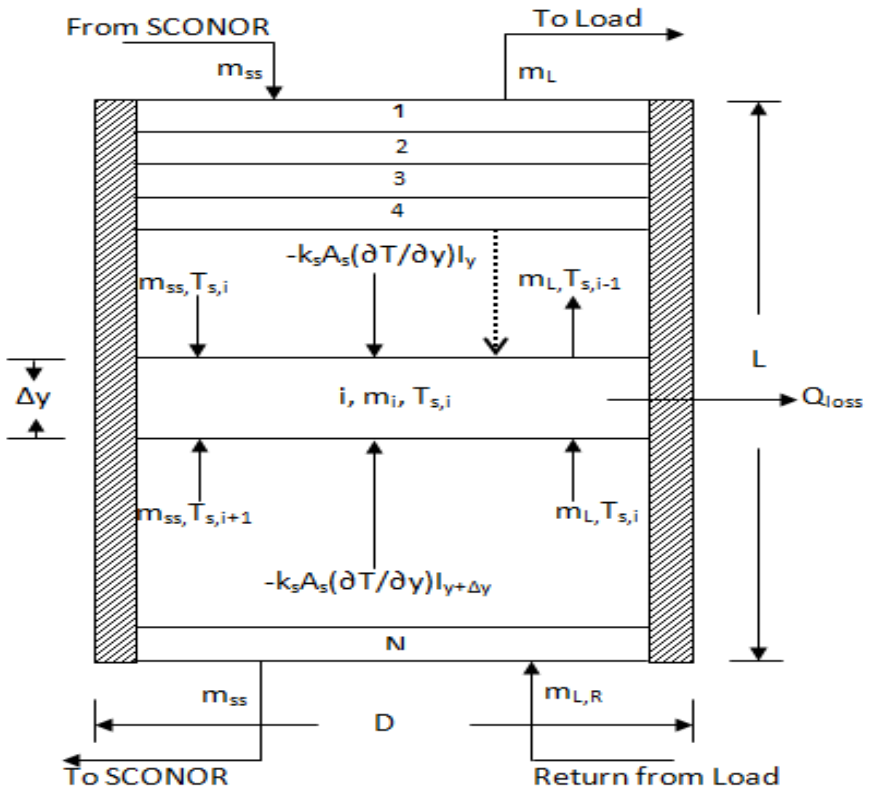

Fig. 3.17 Energy balance on the stratified hot water storage tank

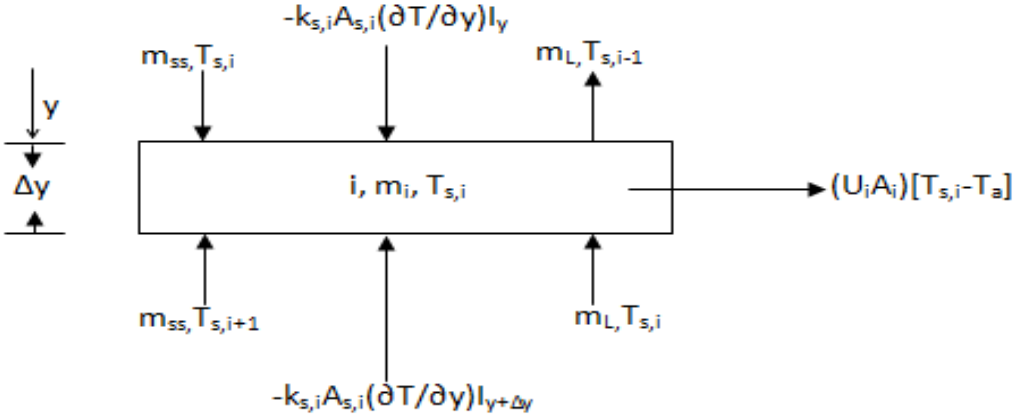

Fig. 3.18 Elemental volume of the i^{th} fluid zone

Applying the general energy balance principle, equation 3.2 can be written for the hot water storage tank as:

$$Energy\ into\ the\ ith\ fluid\ element\ +\ Internal\ heat\ generation\ within\ the\ fluid\ zones$$
$$= Energy\ out\ of\ the\ fluid\ zone$$
$$+\ Rate\ of\ change\ of\ internal\ energy\ of\ the\ fluid\ zone$$

3.194

That is,

$$Q_{in-hst} + Q_{igen,fluid\ zones-hst} = Q_{out-hst} + \dot{Q}_{int-hst} \quad 3.195$$

Considering Fig. 3.18, the net energy flowing into the i^{th} fluid zone of the hot storage tank, Q_{in-hst} is given by,

$$Q_{in-hst} = \dot{m}_{ss} C_{p_{ss}} T_{ph} \xi_{ss}^{i} - \dot{m}_{i} C_{p_i} T_{s,i} \xi_{ss}^{i} + \left(-k_{s,i} A_{s,i} \frac{\partial T_{s,i}}{\partial y}|_{y}\right) \quad 3.196$$

The net energy outflow from the i^{th} fluid zone $Q_{out-hst}$ is also given as:

$$Q_{out-hst} = \dot{m}_{L} C_{p_L} T_{L} \xi_{L}^{i} - \dot{m}_{i} C_{p_i} T_{s,i} \xi_{L}^{i} + (UA)_{s,i}\left[T_{s,i} - T_{a}\right] + \left(-k_{s,i} A_{s,i} \frac{\partial T_{s,i}}{\partial y}|_{y+\Delta y}\right) \quad 3.197$$

The thermal energy of the i^{th} fluid zone increases from the net heat flow into the fluid zone. This is expressed by the time rate of change of the heat capacity of the i^{th} fluid zone, given by:

$$\dot{Q}_{int-hst} = \dot{m}_{i} C_{p_i} \frac{\partial T_{s,i}}{\partial t} \quad 3.198$$

Therefore, the energy balance around the i^{th} fluid element is obtained by substituting equations 3.196, 3.197 and 3.198 respectively into equation 3.195, resulting in:

$$\dot{m}_{ss} C_{p_{ss}} T_{ph} \xi_{ss}^{i} - \dot{m}_{i} C_{p_i} T_{s,i} \xi_{ss}^{i} + \left(-k_{s,i} A_{s,i} \frac{\partial T_{s,i}}{\partial y}|_{y}\right) + Q_{igen,fluid\ zones} =$$
$$\dot{m}_{L} C_{p_L} T_{L} \xi_{L}^{i} - \dot{m}_{i} C_{p_i} T_{s,i} \xi_{L}^{i} + (UA)_{s,i}\left[T_{s,i} - T_{a}\right] + \left(-k_{s,i} A_{s,i} \frac{\partial T_{s,i}}{\partial y}|_{y+\Delta y}\right) + \dot{m}_{i} C_{p_i} \frac{\partial T_{s,i}}{\partial t} \quad 3.199$$

Since in the selective (absorber) surface and load sides respectively, the mass flow rate is constant (assumption vi), it means that $\dot{m}_{i} = \dot{m}_{ss}, C_{p_i} = C_{p_{ss}}\ and\ \dot{m}_{i} = \dot{m}_{L}, C_{p_i} = C_{p_L}$ respectively for both sides. Hence, equation 3.199 can be rewritten as:

$$\dot{m}_{ss}C_{p_{ss}}T_{ph}\xi_{ss}^{i} - \dot{m}_{ss}C_{p_{ss}}T_{s,i}\xi_{ss}^{i} + \left(-k_{s,i}A_{s,i}\frac{\partial T_{s,i}}{\partial y}|_{y}\right) + Q_{igen,fluid\ zones} =$$

$$\dot{m}_{L}C_{p_{L}}T_{L}\xi_{L}^{i} - \dot{m}_{L}C_{p_{L}}T_{s,i}\xi_{L}^{i} + (UA)_{s,i}\left[T_{s,i} - T_{a}\right] + \left(-k_{s,i}A_{s,i}\frac{\partial T_{s,i}}{\partial y}|_{y+\Delta y}\right) + \dot{m}_{i}C_{p_{i}}\frac{\partial T_{s,i}}{\partial t}$$

3.200

Where,

ξ_{ss}^{i} is the selective surface control function which can be defined to determine which fluid zone receives water from the SCONOR plate.

ξ_{L}^{i} is the load return control function which can also be defined to determine which fluid zone receives water from the space heating radiator (load).

Therefore, the transient temperature variation in the i^{th} fluid zone is obtained by transforming equation 3.200, given as:

$$\dot{m}_{i}C_{p_{i}}\frac{\partial T_{s,i}}{\partial t} =$$

$$\dot{m}_{ss}C_{p_{ss}}\xi_{ss}^{i}\left[T_{ph} - T_{s,i}\right] - k_{s,i}A_{s,i}\frac{\partial T_{s,i}}{\partial y}|_{y} - \dot{m}_{L}C_{p_{L}}\xi_{L}^{i}\left[T_{s,i} - T_{L}\right] + \left(k_{s,i}A_{s,i}\frac{\partial T_{s,i}}{\partial y}|_{y+\Delta y}\right) +$$

$$Q_{igen,fluid\ zones} - (UA)_{s,i}\left[T_{s,i} - T_{a}\right]$$

3.201

Where,

$Q_{igen,fluid\ zones}$ is the energy generated by the fluid flow from the neighbouring fluid zones.

$\lambda_{s,i}$ is the heat conduction coefficient of fluid zone in the storage tank for the i^{th} fluid zone.

On further simplification of the 2nd and 4th terms in the RHS of equation 3.201, the resulting expression becomes:

$$\dot{m}_{i}C_{p_{i}}\frac{\partial T_{s,i}}{\partial t} = \dot{m}_{ss}C_{p_{ss}}\xi_{ss}^{i}\left[T_{ph} - T_{s,i}\right] - \dot{m}_{L}C_{p_{L}}\xi_{L}^{i}\left[T_{s,i} - T_{L}\right] - k_{s,i}A_{s,i}\frac{\partial T_{s,i}}{\partial y}|_{y} + k_{s,i}A_{s,i}\frac{\partial}{\partial y}\left(T_{s,i} + \frac{\partial T_{s,i}}{\partial y}dy\right) + Q_{igen,fluid\ zones} - (UA)_{s,i}\left[T_{s,i} - T_{a}\right]$$

3.202

$$\dot{m}_i C_{p_i} \frac{\partial T_{s,i}}{\partial t} = \dot{m}_{ss} C_{p_{ss}} \xi_{ss}^i \left[T_{ph} - T_{s,i}\right] - \dot{m}_L C_{p_L} \xi_L^i \left[T_{s,i} - T_L\right] - k_{s,i} A_{s,i} \frac{\partial T_{s,i}}{\partial y}|_y + k_{s,i} A_{s,i} \frac{\partial T_{s,i}}{\partial y} + k_{s,i} A_{s,i} \frac{\partial^2 T_{s,i}}{\partial y^2} dy + Q_{igen,fluid\ zones} - (UA)_{s,i}\left[T_{s,i} - T_a\right]$$

3.203

$$\dot{m}_i C_{p_i} \frac{\partial T_{s,i}}{\partial t} = \dot{m}_{ss} C_{p_{ss}} \xi_{ss}^i \left[T_{ph} - T_{s,i}\right] - \dot{m}_L C_{p_L} \xi_L^i \left[T_{s,i} - T_L\right] + k_{s,i} A_{s,i} \frac{\partial^2 T_{s,i}}{\partial y^2} dy + Q_{igen,fluid\ zones} - (UA)_{s,i}\left[T_{s,i} - T_a\right]$$

3.204

For infinitesimally small distances, $dy = \Delta y$, and hence equation 3.204 becomes,

$$\dot{m}_i C_{p_i} \frac{\partial T_{s,i}}{\partial t} = \dot{m}_{ss} C_{p_{ss}} \xi_{ss}^i \left[T_{ph} - T_{s,i}\right] - \dot{m}_L C_{p_L} \xi_L^i \left[T_{s,i} - T_L\right] + k_{s,i} A_{s,i} \Delta y \frac{\partial^2 T_{s,i}}{\partial y^2} + Q_{igen,fluid\ zones} - (UA)_{s,i}\left[T_{s,i} - T_a\right]$$

3.205

According to assumption (viii), water from the selective SCONOR enters the tank through a fluid zone whose temperature is close but less than the outlet selective surface temperature, where its density closely matches that of the water in the tank. Therefore, the selective SCONOR control function, ξ_{ss}^i is defined to designate the fluid zone that receives water from the SCONOR by the following expression,

$$\xi_{ss}^i = \begin{cases} 1 & if\ T_{s,i-1} > T_{ph} > T_{s,i} \\ 0 & otherwise \end{cases}$$

3.206

In the same vein, from assumption viii, water from load enters the tank through a fluid zone whose temperature is close but greater than the load return temperature, where its density closely matches that of the water in the tank and hence, the load return control function is defined to denote which fluid zone receives water returning from the load (radiator) as follows,

$$\xi_L^i = \begin{cases} 1 & if\ T_{s,i} > T_L > T_{s,i+1} \\ 0 & otherwise \end{cases} \quad 3.207$$

From assumption (iv), there is internal heat generation as a result of the influence of fluid flowing from the neighbouring fluid zones, $i-1$ and $i+1$ into the i^{th} fluid zone. This internal heat generation is designated as $Q_{igen,fluid\ zones}$.

Since at any instant the fluid zones receive energy either through the top (from the selective SCONOR) or through the bottom (from the room radiator), a mixed flow rate can be defined due to up and down flow into the i^{th} fluid zone. Duffie and Beckman (2006) defined this mixed flow rate into the i^{th} fluid zone as:

$$\dot{\chi}_{m,i} = \dot{m}_{ss} \sum_{j=1}^{i-1} \xi_{ss}^j - \dot{m}_L \sum_{j=i+1}^{N} \xi_L^j \quad 3.208$$

The net rate of internal heat flow between the fluid zones can be given as:

$$Q_{int,fluid\ zones} = \dot{\chi}_{m,i} C_{p_i} \Delta T \quad 3.209$$

Therefore, the internal heat generation between the fluid flowing from the $(i-1)^{th}$ fluid zone and the i^{th} fluid zone can be expressed as:

$$Q_{int,i-1\_i} = \dot{\chi}_{m,i} C_{p_i} \left(T_{s,i-1} - T_{s,i}\right) \quad 3.210$$

On substituting equation 3.208 into 3.210, the internal heat generation between the zones can be defined as,

$$Q_{int,i-1\_i} = \left\{ \dot{m}_{ss} \sum_{j=1}^{i-1} \xi_{ss}^j - \dot{m}_L \sum_{j=i+1}^{N} \xi_L^j \right\} C_{p_i} \left(T_{s,i-1} - T_{s,i}\right) \quad 3.211$$

Simplifying further, equation 3.211 results in:

$$Q_{int,i-1\_i} = \left\{ \dot{m}_{ss} C_{p_i} \left(T_{s,i-1} - T_{s,i}\right) \sum_{j=1}^{i-1} \xi_{ss}^{j} - \dot{m}_L C_{p_i} \left(T_{s,i-1} - T_{s,i}\right) \sum_{j=i+1}^{N} \xi_L^j \right\} \quad 3.212$$

Similarly, the internal heat generation as a result of fluid flowing from the $(i+1)^{th}$ fluid zone to the i^{th} fluid zone can be defined as,

$$Q_{int,i+1\_i} = \dot{\chi}_{m,i} C_{p_i} \left(T_{s,i} - T_{s,i+1}\right) \quad 3.213$$

On substituting equation 3.208 into 3.213 and taking the temperature differential between $(1+i)^{th}$ and i^{th} fluid zones in Fig. 3.18, the internal heat generation between the zones can be defined as,

$$Q_{int,i+1\_i} = \left\{ \dot{m}_{ss} \sum_{j=1}^{i-1} \xi_{ss}^{j} - \dot{m}_L \sum_{j=i+1}^{N} \xi_L^j \right\} C_{p_i} \left(T_{s,i} - T_{s,i+1}\right) \quad 3.214$$

On further simplification, equation 3.214 becomes,

$$Q_{int,i+1\_i} = \left\{ \dot{m}_{ss} C_{p_i} \left(T_{s,i} - T_{s,i+1}\right) \sum_{j=1}^{i-1} \xi_{ss}^{j} - \dot{m}_L C_{p_i} \left(T_{s,i} - T_{s,i+1}\right) \sum_{j=i+1}^{N} \xi_L^j \right\} \quad 3.215$$

Therefore, the internal heat generation due to the influence of fluid flowing from the neighbouring fluid zones, $i-1$ and $i+1$, into the i^{th} fluid zone, $Q_{igen,fluid\ zones}$, is expressed as either equation 3.212 or equation 3.215, depending on whether the value of the mixed flow rate is greater than zero or less than zero respectively as follows:

$$Q_{igen,fluid\ zones} = \begin{cases} Q_{int,i-1\_i}, & if\ \dot{\chi}_{m,i} > 0 \\ Q_{int,i+1\_i}, & if\ \dot{\chi}_{m,i} < 0 \end{cases} \quad 3.216$$

Therefore, on substitution for $Q_{int,i-1\_i}$ and $Q_{int,i+1\_i}$, $Q_{igen,fluid\ zones}$ becomes:

$$Q_{igen,fluid\ zones}$$

$$= \begin{cases} \dot{m}_{ss} C_{p_i} \left(T_{s,i-1} - T_{s,i}\right) \sum_{j=1}^{i-1} \xi_{ss}^{j} - \dot{m}_L C_{p_i} \left(T_{s,i-1} - T_{s,i}\right) \sum_{j=i+1}^{N} \xi_L^j, & if\ \dot{\chi}_{m,i} > 0 \\ \dot{m}_{ss} C_{p_i} \left(T_{s,i} - T_{s,i+1}\right) \sum_{j=1}^{i-1} \xi_{ss}^{j} - \dot{m}_L C_{p_i} \left(T_{s,i} - T_{s,i+1}\right) \sum_{j=i+1}^{N} \xi_L^j, & if\ \dot{\chi}_{m,i} < 0 \end{cases} \quad 3.217$$

Finally, the transient energy balance on the i^{th} fluid zone in the tank, is therefore, obtained by substituting equation 3.217 into equation 3.203, and expressed as:

$$\dot{m}_i C_{p_i} \frac{\partial T_{s,i}}{\partial t} = \dot{m}_{ss} C_{p_{ss}} \xi_{ss}^{i} \left[T_{ph} - T_{s,i}\right] + \dot{m}_L C_{p_L} \xi_L^i \left[T_L - T_{s,i}\right] + k_{s,i} A_{s,i} \Delta y \frac{\partial^2 T_{s,i}}{\partial y^2} + (UA)_{s,i} \left[T_a - T_{s,i}\right] + \begin{cases} \dot{m}_{ss} C_{p_i} \left(T_{s,i-1} - T_{s,i}\right) \sum_{j=1}^{i-1} \xi_{ss}^{j} - \dot{m}_L C_{p_i} \left(T_{s,i-1} - T_{s,i}\right) \sum_{j=i+1}^{N} \xi_L^j, & if\ \dot{\chi}_{m,i} > 0 \\ \dot{m}_{ss} C_{p_i} \left(T_{s,i} - T_{s,i+1}\right) \sum_{j=1}^{i-1} \xi_{ss}^{j} - \dot{m}_L C_{p_i} \left(T_{s,i} - T_{s,i+1}\right) \sum_{j=i+1}^{N} \xi_L^j, & if\ \dot{\chi}_{m,i} < 0 \end{cases} \quad 3.218$$

3.2.3.2 Modelling the cold water storage tank

At about 20:00 hours, the nocturnal operation starts. This is essentially because any object placed on any surface on the earth has a higher temperature than the ambient sky and so will radiate most of its energy to the sky, hence becoming cooler in the process. This process continues through the night until about 06:00 hours of the following day and is termed nocturnal radiative cooling. During the nocturnal operation, cold water at ambient temperature enters the selective SCONOR from the top of the tank as shown in Fig. 3.15. Because of the spectral selectivity of the SCONOR, the water looses a substantial amount of heat, mostly within the atmospheric

window spectrum, to the sky and so cools down below its initial ambient temperature. This cold water flows into the cold water tank where it is stored while the operation lasts. The process continues until an equilibrium temperature is achieved and the charging and mixing stop. During the day, the cold water can then be drawn from the tank as from 8:00 hours to 16:00 hours for space cooling for thermal comfort when the ambient becomes moderately or highly hot.

To formulate the differential equation governing the transient behaviour of the cold water storage tank as the tank is being charged and discharged, the following assumptions are made:

i. The cold storage tank is vertically positioned and cylindrical in shape.
ii. Temperature stratification occurs in the tank in the axial direction only, which takes the y-coordinate in the Cartesian plane and hence it is regarded as a Y-cylinder.
iii. The entire tank volume is divided into N-horizontal zones of equal height and uniform temperature, numbered from bottom to top of the tank.
iv. There is no internal heat generation in the tank and the tank is completely mixed and filled, and the fluid velocity in the tank is constant.
v. The mass flow rate from the selective SCONOR into the tank and that from the tank to the load (room convector) are constant.
vi. Water leaves the tank through the top (last zone) to the selective SCONOR and cold water leaves the tank through the bottom (first zone) to the load.
vii. The water from the selective SCONOR enters the tank through a fluid zone whose temperature is close but less than the outlet selective SCONOR temperature where its density closely matches that of the water in the tank while water from load enters the tank through a fluid zone whose temperature is close but greater than the load return temperature, where its density closely matches that of the water in the tank.

viii. The tank is assumed to be perfectly insulated.

3.2.3.2.1 Differential equation of stratification in the cold water tank

For the case of cold water storage tank, the same method of description of the hot water storage tank has been adopted. An N-zones tank is analysed, with each zone considered to be at a uniform temperature $T_{s,1}$, $T_{s,2}$, ..., $T_{s,N}$. Two control functions are also defined, one for the selective SCONOR side and the other for the load (room convector) side. Let these control functions be designated by $\xi^i_{ss,n}$ and $\xi^i_{L,n}$ respectively. The section of the cold storage tank is as shown in Fig. 3.19. The energy balance on an elemental fluid zone in the tank can be given by Fig. 3.20.

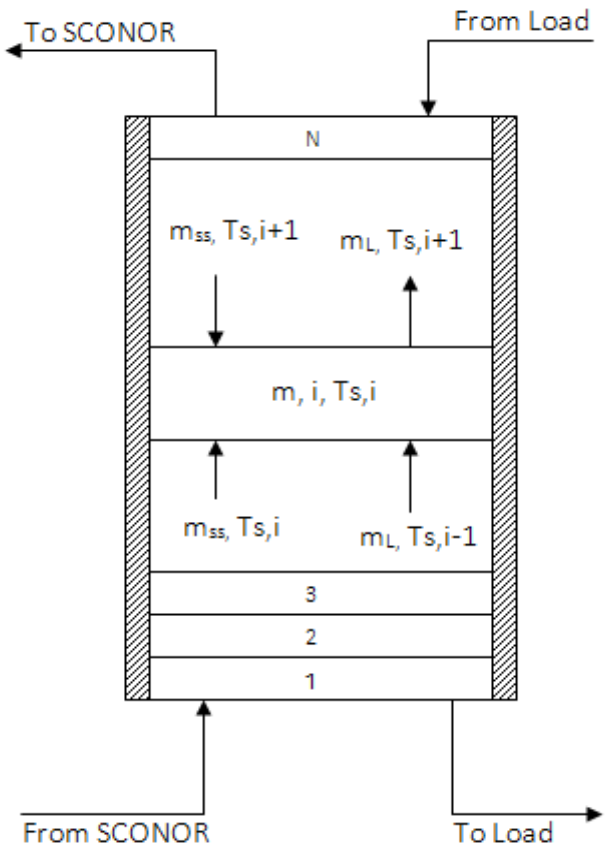

Fig. 3.19 Fully stratified cold water storage tank

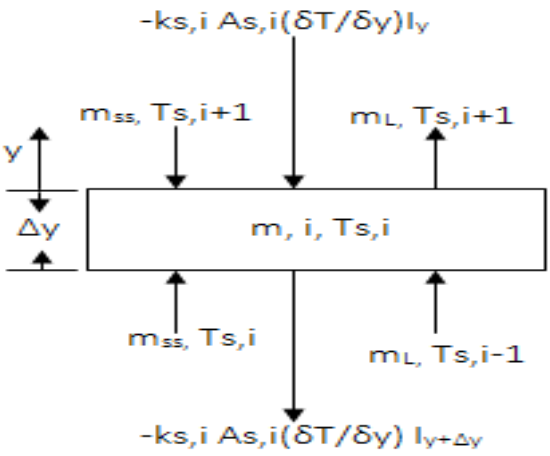

Fig. 3.20 Energy balance on elemental fluid zone in the cold water tank

The energy balance for zone i of an N-zone storage tank can be expressed as,

$$\dot{m}_{ss,n}C_{p_{ss,n}}T_{ss,n}\xi^{i}_{ss,n} - \dot{m}_{i,n}C_{p_{i,n}}T_{sc,i}\xi^{i}_{ss,n} + \left(-k_{s,i}A_{s,i}\frac{\partial T_{sc,i}}{\partial y}|_{y}\right)$$
$$= \dot{m}_{L,n}C_{p_{L,n}}T_{L,n}\xi^{i}_{L,n} - \dot{m}_{i}C_{p_{i}}T_{sc,i}\xi^{i}_{L,n} + \left(-k_{s,i}A_{s,i}\frac{\partial T_{sc,i}}{\partial y}|_{y+\Delta y}\right) + \dot{m}_{i,n}C_{p_{i,n}}\frac{\partial T_{sc,i}}{\partial t} \quad 3.219$$

As in the case of the diurnal operation, during the nocturnal operation, the selective SCONOR (nocturnal radiator) and load sides respectively, have constant mass flow rates according to assumption (vi) in subsection 3.2.3.2. Hence, it can be written that $\dot{m}_{i,n} = \dot{m}_{ss,n}, C_{p_{i,n}} = C_{p_{ss,n}}$ and $\dot{m}_{i,n} = \dot{m}_{L,n}, C_{p_{i,n}} = C_{p_{L,n}}$ respectively for both sides.

Following that, equation 3.219 can be expressed as:

$$\dot{m}_{ss,n}C_{p_{ss,n}}T_{ss,n}\xi^{i}_{ss,n} - \dot{m}_{ss,n}C_{p_{ss,n}}T_{sc,i}\xi^{i}_{ss,n} + \left(-k_{s,i}A_{s,i}\frac{\partial T_{sc,i}}{\partial y}|_{y}\right) =$$
$$\dot{m}_{L,n}C_{p_{L,n}}T_{L,n}\xi^{i}_{L,n} - \dot{m}_{L,n}C_{p_{L,n}}T_{sc,i}\xi^{i}_{L,n} + \left(-k_{s,i}A_{s,i}\frac{\partial T_{sc,i}}{\partial y}|_{y+\Delta y}\right) + \dot{m}_{ss,n}C_{p_{ss,n}}\frac{\partial T_{sc,i}}{\partial t} \quad 3.220$$

Where $\xi^{i}_{ss,n}$ is the SCONOR control function which can be defined to determine which fluid zone receives water from the radiator and $\xi^{i}_{L,n}$ is the load return control function which can also be defined to determine which fluid zone receives water from the room convector (load).

Therefore, the transient temperature variation in the i^{th} fluid zone is obtained by transforming equation 3.220, which yields:

$$\dot{m}_{ss,n}C_{p_{ss,n}}\frac{\partial T_{sc,i}}{\partial t} = \dot{m}_{ss,n}C_{p_{ss,n}}\xi^{i}_{ss,n}\left(T_{ss,n} - T_{sc,i}\right) - \dot{m}_{L,n}C_{p_{L,n}}\xi^{i}_{L,n}\left(T_{L,n} - T_{sc,i}\right) - \lambda_{s,i}A_{s,i}\frac{\partial T_{s,i}}{\partial y} + k_{s,i}A_{s,i}\frac{\partial T_{s,i}}{\partial y} + k_{s,i}A_{s,i}\frac{\partial^2 T_{s,i}}{\partial y^2}dy \quad 3.221$$

$$\dot{m}_{ss,n}C_{p_{ss,n}}\frac{\partial T_{sc,i}}{\partial t} = \dot{m}_{ss,n}C_{p_{ss,n}}\xi^{i}_{ss,n}\left(T_{ss,n} - T_{sc,i}\right) - \dot{m}_{L,n}C_{p_{L,n}}\xi^{i}_{L,n}\left(T_{L,n} - T_{sc,i}\right) + \lambda_{s,i}A_{s,i}\frac{\partial^2 T_{s,i}}{\partial y^2}dy \quad 3.222$$

According to assumption viii of subsection 3.2.3.2, water from the SCONOR enters the cold tank through a fluid zone whose temperature is close but less than the outlet SCONOR temperature, where its density closely matches that of the water in the tank. Therefore, the SCONOR control function, $\xi^{i}_{ss,n}$ is defined to designate the fluid zone that receives water from the radiator by the following expression,

$$\xi^{i}_{ss,n} = \begin{cases} 1 & if\ T_{sc,i-1} < T_{ss,n} < T_{sc,i} \\ 0 & otherwise \end{cases} \quad 3.223$$

In the same vein, as stated in assumption viii, water from load (room convector) enters the cold storage tank through a fluid zone whose temperature is close but greater than the load return temperature, where its density closely matches that of the water in the tank and hence, the load (convector) return control function is defined to denote which fluid zone receives water returning from the load (convector) as follows,

$$\xi^{i}_{L,n} = \begin{cases} 1 & if\ T_{sc,i} < T_{L,n} < T_{sc,i+1} \\ 0 & otherwise \end{cases} \quad 3.224$$

3.2.4 Space Conditioning for Thermal Comfort

Heating and air conditioning systems use the principles of heat transfer to maintain comfortable indoor conditions for people (Trane, 2011). To quantify the exact capacity of cooling and heating systems which can ensure the required comfortable conditions in the conditioned space, cooling and heating load calculations are expedient. The necessary factors that would enable such computations include information on the design indoor and outdoor conditions, building specifications, specifications of the conditioned space (such as the occupancy, activity level, various appliances and equipment used etc.) as well as any other special requirements of the particular application. In cases of comfort applications, thermal comfort criterion fix the required indoor conditions while the dry bulb and coincident wet bulb temperatures for peak hot and cold months fix the design outdoor conditions, for the respective cooling and heating load computations.

3.2.4.1 Modelling of comfort cooling

The cooling power is the energy needed to provide a reference and comfort temperature in the room to be cooled. This is particularly necessary during moderate to high ambient temperature periods, when the indoor temperature is uncomfortable for the occupants. The cooling need and available means of losses must be known for appropriate sizing of the convector (heat exchanger) that will extract the needed or required heat energy from the room to be conditioned, to make it thermally comfortable for occupants.

Nigeria lies in the tropics and gets extremely hot around the months of December to April annually, creating uncomfortable situation for the populace. This is the more reason mechanical air conditioning systems are installed in buildings to obtain comfortable indoor conditions mostly at such periods. To ameliorate the effect these systems have on the environment and the inherent

excessive cost of installation and maintenance, a green and smart building concept is required through an integrated energy approach, which would exploit green energy for air conditioning purposes. How best to design habitable spaces thermally comfortable for people can be approached in different ways, one being that the space can be insulated externally from the outset while the inside air and interior wall surfaces are cooled (Dobson, 2005). Perfectly insulated thermal mass made of naturally poor-conducting masonry materials do not allow heat transfer. The air inside the room is to be cooled along with the interior walls by bringing the cold water to a point where it can carry out the cooling function via the convector. So, the cooling loads result from heat transfer processes through the building envelope comprising heat gain into the room as a result of infiltration of hot outside air through openings and holes (Q_{infil}); transmission from cracks and holes in the wall (Q_{trans}); and internal heat source due to people, appliances (computers, printers, etc) and light bulbs (Q_{int}). The total cooling load on any building consists of both sensible as well as latent load components. The sensible load affects dry bulb temperature, while the latent load affects the moisture content of the conditioned space. Fig 3.21 shows the heat sources that contribute the loads for the model room to be cooled. The room though a three dimensional enclosure can be idealized as a two dimensional domain.

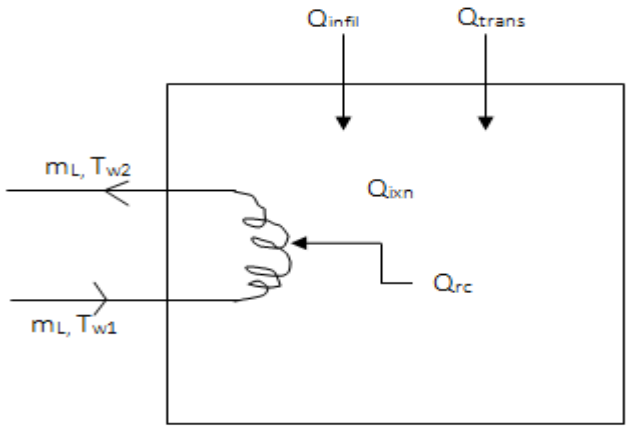

Fig. 3.21 Energy balance on the room control volume

Employing equation 3.2, the energy balance for the room control volume is expressed as:

$$\dot{Q}_{in,r} + \dot{Q}_{i-gen,r} = \dot{Q}_{out,r} + \dot{Q}_{int,r} \quad 3.225$$

From Fig 3.21, the total energy inflow to the room, $\dot{Q}_{in,r}$ can be given as:

$$\dot{Q}_{in,r} = \dot{Q}_{wcst-rc} + \dot{Q}_{trans} + \dot{Q}_{infil} \quad 3.226$$

Where $\dot{Q}_{wcst-rc}$ is the energy of the water from the cold storage tank, entering the convector in the room; $\dot{Q}_{trans}$ is the energy transmitted into the room through the walls while $\dot{Q}_{infil}$ is the energy infiltrated into the room through doors, windows, small cracks and fenestration.

The internal heat generation in the room as a result of people, appliances and light bulbs can be given as:

$$\dot{Q}_{i-gen,r} = \dot{Q}_{people} + \dot{Q}_{appliances} + \dot{Q}_{light\ bulbs} \quad 3.227$$

The total energy out of the room control volume, $\dot{Q}_{out,r}$ is given as:

$$\dot{Q}_{out,r} = \dot{Q}_{wrc-cst} + \dot{Q}_{rc} \quad 3.228$$

$\dot{Q}_{wrc-cst}$ is the energy of the water leaving the room convector to the cold storage tank while $\dot{Q}_{rc}$ is the energy extracted from the room by the convector.

The rate of increase in the internal energy of the room, $\dot{Q}_{int,r}$ is given as:

$$\dot{Q}_{int,r} = m_{air} c_{p_{air}} \frac{dT_r}{dt} \quad 3.229$$

Therefore, the overall energy balance for the room control volume during comfort cooling is obtained by substituting equations 3.226, 3.227, 3.228 and 3.229 into equation 3.225 to yield:

$$\dot{Q}_{wcst-rc} + \dot{Q}_{trans} + \dot{Q}_{infil} + \left(\dot{Q}_{people} + \dot{Q}_{appliances} + \dot{Q}_{light\,bulbs}\right) = \dot{Q}_{wrc-cst} + \dot{Q}_{rc} + m_{air}c_{p_{air}}\frac{dT_r}{dt}$$

3.230

Rearranging and simplifying, equation 3.217 becomes:

$$m_{air}c_{p_{air}}\frac{dT_r}{dt} = \dot{Q}_{wcst-rc} + Q_{trans} + \dot{Q}_{infil} + \left(\dot{Q}_{people} + \dot{Q}_{appliances} + \dot{Q}_{light\,bulbs}\right) - \dot{Q}_{wrc-cst} - \dot{Q}_{rc}$$

3.231

3.2.4.1.1 The Room Convector

The cold water from the cold storage tank is circulated through a convector installed in a model room. Heat is transferred from the air in the room to the cold water circulating in the convector. Since the waterside heat transfer coefficient is much greater than the airside, the convector pipes conveying cold water have to be finned on the airside in order to reduce the overall thermal resistance. In room air conditioning, the standard practice is to use copper tubes finned with aluminum and this has been adopted in the modeling of the convector heat exchanger. To allow for natural convection, the fins should be given large enough spacing and placed high up in the room in a horizontal position (Dobson, 2005). The room convector control volume is as shown in Fig. 3.22.

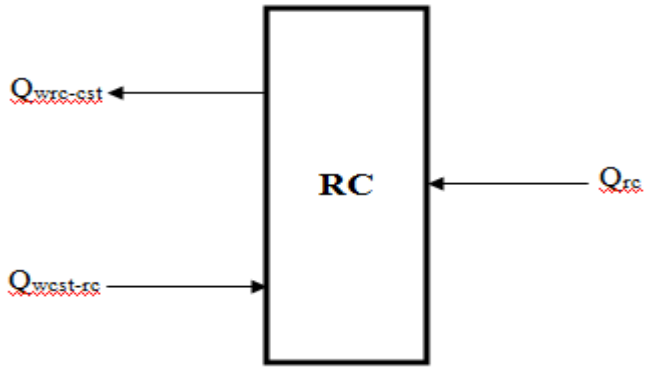

Fig. 3.22 Energy balance on the convector control volume

From Fig. 3.22, the energy from the water flowing from the cold storage tank into the convector heat exchnager, $\dot{Q}_{wcst-rc}$ can be given as:

$$\dot{Q}_{wcst-rc} = \dot{m}_{L,n} c_{p_{L,n}} T_{Ln1} \quad 3.232$$

And that from the convector back to the cold storage tank after exchanging energy with the room, $\dot{Q}_{wrc-cst}$ is given as:

$$\dot{Q}_{wrc-cst} = \dot{m}_{L,n} c_{p_{L,n}} T_{Ln2} \quad 3.233$$

The rate of heat transfer into the convector coil from the air in the room $\dot{Q}_{rc}$ is given by:

$$\dot{Q}_{rc} = \frac{1}{R_{rc}} \left[T_{rc} - T_{L,n} \right] \quad 3.234$$

The inside water and outside air thermal resistances make up the convector thermal resistance expressed as (Dobson, 2005).

$$R_{rc} = \frac{1}{h_{ci} A_{ci}} + \frac{1}{\eta_{fin} h_{fin} A_{fin}} \quad 3.235$$

The waterside and airside heat transfer coefficients can be resolved using appropriate correlations from standard heat transfer texts. Accordingly, from Kreith and Bohn (2000), the waterside heat transfer can be evaluated by the expression:

$$h_{ci} = \frac{k_w}{D_{ci}} R_e^{0.8} P_r^{0.35} \quad 3.236$$

Where R_e is the Reynolds number given by:

$$R_e = \frac{4\dot{m}_w}{\pi D_{ci} \mu_w} \quad 3.237$$

And P_r is the Prandtl number given as:

$$P_r = \frac{c_w \mu_w}{k_w} \quad 3.238$$

The airside heat transfer coefficient is also determined using the following expression (Kreith and Bohn, 2000):

$$h_{fin} = 1.07\left(\frac{\Delta T}{L_{fin}}\right)^{0.25} \quad for \;\; 10^4 < Gr < 10^9 \quad 3.239$$

$$h_{fin} = 1.3\Delta T^{\frac{1}{3}} \quad for \;\; 10^9 < Gr < 10^{12} \quad 3.240$$

The Grashof number is determined by:

$$Gr = \frac{\beta \Delta T g \rho^2 {L_{fin}}^3}{\mu} \quad 3.241$$

β is the coefficient of thermal expansion and can be taken (for an ideal gas) as 1/T if T is in Kelvin, ΔT is the temperature difference between the air and the surface and L_{fin} is the (vertical) length of the fin along which natural convection is taking place.

3.2.4.1.2 Heat gain into the room as a result of transmission (Q_{trans})

The transmission heat gain ($\dot{Q}_{trans}$) fully depends on the room orientation, direct solar radiation through the window or fenestration, actual wall and room construction, inside and outside heat transfer coefficients and time of the day, but for a reasonably well-insulated building and to limit the number of variables (without unduly losing accuracy), transmission heat gain can be conveniently assumed to be from cracks through the wall. Hence, it is expressed as (Dobson, 2005; Trane, 2011; ASHRAE, 2000):

$$\dot{Q}_{trans} = \frac{1}{R_r}[T_a - T_r] \quad 3.242$$

The room resistance R_r is expressed as:

$$R_r = \frac{\delta_{r,wall}}{k_r A_R} \quad 3.243$$

$\delta_{r,wall}$ is the wall thickness and k_r is the wall material thermal conductivity and A_R is the area of the room which is give as.

$$A_R = 2[L_R B_R + H_R B_R + L_R H_R] \quad 3.244$$

Therefore, the heat gained by transmission $\dot{Q}_{trans}$ becomes:

$$Q_{trans} = \frac{2k_r[L_R B_R + H_R B_R + L_R H_R]}{\delta_{r,wall}}[T_a - T_r] \quad 3.245$$

3.2.4.1.3 Heat gain into the room as a result of infiltration (Q_{infil})

Infiltration is the amount of air leaking into a space. In a typical building, air leaks into or out of a space through doors, windows, and small cracks in the building envelope (Trane, 2011, ASHRAE, 2011). During the cooling season, when air leaks into a conditioned space from outdoors, it can contribute to both the sensible and latent heat gain in the space because the outdoor air is typically warmer and more humid than the indoor air. Neglecting humidity effect, the sensible heat gain as a result of infiltration, corresponding to the change of dry-bulb temperature is given as (Dobson, 2005):

$$\dot{Q}_{infil} = C_{infil}[T_a - T_r] \quad 3.246$$

The coefficient of infiltration C_{infil} is given as:

$$C_{infil} = Infiltration\ airflow * density\ of\ air * specific\ heat\ capacity\ of\ air\ at\ constant\ pressure \quad 3.247$$

According to Trane (2011),

$$Infiltration\ airflow = \frac{Volume\ of\ room * No\ of\ Air\ Changes\ in\ the\ room\ Per\ Day}{24 * 3600}\ (\text{per sec}) \qquad 3.248$$

Therefore,

$$C_{infil} = \frac{\rho_{air} c_{p_{air}} ACPD(L_R B_R H_R)}{24 * 3600} \qquad 3.249$$

And the heat gain from infiltration is finally expressed as:

$$Q_{infil} = \frac{\rho_{air} c_{p_{air}} ACPD(L_R B_R H_R)}{24 * 3600}[T_a - T_r] \qquad 3.250$$

The ACPD is the number of air changes in the room per day. It involves estimating the number of air changes per hour in a day that can be expected in spaces of a certain construction quality. Assuming that the model room is of average construction and kept at a positive pressure relative to the ambient conditions (pressurized average construction), the assumed value of air changes/hr of infiltration is 0.3 (Trane, 2011).

3.2.4.1.4 Heat internally generated in the room ($\dot{Q}_{i-gen,r}$)

This is the heat that originates from the room due to people, appliances, lights and equipment. All of these sources contribute sensible heat to the room while people and some appliances contribute latent heat to the room. The internal heat generation as a result of people, appliances and light bulbs is given as (ASHRAE 2011):

$$\dot{Q}_{i-gen,r} = \dot{Q}_{people} + \dot{Q}_{appliances} + \dot{Q}_{light\ bulbs} \qquad 3.251$$

3.2.4.1.4.1 Heat generated by people

The amount of heat released by the body varies with age, physical size, gender, type of clothing, and level of physical activity. The table below shows typical sensible and latent heat gains per person based on the level of physical activity. The model room is a typical office space with a moderately active work.

Table 3.1 Heat generated by people (source: ASHRAE, 2005)

Degree of Activity		Total Heat, W: Adult Male	Total Heat, W: Adjusted, M/F[a]	Sensible Heat, W	Latent Heat, W	% Sensible Heat that is Radiant[b]: Low V	% Sensible Heat that is Radiant[b]: High V
Seated at theater	Theater, matinee	115	95	65	30		
Seated at theater, night	Theater, night	115	105	70	35	60	27
Seated, very light work	Offices, hotels, apartments	130	115	70	45		
Moderately active office work	Offices, hotels, apartments	140	130	75	55		
Standing, light work; walking	Department store; retail store	160	130	75	55	58	38
Walking, standing	Drug store, bank	160	145	75	70		
Sedentary work	Restaurant[c]	145	160	80	80		
Light bench work	Factory	235	220	80	140		
Moderate dancing	Dance hall	265	250	90	160	49	35
Walking 4.8 km/h; light machine work	Factory	295	295	110	185		
Bowling[d]	Bowling alley	440	425	170	255		
Heavy work	Factory	440	425	170	255	54	19
Heavy machine work; lifting	Factory	470	470	185	285		
Athletics	Gymnasium	585	525	210	315		

Notes:
1. Tabulated values are based on 24°C room dry-bulb temperature. For 27°C room dry bulb, the total heat remains the same, but the sensible heat values should be decreased by approximately 20%, and the latent heat values increased accordingly.
2. Also refer to Table 4, Chapter 8, for additional rates of metabolic heat generation.
3. All values are rounded to nearest 5 W.

[a]Adjusted heat gain is based on normal percentage of men, women, and children for the application listed, with the postulate that the gain from an adult female is 85% of that for an adult male, and that the gain from a child is 75% of that for an adult male.

[b]Values approximated from data in Table 6, Chapter 8, where *V* is air velocity with limits shown in that table.

[c]Adjusted heat gain includes 18 W for food per individual (9 W sensible and 9 W latent).

[d]Figure one person per alley actually bowling, and all others as sitting (117 W) or standing or walking slowly (231 W).

Since a portion of the heat transferred by the occupants is in the form of radiation, a Cooling Load Factor (CLF) should be used similar to that used for radiation heat transfer through fenestration. The heat generated by people is divided into sensible and latent heat, given as (ASHRAE, 2011):

$$\dot{Q}_{people} = \dot{Q}_{sen} + \dot{Q}_{lat} \qquad 3.252$$

The sensible heat component due to occupants is then estimated by:

$$\dot{Q}_{sen} = N_p * SHGPP * CLF \qquad 3.253$$

Since the latent heat gain from the occupants is instantaneous the CLF for latent heat gain is 1.0, thus the latent heat gain due to occupants is given by:

$$\dot{Q}_{lat} = N_p * LHGPP \qquad 3.254$$

N_p is number of people, SHGPP is sensible heat gain per person (provided by table 3.1) and CLF is a dimensionless number referred to as the Cooling Load Factor, used to account for the capacity of the room to absorb and store energy. The value of CLF depends on the construction of the interior partition walls in the room, the type of floor covering, the total number of hours

the room is occupied and the number of hours since the people entered the room. Table 3.2 shows the Cooling Load Factors for people.

Table 3.2 Cooling Load Factors for people (source: Trane, 2011)

total hours in space	hours after people enter space											
	1	2	3	4	5	6	7	8	9	10	11	12
2	0.65	0.74	0.16	0.11	0.08	0.06	0.05	0.04	0.03	0.02	0.02	0.01
4	0.65	0.75	0.81	0.85	0.24	0.17	0.13	0.10	0.07	0.06	0.04	0.03
6	0.65	0.75	0.81	0.85	0.89	0.91	0.29	0.20	0.15	0.12	0.09	0.07
8	0.65	0.75	0.81	0.85	0.89	0.91	0.93	0.95	0.31	0.22	0.17	0.13
10	0.65	0.75	0.81	0.85	0.89	0.91	0.93	0.95	0.96	0.97	0.33	0.24

Therefore, substituting equations 3.253 and 3.254 into 3.252, the heat generated by people in the room becomes:

$$\dot{Q}_{people} = N_p\big((SHGPP * CLF) + LHGPP\big) \qquad 3.255$$

3.2.4.1.4.2 Heat gain in the room by appliances

There are many types of appliances and equipment in restaurants, schools, office buildings, hospitals, and other types of buildings. This equipment may generate a significant amount of heat and should be accounted for when estimating the space cooling load. Often, the only available information about heat gain from appliances is the data obtained from the appliance nameplate. Most of the appliances produce only sensible heat (Trane, 2011). According to ASHRAE (1997), the most common office appliances include a desktop computer and monitor, alongside a variety of shared devices like printers, scanners, and copy and FAX machines. Nameplate ratings of such equipment should be significantly discounted. Also, because peak use of all appliances does not occur simultaneously, diversity in usage patterns (equipment type, user habit) must be considered separately. Table 3.3 shows a summary of average test results for 25083m^2 of office space measured in five different buildings, in which the average electrical appliance heat gain was approximately 10 W/m^2 (ASHRAE, 1997).

Table 3.3 Heat gain versus nameplate rating from electrical office appliances

Equipment Tested	Nameplate Rating, W	Measured Total Power Consumption, W	Radiant Power, W	Radiant Power, %	Convective Power, %
15 in. monitor energy saver (white screen)	220	78	28.8	37.1	62.9
Laser printer	836	248	26.6	10.7	89.3
Desktop copier	1320	181	25.9	14.3	85.7
Personal computer (Brand 1) and 17 in. monitor (white screen)	575	133	29.7	22.3	77.7
Personal computer (Brand 2) and 17 in. monitor (white screen)	420	125	35.7	28.6	71.4

Since earlier models of microcomputers and monitors show little difference in heat generation whether in use or idle, unlike the contemporary units with "Power Saver" features which significantly reduce power consumption when idle, a typical office room with a computer, typical of the model room in this study, it can be safely assumed that there are 5.4W/m^2 of computers and office equipment in the room (ASHRAE, 1997). Therefore, the total heat gain from appliances given by the second term in the RHS of equation 3.251 is given by:

$$\dot{Q}_{appliances} = \frac{5.4W}{m^2} * A_R \qquad 3.256$$

3.2.4.1.4.3 Heat generated from light bulbs

Lighting contributes sensible heat to the conditioned space. Part of the energy from lights is given out by convection heat transfer. This is picked up instantaneously by the air conditioning system. The remaining part of the energy from lights having been absorbed by the walls, floors and furniture is later radiated into the room after a time lag (Trane, 2011). Since the heat transferred from the lighting system consists of both radiation and convection, a Cooling Load Factor (CLF) is used to account for the time lag. Thus the sensible cooling load due to lighting system is given by (Trane, 2011):

$$\dot{Q}_{light\ bulbs} = \sum(W_t F_{ba}\ CLF) \qquad 3.257$$

Where W_t represents the total lights wattage; F_{ba} is the ballast factor (which is 1.2 for fluorescent lights and 1.0 for incandescent lights). The Cooling Load Factor (CLF) accounts for the capacity of the space to absorb and store the energy generated by the lights. If the lights are left on 24 hours a day, or if the air-conditioning system is shut off or set back at night, the CLF is assumed to be equal to 1.0.

Therefore, the total heat generated internally in the room can be estimated by substituting equations 3.255, 3.256 and 3.257 into 3.251 and the resulting expression becomes:

$$\dot{Q}_{i-gen,r} = N_p\left((SHGPP * CLF) + LHGPP\right) + \left(\frac{5.4W}{m^2} * A_R\right) + \sum(W_t F_{ba}\ CLF) \qquad 3.258$$

Therefore, the equation for the temperature variation in the cooled room during the day can be obtained by making the substitutions of equations 3.232, 3.233, 3.234, 3.245, 3.250 and 3.258 into equation 3.231. The resulting expression is as follows:

$$m_{air}c_{p_{air}}\frac{dT_{rc}}{dt} =$$

$$\dot{m}_{L,n}c_{p_{L,n}}\left(T_{L,n1} - T_{L,n2}\right) + \frac{2k_r[L_R B_R + H_R B_R + L_R H_R]}{\delta_{r,wall}}[T_a - T_r] + \frac{\rho_{air}c_{p_{air}}APCD(L_R B_R H_R)}{24*3600}[T_a - T_r] +$$

$$\left(N_p\left((SHGPP * CLF) + LHGPP\right) + \left(\frac{5.4W}{m^2} * A_R\right) + \sum(W_t F_{ba}\ CLF)\right) - \frac{1}{R_{rc}}\left[T_r - T_{L,n}\right] \qquad 3.259$$

3.2.4.2 Modelling of comfort heating

In Nigeria, comfort heating has not received a wide attention even though there are periods when temperatures become extremely low requiring heating to enhance comfortable indoor condition for people. However, where space heating systems exist, they utilize conventional energy from fossil fuel resources (oil, coal and natural gas) for heating purposes thereby increasing energy bills and greenhouse gas emissions. Sequel to this, the integration of solar heating systems into contemporary buildings will not only bring about drastic reduction in energy bills in the long run

but also reduce emission of carbon dioxide into the atmosphere and at the same time address the rural energy availability challenge resulting from non-wide electricity grid coverage.

The heating power is the energy needed to provide a reference and comfort temperature in the room (space) to be heated. The space heating load is the rate at which heat must be added to a space in order to maintain the optimum dry bulb temperature desired in the space. This is particularly necessary during moderate to low temperature ambient periods. The heating need and available means of losses must be known for appropriate sizing of the radiator (heat exchanger) that will deliver the needed or required heat energy into the room (space) to make it thermally comfortable for occupants. The available means of losses include the walls, solar gains, people and air renewal in the room. In general, the heating load calculation is performed assuming the worst-case conditions for the space in question (i.e. in extreme conditions from an outdoor base temperature (Trane, 2011; Zeghib and Chaker, 2015). The water heated by the selective SCONOR and stored in reservoir A (Fig. 3.1) is used to meet the heating need. Only valves H, O, F and D are open. The stored hot water flows into the radiator when valve G and pump B are turned on and returns to the tank through valve D. The process continues for about 8 hours from 00:00-08:00 hours.

The modelled room with several thermal volumes namely heat loss by transmission and air renewal from the room, internal heat generation as result of people and appliances as well as heat addition from the hot tank and the return heat to the tank after heating, is as shown in Fig. 3.23. The walls are at thermal equilibrium with the ambient.

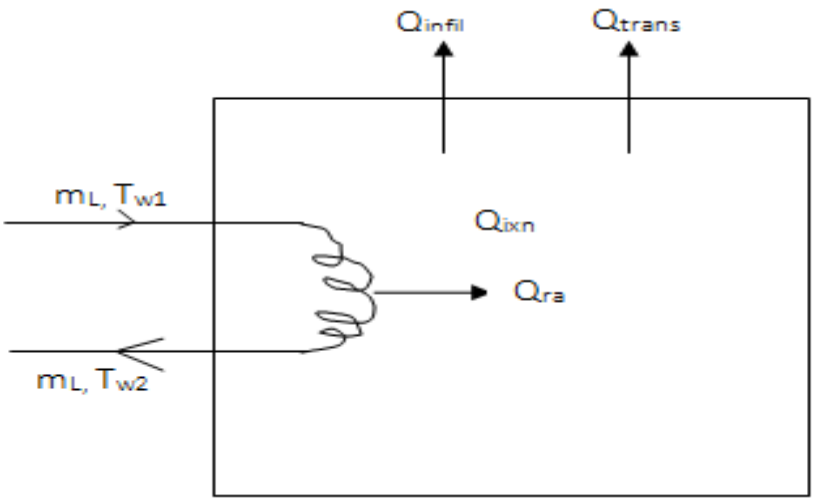

Fig. 3.23 Energy balance on the room control volume (heating)

Following the same assumptions made for the room during comfort cooling phase, the energy balance around the control volume of Fig. 3.23 is given as:

$$Heat\ gain\ entering\ the\ room\ +\ Heat\ generated\ in\ the\ room\ =\ Heat\ leaving\ the\ room\ +\ Change\ in\ internal\ energy\ of\ the\ room \quad 3.260$$

Employing equation 3.2, this can be mathematically written as:

$$\dot{Q}_{in,r_h} + \dot{Q}_{i-gen,r_h} = \dot{Q}_{out,r_h} + \dot{Q}_{int,r_h} \quad 3.261$$

From Fig 3.23, the total energy flow into the room, $\dot{Q}_{in,r_h}$ becomes:

$$\dot{Q}_{in,r_h} = \dot{Q}_{whst-ra} + \dot{Q}_{ra} \quad 3.262$$

Where $\dot{Q}_{whst-ra}$ is the energy of the water flowing from the hot storage tank to the room radiator and $\dot{Q}_{ra}$ is the energy gain by the room from the radiator.

The internal heat generation in the room as a result of people, appliances and light bulbs can be given as:

$$\dot{Q}_{i-gen,r_h} = \left(\dot{Q}_{people} + \dot{Q}_{appliances} + \dot{Q}_{light\ bulbs}\right) \quad 3.263$$

The total energy out of the room control volume, $\dot{Q}_{out,r_h}$ is given as:

$$\dot{Q}_{out,r_h} = \dot{Q}_{wra-hst} + \dot{Q}_{trans} + \dot{Q}_{air\,renewal} \quad 3.264$$

The rate of increase in the internal energy of the room, $\dot{Q}_{int,r_h}$ is given as:

$$\dot{Q}_{int,r} = m_{air} c_{p_{air}} \frac{dT_{rh}}{dt} \quad 3.265$$

Therefore, the overall energy balance for the room control volume during comfort heating is obtained by substituting equations 3.262, 3.263, 3.264 and 3.265 into equation 3.261 to yield:

$$\dot{Q}_{whst-ra} + \dot{Q}_{ra} + \left(\dot{Q}_{people} + \dot{Q}_{appliances} + \dot{Q}_{light\ bulbs}\right) = \dot{Q}_{wra-hst} + \dot{Q}_{trans} + \dot{Q}_{air\ renewal} + m_{air} c_{p_{air}} \frac{dT_{rh}}{dt} \quad 3.266$$

Equation 3.266 simplifies to:

$$m_{air} c_{p_{air}} \frac{dT_{rh}}{dt} = \dot{Q}_{whst-ra} + \dot{Q}_{ra} + \left(\dot{Q}_{people} + \dot{Q}_{appliances} + \dot{Q}_{light\ bulbs}\right) - \dot{Q}_{wra-hst} - \dot{Q}_{trans} - \dot{Q}_{air\ renewal} \quad 3.267$$

3.2.4.2.1 The radiator control volume

The common practice is to equip homes with low temperature radiators to meet the heating needs. However, European Standard Radiators have their heat outputs tested to EN 442 Delta T equal to 50^{o}C, relating to a water temperature of 75/65^{o}C and a room temperature of 20°C. Due to a lower supply temperature, the exchange surface of radiators at low-temperature with ambient air must be larger. They supply heat through a combination of radiation and convection, and their function is to maintain the desired air temperature in the room.

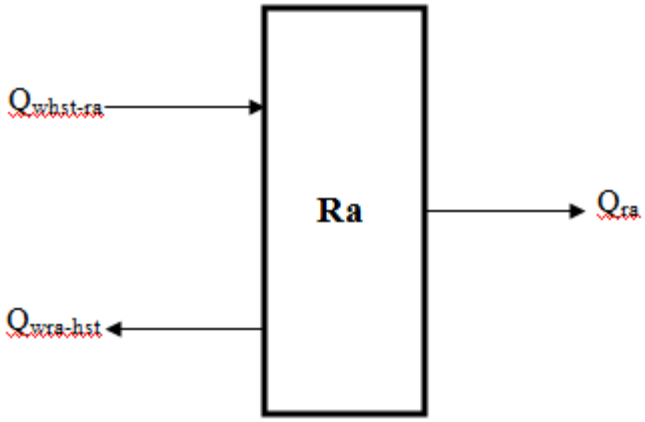

Fig. 3.24 Energy balance on the radiator control volume

From Fig. 3.24, hot water from the tank enters the radiator which transfers heat into the room and finally returns to the tank through the bottom of the tank. The energy of the hot water from the hot water storage tank (reservoir A) entering the radiator can be expressed as:

$$\dot{Q}_{whst-ra} = \dot{m}_{Lh} c_{p_{Lh}} T_{Lh,1} \qquad 3.268$$

While that of the water leaving the radiator coils back to reservoir A is expressed as:

$$\dot{Q}_{wra-hst} = \dot{m}_{Lh} c_{p_{Lh}} T_{Lh,2} \qquad 3.269$$

The heat emitted from the radiator is simply the difference between equations 3.268 and 3.269 and can be modelled as:

$$\dot{Q}_{ra} = \frac{1}{R_{ra}} (T_{Lh} - T_{rh}) \qquad 3.270$$

The radiator thermal resistance R_{ra} constitute the inside water and outside air thermal resistances

$$R_{ra} = \frac{1}{h_{ra,i} A_{ra,i}} + \frac{1}{\eta_{fin,r} h_{fin,r} A_{fin,r}} \qquad 3.271$$

According to Kreith and Bohn (2000), the waterside heat transfer coefficient can be evaluated by the expression:

$$h_{ra,i} = \frac{k_w}{D_{ra,i}} R_e^{0.8} P_r^{0.35} \qquad 3.272$$

For the low temperature radiator case, the Reynolds number, Prandtl number, air side heat transfer coefficient and the Grashof number can be evaluated using equations 3.237, 3.238, 3.239, 3.240 and 3.241 as detailed in section 3.2.4.1.1, given respectively as:

$$R_e = \frac{4\dot{m}_w}{\pi D_{ci}\mu_w} \quad 3.237$$

$$P_r = \frac{c_w \mu_w}{k_w} \quad 3.238$$

$$h_{fin,r} = 1.07\left(\frac{\Delta T}{L_{fin}}\right)^{0.25} \quad for \;\; 10^4 < Gr < 10^9 \quad 3.239$$

$$h_{fin,r} = 1.3\Delta T^{\frac{1}{3}} \quad for \;\; 10^9 < Gr < 10^{12} \quad 3.240$$

$$Gr = \frac{\beta \Delta T g \rho^2 {L_{fin}}^3}{\mu} \quad 3.241$$

Where, as before β is the coefficient of thermal expansion and can be taken (for an ideal gas) as 1/T if T is in Kelvin, ΔT is the temperature difference between the air and the surface and L_{fin} is the (vertical) length of the fin along which natural convection is taking place on the low temperature radiator surface. Since the fluid (water) thermo-physical properties remain unchanged, the above variables are evaluated with radiator properties.

3.2.4.2.2 Internal heat generation and heat losses by transmission and air renewal

The internal energy generated in the room due to people, appliances and light bulbs $\dot{Q}_{i-gen,r_h}$, is also expressed as equation 3.246, without including the cooling load factor terms, as:

$$\dot{Q}_{i-gen,r_h} = N_p(SHGPP + LHGPP) + \left(\frac{5.4W}{m^2} * A_R\right) + \sum(W_t F_{ba} F_u) \quad 3.273$$

Losses by transmission occur through walls, ceilings, thermal bridges and windows, and it can be expressed by the equation:

$$Q_{trans} = UA_T\Delta T = \frac{A_T(T_r - T_a)}{R_T} \quad 3.274$$

The above equation (3.274) would depend on the room orientation, direct solar radiation through windows or fenestration, actual wall and roof construction details and inside and outside wall heat transfer coefficients as well as the time of day but for a reasonably well-insulated building and to limit the number of variables (without unduly losing accuracy), it suffices to give acceptable result. Therefore, the transmission heat losses would be same as equation 3.245 with different indoor and ambient temperatures.

$$Q_{trans} = \frac{2k_r[L_R B_R + H_R B_R + L_R H_R]}{\delta_{r,wall}}[T_{rh} - T_{ah}] \quad 3.275$$

The heat losses from air renewal $\dot{Q}_{air,renewal}$, is the heat lost from infiltration and ventilation. Since there is need to heat up the room, it is appropriate to assume that both natural and mechanical ventilation are absent (i.e. all windows and doors are tightly closed and no fan is working in the room). Hence, heat loss by air renewal is only due to air infiltration into the room. It is given by equation 3.250. However, in the case of comfort heating, the indoor and outdoor temperatures differ from the case of comfort cooling and so infiltration loss is given as:

$$Q_{infil} = \frac{\rho_{air} c_{p_{air}} ACPD(L_R B_R H_R)}{24*3600}[T_{rh} - T_{ah}] \quad 3.276$$

Therefore, the equation for the temperature variation in the heated room during heating periods (00:00-08:00hrs) can be obtained by making the substitutions of equations 3.268, 3.269, 3.270, 3.273, 3.274 and 3.275 into equation 3.267 and simplifying. The resulting expression is given as:

$$m_{air}c_{p_{air}}\frac{dT_{rh}}{dt} = \dot{m}_{Lh}c_{p_{Lh}}\left(T_{Lh,1} - T_{Lh,2}\right) + \frac{1}{R_{ra}}\left(T_{Lh} - T_{rh}\right) + \left(N_p(SHGPP + LHGPP) + \left(\frac{5.4W}{m^2} * A_R\right) + \sum(W_t F_{ba} F_u)\right) - \frac{2k_r[L_R B_R + H_R B_R + L_R H_R]}{\delta_{r,wall}}\left[T_{rh} - T_{ah}\right] - \frac{\rho_{air}c_{p_{air}} ACPD(L_R B_R H_R)}{24*3600}\left[T_{rh} - T_{ah}\right] \quad 3.277$$

3.3 Numerical Implementation

3.3.1 Formulation of finite element equations

Finite element method (FEM) is employed for the numerical implementation of the transient thermal performance of the hybrid solar collector/nocturnal radiator (SCONOR). Knowledge of temperature distribution enables the determination of thermal stresses developed inside heated bodies (Rao, 1989). The finite element method provides a more accurate numerical solution of any physical problem than other methods (finite difference), by using known physical principles to develop algebraic equations describing the approximate solution to the problem. It applies the descritisation of the descriptive differential equations on the entire problem domain and not just at specified discrete or integration points. The physical domain is represented with finite elements (or cells) to enable realization of approximate solutions to the problem based on numerical techniques and digital computation. The crux of the finite element method is that the values of the field variables are not just computed at the nodes but also at the non-nodal points (or interior elements) by interpolation of the nodal values to approximate the values of such points (Hutton, 2004). Finite element analysis has gained prominent importance in the solution of non-structural problems such as heat transfer, fluid mechanics and fluid flow problems (Bathe, 1982; Rao, 1989; Hutton, 2004).

3.3.2 Computational domain

For the purpose of generating a numerical solution to the mathematical models developed, the problem domain is created and meshed in a FlexPDE environment as shown in Fig. 3.25.

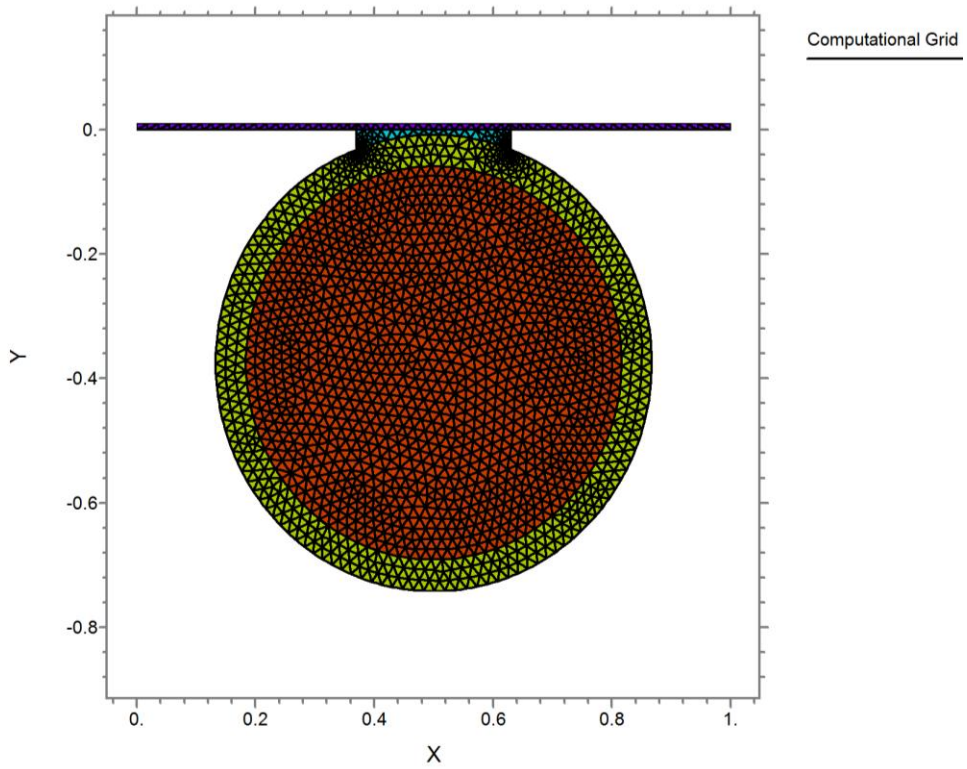

Fig. 3.25 Computational Domain

The computational domain is the assemblage of four regions, namely, the SCONOR, bond, riser tube and water flowing through the tube. During the solar heating and plate cool down phases, the model equations 3.24, 3.33, 3.49 and 3.59 are applied to the SCONOR, bond, tube and fluid respectively while during the nocturnal cooling phase the model equations 3.157, 3.163, 3.167 and 3.179 are applied for the water, tube, bond and SCONOR respectively. The model equations for the SCONOR and bond are in Cartesian coordinates while those of the tube and water are in cylindrical polar coordinates. To enable the numerical solution of the model equations simultaneously for the four regions, cylindrical polar coordinates are transformed to the Cartesian coordinates while regionally dependent variables are defined to ensure that each of the

model equations is implemented on the grids representing its defined region. With the coordinate transformation to be done on the tube/fluid regions, the computational domain can now be represented by a general Cartesian coordinate with axes defined by $0 \leq x \leq W$ and $0 \leq y \leq L$, subject to imposition of region-specific boundary conditions on the exterior elements. Therefore, a finite element formulation of a general two dimensional (2-D) conduction equation representing the SCONOR will suffice. The equation will be reduced to the appropriate forms applicable to the bond, tube and fluid regions, using the assumptions in section 3.2.1.1. Finally, the equations are coupled or assembled with the aid of the regionally dependent factors for simultaneous solution.

3.3.3 Finite element formulation of model equations

Field problems governed by differential equations are correctly resolved by employing the Galerkin's method of weighted residuals as a tool for finite element formulation (Hutton, 2004; Bathe 1982). The method of weighted residual is fully described in advanced engineering or finite element texts. This seeks to minimize the residual error.

The finite element formulation is achieved by dividing the computational domain into finite-length of 2-D triangular elements. The computational domain comprises 3401 meshes of triangular elements (or cells) and 1819 nodes. For the SCONOR region, the temperature distribution of the 2-D quadratic triangular elements with M nodes is discretized by:

$$T(x,y,t) = \sum_{i=1}^{M} N_i(x,y)T_i(t) = [N]\{T(t)\} \qquad 3.278$$

where T_i represent the unknown nodal temperatures at the nodes to be determined, $N_i(x,y)$ are the interpolation functions, which represent the functions of the independent variables that describe the variation of the field variables (i.e. unknown temperatures) within the finite element,

$[N]$ is the row matrix of interpolation functions and $\{T\}$ is the column matrix of nodal temperatures and t is the transient term.

Applying the Galerkin FEM, the residual equations corresponding to equation 3.24 for each cell in the SCONOR are:

$$\iint_A N_i(x,y)\left[\frac{\partial}{\partial x}\left(k_x\delta_{ss}\frac{\partial T_{ss}^{(e)}}{\partial x}\right)+\frac{\partial}{\partial y}\left(k_y\delta_{ss}\frac{\partial T_{ss}^{(e)}}{\partial y}\right)+Q_{solar}-U_L\left(T_{ss}^{(e)}-T_a\right)-\rho c_p\delta_{ss}\frac{\partial T_{ss}^{(e)}}{\partial t}\right]dA=0 \quad 3.279$$

To further simplify equation 3.279, Green-Gauss Theorem is applied to the first two integrals.

$$\delta_{ss}\iint_A\left[\frac{\partial}{\partial x}\left(k_x\frac{\partial T_{ss}^{(e)}}{\partial x}\right)N_i+\frac{\partial}{\partial y}\left(k_y\frac{\partial T_{ss}^{(e)}}{\partial y}\right)N_i\right]dA=-\delta_{ss}\oint_s\left(q_xn_x+q_yn_y\right)N_i dS-\delta_{ss}\iint_A\left(k_x\frac{\partial T_{ss}^{(e)}}{\partial x}\frac{\partial N_i}{\partial x}+k_y\frac{\partial T_{ss}^{(e)}}{\partial y}\frac{\partial N_i}{\partial y}\right)dA \quad 3.280$$

Substituting equation 3.280 into equation 3.279 and simplifying, gives:

$$-\iint_{A^{(e)}}\left(k_x\frac{\partial T_{ss}^{(e)}}{\partial x}\frac{\partial N_i}{\partial x}+k_y\frac{\partial T_{ss}^{(e)}}{\partial y}\frac{\partial N_i}{\partial y}\right)\delta_{ss}dA-\delta_{ss}\oint_{\Omega^{(e)}}\left(q_xn_x+q_yn_y\right)N_i d\Omega+\iint_{A^{(e)}}Q_{solar}dA-\iint_{A^{(e)}}U_L\left(T_{ss}^{(e)}-T_a\right)dA-\iint_{A^{(e)}}\rho c_p\delta_{ss}\frac{\partial T_{ss}^{(e)}}{\partial t}dA=0 \quad 3.281$$

simplifying further,

$$\iint_{A^{(e)}}\left(k_x\frac{\partial T_{ss}^{(e)}}{\partial x}\frac{\partial N_i}{\partial x}+k_y\frac{\partial T_{ss}^{(e)}}{\partial y}\frac{\partial N_i}{\partial y}\right)\delta_{ss}dA+U_L\iint_{A^{(e)}}T_{ss}^{(e)}N_i dA+\iint_{A^{(e)}}\rho c_p\delta_{ss}\frac{\partial T_{ss}^{(e)}}{\partial t}dA=\iint_{A^{(e)}}Q_{solar}N_i dA+U_LT_a\iint_{A^{(e)}}N_i dA-\delta_{ss}\oint_{\Omega^{(e)}}\left(q_xn_x+q_yn_y\right)N_i d \quad 3.282$$

Equation 3.282 is a system of M equations for each of the nodes. The left hand side represents the unknown temperature distribution and the right hand side comprises the solar loading, surface convection and boundary heat flux.

Using equation 3.278 and considering assumption (iii) for material homogeneity, equation 3.282 can be expressed in matrix notation as:

$$\iint_{A^{(e)}} k\left(\left[\frac{\partial N}{\partial x}\right]^T\left[\frac{\partial N}{\partial x}\right]+\left[\frac{\partial N}{\partial y}\right]^T\left[\frac{\partial N}{\partial y}\right]\right)\{T_{ss}\}\delta_{ss}dA + U_L\iint_{A^{(e)}}[N]^T[N]\{T_{ss}\}dA + \iint_{A^{(e)}}\left[\frac{\partial N}{\partial t}\right]^T\rho c_p\delta_{ss}dA = \iint_{A^{(e)}}Q_{solar}[N]^T dA + U_L T_a\iint_{A^{(e)}}[N]^T dA - \oint_{\Omega^{(e)}}q_\Omega n_\Omega [N]^T\delta_{ss}d\Omega \quad 3.283$$

The first two terms of the LHS of equation 3.283 is known as the MxM conductance matrix for the triangular elements and can be expressed as:

$$[K^{(e)}] = \iint_{A^{(e)}}\left(\left[\frac{\partial N}{\partial x}\right]^T\left[\frac{\partial N}{\partial x}\right]+\left[\frac{\partial N}{\partial y}\right]^T\left[\frac{\partial N}{\partial y}\right]\right)\{T_{ss}\}k\delta_{ss}dA + U_L\iint_{A^{(e)}}[N]^T[N]\{T_{ss}\}dA \quad 3.284$$

The first integral in equation 3.284 represents the conduction stiffness while the second integral is the surface convection to the ambient.

The third term in the LHS of equation 3.283 represents the transient term, which can be expressed in column matrix form as:

$$\left[K_t^{(e)}\right] = \iint_A [N]^T[N]\{T_{ss}\}\rho c_p\delta_{ss}dA \quad 3.285$$

The solar loading (i.e. the first integral in the RHS of equation of 3.283) can also be described in a column matrix form as:

$$\left\{f_{Qa}^{(e)}\right\} = \iint_{A^{(e)}} Q_{solar}\{N\}dA \quad 3.286$$

where $\left\{f_{Qa}^{(e)}\right\}$ is the element forcing function.

Similarly, the element forcing functions for the surface convection and boundary heat flux can be expressed respectively as:

$$\left\{f_{U_L}^{(e)}\right\} = U_L T_a\iint_{A^{(e)}}\{N\}dA \quad 3.287$$

$$\left\{f_{\Omega}^{(e)}\right\} = -\oint_{\Omega^{(e)}} q_\Omega n_\Omega\{N\}\delta_{ss}d\Omega \quad 3.288$$

where $[N]^T = \{N\}$ is Mx1 column matrix of interpolation functions.

Therefore equation 3.283 can be re-written by assembling the conductance matrices and forcing functions for the transient term, conduction, surface convection and boundary flux to yield:

$$\left[K^{(e)}\right]\{T_{ss}\} + \left[K_t^{(e)}\right]\{\dot{T}_{ss}\} = \left\{f_{Qa}^{(e)}\right\} + \left\{f_{U_L}^{(e)}\right\} + \left\{f_{\Omega}^{(e)}\right\} \quad 3.289$$

Equation 3.289 is the general assemblage of finite element for the 2-D heat conduction with applied surface heat flux (solar loading) to the elements and surface convection from the elements to the ambient. The term $\left\{f_{\Omega}^{(e)}\right\}$ defines explicitly the boundary flux.

3.3.3.1 Initial and boundary conditions

2-D conduction with boundary flux and surface convection is subject to three kinds of boundary conditions. Equation 3.289 is subject to the following initial and boundary conditions:

$$T(x,y,t) = T_a \; for \; t > 0 \; on \; \Omega_1 \quad 3.290$$

$$k_x \frac{\partial T}{\partial x} l_x + k_y \frac{\partial T}{\partial y} l_y + q = 0 \quad for \; t > 0 \; on \; \Omega_2 \quad 3.291$$

$$k_x \frac{\partial T}{\partial x} l_x + k_y \frac{\partial T}{\partial y} l_y + h(T_{ss} - T_a) = 0 \quad for \; t > 0 \; on \; \Omega_3 \quad 3.292$$

Since equation 3.289 is first order in time, only one initial condition is required and is given as:

$$T(x,y,t=0) = T_a \quad 3.292$$

Applying the boundary conditions on the boundary flux forcing functions, $\left\{f_{\Omega}^{(e)}\right\}$, for the element, equation 3.288, for the three defined boundary surfaces, yields:

On the boundary surface Ω_1:

$$-\oint_{\Omega^{(e)}} q_{\Omega} n_{\Omega} \{N\} \delta_{ss} d\Omega_1 = 0 \quad 3.293$$

That is:

$$\frac{\partial T}{\partial x} = \frac{\partial T}{\partial y} = 0 \quad 3.295$$

On the boundary surfaces Ω_2 and Ω_3, solar heat flux and edge convection conditions are specified respectively. Therefore, the boundary flux forcing function of equation 3.288 becomes:

$$\left\{f_{\Omega}^{(e)}\right\} = -\oint_{\Omega_2^{(e)}+\Omega_s^{(e)}}\left[q_{\Omega_2} n_{\Omega_2}\{N\}\delta_{ss} + q_{\Omega_s} n_{\Omega_s}\{N\}\delta_{ss}\right]d\Omega \quad 3.296$$

$$\left\{f_{\Omega}^{(e)}\right\} = -\oint_{\Omega_2^{(e)}+\Omega_s^{(e)}}\left[q_{solar} n_{\Omega_2} + h(\mathrm{T}_{ss}^{(e)} - T_a)\right]\{N\}\delta_{ss}d\Omega \quad 3.297$$

$$\left\{f_{\Omega}^{(e)}\right\} = -\oint_{\Omega_2^{(e)}}\left[q_{solar} n_{\Omega_2}\right]\{N\}\delta_{ss}d\Omega_2 - \oint_{\Omega_s^{(e)}}\left[h(\mathrm{T}_{ss}^{(e)} - T_a)\right]\{N\}\delta_{ss}d\Omega_3 \quad 3.298$$

where the solar flux on the boundary surface Ω_2 is given by the forcing function:

$$\left\{f_{\Omega_2}^{(e)}\right\} = -\oint_{\Omega_2^{(e)}}\left[q_{solar} n_{\Omega_2}\right]\{N\}\delta_{ss}d\Omega_2 \quad 3.299$$

Since the edge convection involves the nodal temperature, the second term in the RHS of equation 3.298 can be re-written as:

$$-\oint_{\Omega_s^{(e)}}\left[h(\mathrm{T}_{ss}^{(e)} - T_a)\right]\{N\}\delta_{ss}d\Omega_3 = -\oint_{\Omega_s^{(e)}} h[N]^T[N]\{\mathrm{T}_{ss}^{(e)}\}\delta_{ss}d\Omega_3 + \oint_{\Omega_s^{(e)}} hT_a\{N\}\delta_{ss}d\Omega_3 \quad 3.300$$

This implies that the forcing of equation 3.300 applied on the boundary surface Ω_3 can be expressed as:

$$\left\{f_{\Omega_s}^{(e)}\right\} = -\left[\mathrm{K}_{h\Omega_s}^{(e)}\right]\{T_{ss}\} + \left\{f_{h\Omega_s}^{(e)}\right\} \quad 3.301$$

Where $\left[\mathrm{K}_{h\Omega_s}^{(e)}\right]$ is an additional stiffness to the element conductance matrix (see equation 3.284) as a result of convection on the boundary elements spanning the boundary surface Ω_3.

Substituting equations 3.299 and 3.301 into equation 3.298 gives the total boundary flux forcing function as:

$$\left\{f_{\Omega}^{(e)}\right\} = \left\{f_{\Omega_2}^{(e)}\right\} - \left[\mathrm{K}_{h\Omega_s}^{(e)}\right]\{T_{ss}\} + \left\{f_{h\Omega_s}^{(e)}\right\} \quad 3.302$$

Substituting equation 3.302 into equation 3.289 results in:

$$\left[K^{(e)}\right]\{T_{ss}\} + \left[C_t^{(e)}\right]\{\dot{T}_{ss}\} = \left\{f_{Qa}^{(e)}\right\} + \left\{f_{U_L}^{(e)}\right\} + \left\{f_{\Omega_2}^{(e)}\right\} - \left[\mathrm{K}_{h\Omega_s}^{(e)}\right]\{T_{ss}\} + \left\{f_{h\Omega_s}^{(e)}\right\} \quad 3.303$$

Simplifying, equation 3.303 becomes:

$$\left[K_t^{(e)}\right]\{\dot{T}_{ss}\} + \left[K^{(e)}\right]\{T_{ss}\} + \left[K_{h\Omega_s}^{(e)}\right]\{T_{ss}\} = \left\{f_{Qa}^{(e)}\right\} + \left\{f_{U_L}^{(e)}\right\} + \left\{f_{\Omega_2}^{(e)}\right\} + \left\{f_{h\Omega_s}^{(e)}\right\} \quad 3.304$$

Equation 3.304 is the final transient finite element equation for each element of the hybrid SCONOR. $K_t^{(e)}$ is the element capacitance matrix which defines the capacity of the element to store heat.

Finally, equation 3.304 is transformed into a global equation to be applied to all the nodes in the computational domain using a numerical solver in a digital computer. The global equation is expressed by dropping the element terms, as:

$$[K_t]\{\dot{T}_{ss}\} + \left[K + K_{h\Omega_s}\right]\{T_{ss}\} = \{F_{Qa}\} + \{F_{U_L}\} + \{F_{\Omega_2}\} + \{F_{\Omega_s}\} \quad 3.305$$

Equation 3.305 is a set of ordinary, coupled first order differential equations in time that can be solved using the finite difference method (FDM). This simply means that the transient term in a transient finite element formulation is resolved with the use of appropriate finite difference scheme, since finite element method adopts a time-matching algorithm used in finite difference methods in resolving transient problems (Rao, 1982; Hutton, 2004).

Employing the implicit Boundary Difference Method (BDM) that is unconditionally stable, the transient term in equation 3.305 is approximated as:

$$\dot{T}_{ss}(t) \cong \frac{T^t - T^{(t-\Delta t)}}{\Delta t} \quad 3.306$$

Substituting equation 3.306 into 3.305 will result in:

$$[K_t]\left(\frac{T_{ss}{}^t - T_{ss}{}^{(t-\Delta t)}}{\Delta t}\right) + \left[K + K_{h\Omega_s}\right]\{T_{ss}(t)\} = \{F_{Qa}(t)\} + \{F_{U_L}(t)\} + \{F_{\Omega_2}(t)\} + \{F_{\Omega_s}(t)\} \quad 3.307$$

$$[K_t]\left(T_{ss}{}^t - T_{ss}{}^{(t-\Delta t)}\right) + \Delta t\left[K + K_{h\Omega_s}\right]\{T_{ss}(t)\} = \Delta t\left(\{F_{Qa}(t)\} + \{F_{U_L}(t)\} + \{F_{\Omega_2}(t)\} + \{F_{\Omega_s}(t)\}\right) \quad 3.308$$

For $t = t_i$ and $t - \Delta t = t_{i-1}$, equation 3.308 can be re-written as:

$$[K_t]\left(T_{ss(t_i)} - T_{ss(t_{i-1})}\right) + \Delta t\left[K + K_{h\Omega_3}\right]\{T_{ss}(t_i)\} = \Delta t\left(\{F_{Qa}(t_i)\} + \{F_{U_L}(t_i)\} + \{F_{\Omega_2}(t_i)\} + \{F_{\Omega_3}(t_i)\}\right) \quad 3.309$$

Equation 3.309 simplifies to:

$$\left([K_t] + [K]\Delta t + [K_{h\Omega_3}]\Delta t\right)\{T_{ss(t_i)}\} = [K_t]\{T_{ss(t_{i-1})}\} + \Delta t\left(\{F_{Qa}(t_i)\} + \{F_{U_L}(t_i)\} + \{F_{\Omega_2}(t_i)\} + \{F_{\Omega_3}(t_i)\}\right) \quad 3.310$$

With nodal temperatures at time t_{i-1} or t_i known, FlexPDE uses modified Newton-Raphson iteration to generate a time-matching algorithm that would solve for the unknown temperatures at time steps with equation 3.310. The subscript "i" ranges from 6-18 during solar water heating mode; 18-20 during plate cool down phase and 20-30 during the nocturnal water cooling mode, spanning a period of 24 hours.

3.3.3.2 The bond region

Even though the bond is treated as a 1-D heat conduction in section 3.2.1.3, to enable its numerical descritization in the global coordinate system of the computational domain where the whole SCONOR-bond-tube-fluid regions are defined in a 2-D Cartesian plane, the above finite element formulation method is applied in the bond region. Equation 3.33 for the bond region can be transformed into the form of the global equation 3.307 by relaxing the element forcing functions for solar flux, surface convection and boundary surfaces Ω_2 and Ω_3 and employing appropriate boundary conditions. Therefore, the global equation for the bond region becomes:

$$[K_t]\{\dot{T_b}\} + [K]\{T_b\} = \{F_{\Omega_1}\} \quad 3.311$$

Subject to the boundary conditions:

$$\left.\begin{aligned}\Omega_1: \left(\frac{\partial T}{\partial y}\right)_{(0,0-0,1)} &= \left(\frac{\partial T}{\partial y}\right)_{(1,0-1,1)} = 0\\ \left(\frac{\partial T}{\partial y}\right)_{(0,1-1,1)} &= -\frac{k_b}{\delta_b}(T_{ss} - T_b)\\ \left(\frac{\partial T}{\partial y}\right)_{(0,0-1,0)} &= -\frac{k_b}{\delta_b}(T_b - T_t)\end{aligned}\right\} \quad 3.312$$

3.3.3.3 The tube/fluid region

The basic relation between the cylindrical polar coordinates $(r, \emptyset)$ and the rectangular coordinates (x, y) can be employed to transform equation 3.49 for the tube/fluid region into the (x, y) coordinate system so as to enable its solution in the global (x, y) coordinate of the computational domain. Details of this transformation are shown in standard texts on advanced engineering mathematics and finite element. According to Hutton (2004), cylindrical polar coordinates in $(r, \emptyset)$-plane is expressed in Cartesian coordinates as:

$$\frac{1}{r}\frac{\partial}{\partial r}\left(r\frac{\partial T}{\partial r}\right) + \frac{1}{r^2}\frac{\partial}{\partial \emptyset}\left(\frac{\partial T}{\partial \emptyset}\right) = \frac{\partial^2 T}{\partial x^2} + \frac{\partial^2 T}{\partial y^2} \quad 3.313$$

Therefore, the right hand side of equation 3.49 for the tube/fluid regions can be written as:

$$\frac{1}{r}\frac{\partial}{\partial r}\left(r\frac{\partial T_t}{\partial r}\right) + \frac{1}{r^2}\frac{\partial}{\partial \emptyset}\left(\frac{\partial T_t}{\partial \emptyset}\right) = \frac{\partial^2 T_t}{\partial x^2} + \frac{\partial^2 T_t}{\partial y^2} \quad 3.314$$

With this transformation, the Galerkin finite element formulation for the SCONOR can also be applied to these regions with specified boundary fluxes of the type of boundary surface Ω_1. The solar flux and convection loadings on boundary surfaces Ω_2 and Ω_3 are also relaxed. Hence, the global equation for the tube region becomes:

$$[K_t]\{\dot{T}_t\} + [K]\{T_t\} = \{F_{\Omega_1}\} \quad 3.315$$

Subject to the boundary condition:

$$\left.\begin{aligned}\left(\frac{\partial T}{\partial y}\right)_{(0,0-1,0)} &= \left(\frac{\partial T}{\partial r}\right)_{r=r_o} = -\frac{k_t}{\delta_t}(T_b - T_t) \\ \left(\frac{\partial T}{\partial r}\right)_{r=r_{o-}r_i} &= \pi D_i h_{wi}(T_t - T_w)\end{aligned}\right\} \quad 3.316$$

And finally, the global equation for the fluid region becomes:

$$[K_t]\{\dot{T_w}\} + [K]\{T_w\} = \{F_{\Omega_1}\} \quad 3.317$$

Subject the convection at the tube/fluid boundary surface:

$$\left(\frac{\partial T}{\partial r}\right)_{r=r_{o-}r_i} = \pi D_i h_{wi}(T_t - T_w) \quad 3.318$$

The accuracy of finite element analysis much depends on the polynomial or interpolation functions adopted (Hutton 2004; Rao 1982; Bathe 1989; Ogueke, 2005). The distribution of unknown variables (temperature) in the elements is approximated using interpolation functions, the choice of which depends on the capability of finite element software of choice, the computer power and time available for numerical computation. Higher order polynomials require high disk space and increase computer time considerably but provide more accurate results. Therefore, 2-order quadratic triangular elements as shown in Fig. 3.25 are employed for this work to ensure results that are highly accurate.

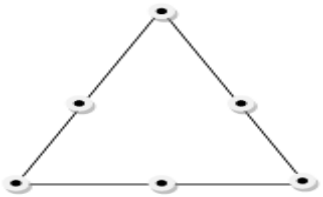

Fig. 3.25 Quadratic triangular element

For a 2-D quadratic triangular element, complete polynomial representation of the variable (temperature) is given as (Hutton, 2004):

$$T(x,y) = a_0 + a_1 x + a_2 y + a_3 x^2 + a_4 xy + a_5 y^2 \quad 3.319$$

The polynomial in equation 3.319 can be expressed in terms of interpolation functions and nodal temperatures substituting into equation 3.279.

$$a_0 + a_1 x + a_2 y + a_3 x^2 + a_4 xy + a_5 y^2 = \sum_{i=1}^{M} N_i(x,y) T_i(t) = [N]\{T(t)\} \quad i = 1,2,\ldots 6 \tag{3.320}$$

Because of the quadratic polynomial representation of temperature, each interpolation is a quadratic function and must be such that its value is unity at its own node zero at other nodes. Applying these conditions at each node, the interpolation functions that ensure numerical solution convergence for the elements are given as (Hutton, 2004).

$$\left.\begin{aligned} N_1 &= L_1(2L_1 - 1 \\ N_2 &= L_2(2L_2 - 1 \\ N_3 &= L_3(2L_3 - 1 \\ N_4 &= 4L_1L_2 \\ N_5 &= 4L_2L_3 \\ N_6 &= 4L_1L_3 \end{aligned}\right\} \tag{3.321}$$

The interpolation functions are then integrated over the domain of the element by expressing them in area coordinates as (Hutton, 2004):

$$\iint_A L_1^a L_2^b L_3^c \, dA = (2A)\frac{a!b!c!}{(a+b+c+2)!} \tag{3.322}$$

The stiffness matrices are then computed using the interpolation functions and area coordinates in the global coordinate equation for each region.

3.3.4 Numerical simulations

There are many multiphysics solvers available such as ANSYS FLUENT, CFX, COMSOL multiphysics, Autodesk CFD, etc, that implement finite element and finite volume numerical approximations. Even though they all have their capabilities and limitations, most of them employ customized equations and so cannot allow the user input his own equations as they apply to his model development. However, FlexPDE has such a flexible feature that enables the user defines his own model equations as developed under his assumptions, hence, the preference for FlexPDE. The numerical simulations of the model equations were carried out with a code written

by the researcher at the Department of Mechanical Engineering, Federal University of Technology, Owerri, Nigeria, using FlexPDE multiphysics scripted model builder and numerical solver, version 7.12.

FlexPDE is a scripted finite element model builder and numerical solver. It uses a script written by the user to perform operations necessary to turn a description of partial and ordinary differential equations system into a finite element model, solve the system of equations, and present graphical and tabular output of the results using the Galerkin method of weighted residuals described above (PDE Solutions, 2018). FlexPDE performs the entire range of functions necessary to solve partial differential equation systems. It has an editor for preparing scripts, geometry and mesh generators for building finite element meshes, a finite element solver for numerical solutions, and a graphics system to post-process results. Hence, it is entirely a problem solving environment. The script completely describes the equation system and problem domain, so there is no uncertainty about what equations are being solved, as might be the case with a fixed-application program. New variables, new equations or new terms may be added at will, so there is never a case of the software being unable to represent a different loss term, or a different physical effect. FlexPDE solves systems of first or second order linear or non-linear partial differential equations by applying a modified Newton-Raphson iteration process in nonlinear systems.

3.3.4.1 FlexPDE scrpting procedure

The problem description script is a readable text file. The contents of the file comprise a number of sections, each identified by a header. The fundamental sections are:

TITLE: this shows a descriptive label for the output.

SELECT: this section is in-built user controls which when selected, overrides the default behaviour of FlexPDE.

VARIABLES: here the dependent variables are specified.

DEFINITIONS: where useful parameters, relationships or functions are defined.

EQUATIONS: the number of variables specified determines the number of differential equations as each variable is associated with a partial differential equation.

BOUNDARIES: the geometry is described by walking the perimeter of the domain, stringing together line or arc segments bounding the figure.

MONITORS and PLOTS: desired graphical output is listed, including any combination of contour, surface, and elevation or vector plots.

END: this section completes the script.

FlexPDE is a fully integrated PDE solver, combining several internal facilities to provide a complete problem solving system:

(i) A script editing facility with syntax highlighting which provides a full text editing facility and a graphical domain preview.

(ii) A symbolic equation analyzer which expands defined parameters and equations, performs spatial differentiation, and symbolically applies integration by parts to reduce second order terms to create symbolic Galerkin equations. It then symbolically differentiates these equations to form the Jacobian coupling matrix.

(iii) A mesh generation facility constructs a triangular or tetrahedral finite element mesh over a two or three-dimensional problem domain. In two dimensions, an arbitrary domain is filled with an unstructured triangular mesh.

(iv) A Finite Element numerical analysis facility selects an appropriate solution scheme for steady-state, time-dependent or eigenvalue problems, with separate procedures for linear and nonlinear systems

(v) An adaptive mesh refinement procedure measures the adequacy of the mesh and refines the mesh wherever the error is large. The system iterates the mesh refinement and solution until a user-defined error tolerance is achieved.

(vi) A dynamic time-step control procedure measures the curvature of the solution in time and adapts the time integration step to maintain accuracy.

(vii) A graphical output facility which accepts arbitrary algebraic functions of the solution and plots contour, surface, vector or elevation plots.

(viii) A data export facility writes text reports in many formats, including simple tables, full finite element mesh data, CDF, VTK or TecPlot compatible files.

Proper specification of boundary conditions is crucial to the solution of a PDE system. In a FlexPDE script, boundary conditions are presented as the boundary is being described. The primary types of boundary condition are VALUE and NATURAL. The VALUE (or Dirichlet) boundary condition specifies the value that a variable must take on the boundary of the domain while the NATURAL boundary condition specifies a flux at the boundary of the domain.

3.3.4.2 Grid Independence

In order to obtain a solution independent of grid distribution, grid sensitivity tests were performed by tracing the temperature variation against different number of grids. It is found that the solution became almost independent of grid distribution from about 3401 grid cells and 1819 nodes.

3.3.4.3 Numerical solution stability

FlexPDE employs a variable order implicit backward difference method (BDM) in the implementation of the time integration of the transient term in the model equations of transient problems (PDE Solutions, 2017). The second-order implicit BDM gives the best trade-off between stability, smoothness and speed of numerical solutions and so since the backward difference method (BDM) employed in the descritization of the transient terms in the model equations is unconditionally stable, the solution does not have any stability problem. In resolving the convection terms, it applies an upwind factor to add diffusion term along the heat flow direction to stabilize the computation. The dynamic time-step control procedure measures the curvature of the solution in time and adapts the time integration step to maintain accuracy.

3.3.4.4 Convergence Criteria

Convergence determines solution accuracy of finite element analysis. The convergence criteria for a finite element analysis to approximate the exact solution is that the interpolation function of equation 3.278,

$$T(x,y) = \sum_{i=1}^{M} N_i(x,y) T_i \qquad 3.278$$

must satisfy the compatibility and completeness requirements.

The compatibility requirement entails that that the temperature and its derivatives up to one order less than the highest order derivative appearing in the integral formulation of the equations must be continuous to avoid jump discontinuities in temperature distribution, while the completeness requirement entails that the temperature and its partial derivative up to and including the highest order derivative appearing in the integral formulation must be capable of assuming constant

values within the limit of element size shrinking to zero in mesh refinement and as such there is no heat flux through the element but a state of constant temperature.

Mesh refinement enhances convergence. Meshes are either h- or p-refined. In h-refinements, the number of elements is increased with reduced element sizes while in p-refinements, there is no reduction in element sizes but higher order polynomials are employed as interpolation functions (Hutton, 2004). The adaptive mesh refinement of FlexPDE uses a p-refinement procedure using quadratic or cubic finite element interpolation to iterate the mesh and solution until a defined residual error limit of 1e-6 is achieved, thus satisfying the above two conditions as the numerical solution converges to the exact solution.

3.3.4.5 Outline of simulations undertaken

Numerical simulations were run to predict the performance of the system during the solar heating and nocturnal cooling modes both for instantaneous SCONOR performance and accumulative performance in the storage systems. The simulations were undertaken as follows:

(i) The first simulation was done on the SCONOR alone to ascertain the heat flow pattern on the plate since the whole plate surface is exposed to incoming solar radiation. Thermal camera could have been useful to provide this information but none was available in the study area. This was done from 6:00-18:00 hours.

(ii) The second simulation was done on the entire SCONOR-bond-tube-fluid regions to predict its seasonal performance during the solar heating mode from 6:00-18:00 hours as an open system and then its long term performance by incorporating the hot water storage tank to investigate the storage capacity of the system also from 6:00-18:00 hours.

(iii) Immediately the water circulating pump is turned off at 18:00 hours, another simulation was done to investigate the possibility of indoor comfort heating using the thermal energy of water in the hot storage tank from 18:00-30:00 hours.

(iv) The transition from end of solar heating at 18:00 hours and the beginning of nocturnal cooling at 20:00 hours was investigated by another round of simulation to ascertain the possibility of the system to cool down to ambient conditions at the onset of nocturnal cooling.

(v) At 20:00 hours, the pump circulating water through the SCONOR is turned on and the simulation runs for nocturnal water cooling commenced. Nocturnal cooling of water was investigated for the open operation case from 20:00-30:00 hours of the next day for each day of the run. This was done for the seasonal performance of the system. It's long term performance was also investigated by incorporating the water storage system where the cooled water is stored for use in indoor comfort cooling from 08:00-17:00 hours of during day. Stratifications in the cold storage tank during storage and comfort cooling were also simulated.

(vi) The model results were also compared with results obtained from literature as validation studies and finally, parametric analyses were done to investigate the effects of bond specifications, coating materials, tube spacing, number of windscreen, and latitude on the performance of the system.

Results obtained from all the numerical simulations, model results comparisons and parameterization are presented and discussed in the next chapter while the numerical data generated from the simulations, used in plotting the graphs shown in the next chapter are presented in the appendix.

CHAPTER 4

Results and Discussion

4.1 Results

The results obtained from this study are presented in Figs 4.1-4.82. Figs 4.1-4.53b illustrate the thermal distribution and seasonal performance predictions of the SCONOR using Owerri, Nigeria climatic data. Figs 4.54-4.57 show the performance predictions in other Nigerian cities. Figs 4.58-4.64 show stratification in the storage tanks and space conditioning profiles. Figs 4.65-4.69b are the benchmarking profiles, while Figs 4.70-4.82 illustrate the parametric analyses.

4.1.1 Thermal distribution on the SCONOR

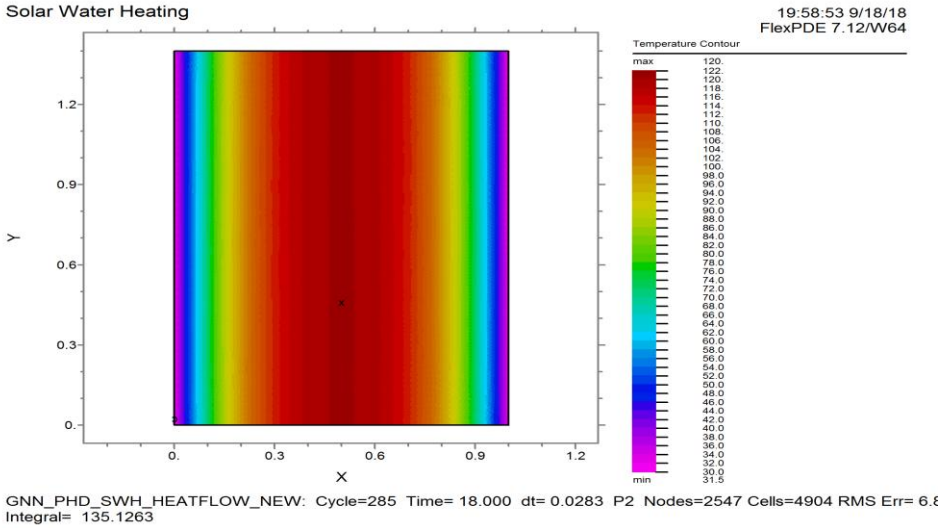

Fig. 4.1 Heat flow contour along the SCONOR

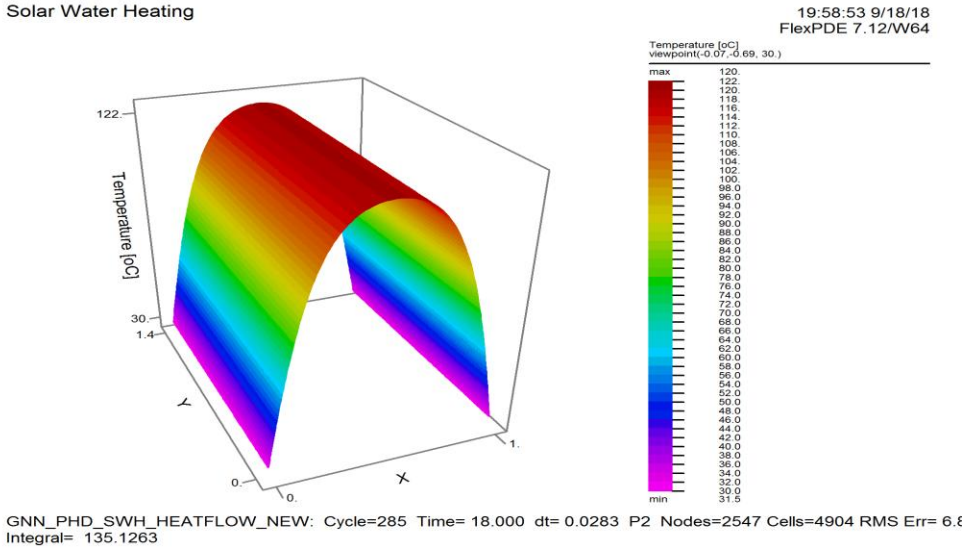

Fig. 4.2 Surface plot of temperature along SCONOR x- and y-coordinates

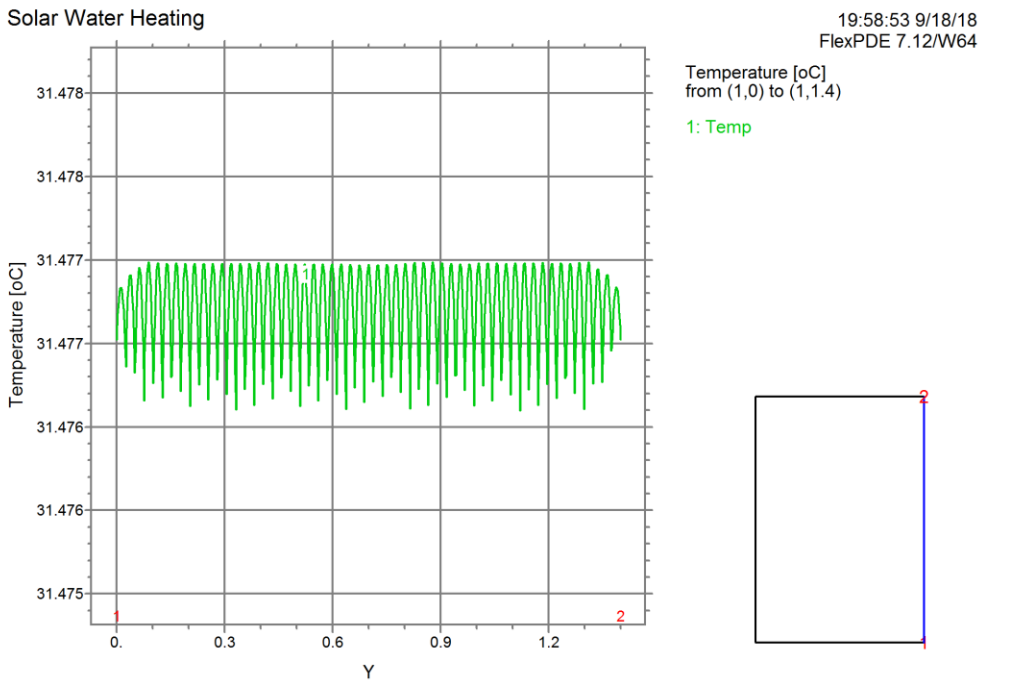

Fig. 4.3 Temperature variation along SCONOR length

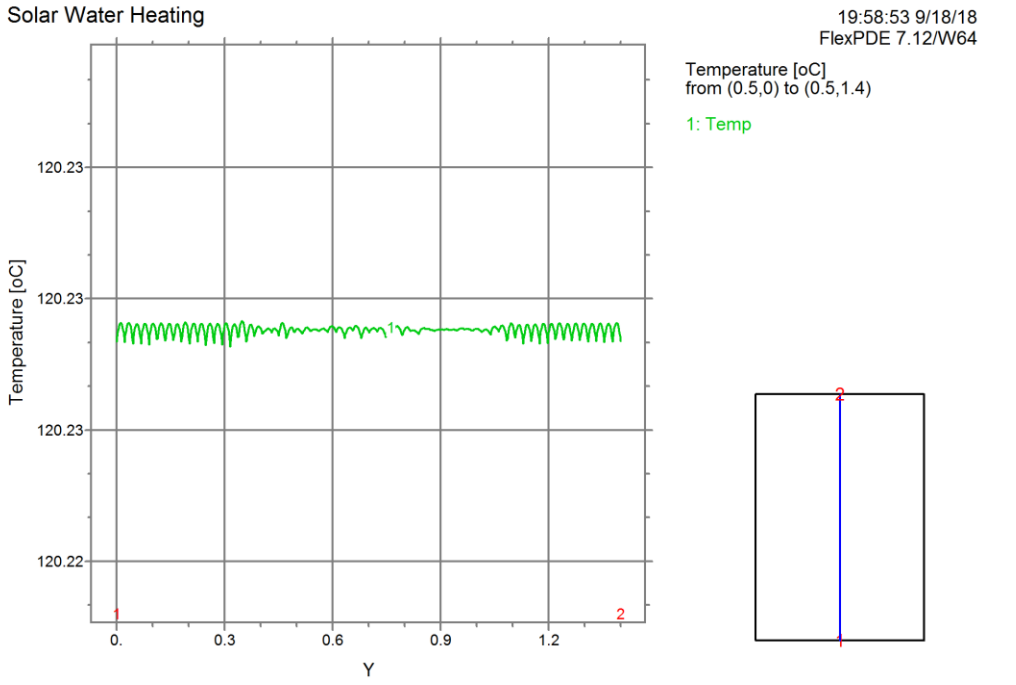

Fig. 4.4 Temperature variation along SCONOR centre

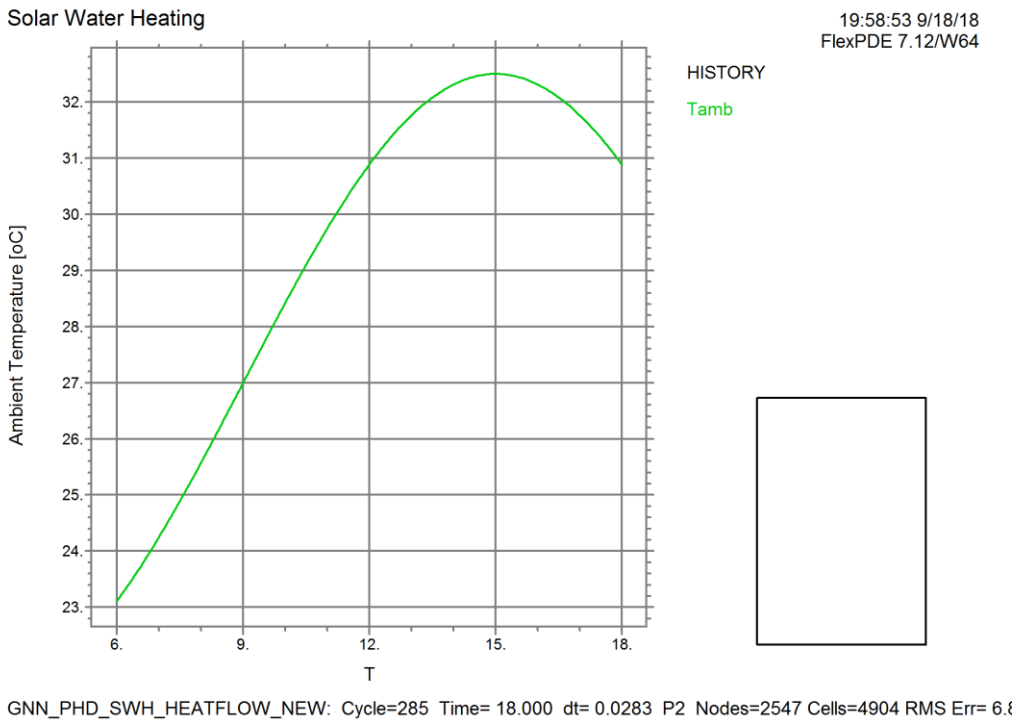

Fig. 4.5 Ambient temperature of the test day (29/01/2017)

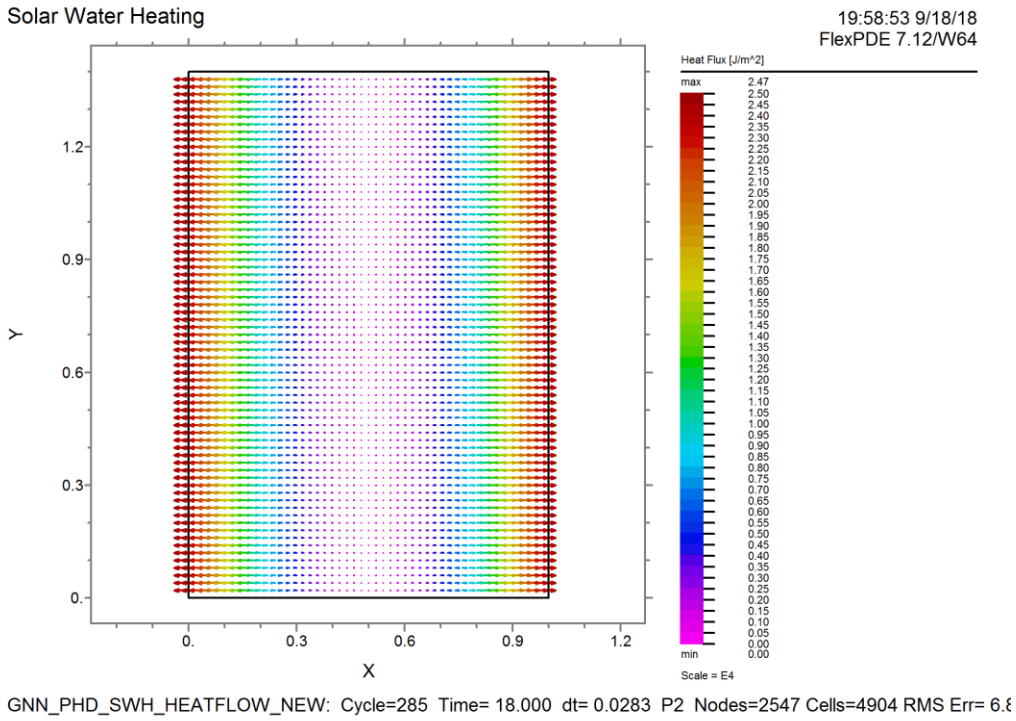

Fig. 4.6 Heat flux pattern on the SCONOR

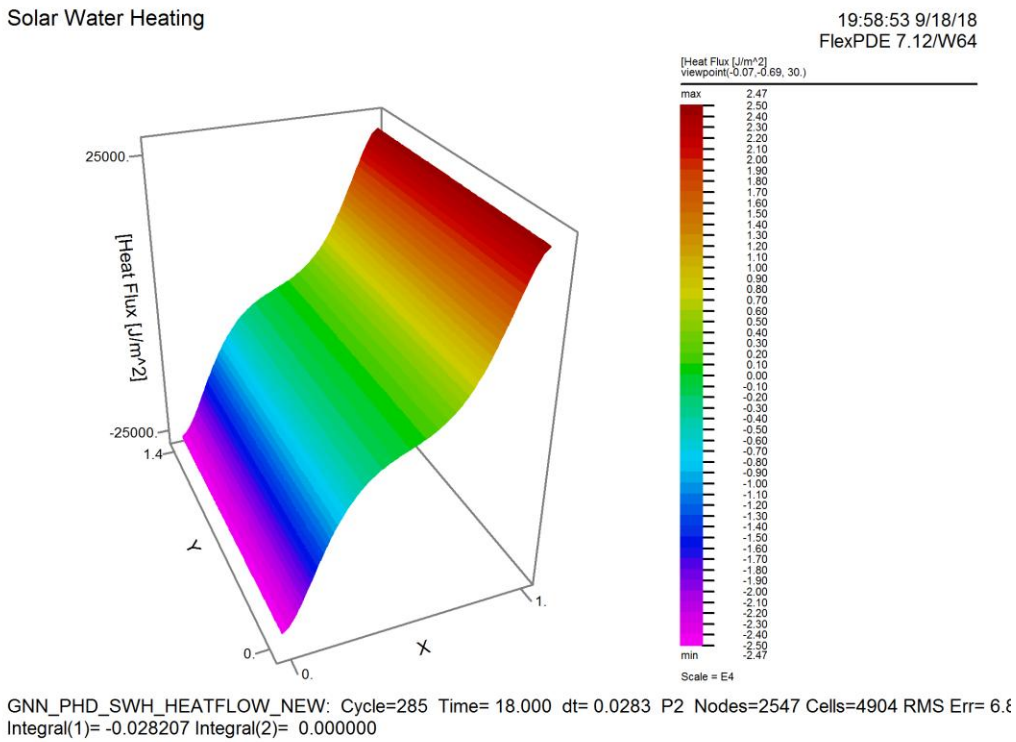

Fig 4.7 Surface plot of heat flux on the SCONOR

4.1.2 Performance predictions using Owerri climatic data

4.1.2.1 Solar water heating in the SCONOR

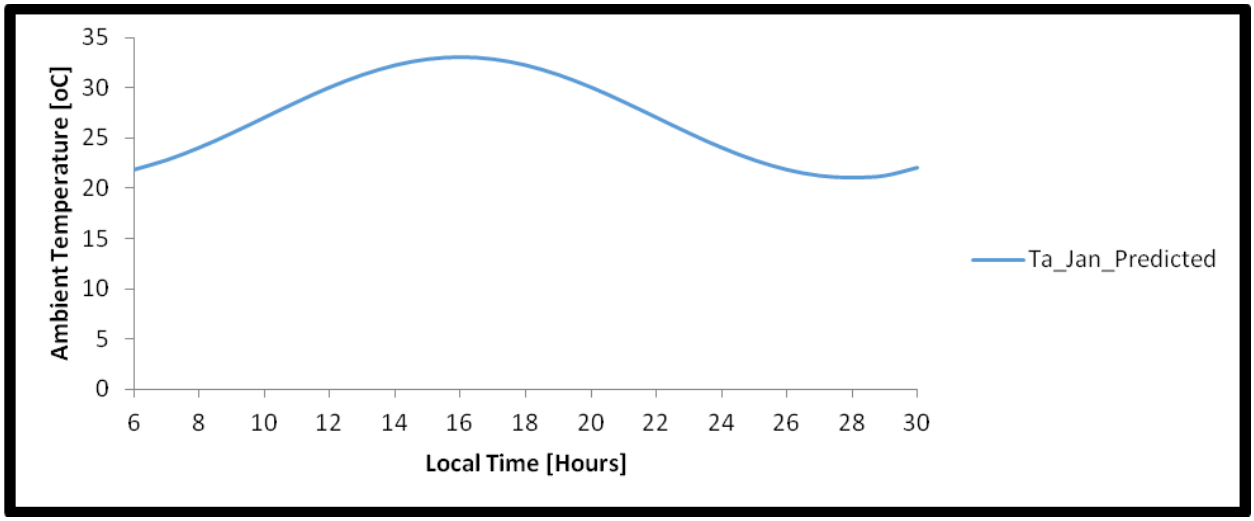

Fig. 4.8 Predicted ambient temperature in Owerri in January 2017.

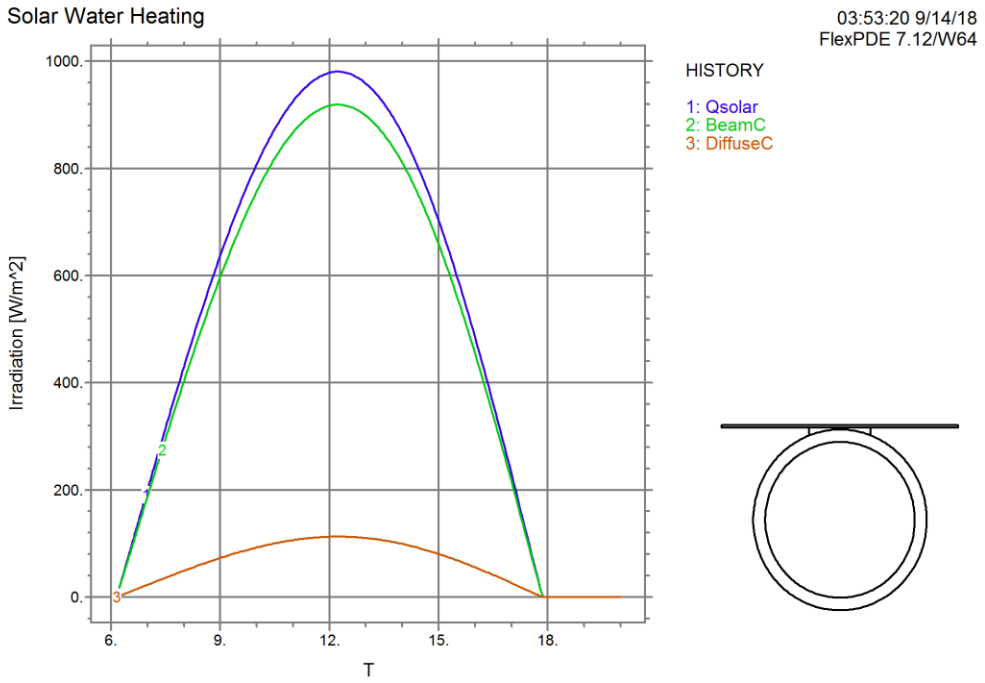

Fig. 4.9 Predicted Beam, diffuse and total irradiation in January 2017.

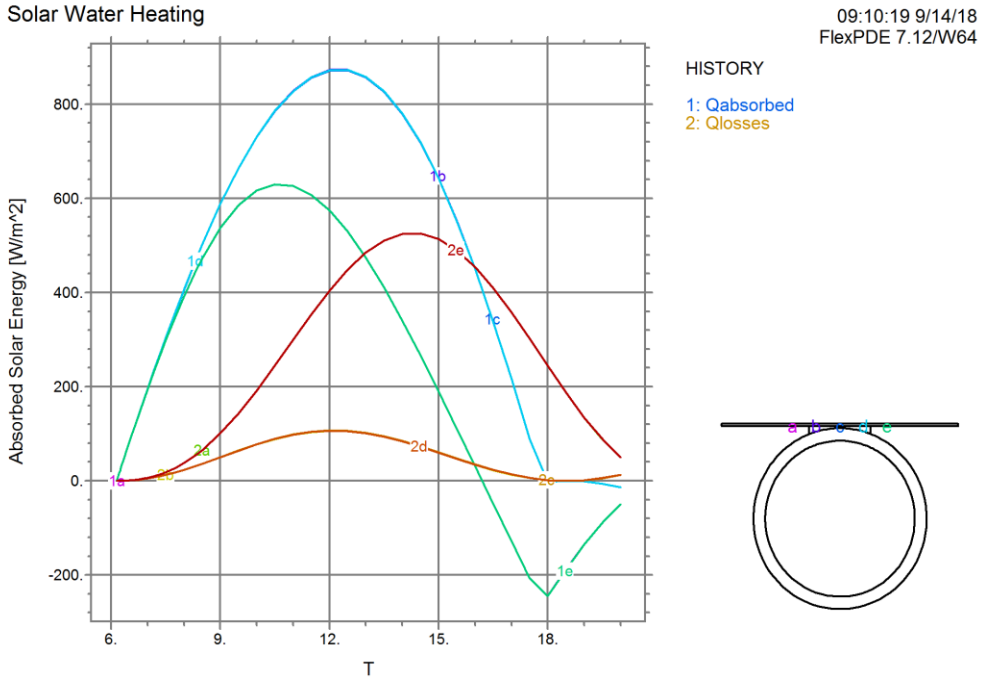

Fig. 4.10 Predicted thermal energy absorption and losses in January 2017.

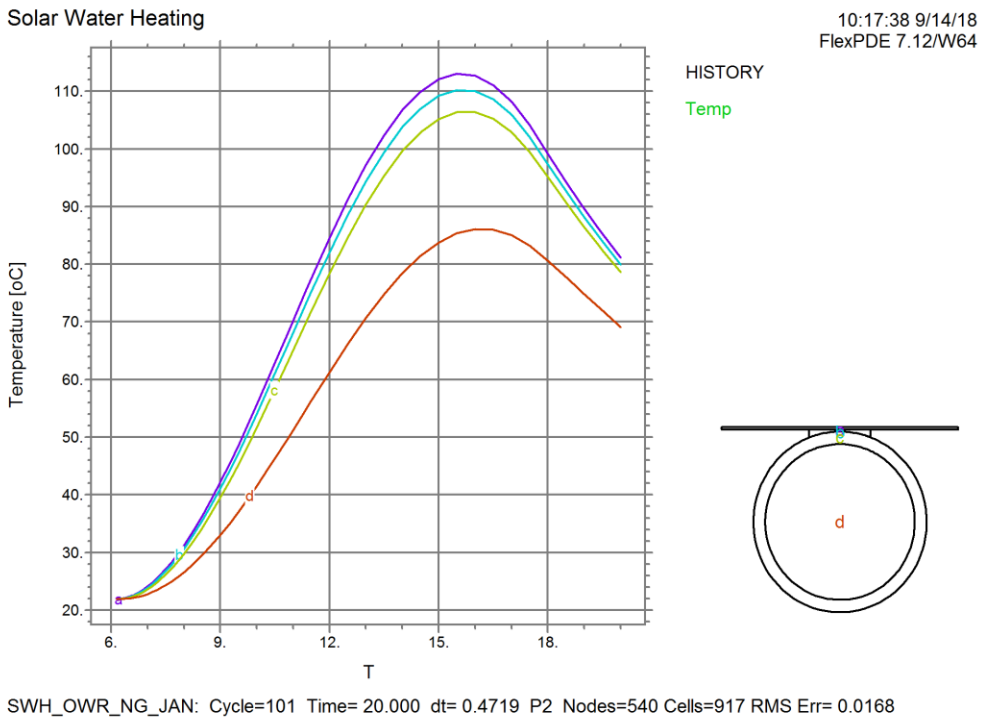

Fig. 4.11 Predicted SCONOR, bond, tube and water temperatures in January.

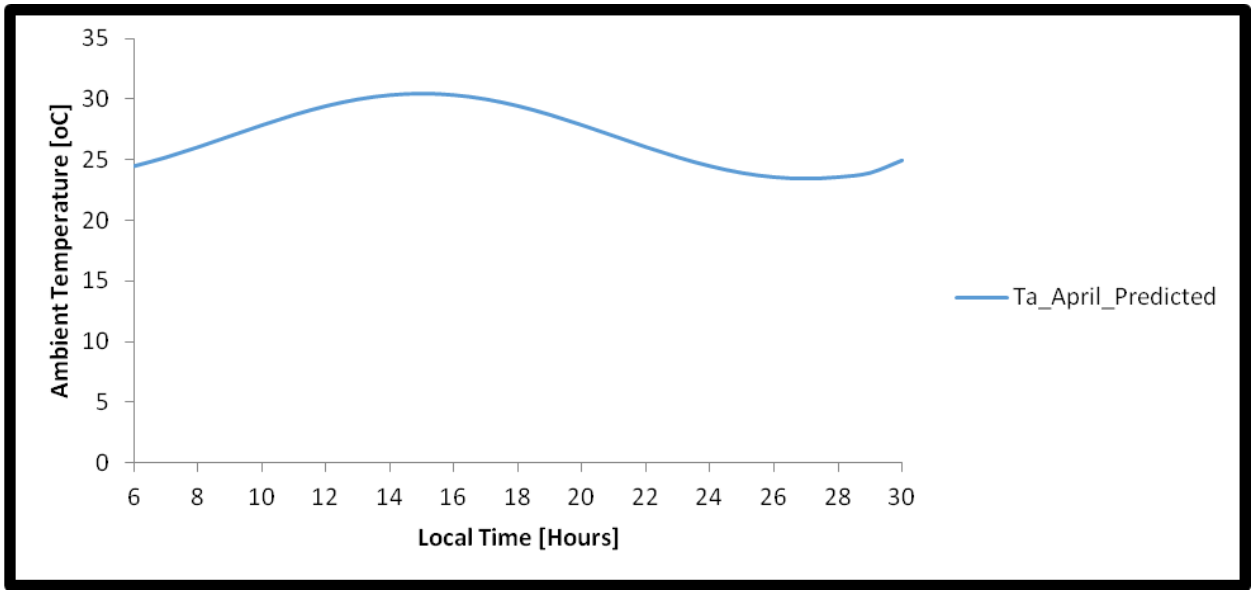

Fig 4.12 Predicted ambient Temperature in Owerri in April 2017

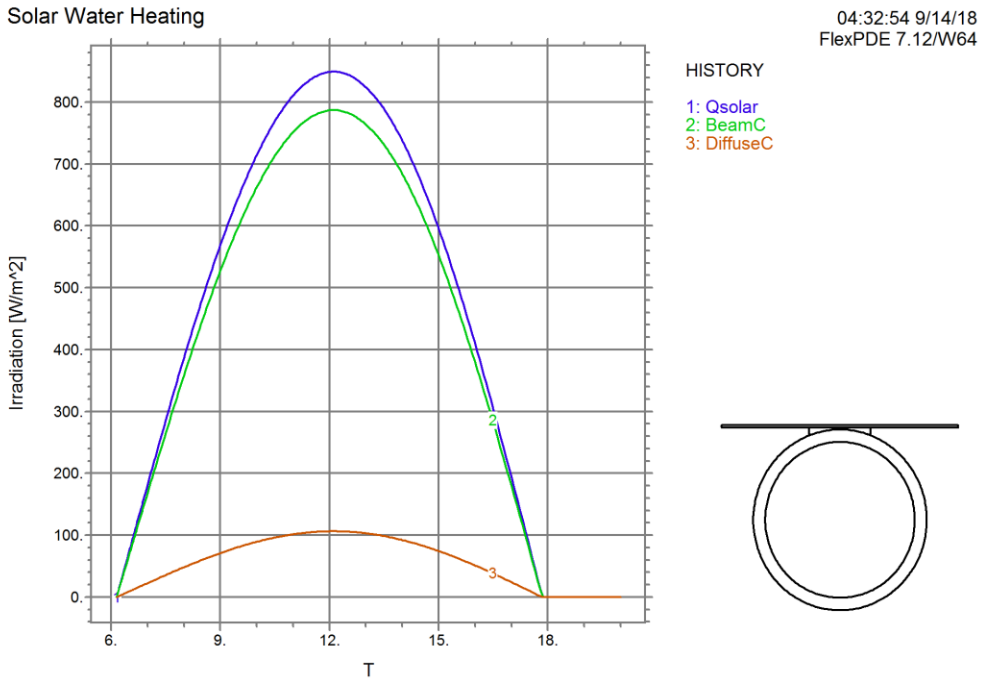

Fig 4.13 Predicted beam, diffuse and total irradiation in April.

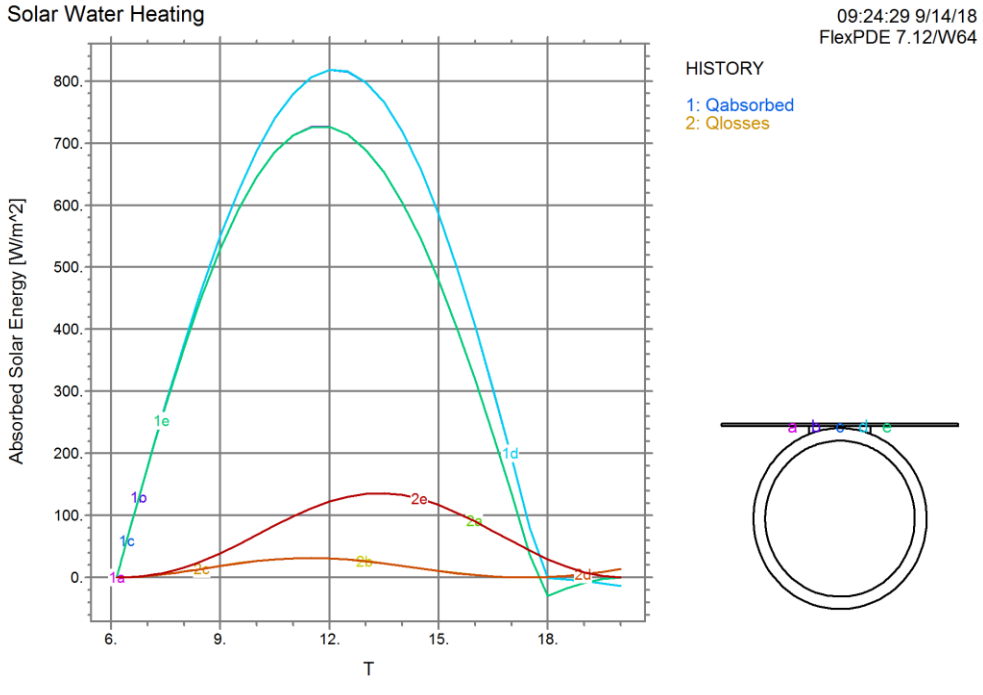

Fig. 4.14 Predicted thermal energy absorption and losses in April 2017

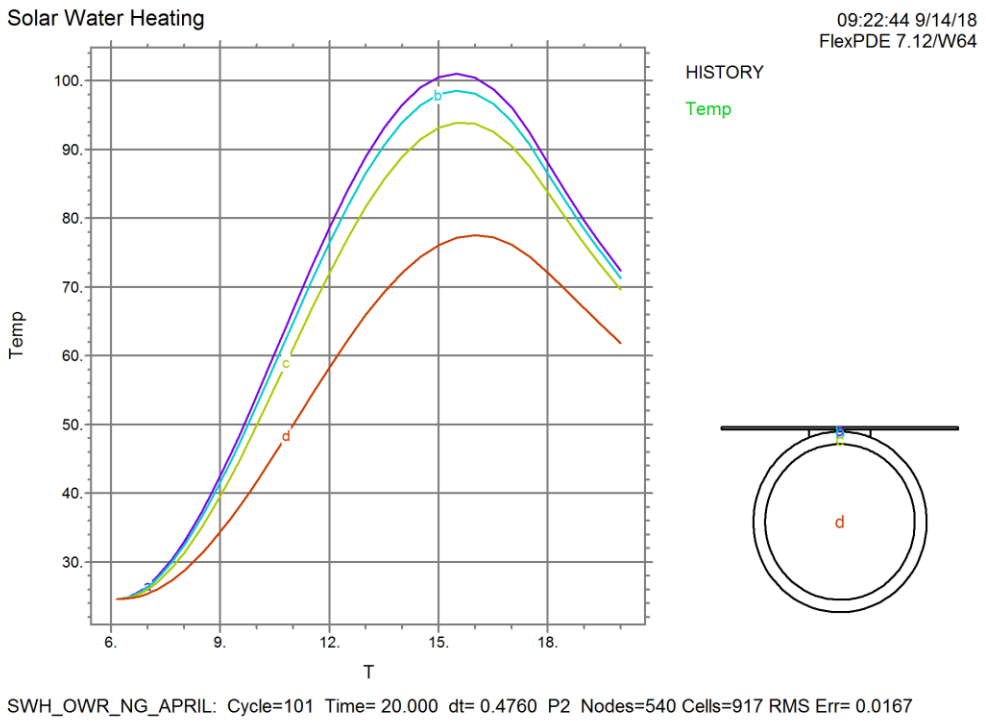

Fig. 4.15 Predicted SCONOR, bond, tube and water temperatures in April

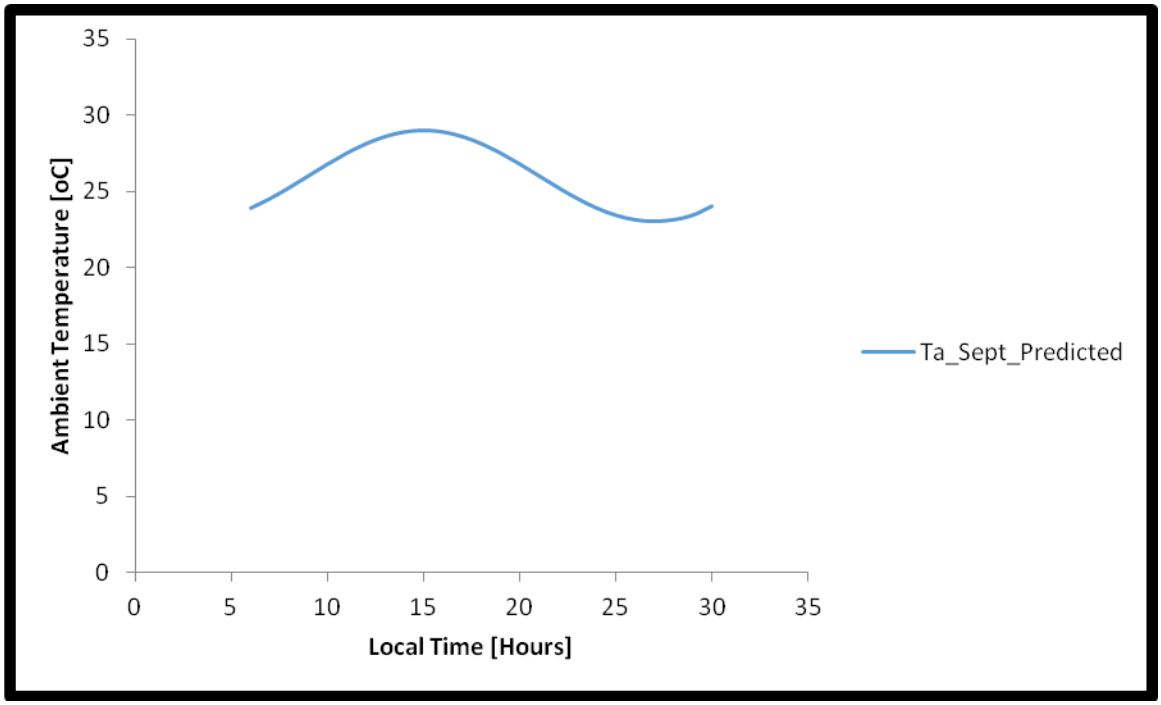

Fig. 4.16 Predcited ambient Temperature in Owerri in September 2017

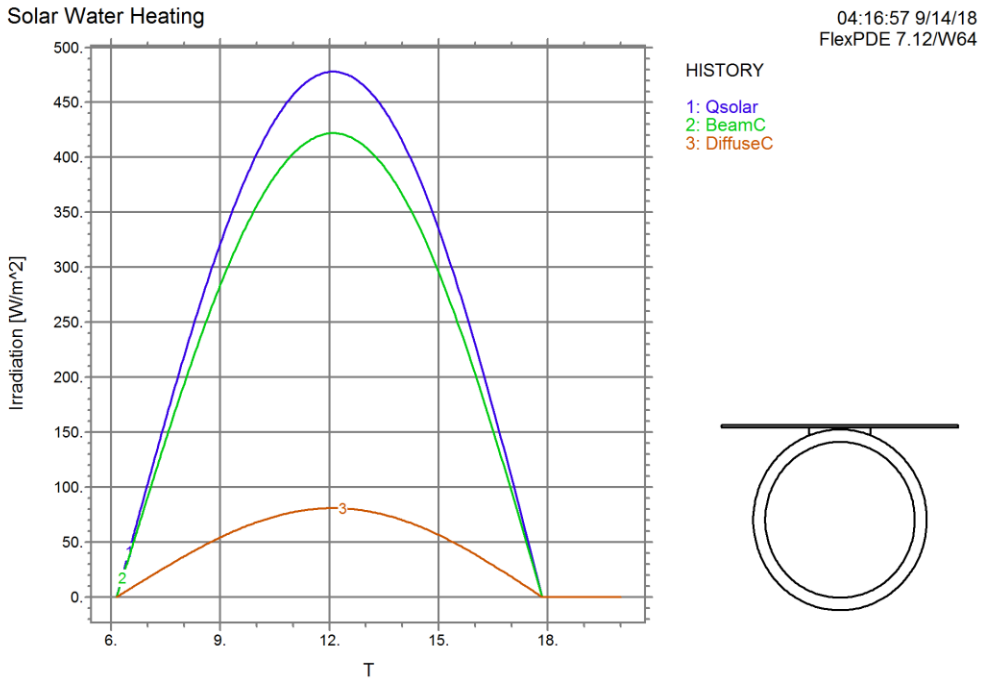

Fig 4.17 Predicted beam, diffuse and total solar irradiation in September 2017

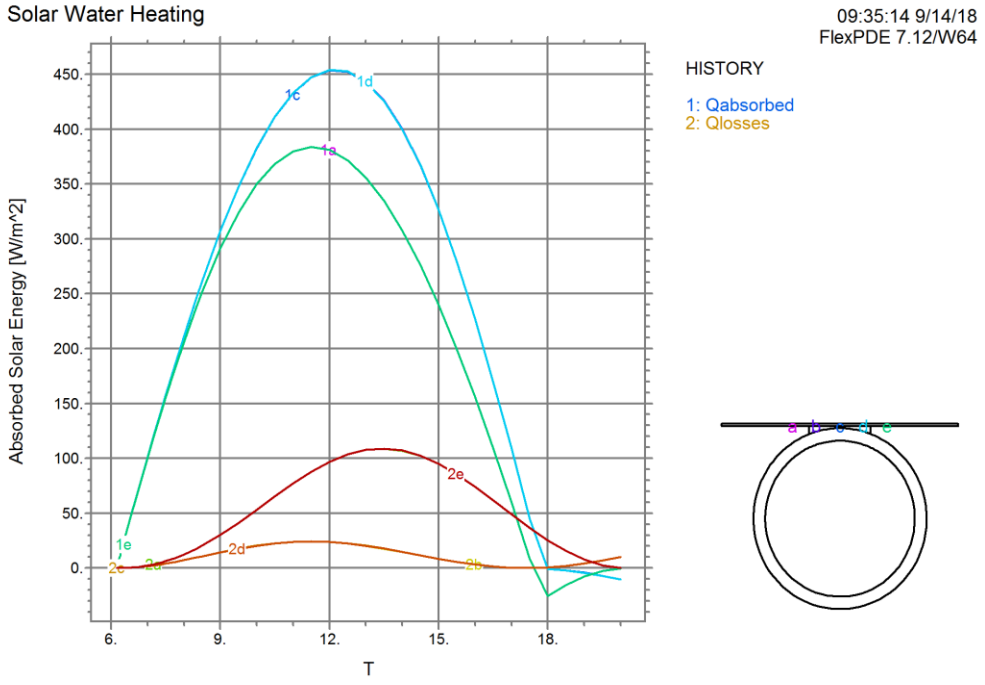

Fig. 4.18 Predicted thermal energy absorption and losses in September 2017

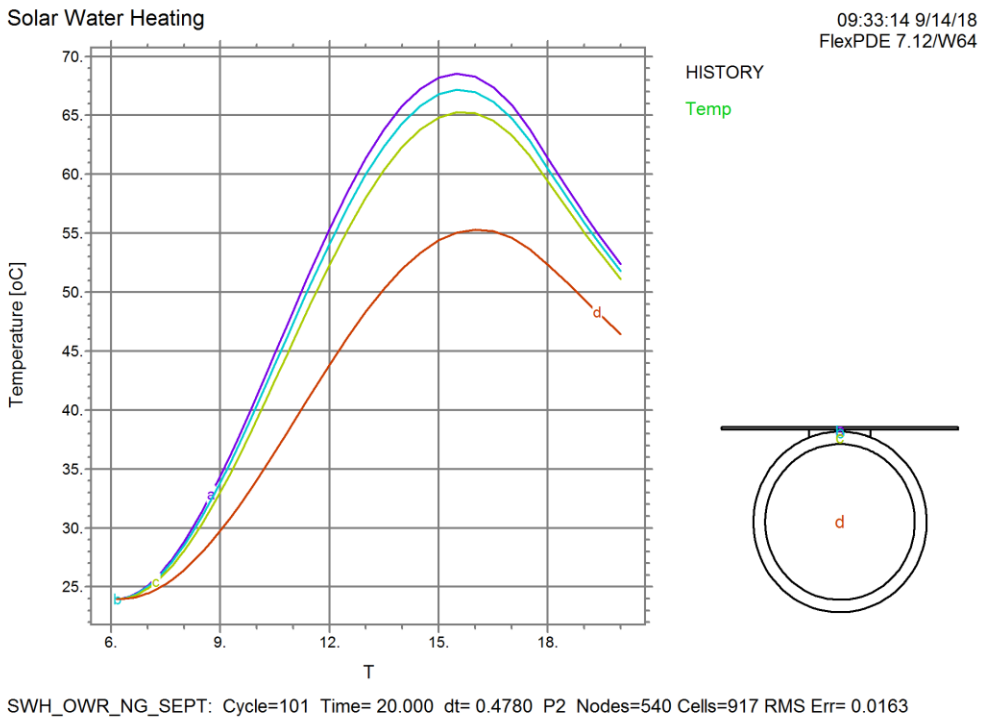

Fig. 4.19 Predicted SCONOR, bond, tube and water temperatures in September 2017

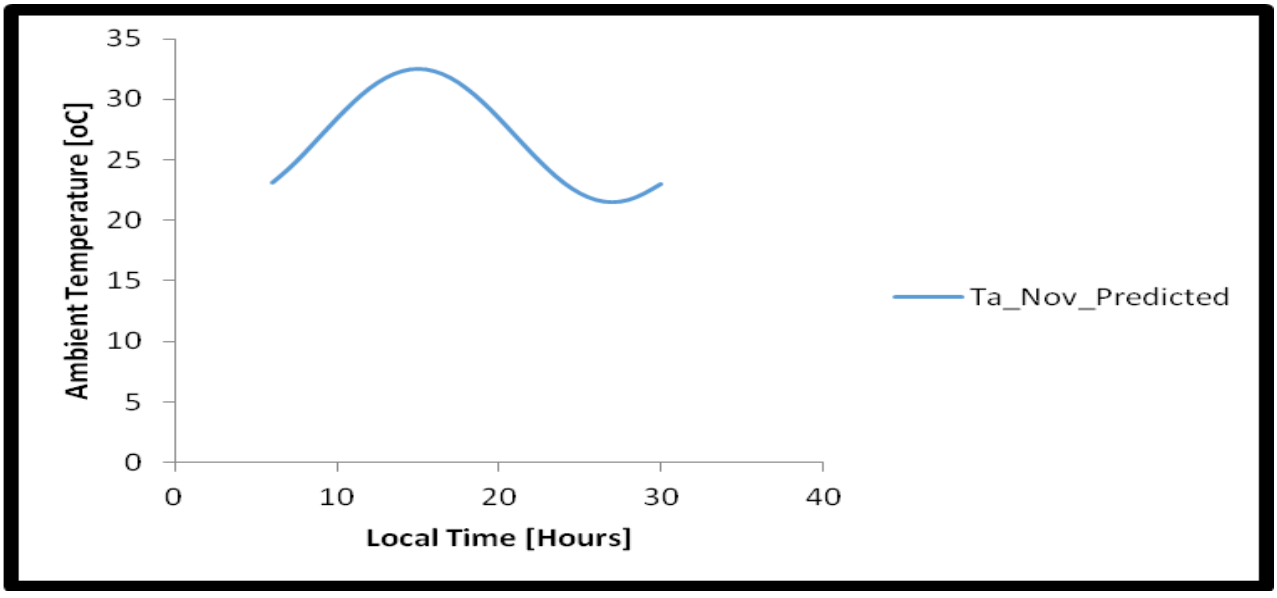

Fig. 4.20 Predicted ambient Temperature in Owerri in November 2017

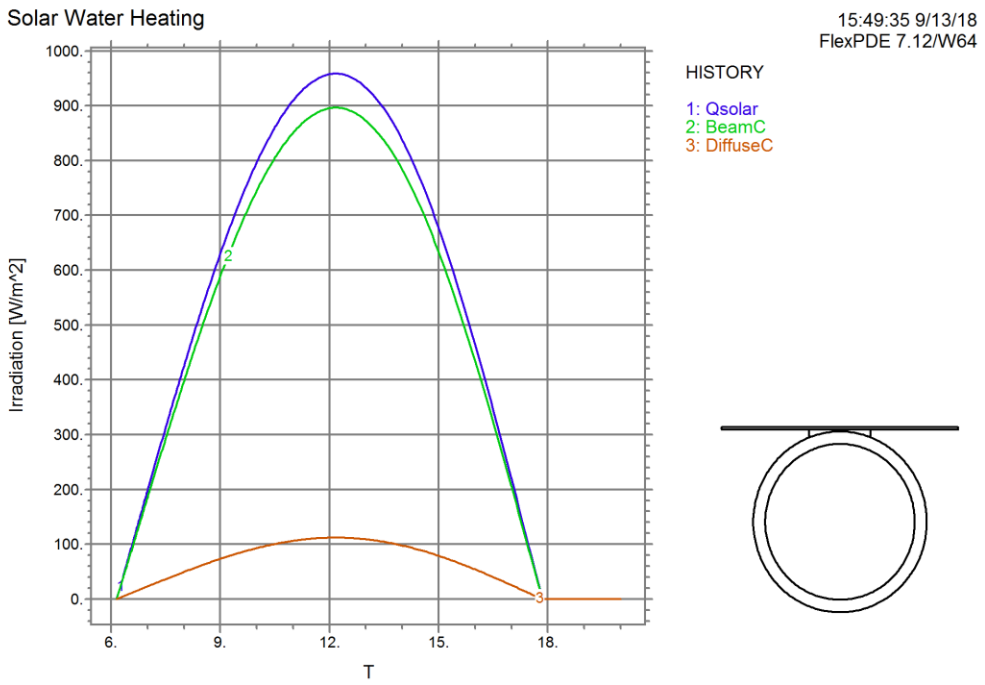

Fig. 4.21 Predicted beam, diffuse and total solar irradiation in November 2017

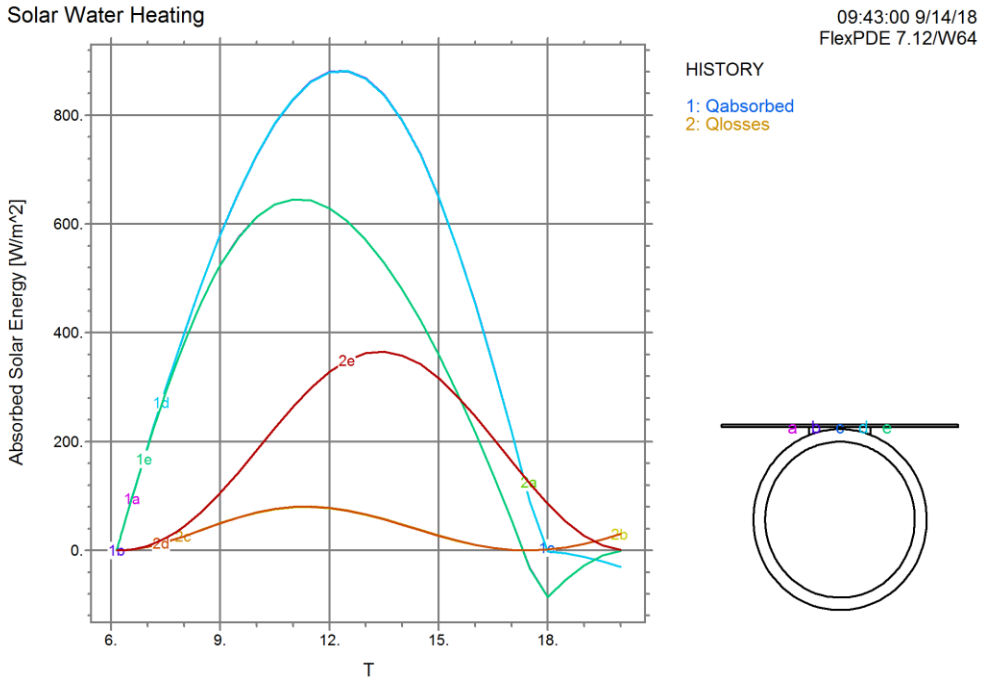

Fig. 4.22 Predicted thermal energy absorption and losses in November 2017

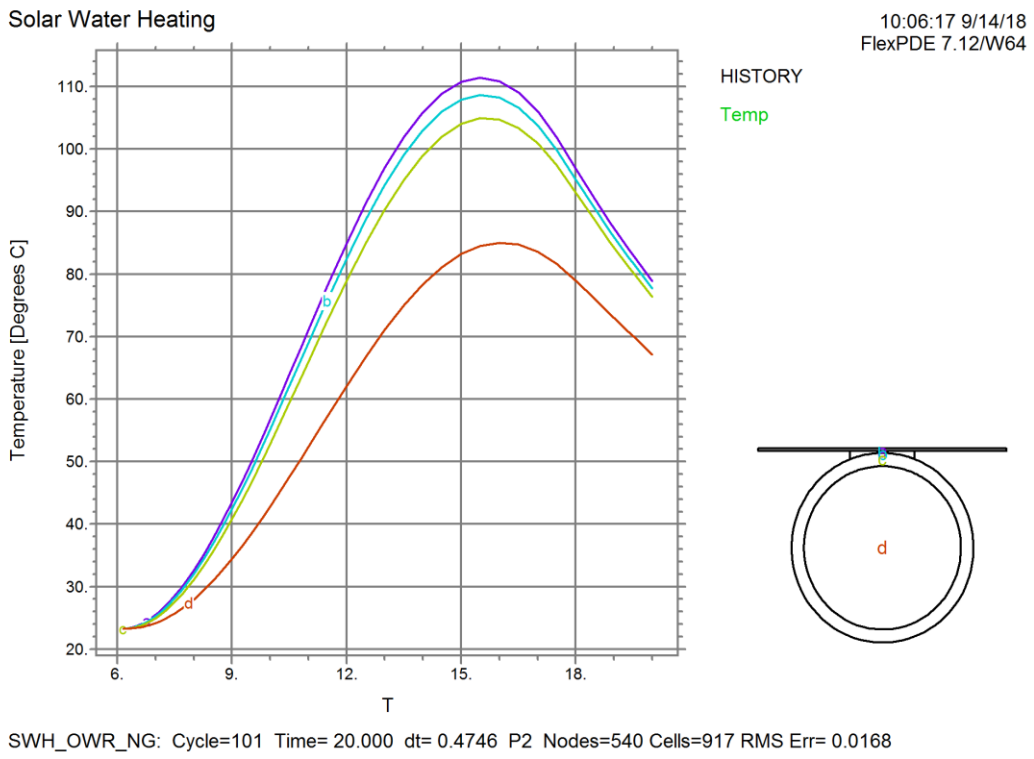

Fig. 4.23 Predicted SCONOR, bond and tube, and water Temperatures in November 2017

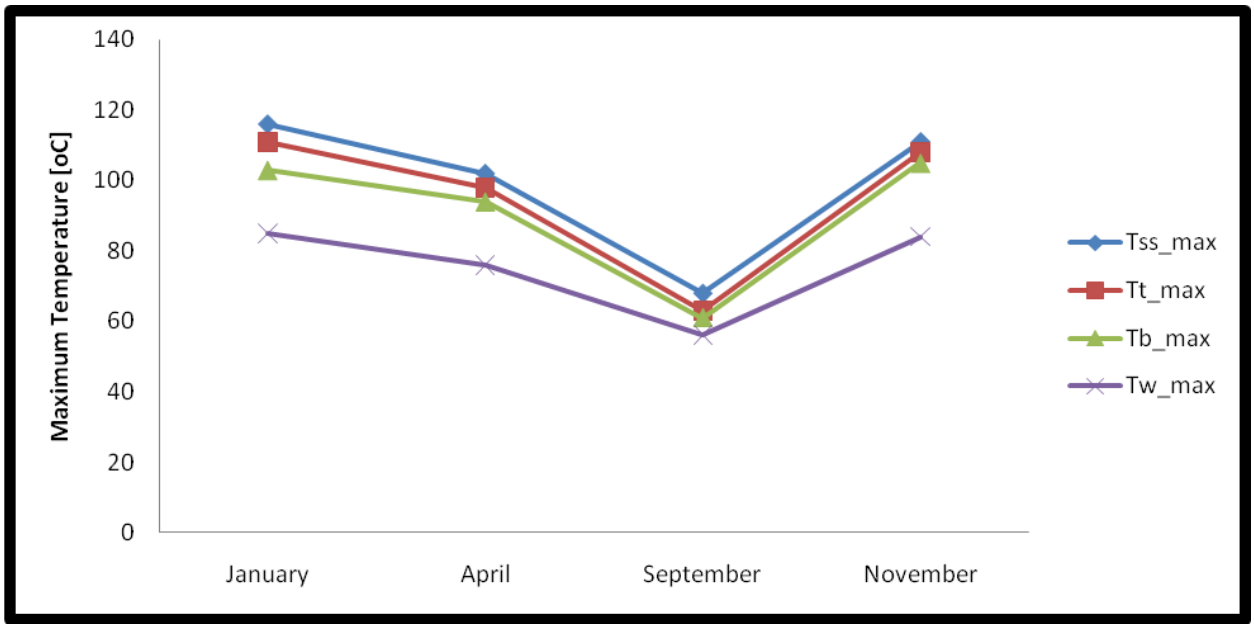

Fig. 4.24 Maximum temperatures of SCONOR plate , tube and bond, and water versus months of the year studied for the diurnal heating phase

4.1.2.2 SCONOR cool-down phase

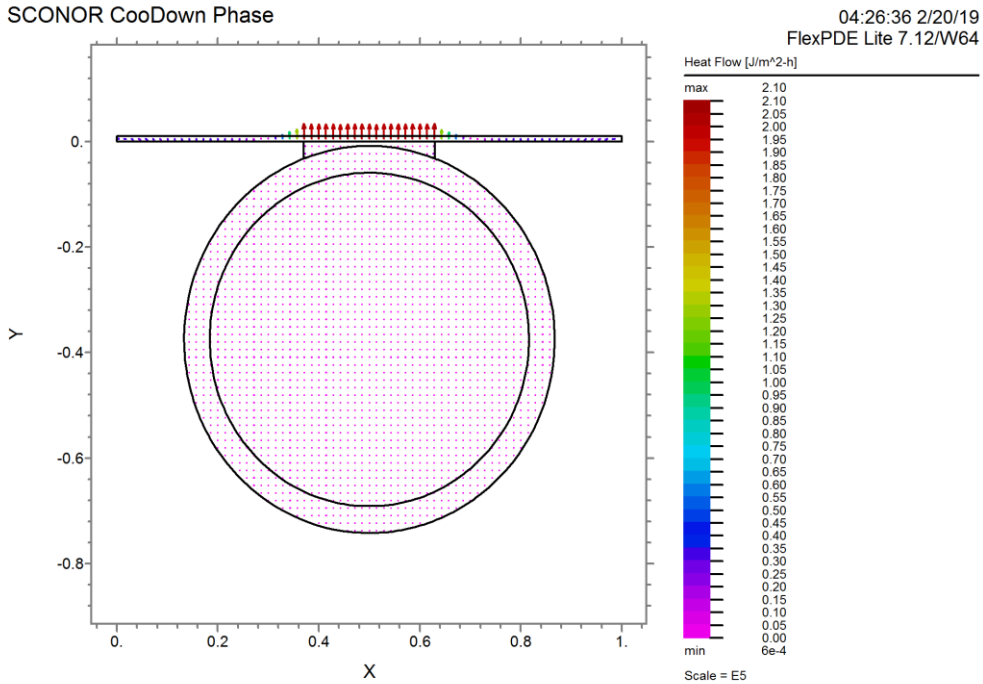

Fig. 4.25 Vector plot of heat flow during cooldown period in January

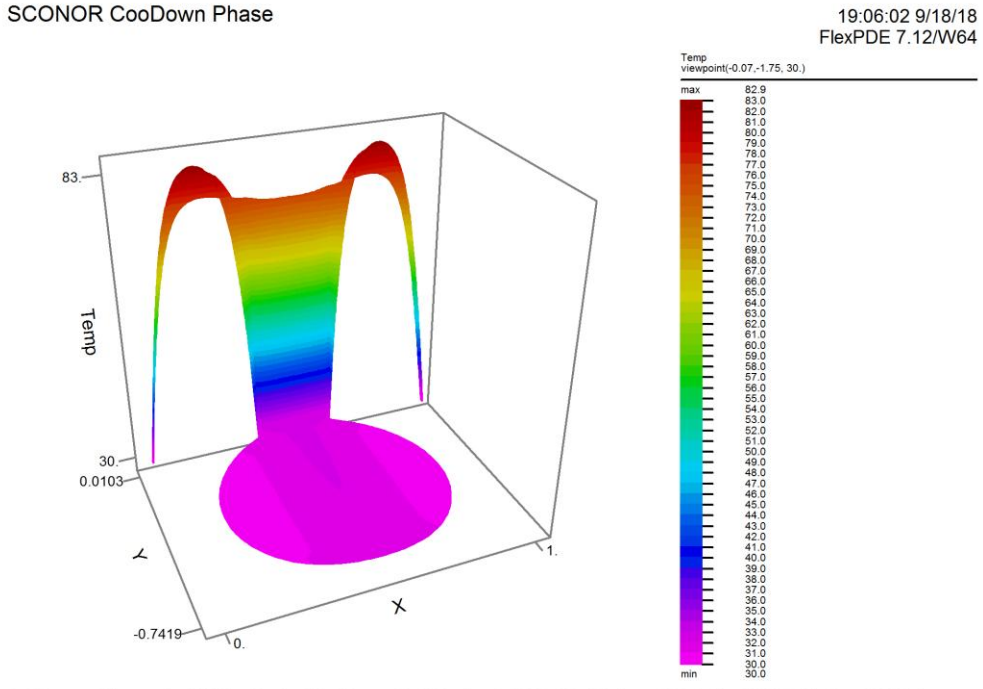

Fig. 4.26 Surface plot of Temperature during cooldown period in January

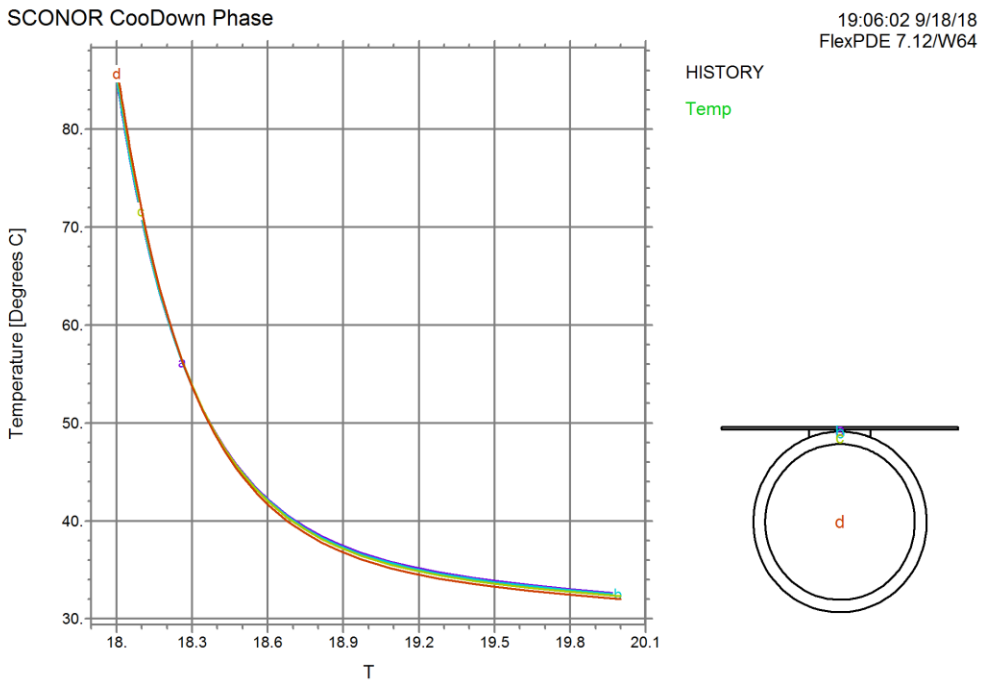

Fig. 4.27 Temperature variation with time during cooldown period in January

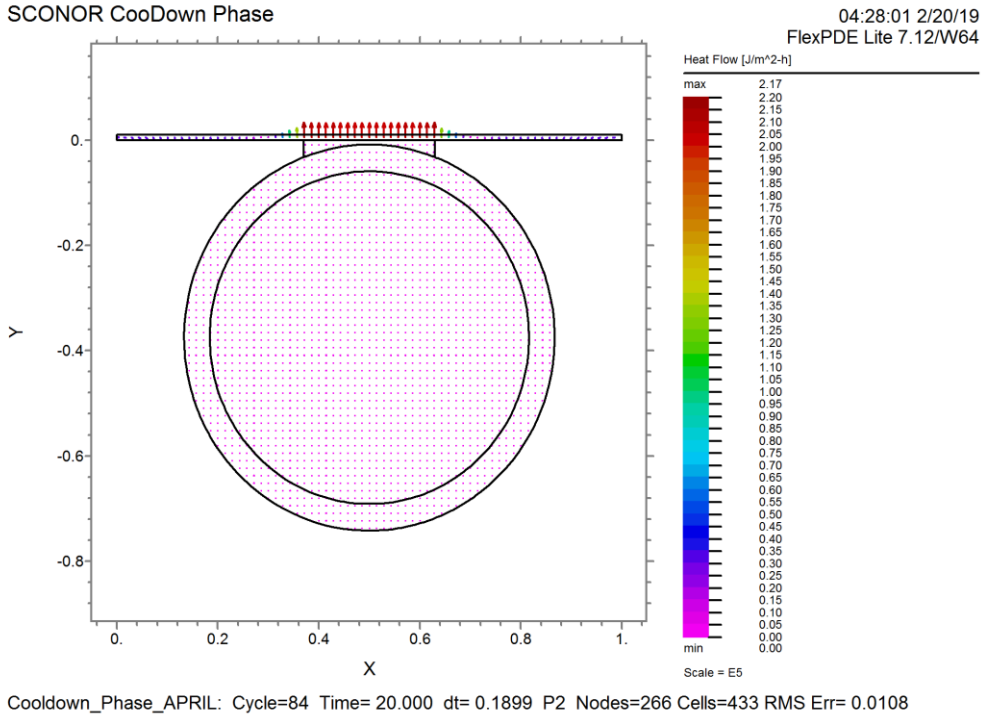

Fig. 4.28 Vector plot of heat flow during cooldown period in April

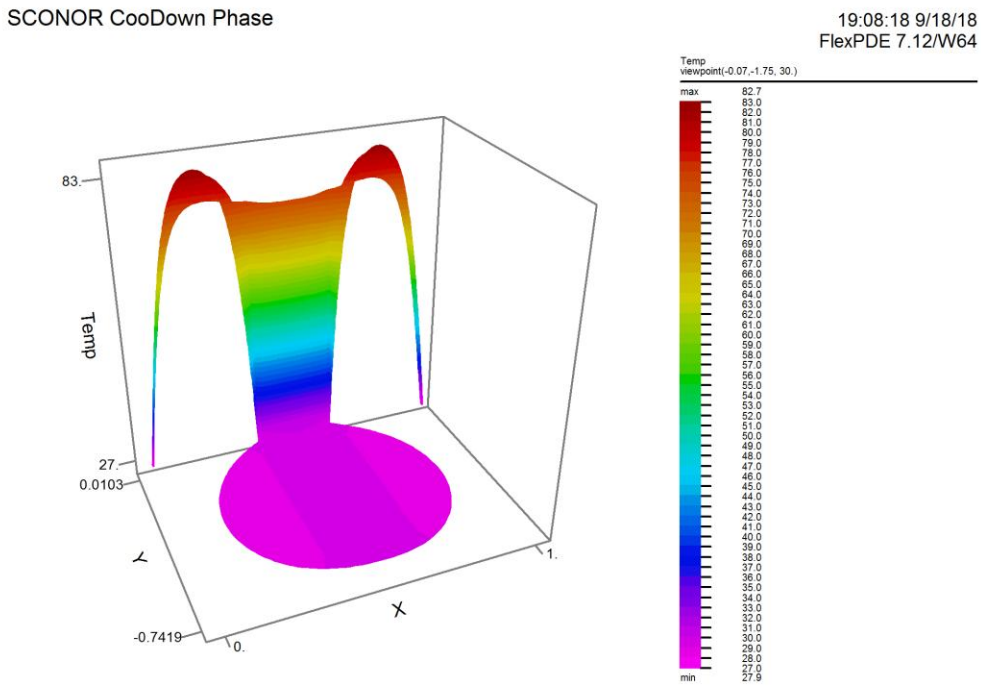

Fig. 4.29 Surface plot of Temperature during cooldown period in April

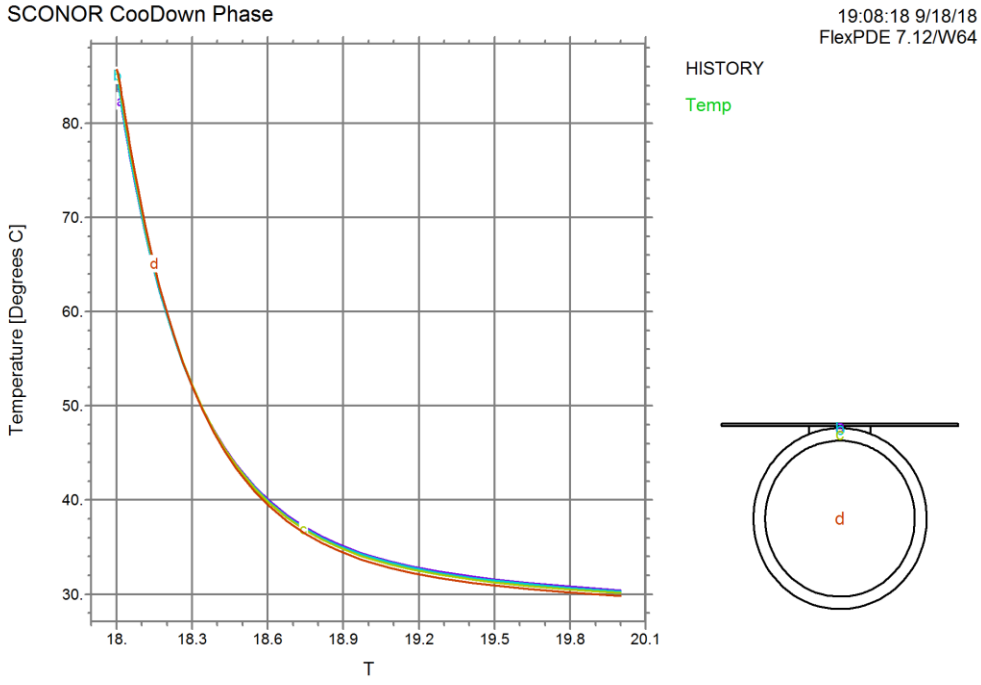

Fig. 4.30 Temperature variation with time during cooldown period in April

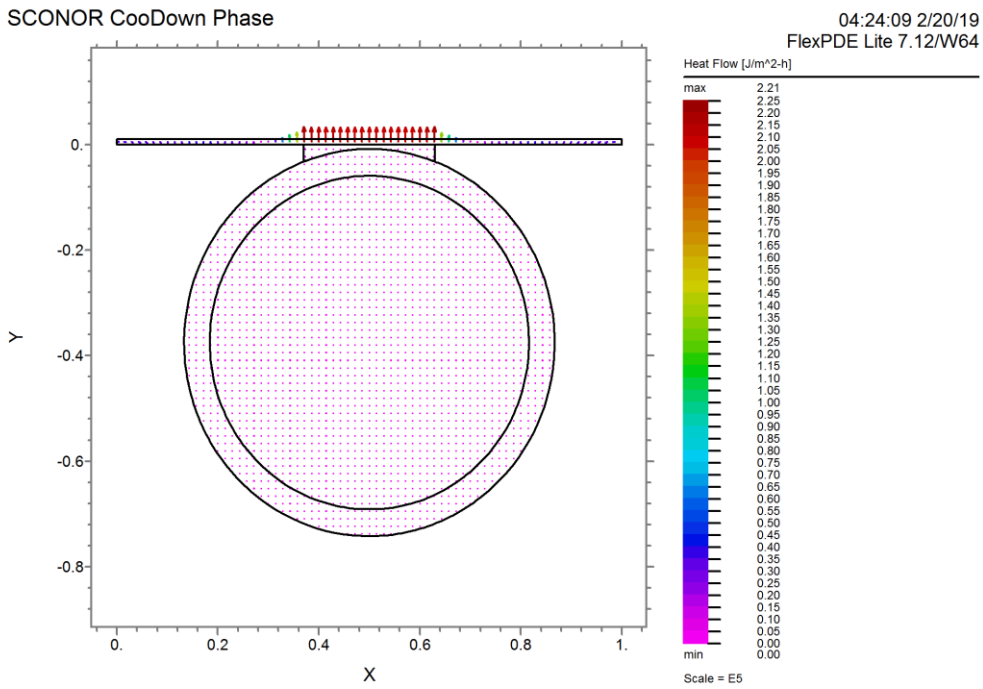

Fig. 4.31 Vector plot of heat flow during cooldown period in September

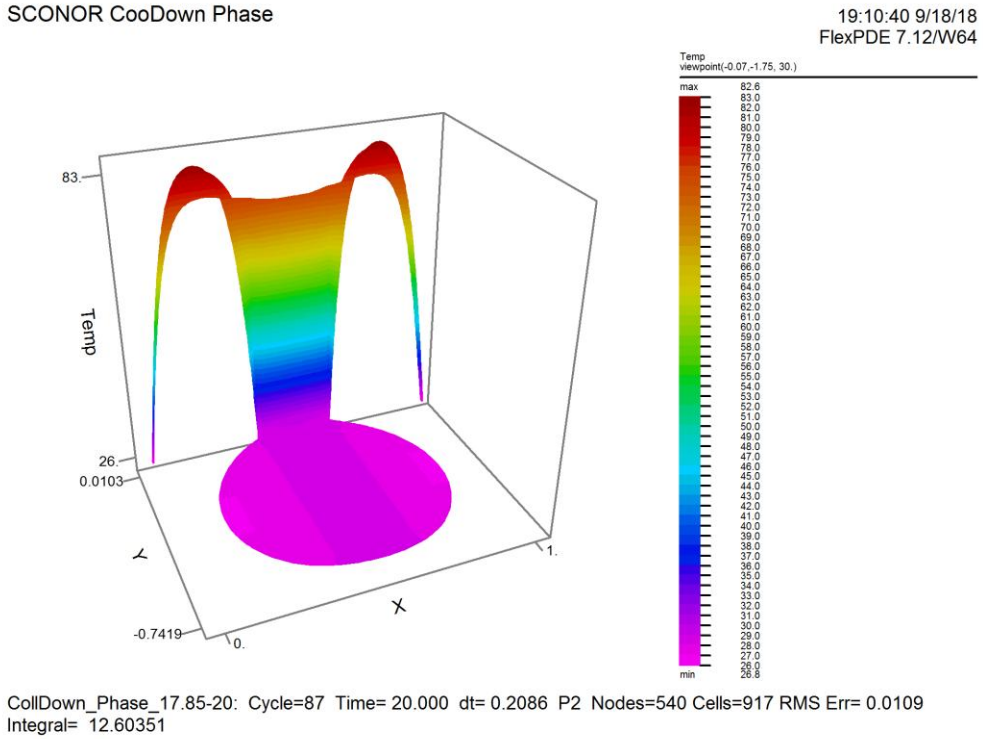

Fig. 4.32 Surface plot ot Temperature during cooldown period in September

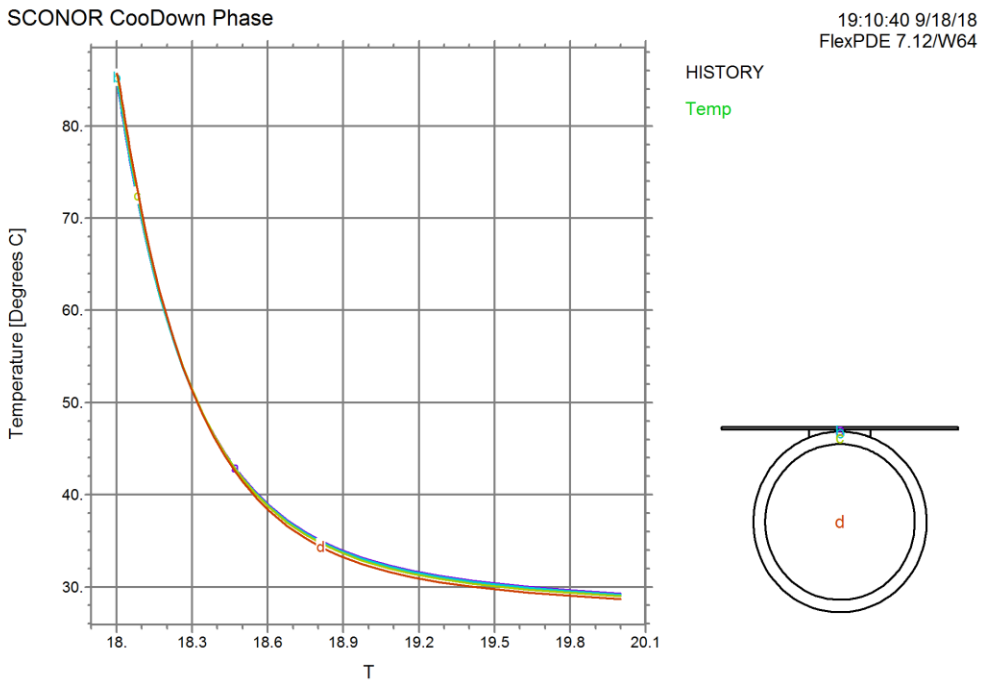

Fig. 4.33 Temperature variation with time during cooldown period in September

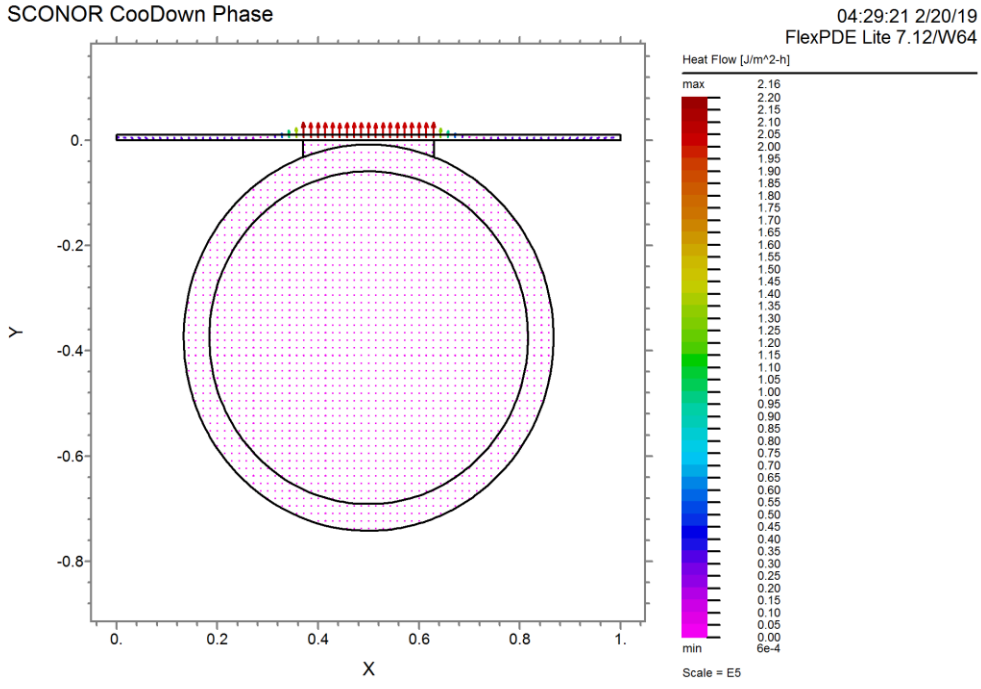

Fig. 4.34 Temperature vector during cooldown period in November

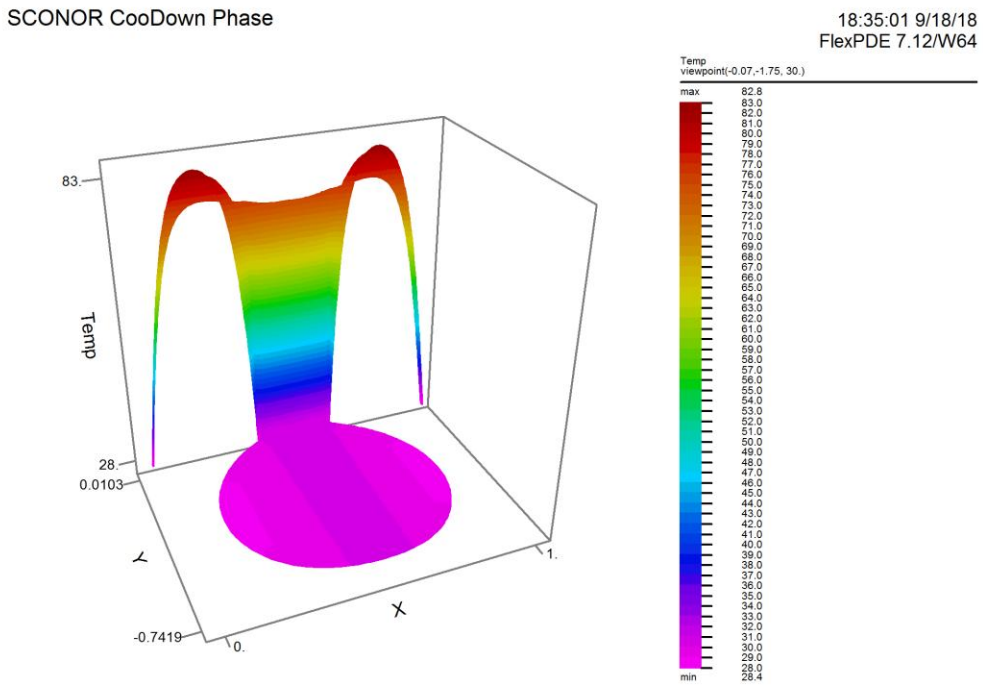

Fig. 4.35 Surface plot of Temperature during cooldown period in November

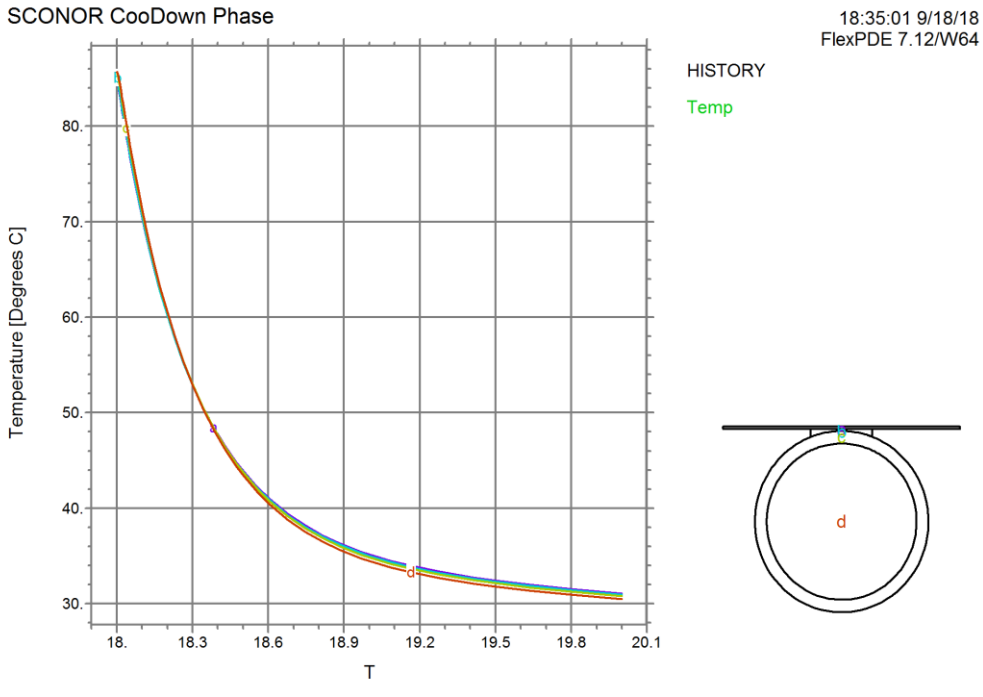

Fig. 4.36 Temperature variation with time during cooldown period in November

4.1.2.3 Nocturnal water cooling in the SCONOR

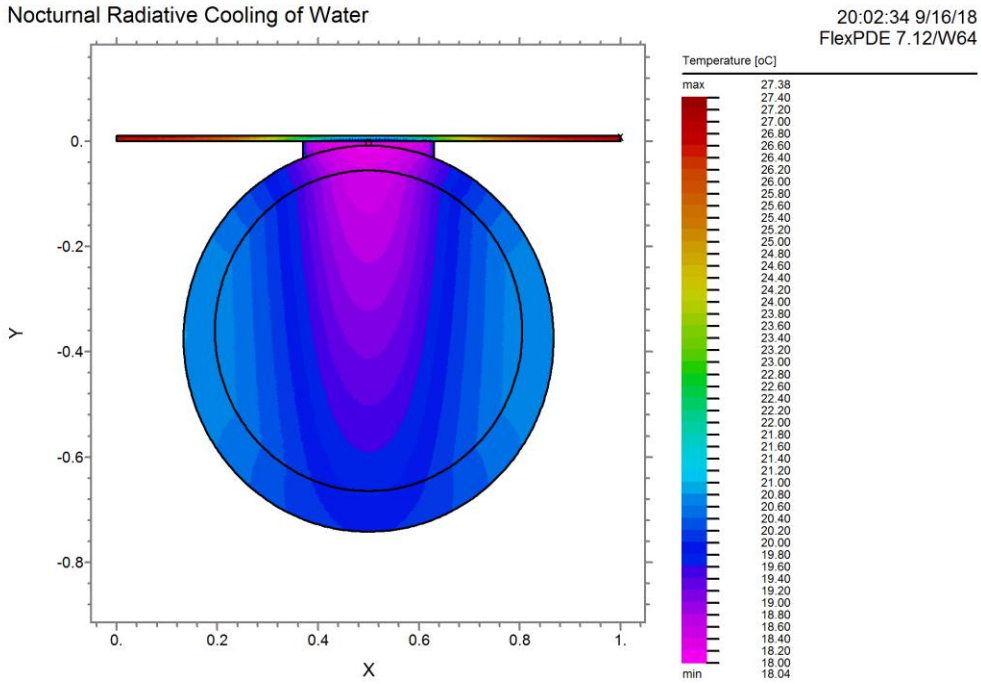

NWC_OWR_JAN: Cycle=580 Time= 30.000 dt= 0.0826 P3 Nodes=1877 Cells=3517 RMS Err= 3.8e-4
Integral= 8.744127

Fig. 4.37 Temperature contour during nocturnal water cooling in January

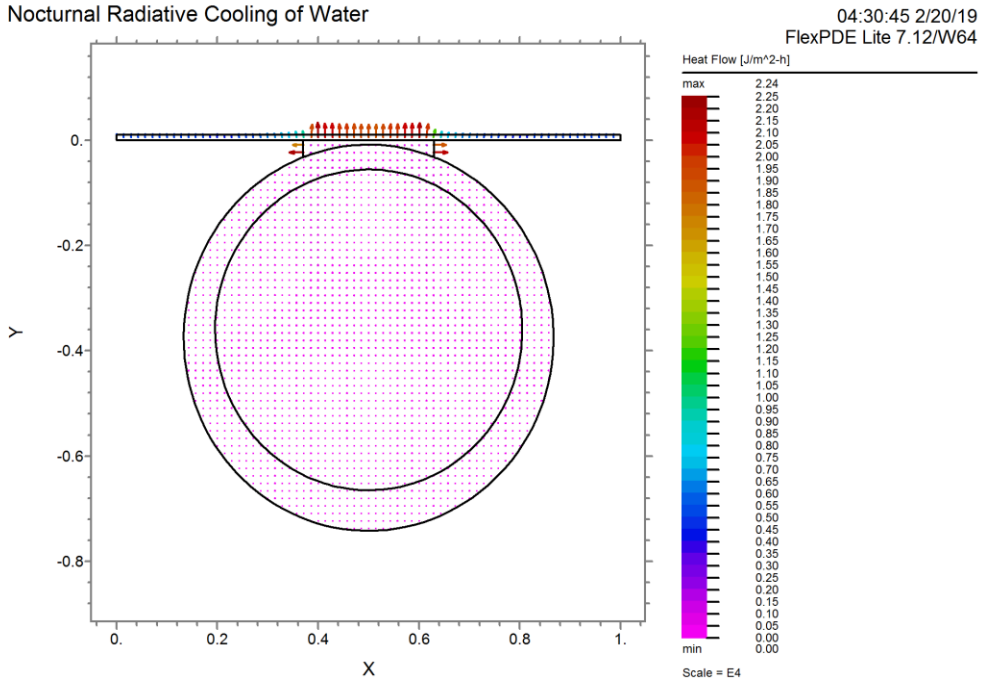

NWC_OWR_JAN19: Cycle=567 Time= 30.000 dt= 0.0819 P2 Nodes=261 Cells=423 RMS Err= 0.0016

Fig. 4.38 Vector plot of heat flow during nocturnal water cooling in January

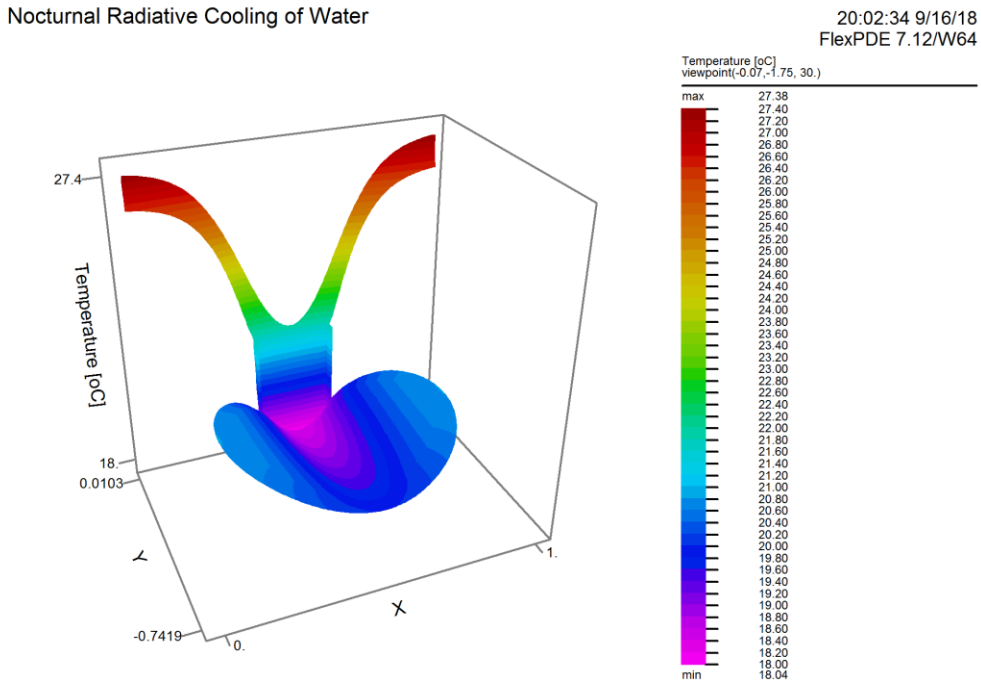

Fig. 4.39 Surface plot of Temperature during nocturnal water cooling in January

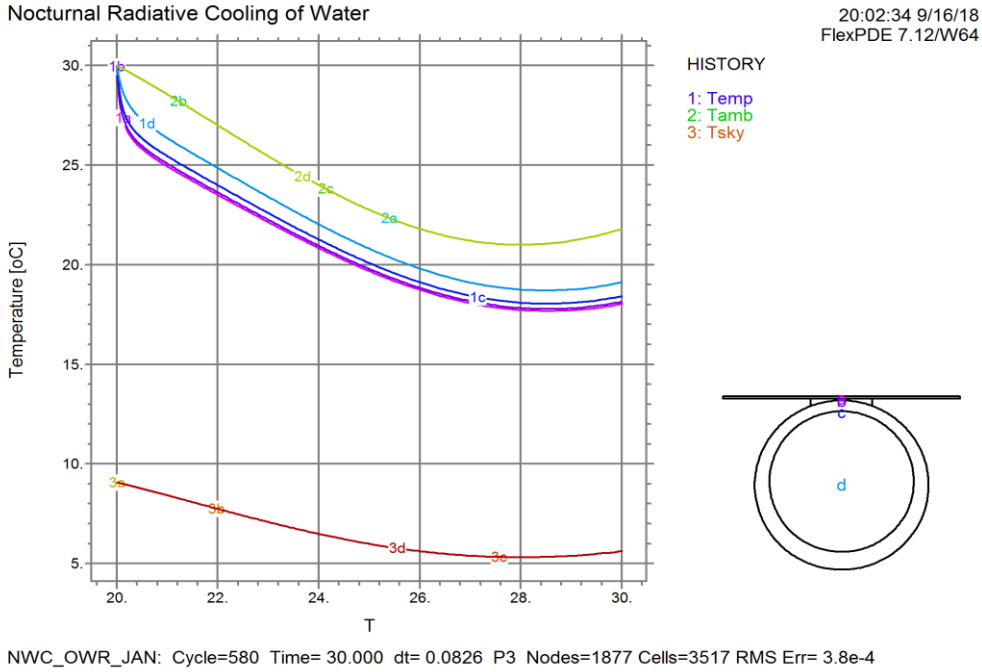

Fig . 4.40 Predicted SCONOR, bond, tube, water, ambient and sky temperatures during nocturnal water cooling in January

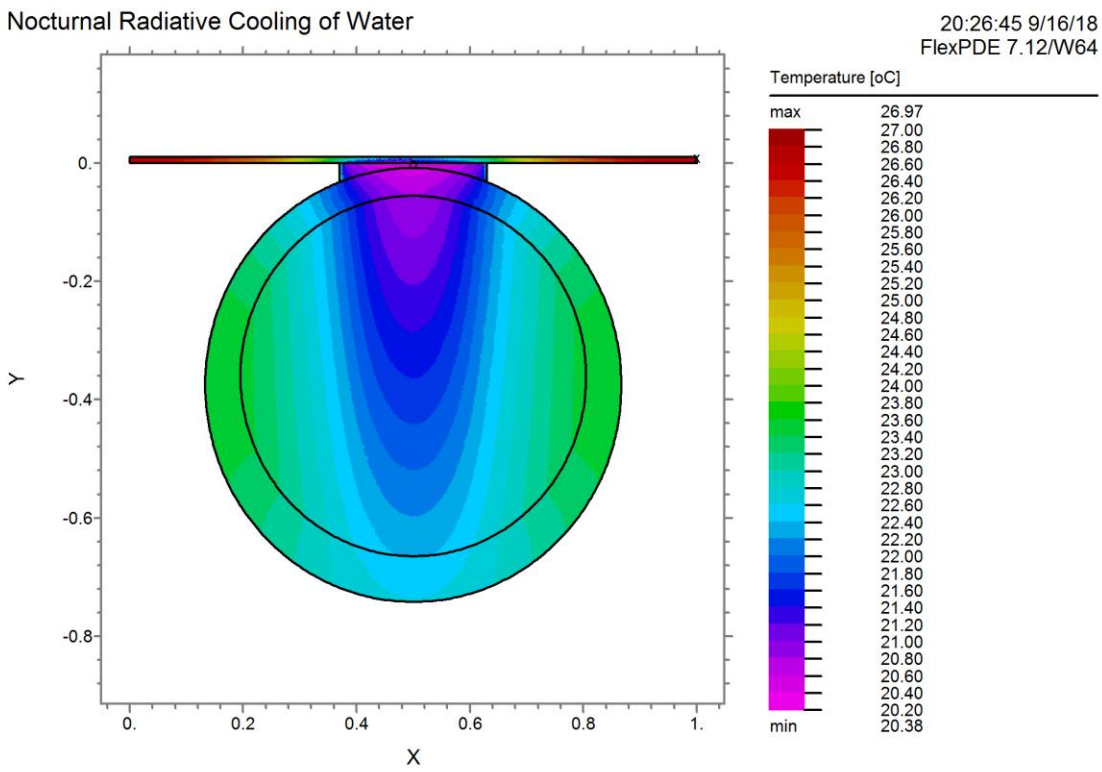

Fig. 4.41 Temperature contour during nocturnal water cooling in April

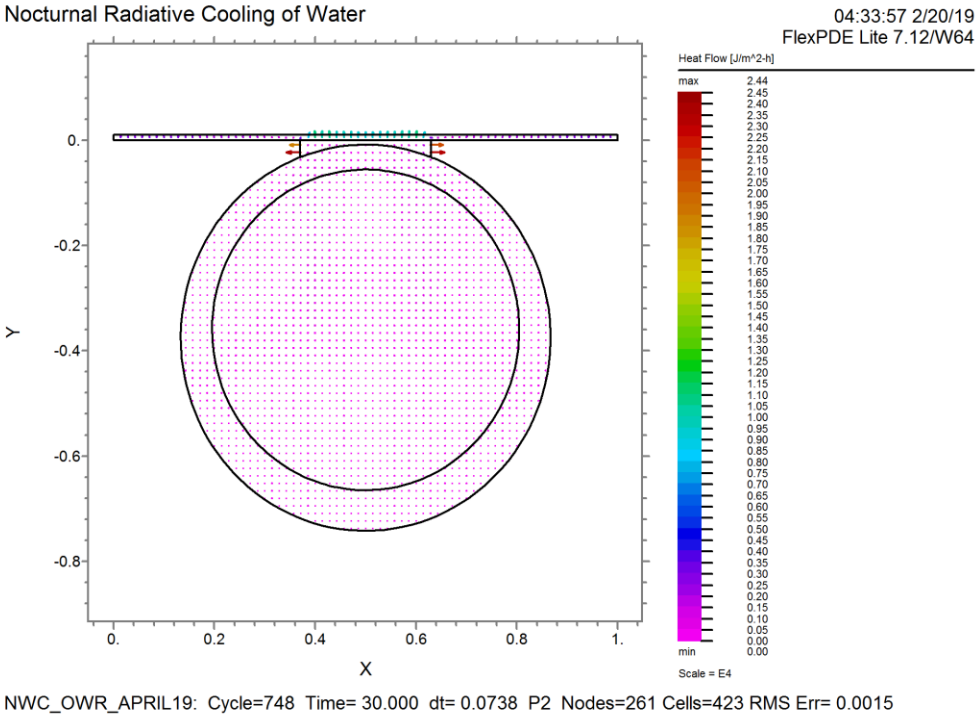

Fig. 4.42 Vector plot of heat flow during nocturnal water cooling in April

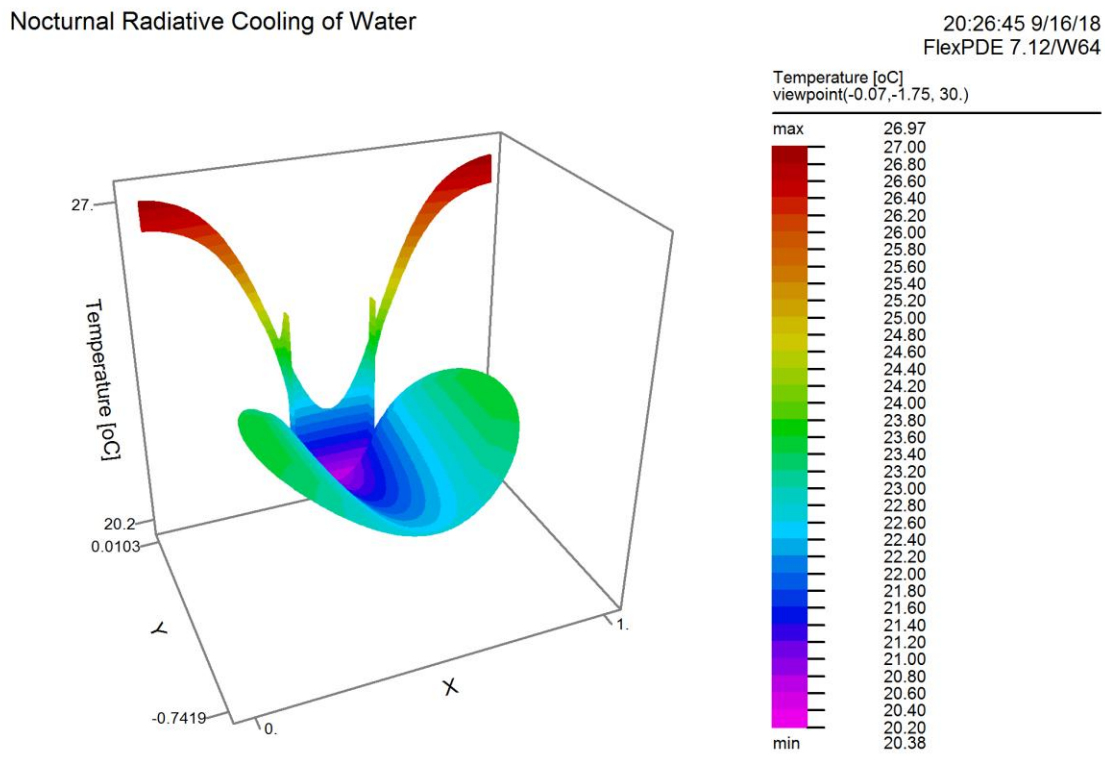

Fig. 4.43 Surface plot of temperature during nocturnal water cooling in April

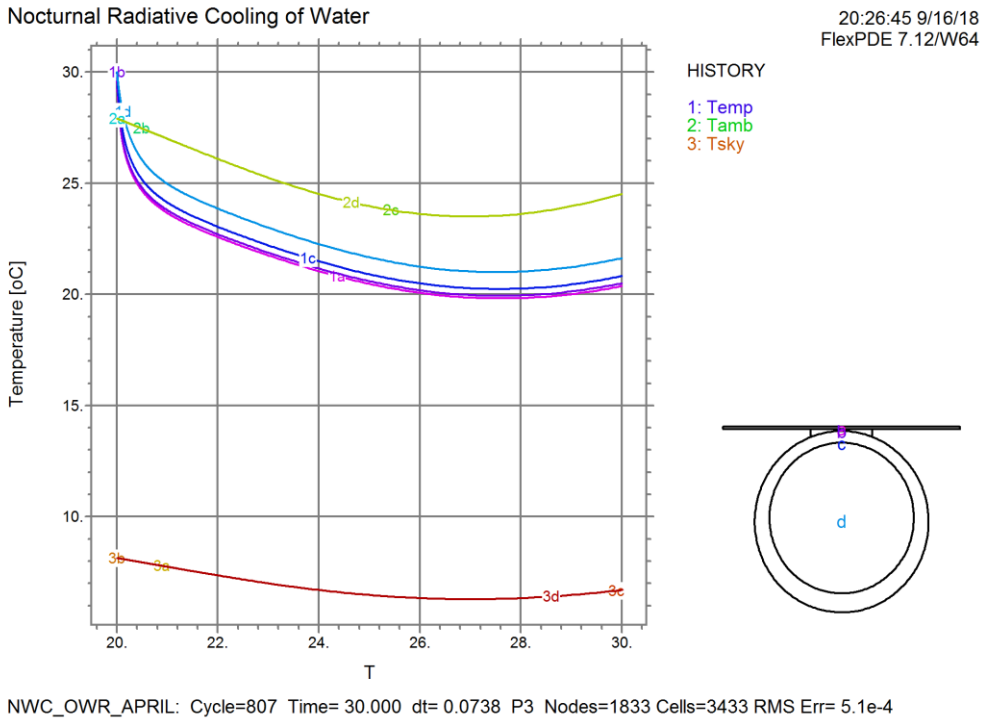

Fig. 4.44 Predicted SCONOR, bond, tube, water, ambient and sky temperatures during nocturnal water cooling in April

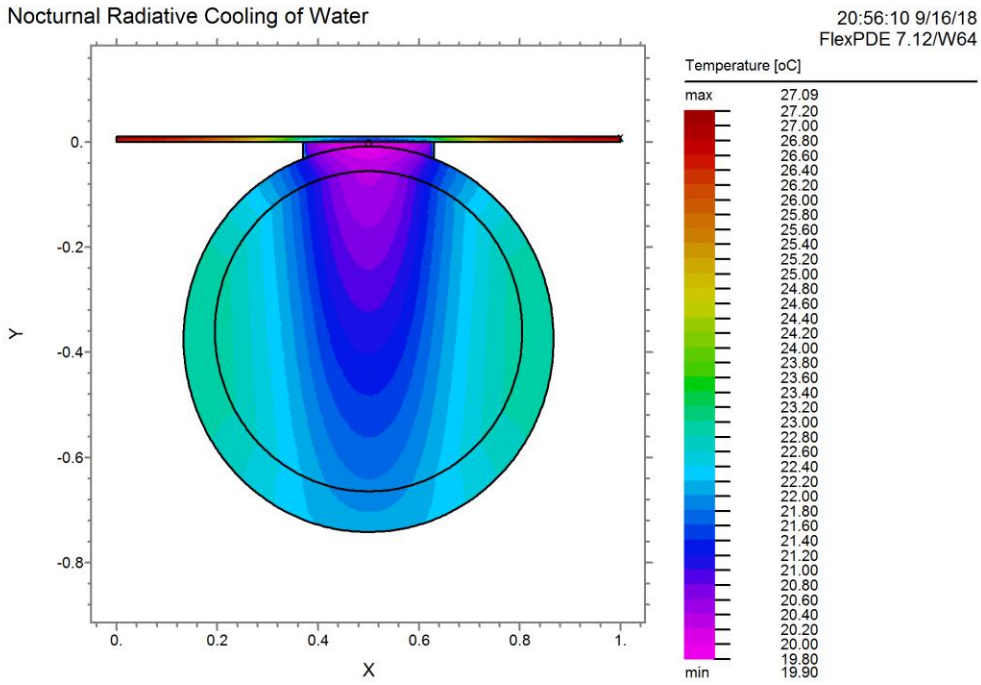

Fig. 4.45 Temperature contour during nocturnal water cooling in September

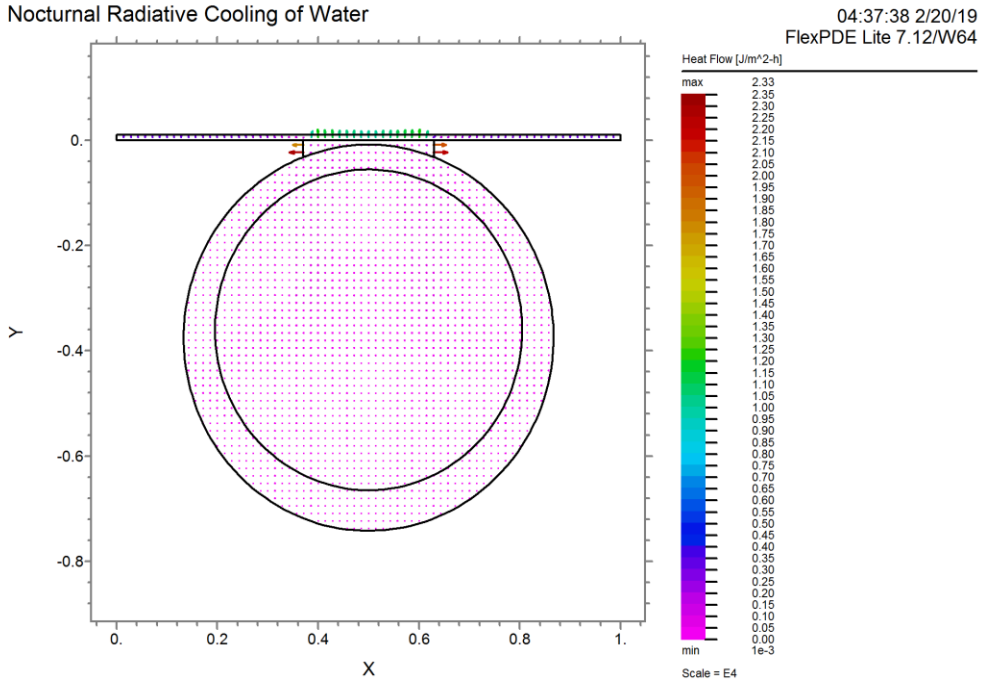

Fig. 4.46 Vector plot of heat flow during nocturnal water cooling in September

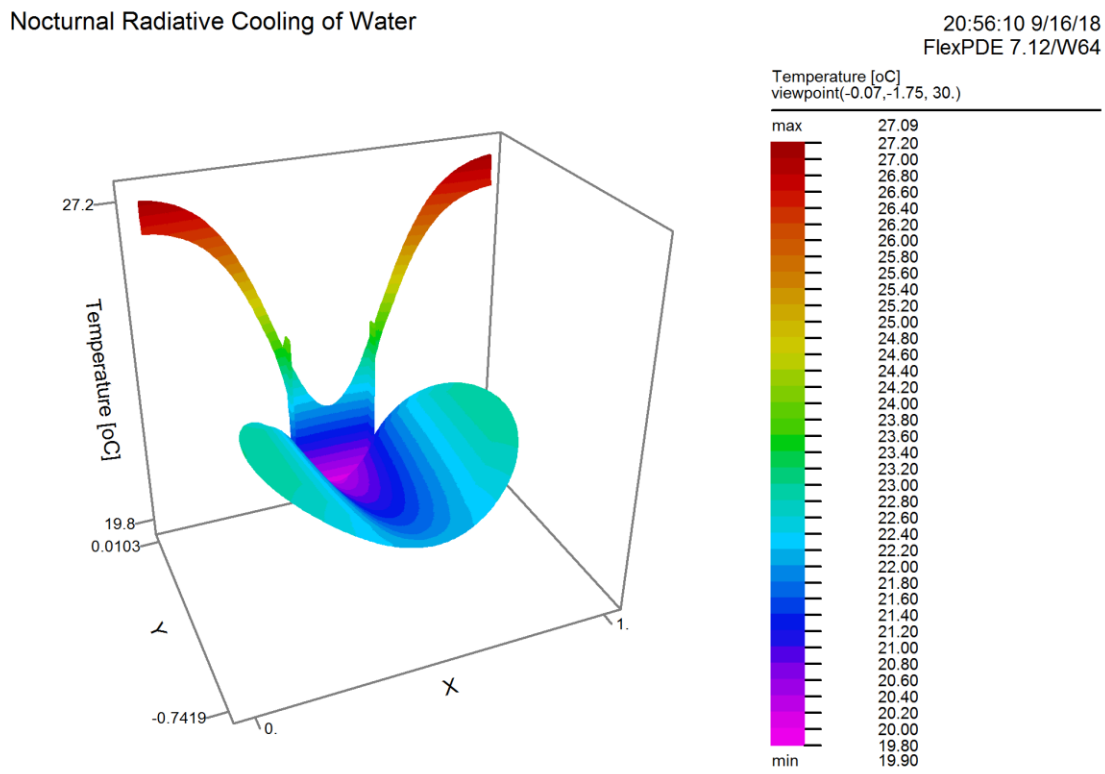

Fig. 4.47 Surfaace plot of Temperature during nocturnal water cooling in September

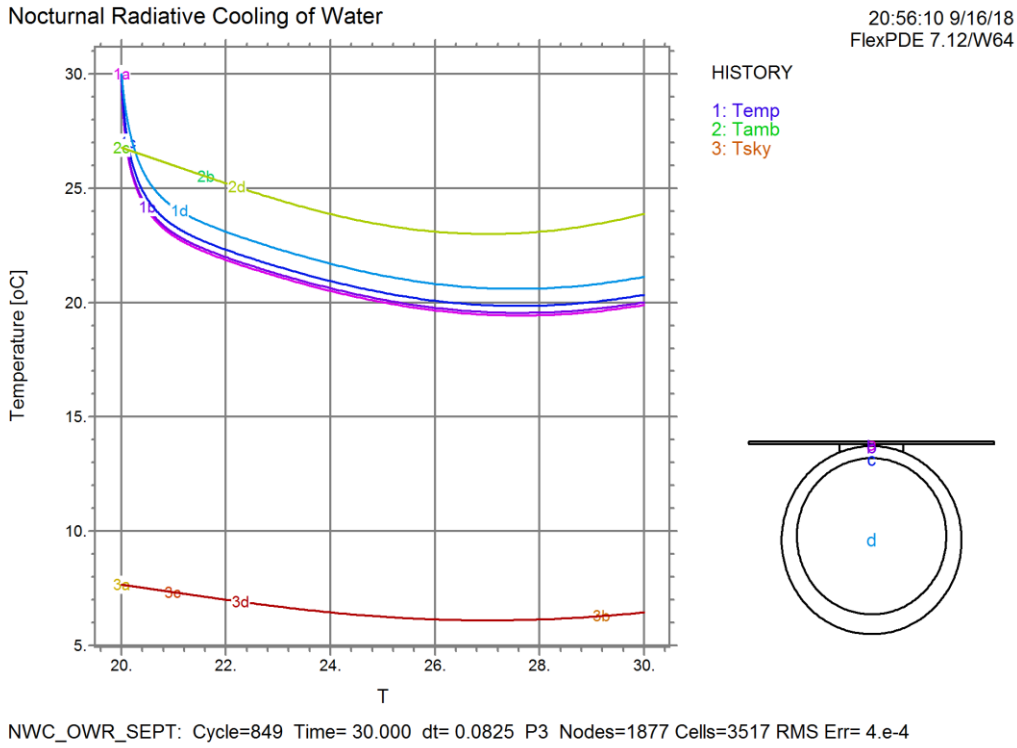

Fig. 4.48 Predicted SCONOR, bond, tube, water, ambient and sky temperatures during nocturnal water cooling in September.

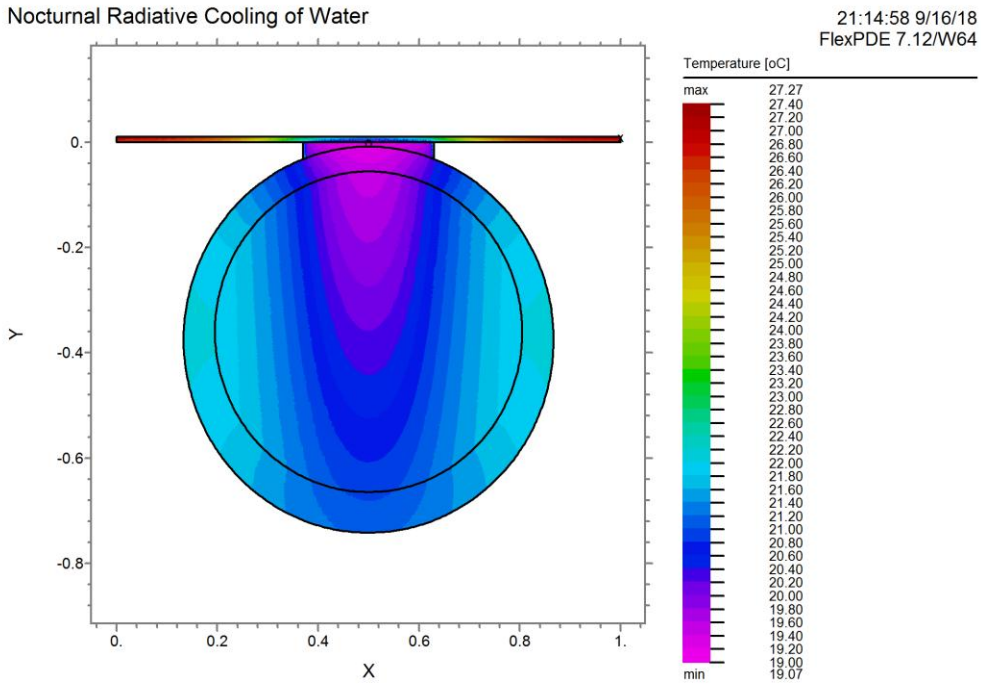

Fig. 4.49 Temperature contour during nocturnal water cooling in November

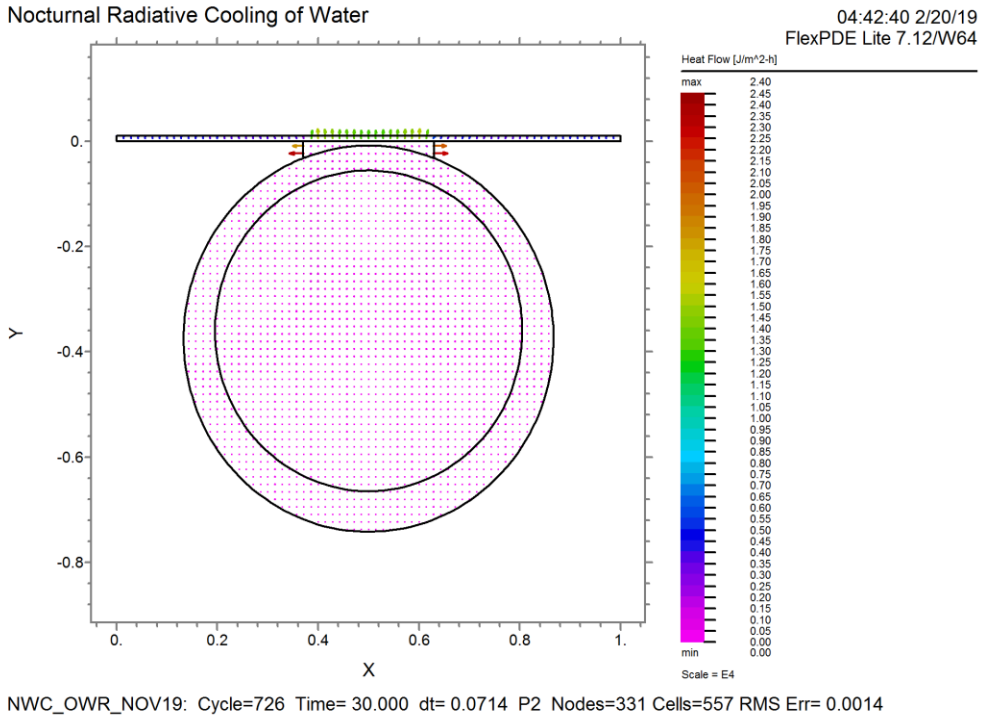

Fig. 4.50 Vector plot of heat flow during nocturnal water cooling in November

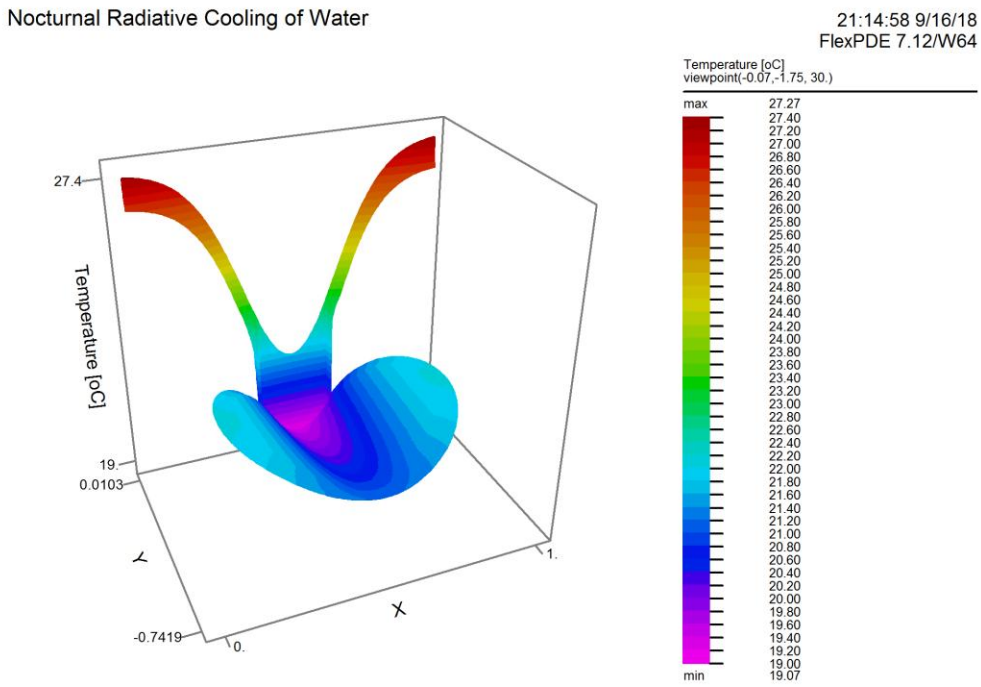

Fig. 4.51 Surface plot of Temperature during nocturnal water cooling in November

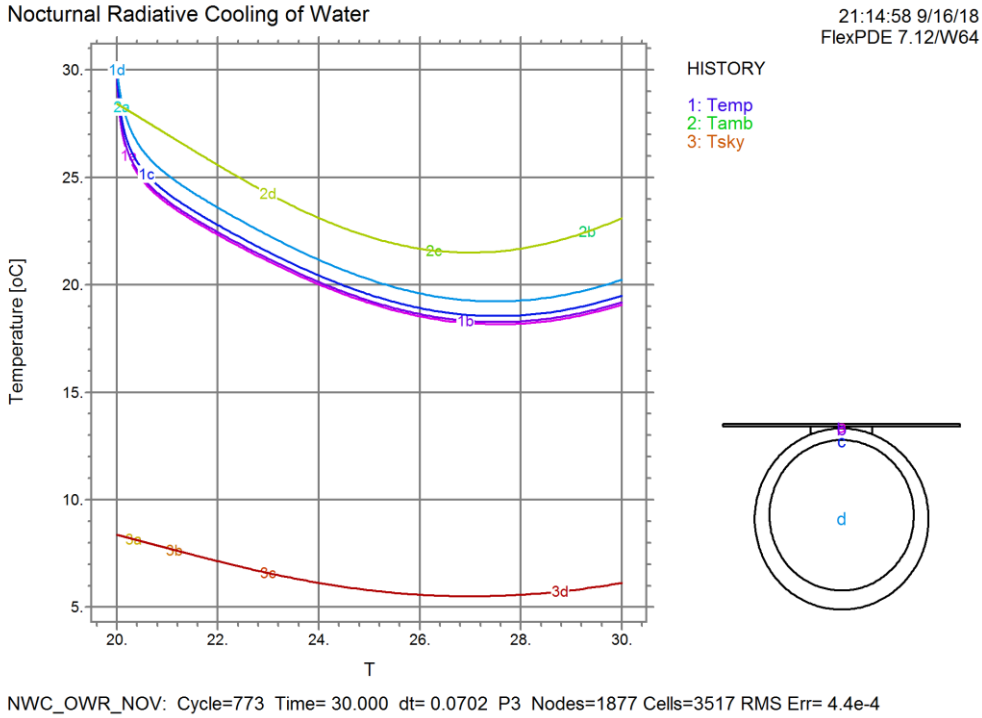

Fig. 4.52 Predicted SCONOR, bond, tube, water, ambient and sky temperatures during nocturnal water cooling in November

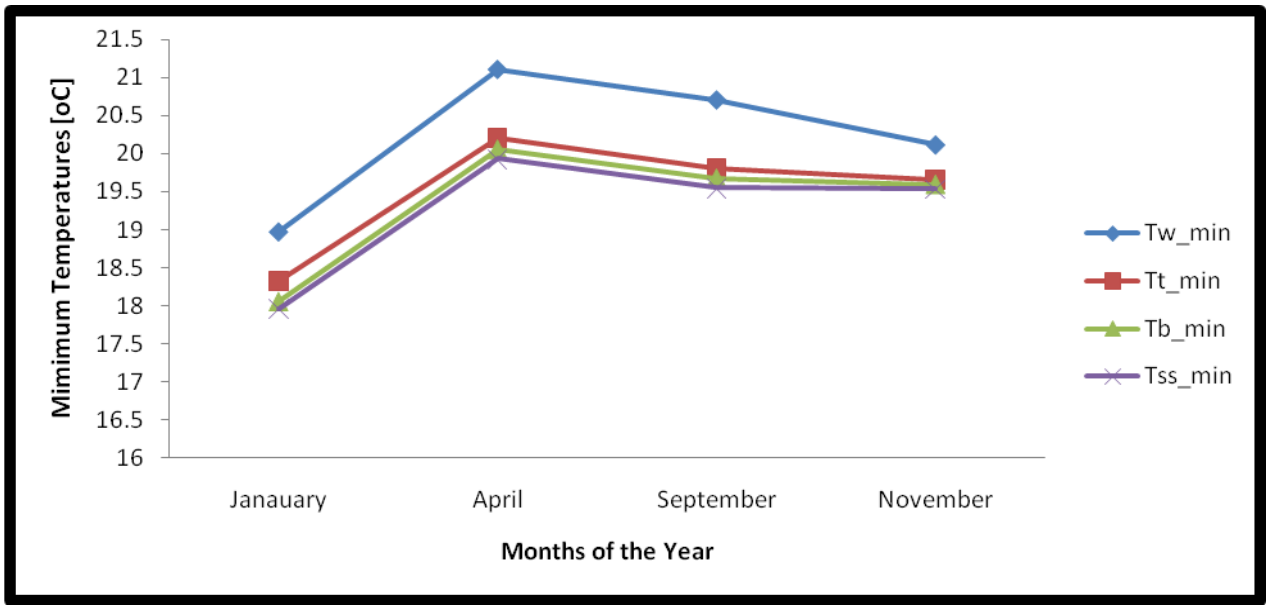

Fig. 4.53 Minimum temperatures of water, tube and bond and SCONOR versus months of the year studied for the nocturnal cooling phase

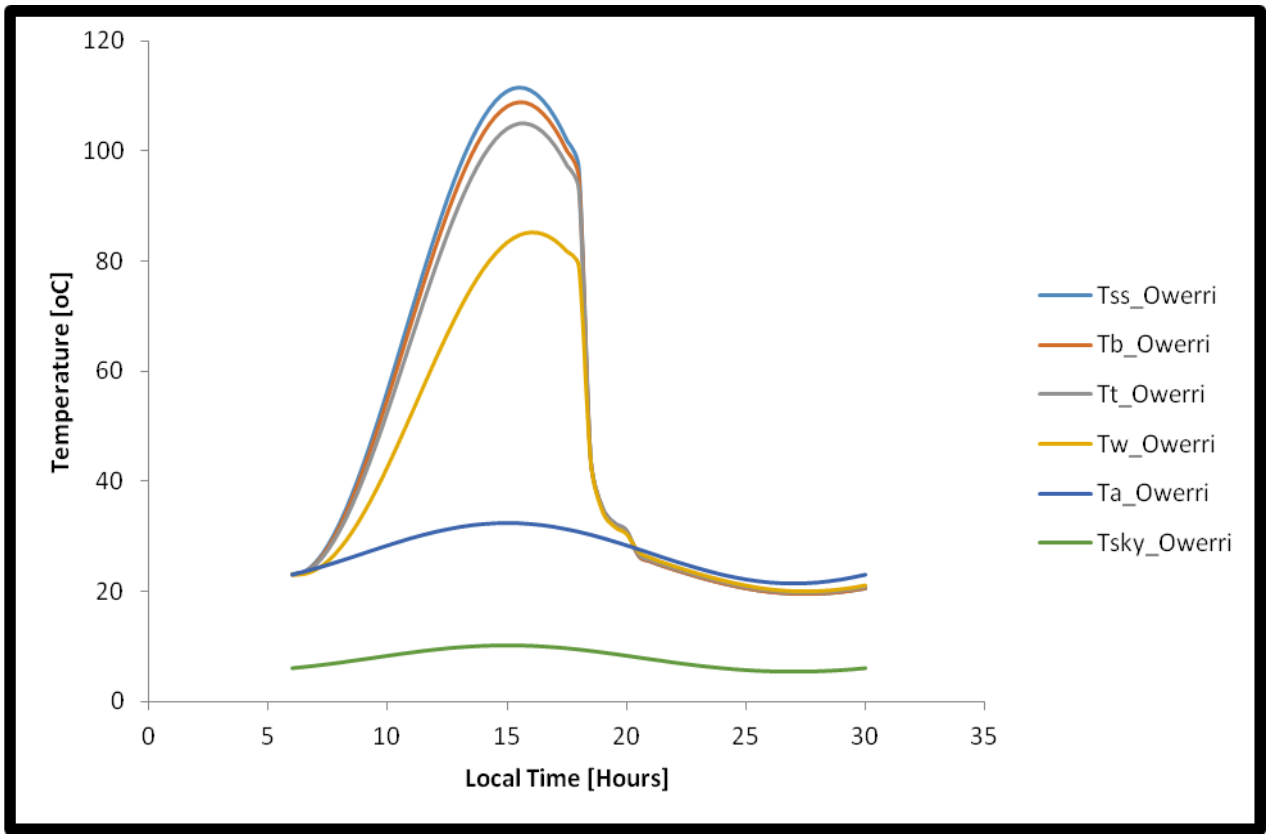

Fig. 4.53b Predicted SCONOR, bond, tube and water temperatures during 24-hour cycle in November in Owerri.

4.1.3 Performance evaluations during 24-hour period in 5 Nigerian cities

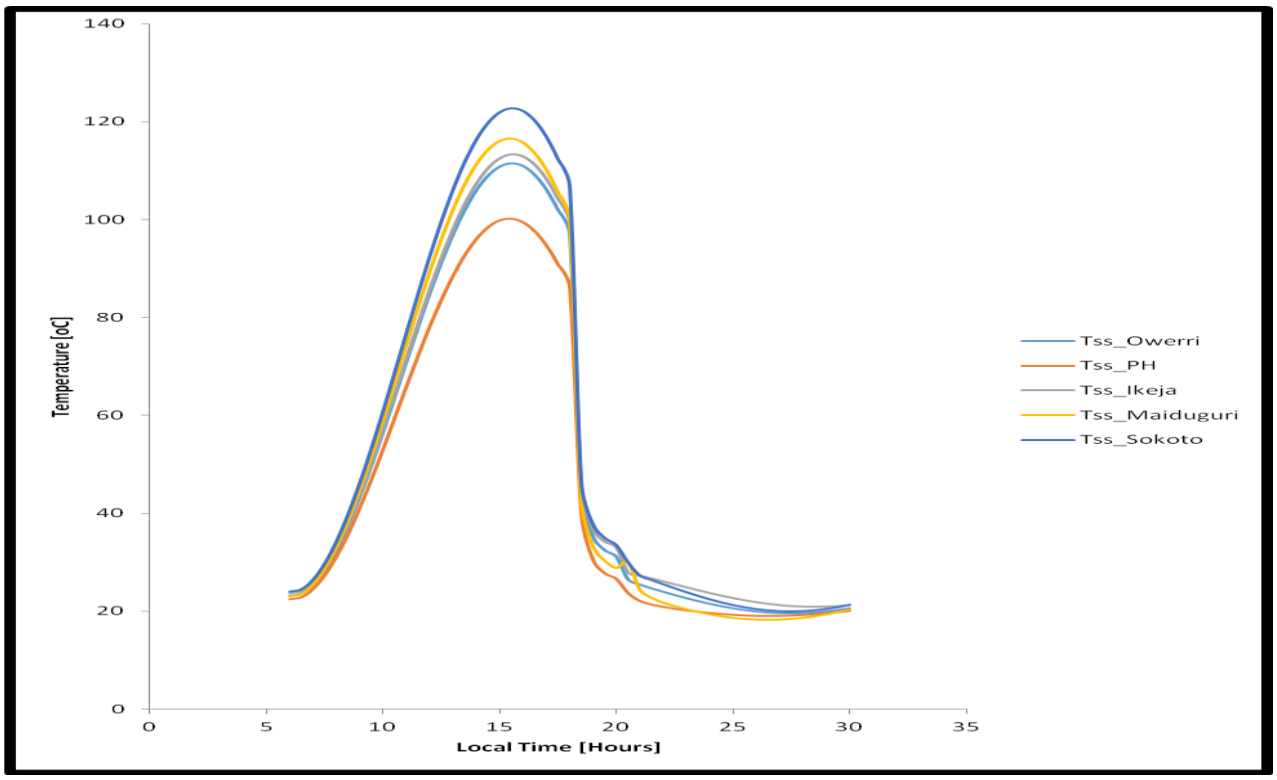

Fig. 4.54 Comparison of predicted SCONOR temperatures in 5 Nigerian cities

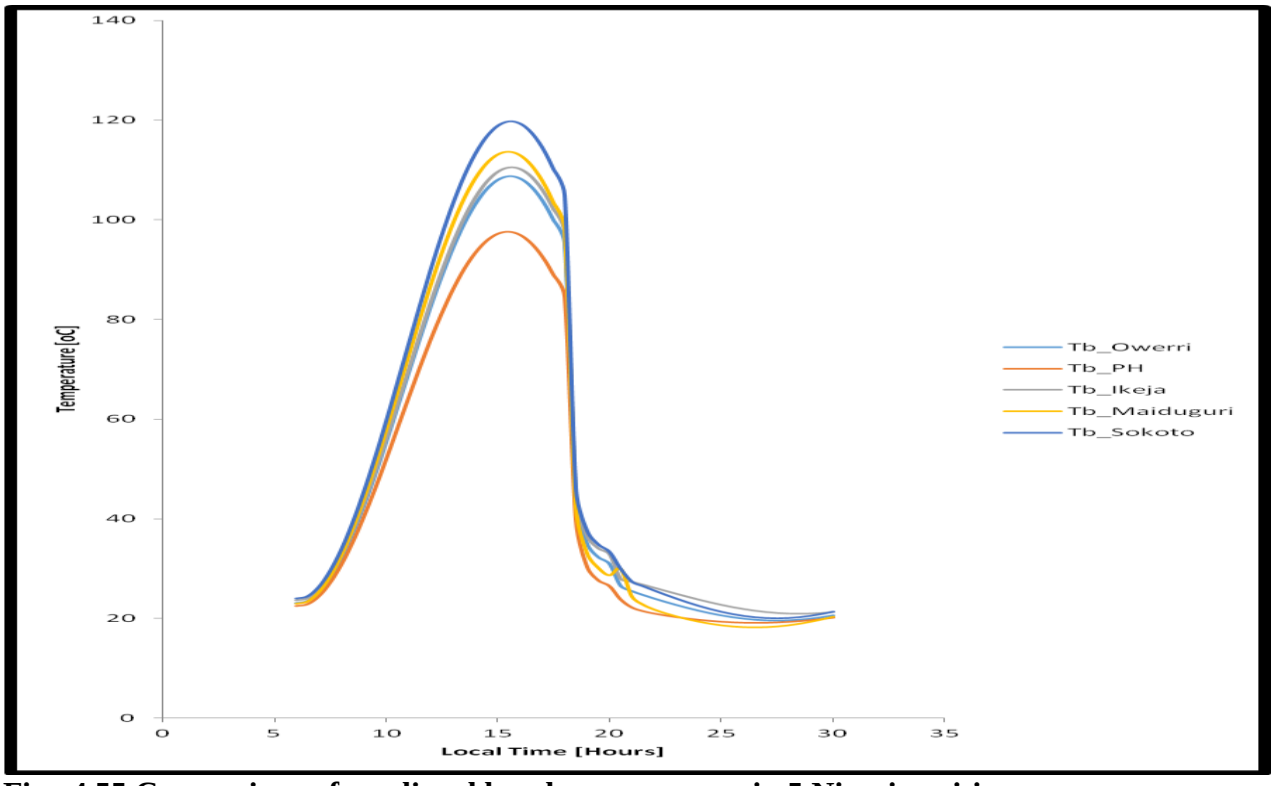

Fig. 4.55 Comparison of predicted bond temperatures in 5 Nigerian cities

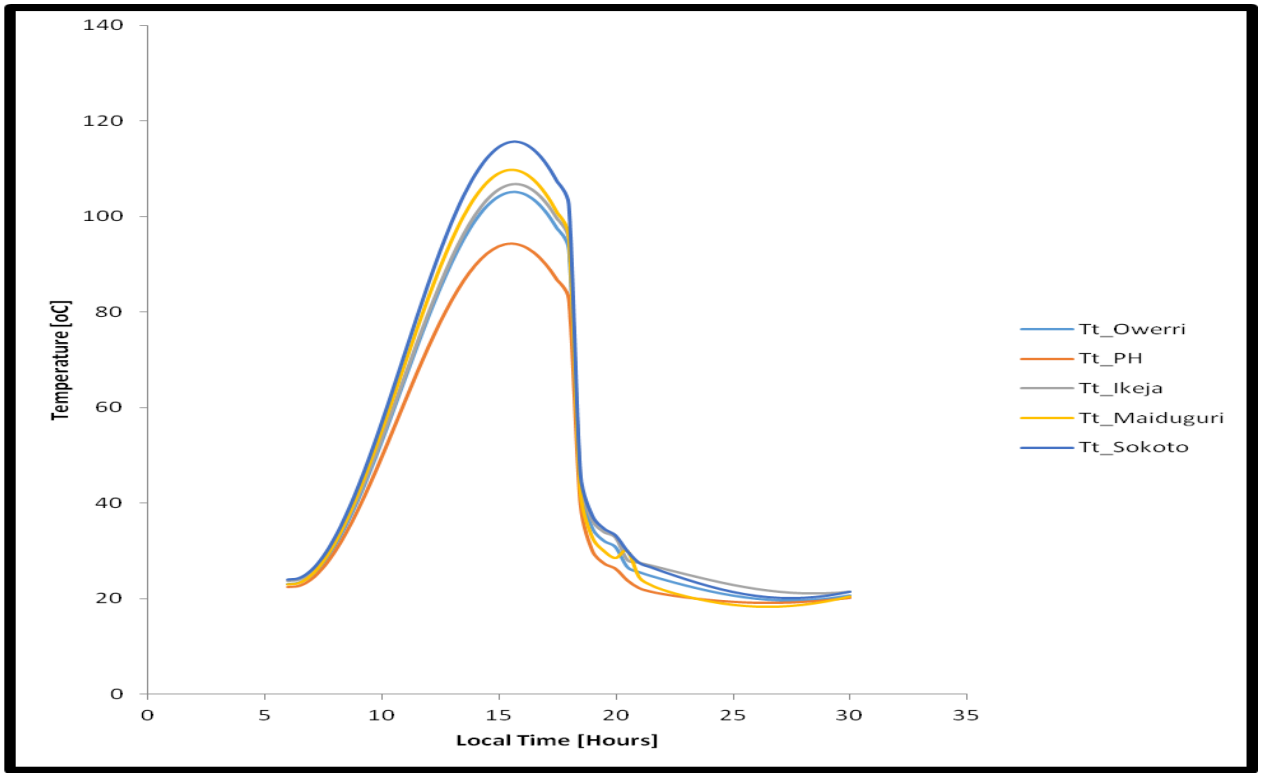

Fig. 4.56 Comparison of predicted tube temperatures in 5 Nigerian cities

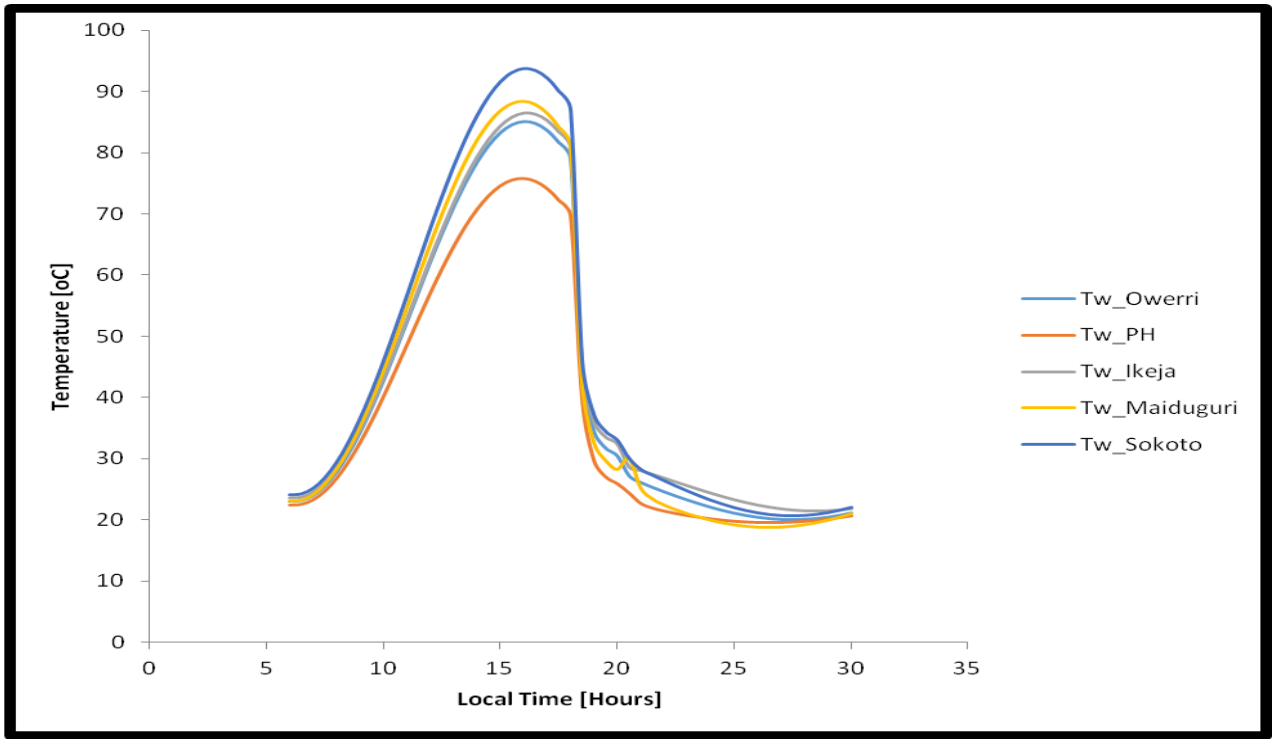

Fig. 4.57 Comparison of predicted water temperatures in 5 Nigerian cities

4.1.4 Stratification in the storage tanks and space conditioning

4.1.4.1 Diurnal stratification and nighttime comfort heating

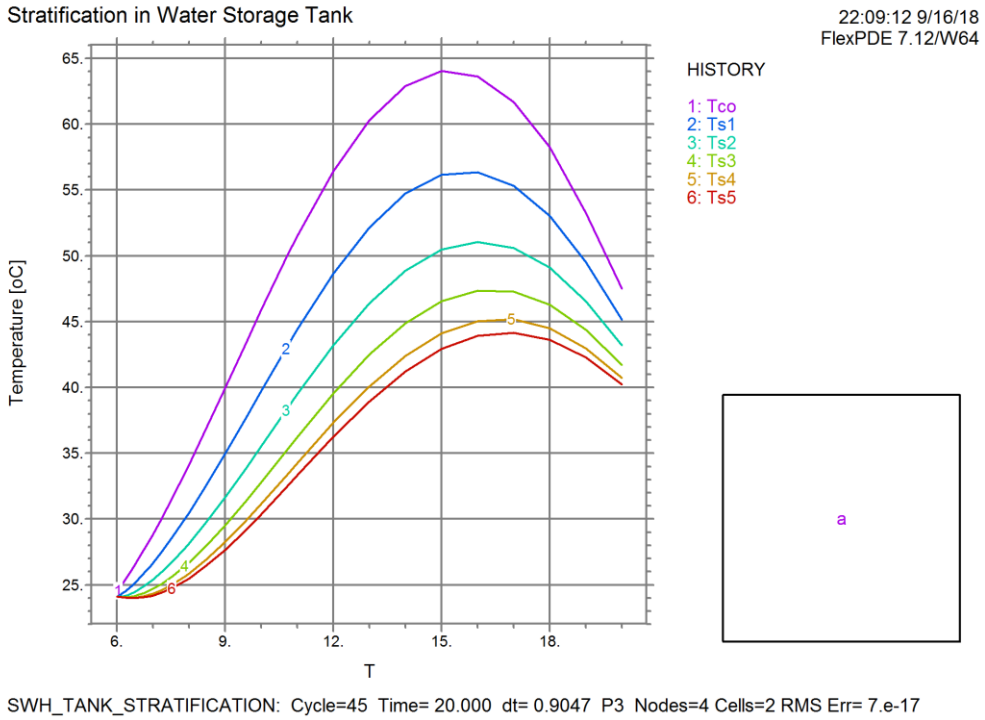

Fig. 4.58 Predicted Temperature stratification inside the hot water storage tank

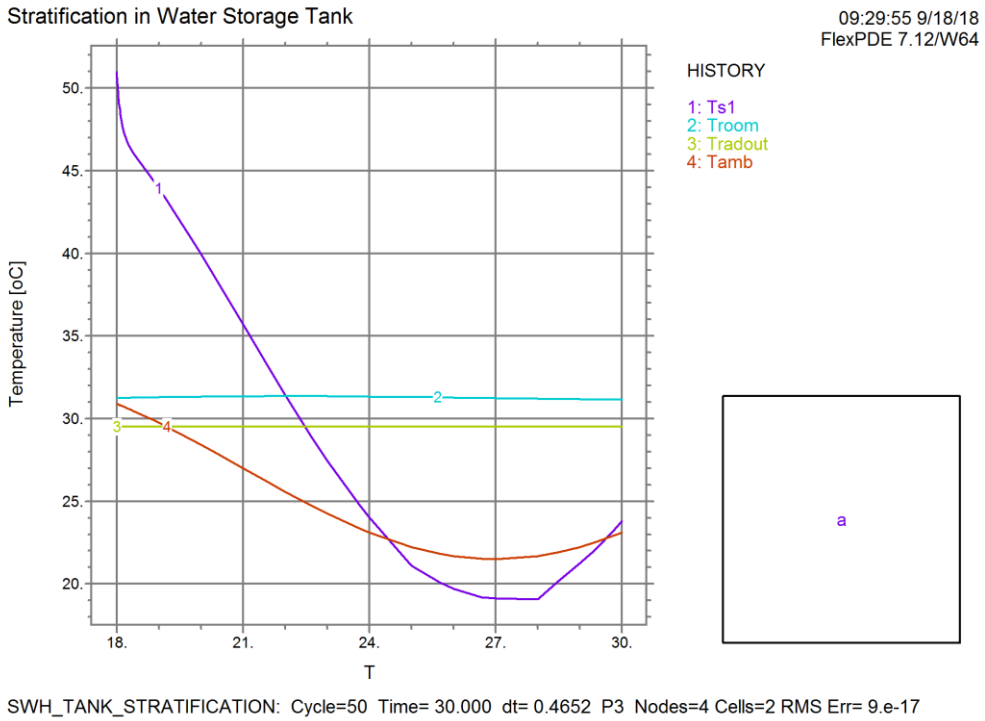

Fig. 4.59 Top of tank, ambient and Predicted indoor room and radiator outlet Temperatures during comfort heating

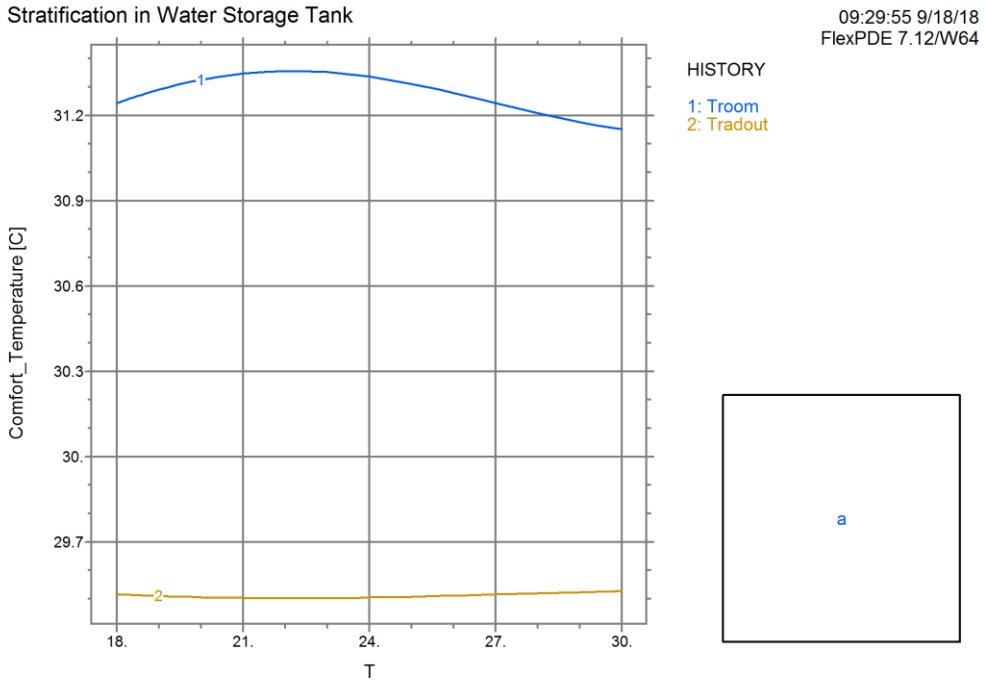

Fig. 4.60 Predicted indoor heated and radiator outlet Temperatures

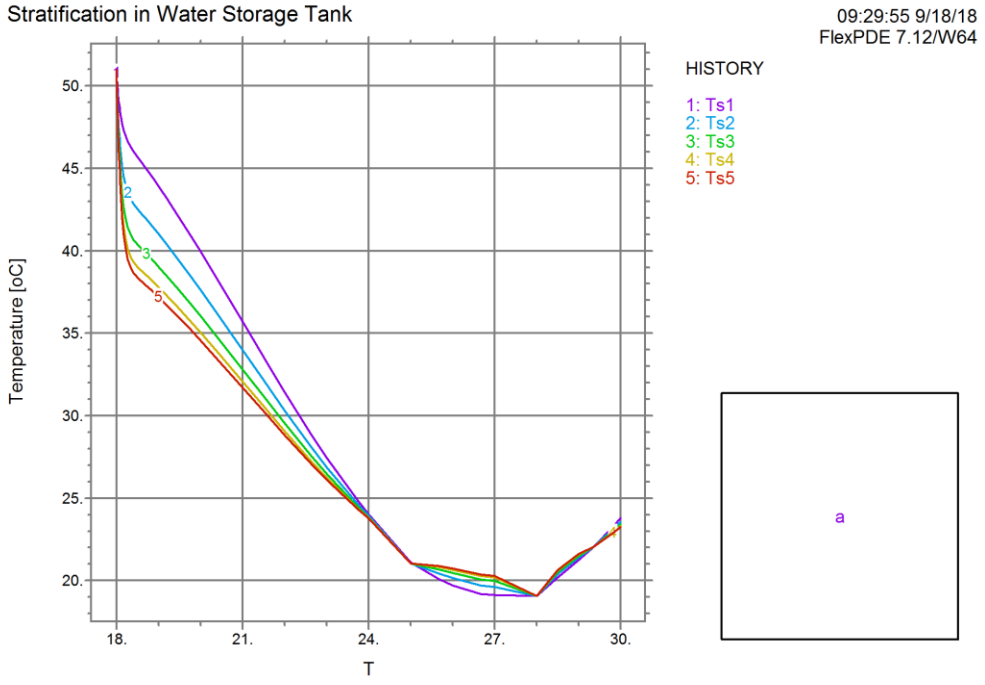

Fig. 4.61 Effect of comfort heating on stratification in the hot water storage tank

4.1.4.2 Nocturnal stratification and daytime comfort cooling

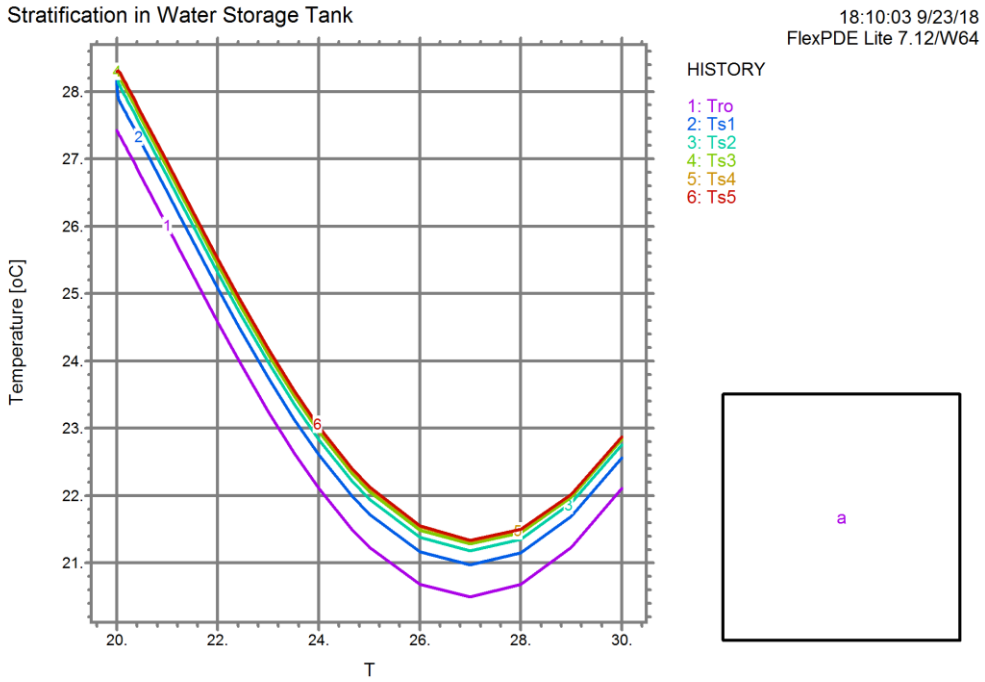

STRAT_NWC_CSPET: Cycle=42 Time= 30.000 dt= 0.8078 P3 Nodes=4 Cells=2 RMS Err= 1.e-15

Fig. 4.62 Predicted Temperature stratification inside the cold water storage tank

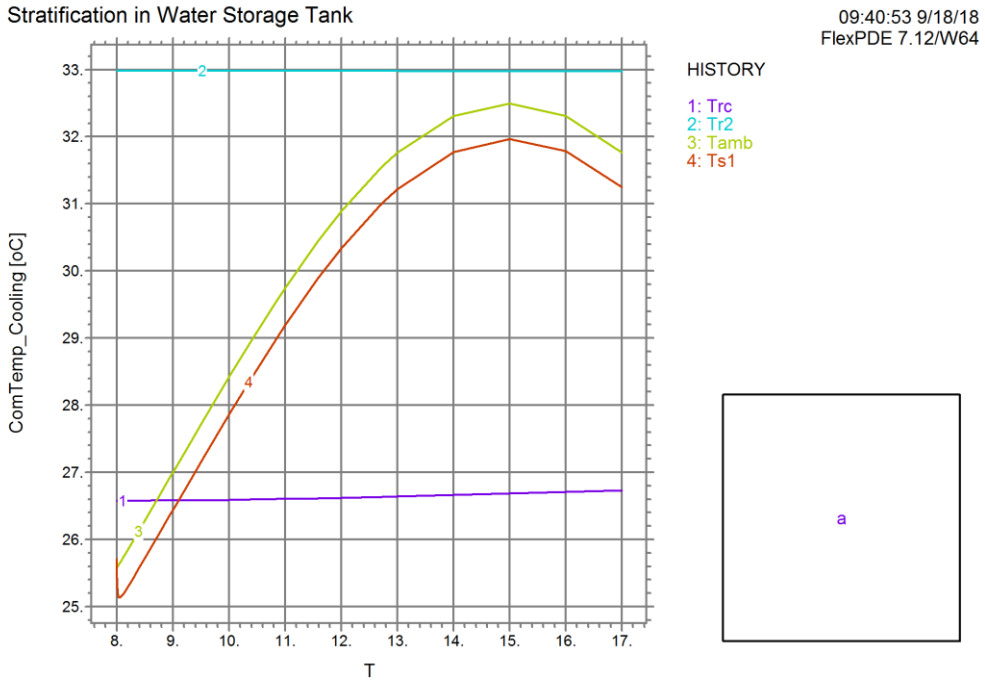

STRAT_COMFCOOL: Cycle=42 Time= 17.000 dt= 0.9088 P3 Nodes=4 Cells=2 RMS Err= 1.e-16

Fig. 4.63 Bottom of tank, ambient and Predicted indoor room and convector outlet Temperatures during comfort cooling

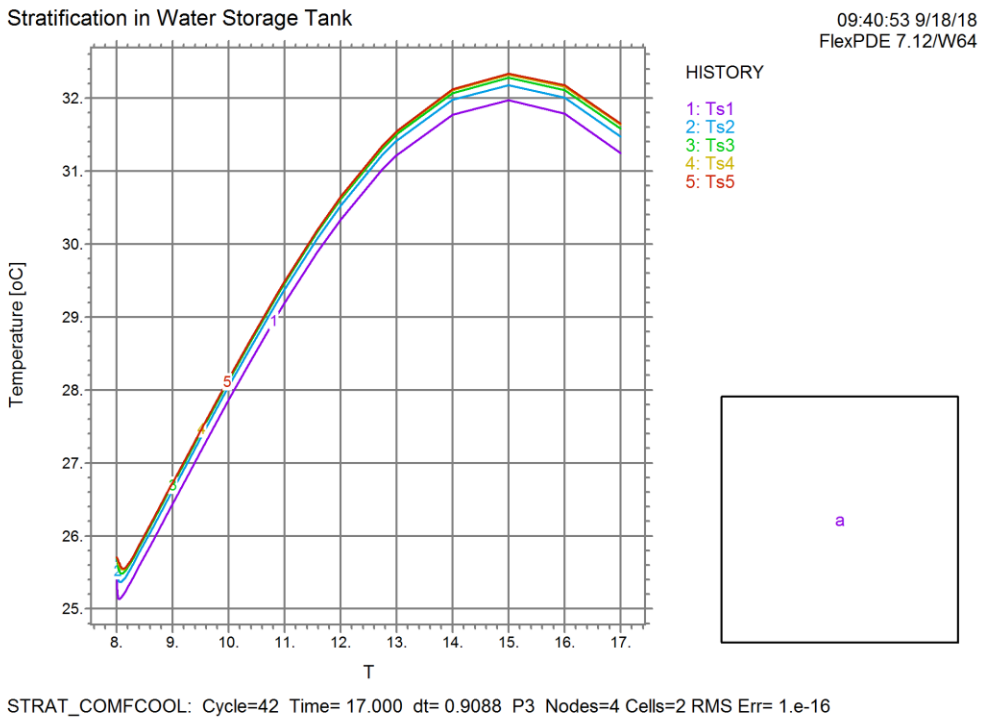

Fig. 4.64 Effect of comfort cooling on stratification in the cold water storage tank

4.1.5 Comparison of present model results with existing results

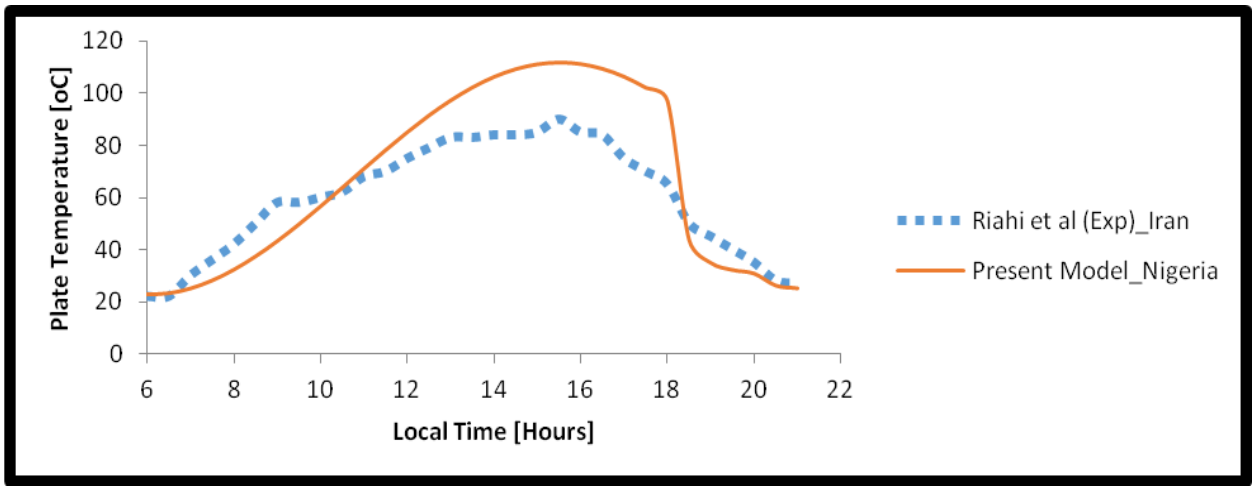

Fig. 4.65 Comparison of predicted SCONOR temperature with Riahi et al (2011) experimental results during diurnal solar heating

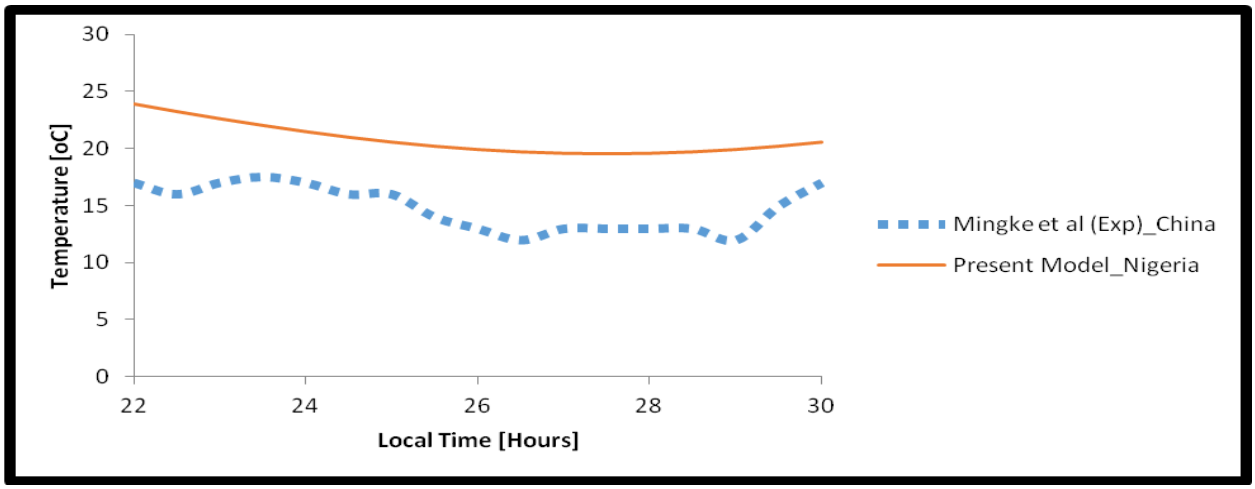

Fig. 4.66 Comparison of predicted SCONOR temperature with Mingke et al (2015) experimental results during nocturnal cooling

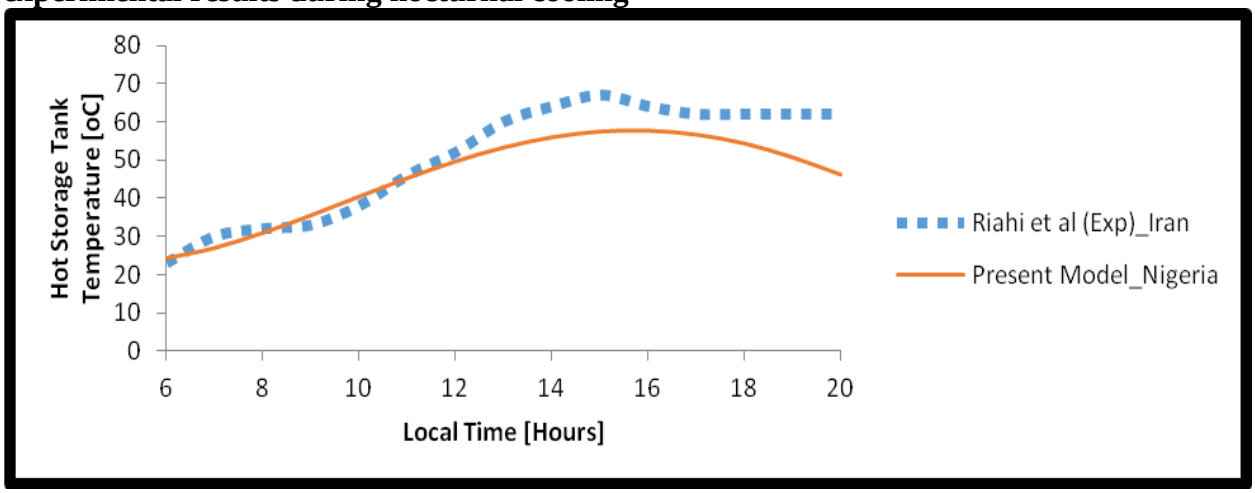

Fig. 4.67 Comparison of predicted hot storage tank temperature with experimental results carried out in Iran during diurnal solar heating

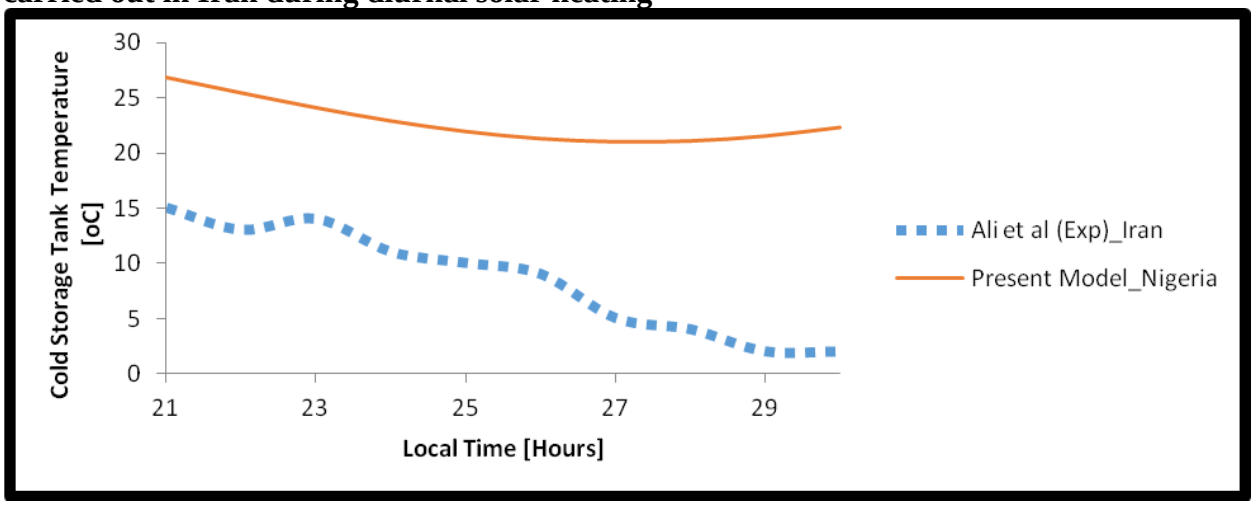

Fig. 4.68 Comparison of predicted cold storage tank temperature with experimental results carried out in Iran during nocturnal cooling

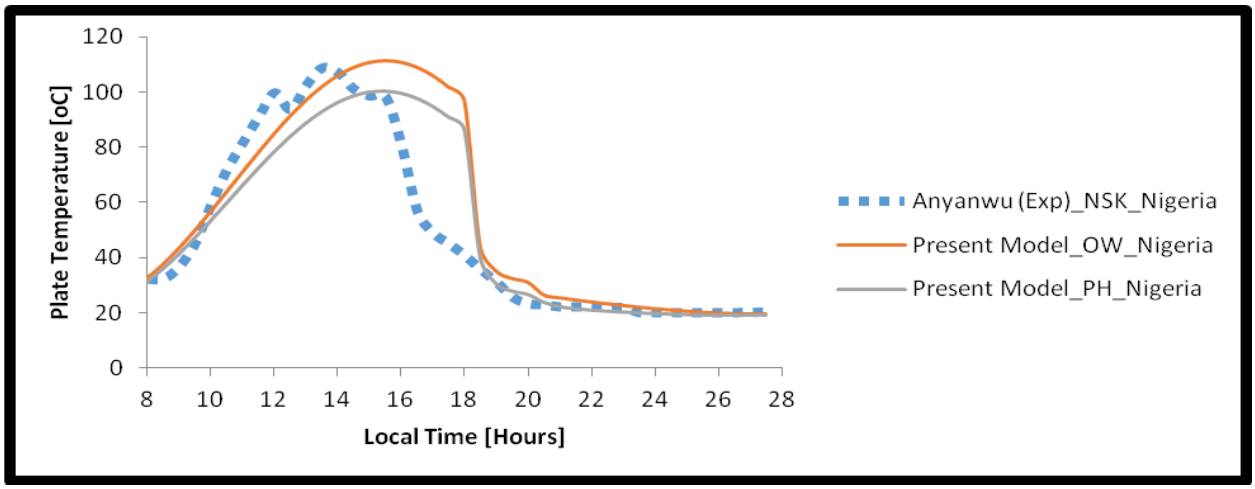

Fig. 4.69a Comparison of predicted SCONOR temperature with experimental results carried out in Nigeria during the 24-hour cycle

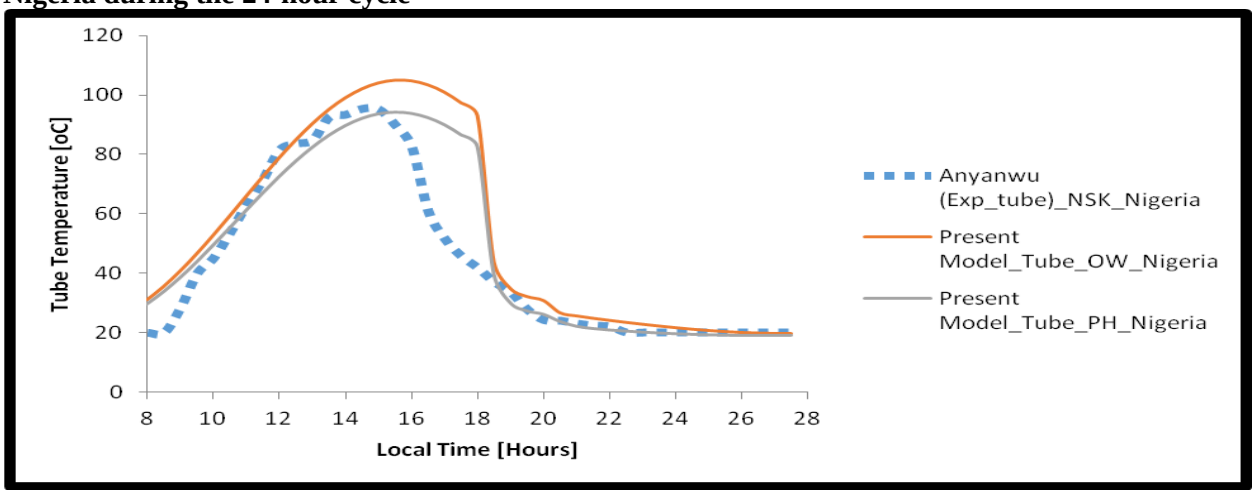

Fig. 4.69b Comparison of predicted tube temperature with experimental results carried out in Nigeria during the 24-hour cycle

4.1.6 Parametric analyses

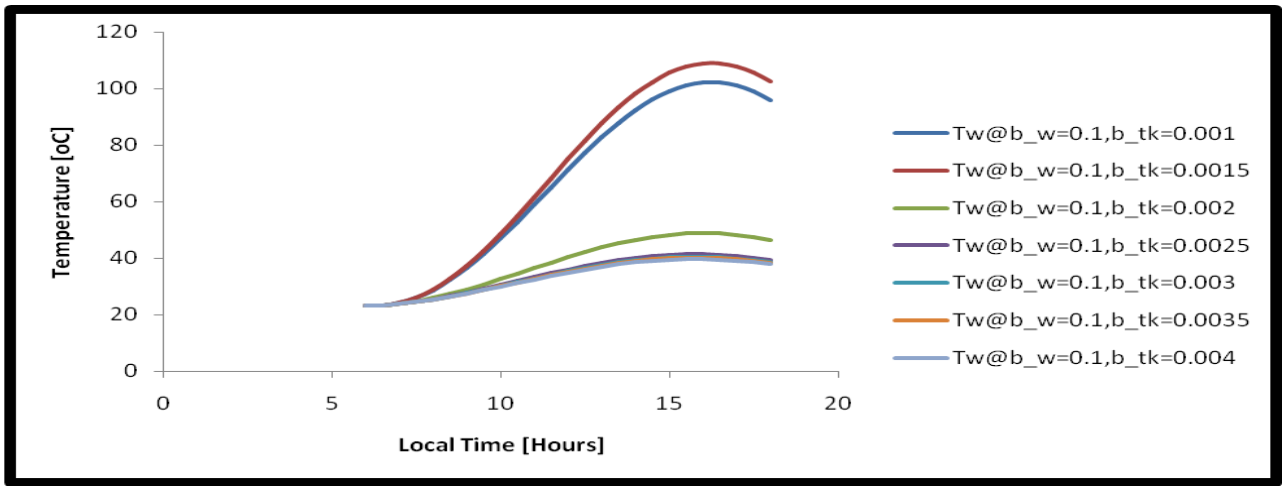

Fig. 4.70 Effect of 0.1m bond width at varying thicknesses on the SCONOR performance

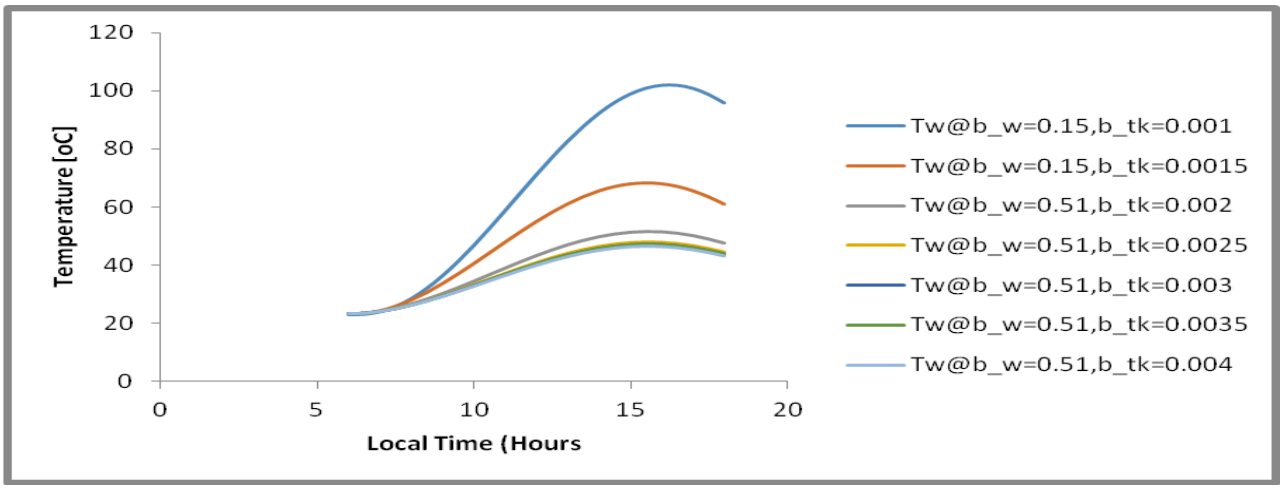

Fig. 4.71 Effect of 0.15m bond width at varying thicknesses on the SCONOR performance

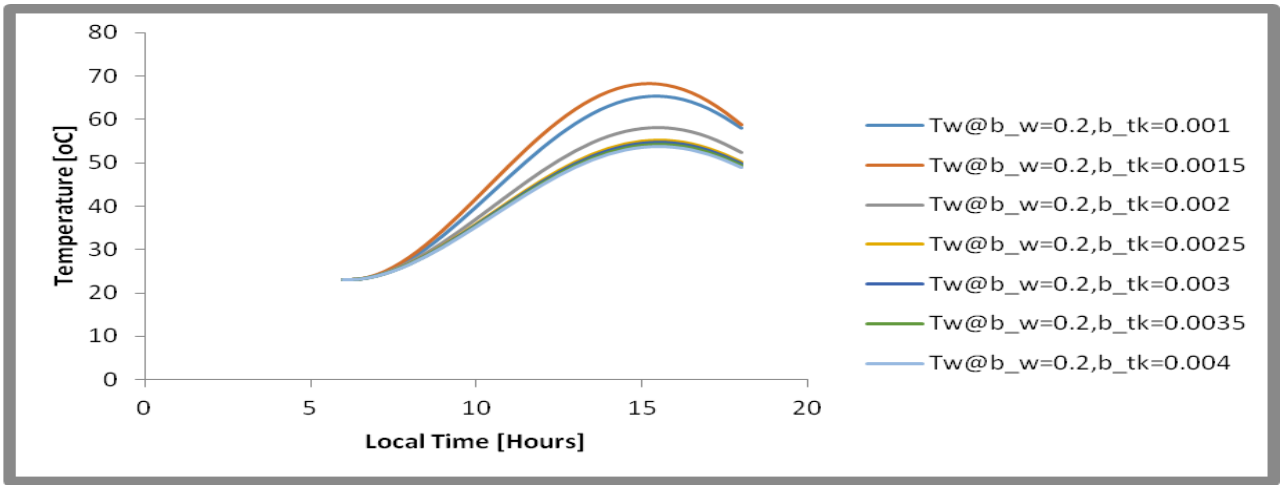

Fig. 4.72 Effect of 0.2m bond width at varying thicknesses on the SCONOR performance

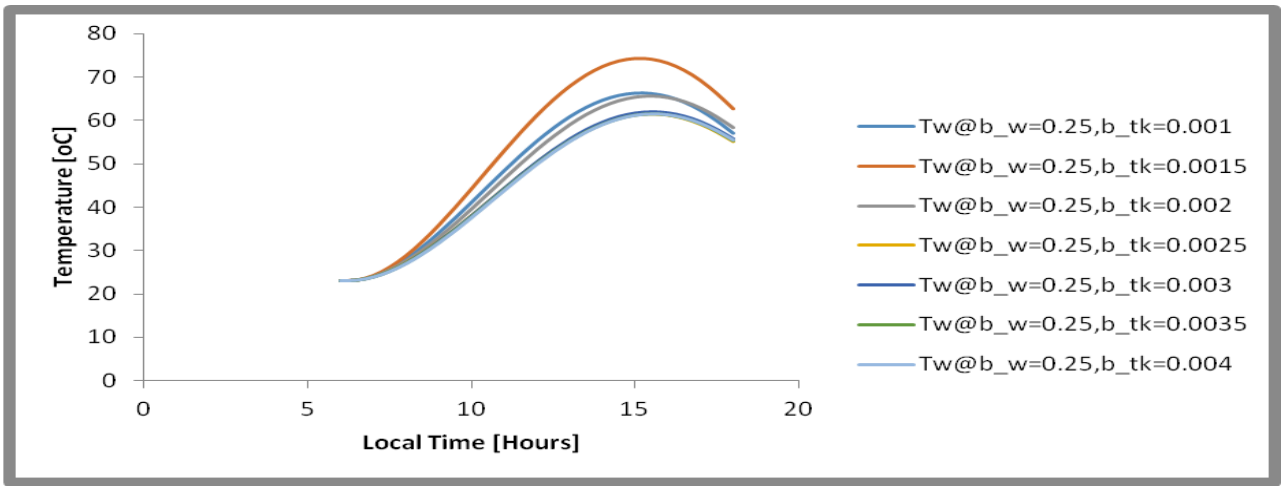

Fig. 4.73 Effect of 0.25m bond width at varying thicknesses on the SCONOR performance

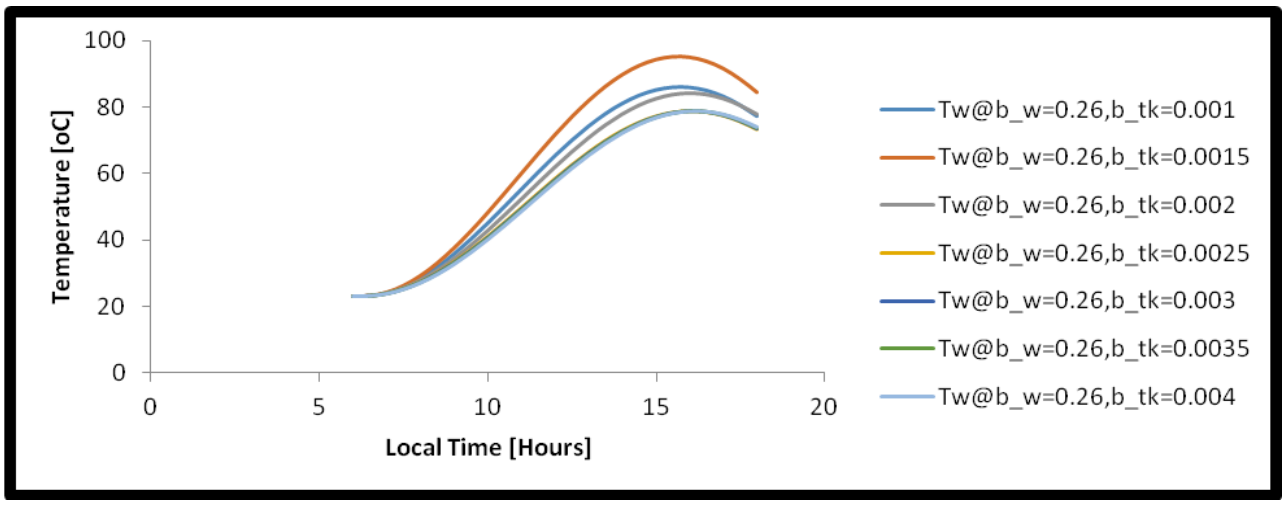

Fig. 4.74 Effect of 0.26m bond width at varying thicknesses on the SCONOR performance

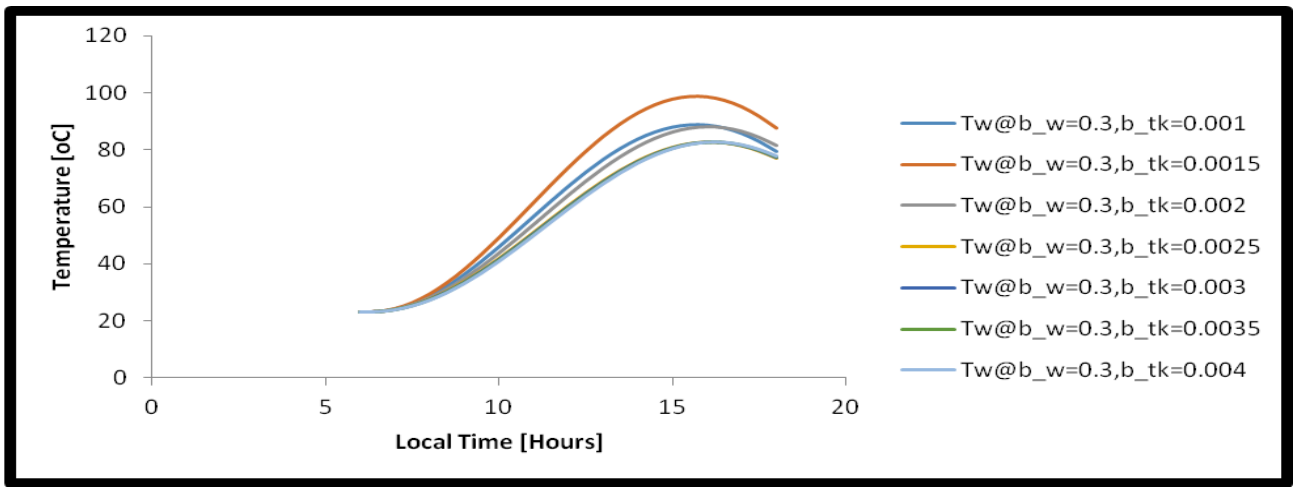

Fig. 4.75 Effect of 0.3m bond width at varying thicknesses on the SCONOR performance

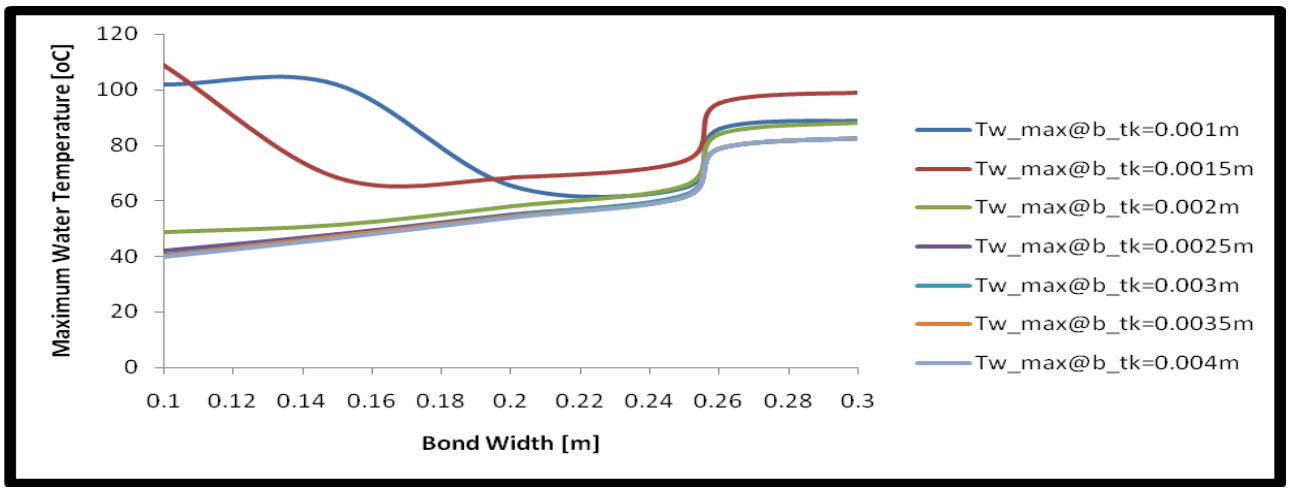

Fig. 4.76 Effect of bond width and thickness on maximum water temperatures

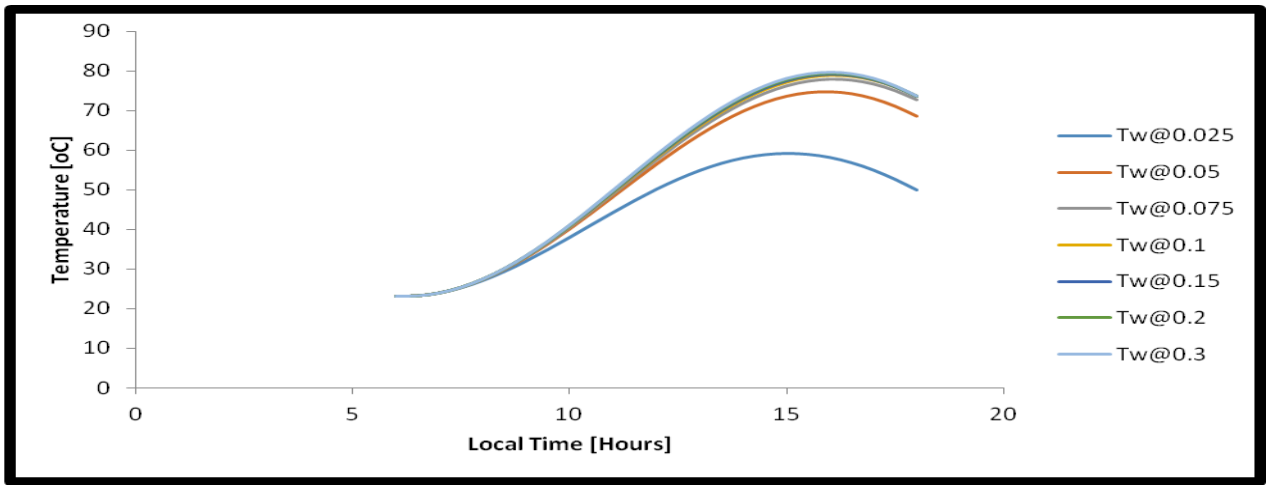

Fig. 4.77 Effect of riser tube spacing on the SCONOR performance

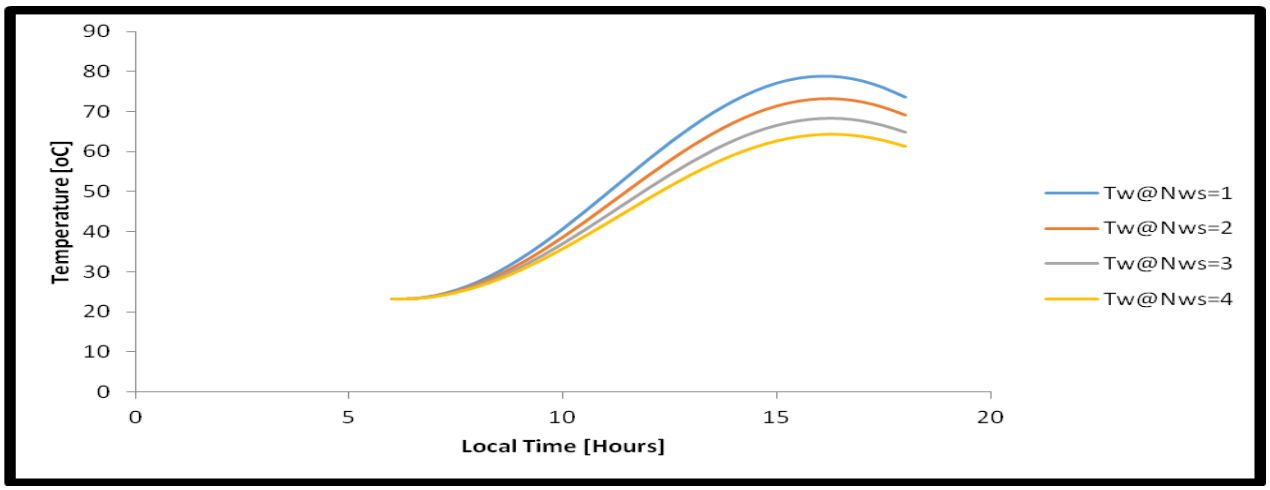

Fig. 4.78 Effect of number of polyethylene windscreen on the SCONOR performance

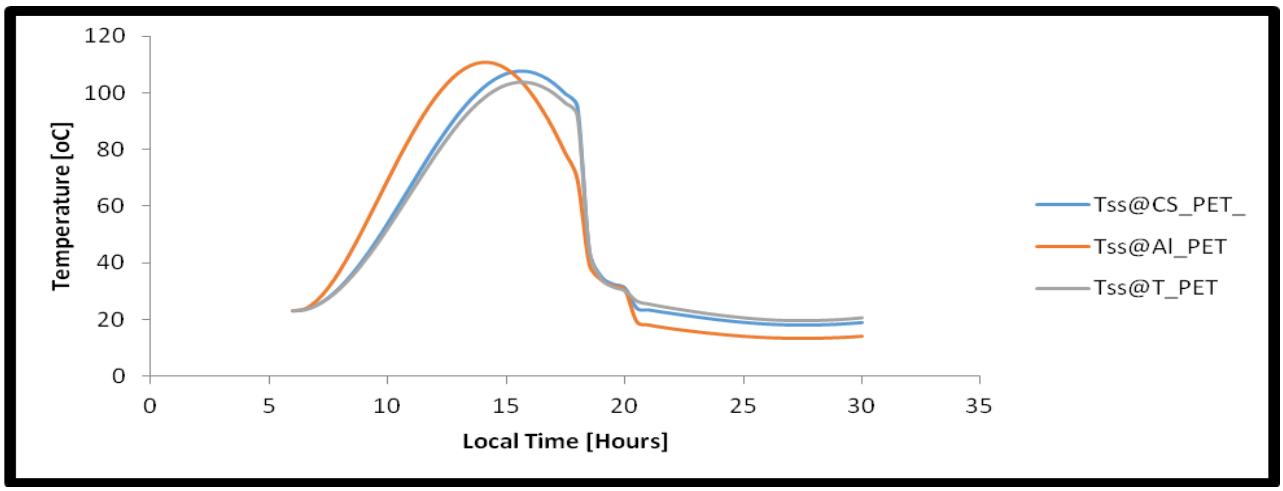

Fig. 4.79 Effect of PET coating on carbon steel, aluminium and titanium on the SCONOR temperature

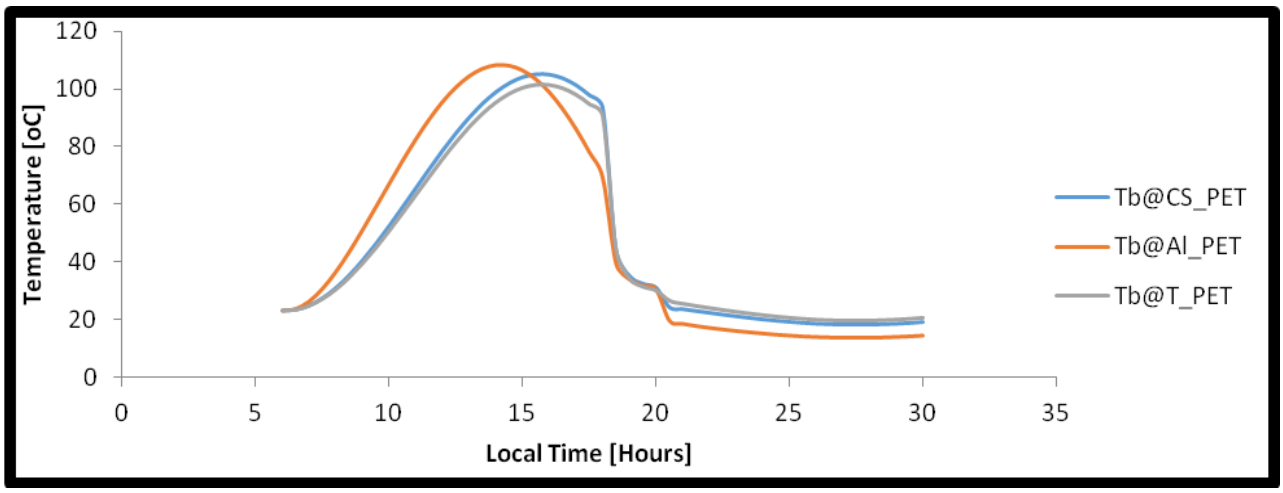

Fig. 4.80 Effect of PET coating on carbon steel, aluminium and titanium on the bond temperature

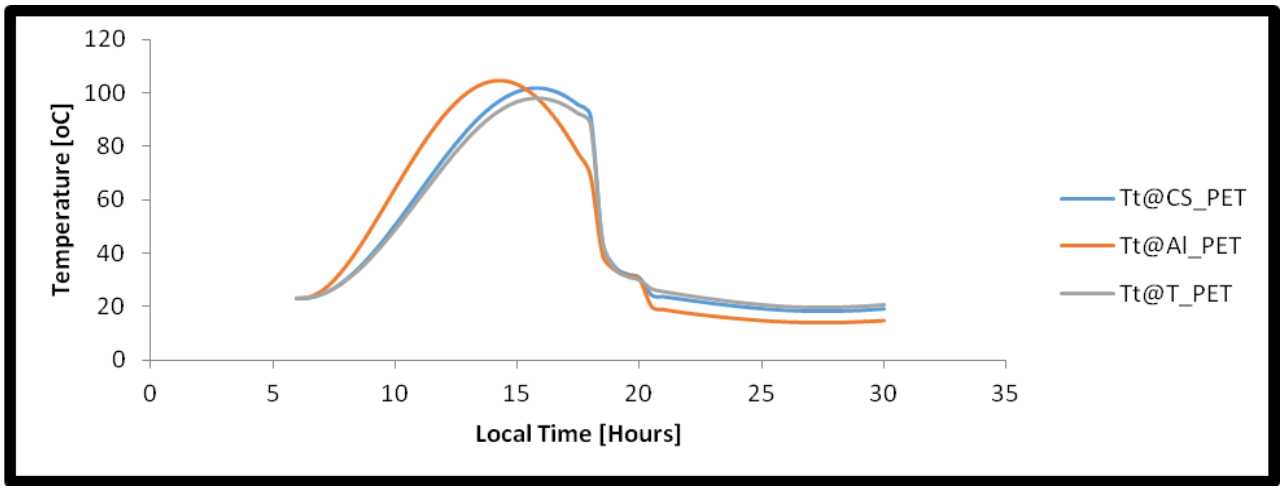

Fig. 4.81 Effect of PET coating on carbon steel, aluminium and titanium on the tube temperature

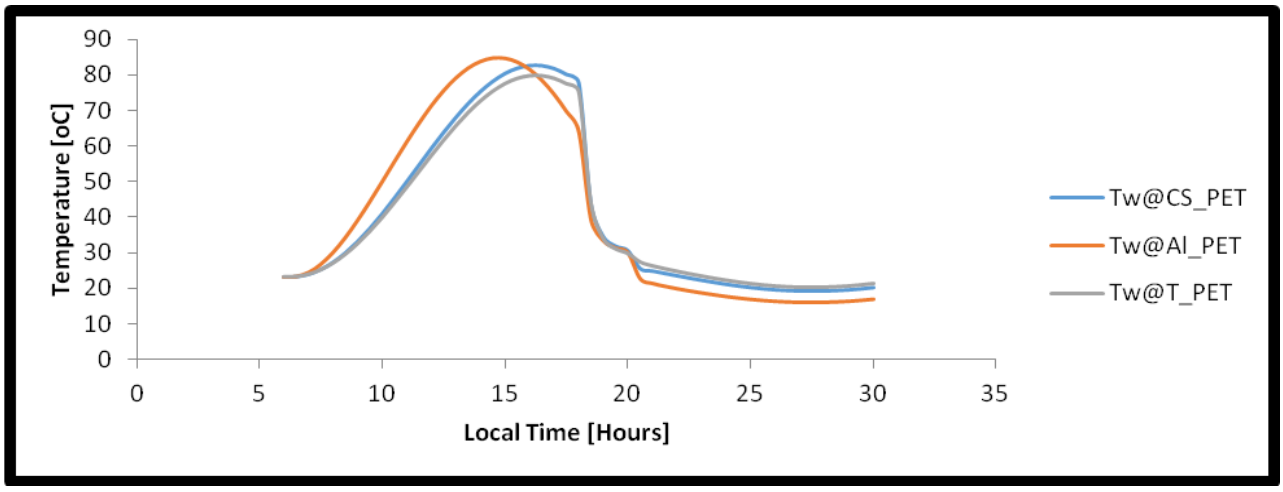

Fig. 4.82 Effect of PET coating on carbon steel, aluminium and titanium on the water temperature

4.2 Discussion

4.2.1 Thermal energy distribution on the SCONOR

Figures 4.1-4.7 show results obtained from a simulation on the SCONOR plate alone to ascertain the nature of thermal energy distribution on it when exposed to incident solar radiation. The contour plot of Fig 4.1 shows that as incident solar energy strikes the plate surface, the absorbed heat energy flows along the x-direction from the two ends of the plate spanning the centre-to-centre distance of the riser tube underneath. The plate absorbs the highest amount of thermal energy at the centre of the tube location. Temperature increased from 32.5-120^{o}C along the fin width. The surface plot of Fig. 4.2 is a 3D topographic display of temperature along the xy-global coordinate while Figs 4.3 and 4.4 are the elevation plots of temperature along the length of the SCONOR at its edge and centre of the plate respectively. These show that it is only in the x-direction that temperature varies significantly in the plate. This temperature variation follows the ambient temperature pattern shown Fig. 4.5. The fluctuations along the length at the middle of plate between two riser tubes as shown in Fig. 4.3, reveals that to any practical intent, there is no variation in temperature along the edge-length of the SCONOR. The temperature is fixed at 31.48^{o}C, while the temperature at the centre in Fig. 4.4 shows that the temperature is fairly constant along the plate centre and fixed at 120.23^{o}C.

Figs 4.6 and 4.7 show the heat flux in the plate. Apart from the energy lost from the SCONOR surface to the ambient, thermal energy is conducted from the centre of the plate (i.e. 0.5m on the dimensionless x-coordinate) towards the edges, opposite the direction of heat flow, from where it is lost by convection to the ambient. About 2.47x10^{4}J/m^{2} (6.86W/m^{2}) of thermal energy is being lost to the ambient from the plate at the edge of the plate.

Normally, the plate is insulated at the four edges along its length and width respectively and since the plate is symmetrical about its centre-to-centre distances of the riser tubes welded underneath, a single riser tube and width equal to centre-to-centre of the tubes will be sufficient to completely model the system.

4.2.2 Predictions using Owerri climatic data

4.2.2.1 Solar water heating in the SCONOR

Figures 4.8-4.11 show the plots of predicted ambient; beam, diffuse and total solar radiation; thermal energy absorption and loss capacity; and SONOR, bond, tube and water temperatures for the city of Owerri in January 17, 2017. Fig. 4.8 shows that the ambient temperature on the test day ranged from 24^{o}C at 06:00 hours to a maximum of 34^{o}C at 15:00 and 16:00 hours respectively. Thereafter, it slightly decreased till 0:00 hours to 22^{o}C and increased slightly to 24^{o}C at 06:00 hours of the next day.

Fig. 4.9 shows the predicted beam, diffuse and total incident solar irradiation on the SCONOR surface on the test day, 17/01/2017. While there is no much difference between the beam component of radiation and total radiation (about 100W/m^2), the diffuse radiation component is very minute in the order of about 100W/m^2. At sunrise, the surface begins to receive solar radiation and reaches maximum values of 880, 100, 980W/m^2 beam, diffuse and total radiation respectively, all at about 12:30 hours. After 12:30 hours, irradiation begins to fall even when ambient temperature is still rising for the three hours as shown in Fig. 4.8.

Fig. 4.10 shows the absorbed thermal energy and the corresponding losses from the collector. Because the water in the tube is at a lower temperature, the highest absorptions of solar energy occurred at the region bounding the bond and the tube with the water. It means that heat

progressively flowed from the edge to the centre of the plate from where it now transfers to the bond, tube and the water. This is in consonance with the thermal distribution shown in Fig. 4.1 as regions of high energy absorptions correspond to the regions of low energy losses and vice versa. Losses also occurred at the lower side of the plate spanning the width which could be as a result of lapses in the lagging of the plate underneath. Improving on this would further improve the thermal performance of the system. The heat absorption capacity of the collector was not significant after 16:30 hours outside the bond region in January and within the bond region, it fizzles out after 18:00 hours. This shows that the bond dimensions have a great influence on the thermal performance of the system.

Fig. 4.11 shows the predicted collector plate, bond, and tube surface and water temperatures. While the solar radiation peaked at 12:30 hours, the plate, bond tube and water temperatures peaked at 15:30 hours. For the month of January, the plate, bond, tube and water received 116, 111, 103 and 85^{o}C respectively. After 12:30 hours, although incident radiation starts dropping, the absorber temperature continues rising for upward of three hours.

Figs 4.12-4.15, represent the plots of predicted ambient; beam, diffuse and total solar radiation; thermal energy absorption and loss capacity; and SONOR, bond, tube and water temperatures for the city of Owerri in April 18, 2017. Fig. 4.12 shows that the ambient temperature on the test day ranged from 24^{o}C at 06:00 hours to a maximum of 32^{o}C at 12:00 hours. Thereafter, it slightly decreased till 0:00 hours to 24^{o}C and increased slightly to 26^{o}C from 01:00-03:00 hours and finally to 25^{o}C at 06:00 hours of the next day.

Fig. 4.13 shows the predicted beam, diffuse and total incident solar irradiation on the SCONOR surface on the test day, 18/04/2017. The beam component of radiation reached a value of about 780W/m^2 at 12:30 hours while the total radiation comprising the beam and diffuse components

reached 850W/m^2 at the same time. There is no much difference between the beam component of radiation and total radiation (about 70W/m^2), which make up the diffuse component. Again, during this month of April, a time lag of about three hours elapsed in between the peak time of solar irradiation and the peak time of ambient temperature.

Fig. 4.14 shows the absorbed thermal energy and the corresponding losses from the collector in April. While the highest absorptions of solar energy occurred at the region bounding the bond and the tube with the water, the lowest absorptions occurred at the fin extension spanning the width of the collector. It shows that heat progressively flowed from the edge to the centre of the plate from where it now transfers to the bond, tube and the water. This is in consonance with the thermal distribution shown in Fig. 4.1 as regions of high energy absorptions correspond to the regions of low energy losses and vice versa. It was also observed just like in January, that losses occurred at the lower side of the plate spanning the width which could be as a result of lapses in the lagging of the plate underneath. The heat absorption capacity of the collector was less than zero after 17:30 hours outside the bond region in April and within the bond region, it becomes zero after 18:00 hours when there is no more solar radiation after sunset. This shows that the bond dimensions have a great influence on the thermal performance of the system. After 18:00 hours, even though there is no more solar absorption, losses continued to occur in the SCONOR because it is being cooled to the ambient condition before the commencement of nocturnal process.

Fig. 4.15 shows the predicted collector plate, bond, and tube surface and water temperatures in April. The SCONOR, bond, tube and water temperatures peaked at 15:30 hours, reaching the values of about 102, 98, 94 and 76^oC respectively. After 12:30 hours, although incident radiation starts dropping, the absorber temperature continues rising for upward of three hours.

Figs 4.16-4.19 presents the plots of predicted ambient; beam, diffuse and total solar radiation; thermal energy absorption and loss capacity; and SONOR, bond, tube and water temperatures for the city of Owerri in September 18, 2017. Fig. 4.16 shows that the ambient temperature on the test day ranged from 24^{o}C at 06:00 hours to a maximum of 30^{o}C at 12:00 hours, a value it slightly maintained with little variations till about 16:00 hours. Thereafter, it slightly decreased till 0:00 hours to 24^{o}C and increased slightly to 25^{o}C from 01:00-04:00 hours and finally to 25^{o}C at 06:00 hours of the next day.

Fig. 4.17 shows the predicted beam, diffuse and total incident solar irradiation on the SCONOR surface on the test day, 18/09/2017. The diffuse, beam and total irradiation peaked to values of about 57W/m2, 420W/m2 and 477W/m2 respectively at 12:30 hours. As in the previous, season, the difference between the three components of irradiation is not significant. During this month of September, a time lag of about 30 minutes elapsed in between the peak time of solar irradiation and the peak time of ambient temperature.

Fig. 4.18 shows the absorbed thermal energy and the corresponding losses from the collector in September under Owerri climatic conditions. While the highest absorptions of solar energy occurred at the region bounding the bond and the tube with the water, the lowest absorptions occurred at the fin extension spanning the width of the collector. It shows that heat progressively flowed from the edge to the centre of the plate from where it now transfers to the water via the bond and tube. This is in consonance with the thermal distribution shown in Fig. 4.1 as regions of high energy absorptions correspond to the regions of low energy losses and vice versa. It was also observed just like in the preceding months, that losses occurred at the lower side of the plate spanning the width which could be as a result of lapses in the lagging of the plate underneath. The heat absorption capacity of the collector was less than zero after 17:30 hours outside the

bond region in April and within the bond region, it becomes zero from 18:00 hours when there is no more solar radiation after sunset. After 18:00 hours, even though there is no more solar absorption, losses continued to occur in the SCONOR because it is being cooled to the ambient condition before the commencement of nocturnal process.

Fig. 4.19 shows the predicted SCONOR, bond, and tube surface and water temperatures in September. The SCONOR, bond, tube and water temperatures peaked at 15:30 hours, reaching the values of about 68, 63, 61 and 56^{o}C respectively. After 12:30 hours, although incident radiation starts dropping, the SCONOR temperature continued rising for upward of three hours. A close look at the ambient temperature shows that it remained around 30oC from 12:00 hours to 16:00 hours with a little drop to 29oC at 15:00 hours. This period matches the period of peak SCONOR, bond, tube and water temperatures.

Figures 4.20-4.23 provides the plots of predicted ambient; beam, diffuse and total solar radiation; thermal energy absorption and loss capacity; and SONOR, bond, tube and water temperatures for the city of Owerri in November, 2017. Fig. 4.20 shows that the ambient temperature on the test day ranged from 25^{o}C at 06:00 hours to a maximum of 32^{o}C at 13:00 hours. It maintained this value till about 15:00 hours and thereafter decreased slightly till 0:00 hours to 24^{o}C and increased slightly to 26^{o}C from 01:00-04:00 hours at 06:00 hours of the next day.

Fig. 4.21 shows the predicted beam, diffuse and total incident solar irradiation on the SCONOR surface on the test day, 29/11/2017. The beam component of radiation reached a value of about 950W/m^2 at 12:30 hours while the total radiation comprising the beam and diffuse components reached 890W/m^2 at the same time. There is no much difference between the beam component of radiation and total radiation (about 60W/m^2), which make up the diffuse component. Again, during this month of November, a time lag of about one hour elapsed in between the peak time

of solar irradiation and the peak time of ambient temperature, although ambient temperature continued to rise till about 15:00 hours.

Fig. 4.22 shows the absorbed thermal energy and the corresponding losses from the collector in November. While the highest absorptions of solar energy occurred at the region bounding the bond and the tube with the water, the lowest absorptions occurred at the fin extension spanning the width of the collector. It shows that heat progressively flowed from the edge to the centre of the plate from where it now transfers to the bond, tube and the water, as in the previous seasons. This is also in consonance with the thermal distribution shown in Fig. 4.1 as regions of high energy absorptions correspond to the regions of low energy losses and vice versa. It was also observed just like in January, April and September that greater losses occurred at the lower side of the plate spanning the width which could be as a result of lapses in the lagging of the plate underneath. The heat absorption capacity of the collector was less than zero after 17:30 hours outside the bond region in November and within the bond region, it becomes zero after 18:00 hours when there is no more solar radiation after sunset. After 18:00 hours, even though there is no more solar absorption, losses continued to occur in the SCONOR because it is being cooled to the ambient condition before the commencement of nocturnal process. The high heat concentration regions represented by 2b, 2c and 2d on the figure appear to record high thermal losses during this period as it begins to rise immediately at 18:00 hours. This is the same case in September as shown in Fig. 4.18. In the month of January, there was no significant variation in thermal energy losses from the SCONOR after 18:00 hours from the regions of high heat concentration 2b, 2c and 2d in Fig. 4.10 until about one hour thirty minutes later beginning at 19:30 hours. This could be as result of the fact that ambient conditions remained fairly around 30^{o}C till 19:00 hours before it witnessed a sharp drop to 26^{o}C at 20:00 hours. The same trend is

observed in April, Fig. 4.14 where the fluctuations in ambient temperature remained at about 1^{o}C from 16:00 hours to 19:00 hours until a sharp drop occurred at 21:00 hours when it became 26^{o}C. Fig. 4.23 shows the predicted SCONOR, bond, and tube surface and water temperatures in November. The SCONOR, bond, tube and water temperatures peaked at 15:30 hours, reaching the values of about 111, 108, 105 and 84^{o}C respectively. After 12:30 hours, although incident radiation starts dropping, the absorber temperature continues rising for upward of three hours.

From the Figures, it shows that the SCONOR absorbed maximum irradiation of 980, 850, 475 and 950W/m^2 for the months of January, April, September and November respectively. For the month of January, the plate, bond, tube and water attained maximum temperatures of 116, 111, 103 and 85^{o}C respectively. In April, the plate, bond, tube and water maximum temperatures are predicted to be 102, 98, 94 and 76^{o}C respectively and in September, they are 68, 63, 61 and 56^{o}C for the plate, bond, tube and water respectively, while in November they are 111, 108, 105 and 84^{o}C respectively. These months are representatives of the late harmattan, early rainfall, late rainfall and early harmattan periods typical of Nigerian climatic environment. While the solar irradiation on the SCONOR at the different seasons peaked at 12:30 hours, the plate, bond, tube and water temperatures peaked at 15:30 hours. This means that after 12:30 hours, although incident radiation starts dropping, the SCONOR (absorber) temperature continued rising for upward of three hours. Riahi and Taherian (2011) reported 80^{o}C maximum temperature of the central riser of the collector plate occurring at 15:00 hours; Balen et al (2003) reported peak temperature of about 62^{o}C at 16:00 hours; Agbo (2011) reported peak absorber temperature occurring at 14:00 hours while Mingke et al (2015) reported peak temperature of 109^{o}C at 12:30 hours. Apart from the 12:30 hours observation, the rest are consistent with the current finding. The maximum temperatures of the plate observed in their studies are lower than the current study

with the exception of Mingke et al. This could be attributed to more efficient modelling of the heat flow process adopted in the bond region of the current study through determination of optimal bond width and thickness that reduced the contact resistance between the absorber plate and water tubing. The amount of thermal energy absorbed by the system during the tested seasons reveals that even during the worst case weather periods, the system can still perform significantly well. The different thermal conductivities of the SCONOR, bond, tube and water inform the variations in their temperatures during the diurnal heating period. The thermal performance of the system will be greatly enhanced if the total amount of heat absorbed by the SCONOR is conducted to the water via the bond and tube. However, the low thermal conductivities of the bond and water bring about a marked but progressive difference in their temperatures. Because of the optimization of the bond region, the thermal resistance in the SCONOR-bond-tube region is greatly reduced leading to reduced temperature differences between in the order of 5, 8 and 18^{o}C for the SCONOR and bond; bond and tube; and tube and water respectively, for instance in January. A look at Figs 4.10 and 4.14 shows that within the regions marked b, c and d on the plots, the rates of solar energy absorptions by the SCONOR are higher than the rate of heat conduction, which will greatly enhance the heat flow into the water around the SCONOR-bond-tube high heat region.

Fig 4.24 shows the maximum temperatures obtained for the months investigated. While the SCONOR performed best in January with maximum water temperature of 85^{o}C, followed by November with maximum water temperature of 84^{o}C, the months of April and September has the least performance with maximum water temperatures of 76 and 56^{o}C respectively.

4.2.2.2 The SCONOR cool down phase

Figs 4.25, 4.26 and 4.27 show the heat flow vector, surface and history (variation of temperature with time) plots of SCONOR-bond-tube-water cool down phase in January and Figs 4.28, 4.29 and 4.30 show the same plots for the SCONOR-bond-tube-water cool down phase in April. Also, Figs. 4.31, 4.32 and 4.33 show the heat flow vector, surface and history plots for the month of September while Figs 4.34, 4.35 and 4.36 show the same plots during November period. The cool down phase begins at about 18:00 hours after sunset (17:51 hours). At this time there will be no need to screen (or cover) the system from exposure to solar radiation since theoretically, it is known that the sun has set. Even though they might be some traces of radiation falling upon the system, one of the properties of spectral selective surfaces is that outside solar radiation and atmospheric window spectra (or bands) the absorptivity of the surface equals its emissivity, and so the net absorption of radiation is zero as it emits all the energy absorbed if any at such periods. However, the insulation box is opened at onset of the cool down process in order to expose the tube bond regions to the ambient air to further enhance heat transfer at a quicker rate. With the transparent windscreen and the SCONOR-bond-tube regions now exposed to the ambient air, the system began to cool down rapidly after a delay period of about 1 hour 30 minutes in January and about 1 hour in April as revealed by high amount of losses initiating from the points labelled 2e in Fig 4.10 and point marked 2d in Fig 4.14 representing thermal energy absorption and losses profiles in January and April respectively. The same trend is also observed in the months of September and November but cooling almost commenced immediately a short while after sunset as shown by the upshot of the line marked 2b, 2c, 2d in Figs 4.18 and 4.22 just a bit after 18:00 hours. At 18:00 hours there in more water circulation in the system but little drops of water at a higher temperature is still left on the inner tube surface. The SCONOR, bond, tube and water that were initially at higher temperatures were observed to drop rapidly to almost equilibrium values

at about 20:00 hours for the different months. In each case, the SCONOR, bond and tube temperatures were a little above the water temperature. This is understandable because the water inside is not exposed to the ambient and so the SCONOR will first cool down, followed by the bond and tube at the interface of weld between them and in that order heat transfer will begin due to the resulting temperature gradient.

Figs 4.25, 4.28, 4.31 and 4.34 showing the vector plots of heat flow from the SCONOR during the cool down phase reveals an interesting feature of the system as significant amount of heat energy is observed leaving the system for each of the months. The figures show that the maximum amount of energy being conducted out of the system for the months of January, April, September and November are respectively 2.10 x 10^5J/m^2-h, 2.17 x 10^5J/m^2-h, 2.21 x 10^5J/m^2-h and 2.16 x 10^5J/m^2-h. This occurs at the bond region of the SCONOR towards the surface. The heat flow direction as indicated by the arrows and the maximum energy losses in September followed by April, have further led credence to the results discussed in the preceding section as periods of low SCONOR performance match these periods of maximum energy losses.

4.2.2.3 Nocturnal cooling of water in the SCONOR

Figs 4.37-4.40 show the contour, heat flow vector, surface and history plots of temperature in the system during the nocturnal cooling of water from 17/01/2017 to 18/01/2017, in Owerri. Fig 4.37 enables the visualization of the temperature distribution in the system during the nocturnal cooling process in the XY global coordinate while Fig 4.38 is the vector plot of heat conduction process in the system during this period. It can be observed that the portion of the SCONOR around the bond-tube-water region losses a greater amount of energy in the order of 2.24 x 10^4J/m^2-h while the portions of the plate outside this region losses energy in the order of 0.7-1.15 x 10^4J/m^2-h. This means that since water is not continuously in direct contact with the plate

along its width excepting at the points of contact with the bond and tube, the plate experienced non-uniform cooling. The surface plot of temperature of Fig 4.39 better reveals the nature of heat flow during the nocturnal cooling process. A higher temperature was observed towards the fin tip at the SCONOR edge, while a lower temperature recorded at the portion around the bond-tube interface. This temperature profile is symmetrical about the centre of the SCONOR-bond-tube region. At the onset of nocturnal cooling and while the process lasts, the water in the tube is at a higher temperature than the tube, bond and SCONOR. Because of this progressive temperature gradient, heat transfer occurs from the water in the tube by convection at the interface between the water and the inner tube walls, from where the heat is transferred by conduction from the tube to the bond and finally to the SCONOR. This heat flows significantly in the x-direction towards the tip of the fin from where it is convected to the ambient. Apart from this energy transfer resulting from the internal energy of the system, heat is also transferred from the surface of the system to the ambient sky at a lower temperature of 3K. Since the system is at a lower temperature than the ambient, the tendency is to gain heat by convection from the ambient, a phenomenon which greatly affects the nocturnal cooling process. This is taken care of by insulation underneath and the windscreen atop the SCONOR that shields it from wind convection. Fig. 4.40 shows that the water, tube, bond and SCONOR progressively cooled from 20:00 hours of 17/01/2017 to 06:00 (i.e. 30 on the T-axis) hours of 18/01/2017. At every point in time their temperatures remained below ambient and above the sky temperature. The lines marked 1d, 1c, 1b and 1a represent the water, tube, bond and SCONOR temperatures respectively while that marked 2 and 3 are the ambient and sky temperatures respectively. Nocturnal cooling started at about 20:30 hours on 17/01/2017 and the least temperature depression occurred at about 28:30 hours (i.e. 4:30am) on 18/01/2017. It was expected that the

temperature would continue to decrease progressively until 06:00 hours of 18/01/2017 but that was not the case as little increases in ambient temperature occurred and corresponding little increases in the water, tube, bond and SCONOR temperatures were also observed. For these reasons the temperature profile in Fig 4.40 experienced an upward movement from the point of minimum depression. Finally, it was seen that the SCONOR cooled from 27.38^{o}C to a temperature of 18.04^{o}C the next day. This means an equilibrium temperature of 18.04^{o}C and a temperature of about 4.96^{o}C below ambient in January.

Figs 4.41-4.44 show the contour, vector, surface and history plots of temperature in the system during the nocturnal cooling of water from 18/04/2017 to 19/04/2017 in Owerri. Fig 4.41 shows the contour plot of temperature distribution in the system during the nocturnal cooling process in April while Fig. 4.42 shows the vector plot of conductive heat flow on the global coordinate. The surface plot of temperature of Fig 4.43 better reveals the nature of heat flow during the nocturnal cooling process. These follow the same trend with the January plots. However, it can be observed that the amount of energy being conducted out of the system has reduced at this time, with the portion of the around the bond-tube-water interface having 1.15 x 10^{4}J/m^{2}-h and that outside this region having 0.65 x 10^{4}J/m^{2}-h. Apart from this energy transfer resulting from the internal energy of the system, heat is also transferred from the surface of the system to the ambient sky presumably at a lower temperature of 3K. Since the system is at a lower temperature than the ambient, the tendency is to gain heat by convection from the ambient, a phenomenon which greatly affects the nocturnal cooling process. This is taken care of by insulation underneath and the windscreen atop the SCONOR that shields it from wind convection. Fig. 4.44 shows that the water, tube, bond and SCONOR progressively cooled from 20:00 hours of 18/04/2017 to 06:00 (i.e. 30 on the T-axis) hours of 19/04/2017. The temperatures remained

below ambient and above the sky temperature throughout the nocturnal process. The lines marked 1d, 1c, 1b and 1a represent the water, tube, bond and SCONOR temperatures respectively while that marked 2 and 3 are the ambient and sky temperatures respectively. Nocturnal cooling started at about 20:30 hours on 18/04/2017 represented by the point on Fig 4.44 where the lines of temperature marked 1d, 1c, 1b and 1a for the water, tube, bond and SCONOR respectively falls below the ambient temperature. At this point, the temperature has sharply dropped to 26.97^{o}C as is revealed on Figs 4.41 and 4.43. The least temperature depression occurred at about 28:00 hours (i.e. 4:00am) on 19/04/2017. It was equally expected that the temperature would continue to decrease progressively until 06:00 hours of 19/04/2017 but that was not the case as little increases in ambient temperature occurred and corresponding little increases in the water, tube, bond and SCONOR temperatures were also observed. For these reasons the temperature profile in Fig 4.44 also experienced an upward movement from the point of minimum depression. Finally, it was seen that the SCONOR cooled from 26.97^{o}C to a temperature of 20.38^{o}C the next day. This means an equilibrium temperature of 20.38^{o}C and about 4.62^{o}C below ambient in April.

Figs 4.45-4.48 show the contour, heat flow vector, surface and history plots of temperature in the system during the nocturnal cooling of water from 18/09/2017 to 19/09/2017 in Owerri. These show at a glance that the system cooled from 27.09^{o}C from the night of 18/09/2017 to 19.90^{o}C in the morning of 19/09/2017. Fig 4.47 represents the surface plot of temperature which better reveals the nature of heat flow during the nocturnal cooling process. This temperature profile is symmetrical about the centre of the SCONOR-bond-tube region and a higher temperature was observed at the portion of the SCONOR outside the bond-tube-water region. The same trend for the months of January and April is still maintained but the quantity of energy being conducted

out of the system at this period as well as the temperature variations differ significantly. This energy was observed to be 0.95 x 10^4J/m^2-h and 0.45 x 10^4J/m^2-h at the portion of the SCONOR around the bond-tube-water region and outside this region respectively. This informs the temperature variation along the fin with (i.e. the width of the SCONOR from the tube centre to the edge of the plate). This does not necessarily mean that the plate is hotter than the tube and its content at this period. Nocturnal cooling is seen occurring since at every portion of the plate the temperature remains below ambient. Fig. 4.48 also shows that the water, tube, bond and SCONOR progressively cooled from 20:00 hours of 18/09/2017 to 06:00 (i.e. 30 on the T-axis) hours of 19/09/2017. At every point in time their temperatures remained below ambient and above the sky temperature. The lines marked 1d, 1c, 1b and 1a represent the water, tube, bond and SCONOR temperatures respectively while that marked 2 and 3 are the ambient and sky temperatures respectively. Nocturnal cooling started at about 20:30 hours also on 18/09/2017 represented by the point on Fig 4.48 where the lines of temperature marked 1d, 1c, 1b and 1a for the water, tube, bond and SCONOR respectively falls below the ambient temperature. At this point, the temperature has sharply dropped to 27.09^{o}C as is revealed on Figs 4.45 and 4.47. The least temperature depression occurred at about 28:00 hours (i.e. 4:00am) on 19/09/2017. Finally, it was observed that the SCONOR cooled from 27.09^{o}C to a temperature of 19.90^{o}C the next day. This means an equilibrium temperature of 19.90^{o}C and about 4.10^{o}C below ambient in September.

Figs 4.49-4.52 show the contour, heat flow vector, surface and history plots of temperature in the global coordinate system during the nocturnal cooling of water from 29/11/2017 to 30/11/2017 in Owerri. While Fig 4.49 presents the temperature distribution in the system during the nocturnal cooling process in the XY global coordinate, Fig. 4.50 shows the vector of heat energy

that is being transferred majorly by the combined effects of convection and conduction from the various components towards the SCONOR surface from where it will be given off to the ambient. Fig. 4.49 shows at a glance that the system cooled from 27.27^{o}C from the night of 29/11/2017 to 19.07^{o}C in the morning of 30/11/2017 and Fig. 4.50 shows that about 1.55 x 10^{4}J/m^{2}-h energy transfer occurred at the portion of the plate around the bond-tube-water region while about 0.75 x 10^{4}J/m^{2}-h energy loss occurred outside this region. Fig 4.51 represents the surface plot of temperature which better reveals the nature of heat flow during the nocturnal cooling process. This temperature profile is also symmetrical about the centre of the SCONOR-bond-tube region, with a progressive temperature observed from the centre of the plate towards the fin tip at the SCONOR edge. At the onset of nocturnal cooling, the water in the tube is at a higher temperature than the tube, bond and SCONOR. Because of this progressive temperature gradient, heat transfer occurs from the water in the tube by convection at the interface between the water and the inner tube walls, from where the heat is transferred by conduction from the tube to the bond and finally to the SCONOR. This heat flows significantly in the x-direction towards the tip of the fin from where it is lost by convection to the ambient. Since the system is at a lower temperature than the ambient, the tendency is to gain heat by convection from the ambient, a phenomenon which greatly affects the nocturnal cooling process. This is taken care of by insulation underneath and the windscreen atop the SCONOR that shields it from wind convection as have been stated previously. Fig. 4.52 shows that the water, tube, bond and SCONOR progressively cooled from 20:00 hours of 29/11/2017 to 06:00 (i.e. 30 on the T-axis) hours of 29/11/2017, with their temperatures remaining below ambient and above the sky temperature throughout the nocturnal cooling period. The lines marked 1d, 1c, 1b and 1a represent the water, tube, bond and SCONOR temperatures respectively while that marked 2 and

3 are the ambient and sky temperatures respectively. Nocturnal cooling started at about 20:30 hours also on 29/11/2017 represented by the point on Fig 4.52 where the lines of temperature marked 1d, 1c, 1b and 1a for the water, tube, bond and SCONOR respectively falls below the ambient temperature. At this point, the temperature has sharply dropped to 27.27^{o}C as is revealed on Figs 4.49 and 4.51. The least temperature depression occurred at about 27:30 hours (i.e. 3:30am) on 30/11/2017. Again, it was equally expected that the temperature would continue to decrease progressively until 06:00 hours of 30/11/2017 but that was not the case as little increases in ambient temperature also occurred and hence the corresponding little increases in the water, tube, bond and SCONOR temperatures that were observed. For these reasons the temperature profile in Fig 4.52 also experienced an upward movement from the point of minimum depression. Finally, it was seen that the SCONOR cooled from 27.27^{o}C to a temperature of 19.07^{o}C the next day. This means an equilibrium temperature of 19.07^{o}C and about 4.93^{o}C below ambient in November.

Fig. 4.53 presents the minima of temperatures obtained for each month of the investigation during the nocturnal cooling process. It aptly reveals that the water temperature remained higher than the tube temperature; the tube temperature higher than the bond temperature whiles the bond temperature remained higher than the SCONOR temperature, progressively in that order throughout the nocturnal cooling period. The months of January and November have the best promise for optimal performance of the SCONOR for nocturnal cooling. This is consistent with expectation since at such periods the environment is less prone to high humidity effects.

Fig. 4.53b shows the 24-hour cycle of the system in the study location for the month of November. This is a combination of the processes described above for November, covering diurnal water heating from 06:00 hours of 29/11/2017 to 18:00 hours of the same day, the cool

down period from 18:00 hours to 20:00 hours of 29/11/2017, which is indicated from the point of sharp drop in temperature to the point where it has reached ambient conditions at 20:00 hours and finally the nocturnal cooling of water from 20:00 hours to 30:00 hours of the next day 30/11/2017.

4.2.3 Performance evaluation in 5 Nigerian cities

The performance predictions for the months of January, April, September and November during the nocturnal cooling mode all follow the same trend. It was observed that throughout the seasons, the nocturnal cooling commenced at the same time in the study location but the cooling capacity varies significantly throughout the period. The potential for nocturnal cooling is higher in January with a temperature depression of 4.96^{o}C below minimum ambient temperature, followed by November with a temperature depression of 4.93^{o}C and April with a temperature depression of 4.62^{o}C and the least is in September with a temperature depression of 4.10^{o}C. This means that on the average in Owerri, Nigeria a 5^{o}C below ambient is common. Other researchers have reported different values at different locations round the globe. Ghasem et al (2010) reported 7^{o}C for the city of Tehran, Iran; Mingke et al (2015) reported 13^{o}C for the city of Heifei, China and Ali et al (2016) reported 18^{o}C for the city of Shiraz, Iran.

This could be greatly attributed to variations in cloud cover and relative humidity during the rainy and harmattan seasons at the present study location and also the various study locations reported. Periods of high relative humidity and high ambient temperature result in less cooling rate (Ahmed and John, 2014), as the rate of the net sky radiation is significantly reduced at such periods. The hourly wind velocity data for the test location were not available; an average value of 2.8±0.81m/s as reported by Anyanwu and Iwuagwu (1995) was used as a constant value

throughout the test period. Since the convective heat transfer coefficient value is proportional to the wind velocity, it means there was heat addition to the water as a result of convection effect from the ambient hence the reduction in the cooling process by radiation from the water to the sky. However, it is evident from the results that the system has the capacity for nocturnal cooling since an average of 5^{o}C below ambient is enough to cover a fraction of cooling demand.

Figs 4.54-4.57 show the performance prediction of the system in five Nigerian cities representing the different five geographical locations in the country with accessible climatic data for the chosen period, 29/11/2017. The five cities include Owerri, Port Harcourt, Ikeja, Maiduguri and Sokoto. This was done to ascertain the heating and cooling capacity of the system for the various cities. The same simulations reported above for the city of Owerri as shown in Figs 4.10 to 4.53 were undertaken for the cities during the early harmattan period typical of the month of November. The figures maintain a uniform trend for the different cities and clearly show that Sokoto has the best promise for solar water heating, followed by Maiduguri, Ikeja, Owerri and finally Port Harcourt while during nocturnal water cooling Port Harcourt showed early improved performance as nocturnal cooling commenced first at about 20:00 hours of 29/11/2017 but at about 0:00 hours of the next day 30/11/2017, Maiduguri witnessed a better performance till 06:00 hours of the day. The city of Port Harcourt still maintained the second lead followed by Owerri, Sokoto and Ikeja respectively.

4.2.4 Stratification in the storage tanks and comfort conditioning

4.2.4.1 Diurnal stratification and nighttime comfort heating

Having ascertained that the system can perform favourably well in different seasons and locations for diurnal heating and nocturnal cooling of water, the accumulative heating rates (or

long term performance) in the storage tank of the system during diurnal solar heating has been numerically investigated by incorporating two 300 litre water storage reservoirs as shown in Fig 3.1. The essence is to determine the amount of thermal energy harnessable from the system under the closed operation mode. At 06:00 hours of 29/11/2017, water in reservoir A is initially at 24^{o}C. Water circulating pump A is turned ON and the pump circulates the water in the reservoir A (hot storage tank) at a flow rate of 0.083kg/s from the bottom of the tank through the SCONOR where it is heated and then leaves the top of the SCONOR back into the tank. The process continues until 18:00 hours when there is no more solar radiation and the pump is turned OFF. At any time during the heating period the temperature at the bottom of the tank after mixing has occurred becomes the inlet temperature into the SCONOR.

As shown in Fig. 4.58, the storage tank was divided into five sections along its height represented as 1, 2, 3, 4, 5 from top to bottom of tank respectively. The figure shows that a high level of stratification occurred in the hot water tank with the top of tank being hotter than the bottom. Ts1 represents the temperature at the top layer in the tank while Ts5 represent the bottom layer. Ts2, Ts3 and Ts4 represent the layer in between the top and bottom. Tco is the outlet SCONOR temperature. At the end of heating period the water from the outlet of the SCONOR attained the highest temperature of about 64^{o}C while the storage tank attained a temperature of about 57.58^{o}C at 16:00 hours. The tank still retained its stratification well into the night. The results of the present model compare well with the findings of Sako et al (2007) who reported an average tank temperature of 60°C at 16:00 hours in a work on solar done on a solar water heating system using a conventional solar collector in Côte D' Ivoire. Zerrouki et al. (2002) also reported an average tank water temperature of 54°C at 18:00 hours in Algeria. Also, Riahi and Taherian (2011) reported an average storage tank temperature of 64^{o}C at 16:00 hours

in a solar water heating system in Iran while Balen et al (2003) reported an average storage tank of 60^{o}C at 16:00 in an Irish climate.

The month of November has been chosen for long term performance evaluation, being the period of early harmattan, with ambient temperatures reaching a maximum of about 32^{o}C during the day and a minimum of about 22^{o}C during the night extending into the early hours of the next day. The tendency at this period is for humans to feel uncomfortable as the body tends to lose heat to the environment. There is therefore need for comfort heating at this period. So, after 18:00 hours, pump A is now OFF. Pump B is turn ON and it begins to circulate the hot water from reservoir A through the low temperature radiator installed in the room. As the water passes through the room radiator, it exchanges its energy with the colder room and flows back into the tank. This process continues until 06:00 hours of 30/11/2017.

As shown in Fig. 4.59, during the comfort heating period from 18:00 hours of 29/11/2017 to 06:00 hours of 30/11/2017, the temperature of the top layer of the storage tank that goes into the low temperature radiator continued to decrease. The only possible explanation to this observation is that its energy is being utilized for maintaining the room temperature at a fairly comfortable value. The ambient temperature in November 29, 2017 showed that at 18:00 hours the temperature was 30^{o}C and at 19:00 hours it has witnessed a sharp drop to 26^{o}C. At this period people have started feeling cold and would desire some level of warmth. It is observed that the room temperature fluctuated between 31.2 from 18:00 hours on 29/11/2017 to 31.1^{o}C on the morning hours of 30/11/2017. This is approximately 5^{o}C above ambient temperature. This favourably compares with the work of Zeghib and Chaker (2015) carried under Algerian climate where a temperature of about 7^{o}C above ambient was reported. The outlet water temperature from the radiator is fairly varied between 29.5 to 29.6^{o}C throughout the comfort heating period

as shown in Fig 4.49 and better presented in Fig. 4.60 also. This is consistent with the expectation as the water loses heat to the room and so cools down before flowing back into the storage tank.

Fig. 4.61 presents the effect of thermal energy loss to the room from the water in the storage tank being circulated through the radiator. As can be seen, even in the course of comfort heating using the thermal energy from the hot water, stratification is maintained in the tank with the top of the tank retaining its highest temperature. This phenomenon continues until about 24 (00:00) hours of 30/11/2017. At this point stratification is almost destroyed in the tank. This continued for about 1 hour till 25 (01:00) hours, after which it resumed again fairly significantly till 28 (04:00) hours of 30/11/2017 where it assumed a uniform temperature. From 04:00 hours stratification was observed but it was no more significant. At about 29.85 (05:51) hours, stratification began again in the tank. An interesting observation here is that the bottom of the tank became cooler from 01:00-05:51 hours as shown by the blue line representing the temperature of the bottom layer of the tank within this period. This observation corresponds to the phenomenon of nocturnal cooling process where the denser water layer settles at the tank bottom. At 05:51 hours, corresponding to the exact sunrise time in the study location, it reverses again, signifying that the water in the tank has now started receiving energy from the sun. As shown in Fig. 4.61, the average temperature of water in the hot storage tank at the end of comfort heating at 06:00 hours of 30/11/2017 is approximately 24^{o}C. This evinces that the assumed initial temperature is admissible.

4.2.4.2 Nocturnal stratification and daytime comfort cooling

At 20:00 hours of 29/11/2017, pump A is turned ON again and all the valves connecting the pipes to the cold water reservoir B are opened. The pump circulates water from the top of the

cold water tank through the SCONOR where it is cooled by nocturnal radiation to the sky. The cooled water flows back into the tank through the bottom. This is to enable the evaluation of the accumulative cooling effect in the storage tank over the entire cooling system. The water circulation continued at flow rate of 0.083kg/s until 06:00 hours of the next morning so that enough cold water can be stored in the tank to be used to provide comfort condition in an office room the next day from 08:00-17:00 hours being operational hours in typical office environments.

Fig. 4.62 shows water stratification in the cold storage tank. Here the tank is divided into five zones along its height numbering from 1 at the bottom to 5 at the top. It is observed from the commencement of the cooling process at 20:00 hours of 29/11/2017 to the end at 06:00 hours of 30/11/2017, there was variation in the temperature of the zones. The warmest zone continuously remained at the top while the coldest remained at the bottom. At the end of the nocturnal cooling of the water by the SCONOR, during the following day 30/11/2017 from 8:00AM to 5:00PM, the cooled water was employed to condition the office space to remain thermally comfortable throughout the specified operational hours. This is shown in Fig. 4.63. The figure reveals that the temperature of the water at the bottom layer of the storage tank that goes into the room convector continued to increase as it exits the convector (i.e. Tr2 of line 2 in the Fig). This could be largely attributed to the obvious it is absorbing energy from the room for maintaining the room temperature at a fairly comfortable value. The ambient temperature line 3 on the Fig. 4.63 reached a maximum of about in November 30, 2017 showed that at 18:00 ho32.5^{o}C at 15:00 hours. At this period people have started feeling hot and would desire some level of comfort. It is observed that the room temperature fluctuated between 26.6 from 08:00 hours on 30/11/2017 to 26.8^{o}C on the evening hours of the same day. This is approximately 5.7^{o}C below ambient

temperature. This also is consistent with the findings of Meir et al (2003) that reported 5^{o}C below ambient in Norway; Dobson (2005) who reported 5^{o}C below ambient in Namibia and Nwaigwe et al (2012) who reported 4.01^{o}C below ambient in Nigeria, for similar works carried out using conventional nocturnal radiators. The outlet water temperature from the convector fairly varied fluctuated around 33^{o}C throughout the comfort cooling period as shown in the figure. This is consistent with the expectation as the water gains heat from the room and so heats up before flowing back into the storage tank. During comfort cooling period from 08:00 to 17:00 hours, as shown in Fig. 4.64, increase in temperature of higher zones at this period is slower than lower zones due largely because water leaves the tank from the bottom of the tank and upper zone replaces the lower zone. And after a while lowest zone gains temperature from its upper zone. Also, there is no remarkable difference between the water entering at the top from the convector and the top zone temperature.

4.2.5 Comparison of present model results with existing results for benchmarking

Figs. 4.65 shows the comparison of the model results with the experimental results of Riahi and Taherian (2011) obtained in a similar work during the solar heating phase in Babol city, Iran. A close look at the figure shows that the model moderately under-predicted the SCONOR temperature during the early hours, over-predicted the temperature in the afternoon and finally moderately under-predicted the temperature. The time at which the SCONOR reached its peak temperature was adequately predicted. Generally, the predicted and measured plate temperature followed the same trend.

Fig. 4.68 is the comparison of the present model results during the nocturnal cooling of water through the SCONOR with the experimental results from the work of Mingke et al (2015). It was

observed that the initial temperature of the plates varied from the beginning of nocturnal cooling. The good thing is that they maintain the same trend. The deviation could be as a result of differing ambient conditions. Since the initial conditions are markedly different, it cannot be said that the model over-predicted the temperature during the test period.

Stratification in the storage tanks were validated using the works of Riahi and Taherian (2011) and that of Ali et al (2016) respectively. The model results closely matched that of experimental at the early period of commencement of heating and fairly under-predict the temperature the rest of the period as shown in Fig 4.66. As it was the case with nocturnal cooling in the SCONOR, storage tank cooling also witnessed a very sharp deviation from the experimental results. Once again, a lower initial temperature of the radiator was used in the Work done in Iran than that used in a tropical country, Nigeria. While the present model predicted an average temperature of $21^{o}C$ at 28:00 hours, that of Ali et al (2016) recorded $2^{o}C$ at 29:00 hours.

Figs 4.68 and 4.69 are comparisons of the model results with a work done in Nsukka Nigeria by Anyanwu (1996). While the model under-predicts the SCONOR temperature in the solar heating phase, the model results closely matched experimental results during the nocturnal cooling process. Fig. 4.69 also reveals that the outer tube temperature was correctly predicted during the solar heating and nocturnal cooling phases with minimal deviations. During the cool down phase, the model over-predicted the SCONOR and outer tube temperatures. However, it can be observed that the model results and experimental results follow the same trend. The variations being noticed could be as a result of periodic fluctuations in ambient conditions and weather data.

4.2.6 Parametric analyses

Figs 4.70-4.75 show the effects of the bond specifications on the performance of the SCONOR. Bond widths were kept constant from 0.1 to 0.3 (dimensionless x-axis) while bond thicknesses were varied to determine the optimum width and thickness for optimum performance of the system. As shown in Fig. 4.70, even though the water absorbed a greater amount of heat at thicknesses of 0.001 and 0.0015m at 0.1m width reaching almost above 100^{o}C, the water temperature drastically reduced to about 50^{o}C from 0.002m bond thickness, decreasing further to a low value of about 40^{o}C at thicknesses of 0.003, 0.0035 and 0.004m.

Fig. 4.71 shows the temperature variation of the water with time at 0.15m bond width and 0.001-0.004m thicknesses. At a point where the bond thickness is 0.001m, the water also attained fairly above 100^{o}C at 16:00 hours. Increasing the thickness further led a sharp drop in the water temperature to about 62^{o}C. Thereafter, it followed the trend of sharp drop in temperature reaching a low of about 45^{o}C from the thicknesses 0.002, 0.003, 0.0035 and 0.004m.

When the bond width is further increased to 0.2m, the variation of water temperature with time became fairly uniform, with 0.2m width and 0.0015m thickness receiving the highest temperature of about 69^{o}C. It is also observed that the absorption of heat energy by the water increased at the thicknesses 0.002, 0.003, 0.0035 and 0.004m. However, only 0.002m thickness attained a temperature of about 52^{o}C at 15:00 hours. At the other thicknesses above 0.002, the water temperature remained below 50^{o}C.

At 0.25m bond width as shown in Fig 4.73, it was observed that the water absorption trend continued the same way but at this specification, the water could only attain fairly above 70^{o}C at 15:30 hours at 0.0015m thickness. At 0.001m and 0.002m the water received almost the same amount of heat attaining equal temperatures of about 60^{o}C at 15:30 hours. This trend was also

seen at 0.003, 0.0035 and 0.004m thicknesses where the water temperatures attained peak values of about 58^{o}C.

A look at Figs 4.74 and 4.75 shows that they maintain the same trend but close observation reveals that at 0.26m width peak temperature occurred at 15:30 hours while it occurred at 16:00 hours with 0.3m width. Again, 0.3m thickness would extend beyond the point of contact of the outer tube surface with the SCONOR. This would amount to wastage of material and increased thermal resistance at the SCONOR-bond-tube interface. This could be the simple explanation of the delay in the water attaining its peak temperature at the point of SCONOR, bond and tube peak temperatures. Hence, for optimum performance of the system a bond width of 0.26m and thickness of 0.003m is recommended. This is because at 0.001 and 0.0015m the SCONOR is having a direct contact with the tube.

Fig. 4.76 shows the plot of maximum water temperatures obtained at different bond width and thicknesses. The water temperature was initially high at the 0.001 and 0.0015m bond thicknesses and at 0.1m bond width. Further increase in bond width resulted in sharp temperature drops at those two thicknesses and at 0.2m width, the temperatures became equal. Beyond 0.2m bond width, the water temperature at 0.0015m bond thickness increased and attained a maximum of 95.06^{o}C at 0.26m bond width whereas the temperature at 0.001m bond thickness dropped. One interesting feature is that above 0.0015m bond thickness, the water temperature steadily increased as the bond width increased, reaching a maximum at 0.26m width but never up to 95.06^{o}C. Therefore, this informs the choice of optimum bond width and thickness as 0.26m and 0.0015m respectively.

Fig. 4.77 presents the effect of riser tube spacing on the SCONOR performance at the different times during the heating operating mode. It was observed that the rate of absorption of energy by

the water increased progressively as shown in the increases in the temperature of water at different times from 0.025 to 0.3m tube spacing. The temperature of the water increased sharply from 0.025m at about 58^{o}C to about 70^{o}C at 0.05m tube spacing. A further increase to 0.075m tube spacing resulted in a little temperature difference from the previous spacing. From 0.1m tube spacing, the temperature difference no longer remained significant. The water has now attained its optimum temperature. This is commensurate with the natural characteristics of the system as increasing the tube spacing increases the fin width. And so, because of varying conductivities of the SCONOR, bond, tube and water, not all the energy received by the SCONOR would be transferred to the water. Therefore, the tendency is that thermal build up occurs on the plate, resulting in the increased water temperature as the plate temperature increases. To meet the heating and cooling demands, 0.1m riser tube spacing is recommended for prototype development.

Fig. 4.78 shows the effect of the number of polyethylene covers on the SCONOR performance at various times of the day during the diurnal heating mode. At a glance, it can be seen that the higher the number of windscreen on the SCONOR surface, the lower the thermal energy absorption by the surface. As the number of windscreen increased from 2 to 4, the amount of heat gained by the water decreased progressively. This is expected as increased number of windscreen would decrease the rate at which radiation is transmitted through it to the absorbing surface (Duffie and Beckman, 2006). For a hybrid absorbing surface therefore, a single windscreen will suffice for optimum performance since it is only when single windscreen was used that the water absorbed the highest temperature.

Figs 4.79-82 show the effect of Polyethylene Terephthalate (PET) spectral selective coating on carbon steel, aluminium and titanium as base solar absorbers. Aluminium possesses the best

promise for optimal absorption and emission followed by carbon steel and finally titanium. This is attributable to the high thermal conductivity of aluminium and its high thermal diffusivity as well. Aluminium has the highest thermal conductivity (204W/mK), followed by steel (54W/mK) and titanium (26W/mK). During the cool down phase, aluminium will maintain a gradual but sharp reduction in its surface temperature. However, welding aluminium to copper tubes requires great expertise coupled with the attendant cost. Hence, carbon steel can be used for the development of hybrid SCONOR once PET powder can be sourced.

CHAPTER 5

Conclusions and Recommendations

5.1 Conclusions

A 2-D mathematical model of a hybrid solar collector/nocturnal radiator (SCONOR) for solar water heating and its nocturnal cooling has been developed from first principle. The model equations were descretised using finite element numerical scheme and subsequently used to numerically investigate the dynamic bahaviour of the hybrid SCONOR for solar heating and nocturnal cooling, by carrying out transient performance predictions of the fluid temperature distributions within the SCONOR during the heating and cooling modes respectively using a computer code written with FlexPDE finite element model builder and numerical solver version 7.12. This was done to evaluate the instantaneous performance of the SCONOR in the heating and cooling modes during the prevailing weather conditions represented by the late harmattan (January), early rainy (April), late rainy (September) and early harmattan (November) seasons in the city of Owerri, typical of any Nigerian city. It was also evaluated for four other cities representing the geographical spread within the country of study during the early harmattan season.

Also another lumped analysis was carried out on both the hybrid SCONOR and hot and cold water storage tanks to evaluate the accumulative heating and cooling rates in the storage tanks. This was done by lumping the energy equations over the entire heating and cooling modes of operations of the system respectively, to evaluate the long term performance in the storage tanks since the average temperatures of the storage tank give an indication of the accumulative long term heating and cooling rates. The thermal energy accumulated in the hot storage tank during the diurnal solar heating was used to provide comfort conditions in a room space during the night

of the study period while the thermal energy accumulated in the cold storage tank during the nocturnal cooling process was used to provide comfort conditions in a moderate office space during the next 9 hours of the following day.

The model results were validated with available experimental data obtained from literature in similar works carried out in other regions of the world. The results obtained from the diurnal solar heating phase were validated with data from the experiment carried out by Riahi and Taherian (2011) in Babol city Iran. The time of occurrence of peak temperatures were accurately predicted while a mean deviation of about 4-8.6^{o}C was observed between the reported data and numerical predictions. The results obtained from instantaneous performance of the SCONOR were validated with the experimental results from the work of Mingke et al (2015) carried out in Heifei, China. For the instantaneous nocturnal performance of the SCONOR, the model results closely matched experimental results with a mean deviation of less than 0.2^{o}C, given that the initial conditions varied at about 7^{o}C which was completely maintained throughout the nocturnal period with minimal fluctuations. The accumulated performance results were validated using the work of Riahi and Taherian (2011) during the diurnal heating mode. The model results closely matched the experimental with a mean deviation of about 0.2-5^{o}C. During the accumulation of thermal energy in the cold storage, the results obtained were validated with the available experimental data in a similar work carried out by Ali et al (2016) in Shiraz, Iran. The large mean deviation is cancelled out by the differential in initial conditions for the two study location. The results obtained from the complete 24-hour period of instantaneous performance of the system was validated using the experimental results from Anyanwu (1996) done at the University of Nigeria, Nsukka where he provided data for the collector plate and tube surface. The model results closely matched experimental for the absorber and radiator functions of the

hybrid system with mean deviations of 3-5^{o}C in the diurnal heating mode and 0.2-1^{o}C in the nocturnal cooling mode. The bond, comfort heating and comfort cooling temperatures were not validated due to lack of data for such validations. However, the observed maintenance of the room temperature at 5^{o}C above ambient during comfort heating in the cold harmattan nights is worth mentioning. This is consistent with the reports from a numerical investigation carried out by Zeghib and Chaker (2015) for space heating using thermal energy from water heated under solar radiation, in Algeria, where they reported 7^{o}C above ambient throughout the 24-hour period. Also, during day comfort cooling, the room space was kept fairly at 5.7^{o}C below ambient during the day. This finding is also consistent with the findings of Meir et al (2003) that reported 5^{o}C below ambient in Norway; Dobson (2005) who reported 5^{o}C below ambient in Namibia and Nwaigwe et al (2012) who reported 4.01^{o}C below ambient in Nigeria, using the accumulated thermal energy of the cold storage tank to provide comfort conditions during the day.

The mean deviations show that they are good agreements between the model and experimental results. Therefore, the models were used to carry out parametric analyses to determine optimum parameters for the building of the physical prototype and setting up of experimental rig for future investigations. The results obtained from model parametric analyses showed that the bond width, bond thickness, tube spacing and number of windscreen have optimum values above or below which the performance of the system is reduced. The optimum bond thickness was determined to be 0.003m at bond width of 0.26m, that of tube spacing is 0.1m while the number of windscreen should not exceed one.

From the foregoing, the models developed predicted the performance of the thermal and dynamic behaviour of the system significantly well.

5.2 Recommendations

For further investigations, the following recommendations are made:

A prototype of hybrid solar collector/nocturnal radiator (SCONOR) should be developed and used as an experimental rig for the performance evaluation of the system behaviour using the materials recommended and the prevailing conditions in the study area. This would provide real field data for further improvement, and hence, commercialization of the system since the atmospheric temperature is believed to be changing and that would nonetheless have great effect on the results.

Since the cool down phase over-predicted the thermal behaviour of the system during the cool down, a more robust attention would be needed to investigate the system behaviour at such period using a more detailed mathematical model.

The model should be parameterized using actual weather data from other regions of the world more especially the regions where experimental data have been curled for validation studies in order to ascertain its predictive capability and accuracy around the globe.

Experimental investigation of the room temperatures during comfort heating and comfort cooling to provide real data for validation of comfort conditioning aspect of this work is highly necessary. Therefore, it is strongly recommended that future works could give that a serious attention.

It is also recommended that potential future researchers in this area should carry out economic optimization studies as well as the overall effect of the integrated energy system on the reduction of carbon dioxide (CO_2) emission to the atmosphere, which is believed to be the primary cause of global warming and climate change. This would be a good and interesting research area since it is obvious that there will be less emission of CO_2 into the atmosphere by the amount of fossil

fuel that goes into water heating and comfort conditioning which would be eliminated by the proposed system.

5.3 Contributions to Knowledge

(i) A comprehensive computer code that would enable numerical simulation of mathematical models developed for the dynamic behaviour of a hybrid solar collector/nocturnal radiator for diurnal solar water heating and nocturnal water cooling for space conditioning has been developed. This code is a good tool for solar water heating and nocturnal water cooling systems performance optimization. It can also be applied to other integrated sustainable energy system. This is to a great extent considered a valuable contribution to the growing body of knowledge on the performance of such systems.

(ii) Previous works have neglected the bond region, treating it as a lumped region with the plate and tube. However, the present work has treated the bond region as a separate zone of appreciable thermal mass to provide an insight into the effect of bond dimensions on the overall performance of the system.

(iii) The SCONOR cool down phase is another area of major contribution to knowledge. The present work has also provided a good insight into the instantaneous behaviour of the system during the cool down phase before the commencement of nocturnal cooling.

(iv) The parametric analyses done have given rise to obtaining the optimal bond width and thickness for optimal performance of the system.

REFERENCES

Adnan Q., Badescu, V. and Dartnall J.W. (2015) Hybrid Solar Collector for Water and Air Heating: Effects of Storage Tank Volume and Air Channel Shape on Efficiency, U.P.B. Sci. Bull., Series D, Vol. 77 (3) Pp 29-40.

Agbo, S. (2011) Analysis of the performance profile of the NCERD thermosyphon solar water heater, National Centre for Energy Research and Development, University of Nigeria, Nsukka, Journal of Energy in Southern Africa, Vol. 22 No 2, Pp 22-26.

Ahmed Y. T. A and John, W. D (2014) Design and Modelling of Water Chilling Production System by the Combined Effects of Evaporation and Night Sky Radiation, Journal of Renewable Energy, Volume 2014, DOI: 10.1155/2014/624502, Pp 1-8.

Ali, A., Karaei, M. A. and Hooman, F (2016) Investigation of Night (Radiative) Cooling Event and Construction of Experimental Radiator, International Journal of Advanced Biotechnology and Research, Volume 7 (5), Pp 1180-1184 .

Alomar, J and Kiss, L. I. (1988) Solar heating and radiative cooling using uncovered flat-plate collectors under Syrian climatic condition, Institute of thermal and systems engineering, Technical University H-1521, Budapest.

Amos, M (2009) Development of an advanced passive solar still with separate condenser, PhD Thesis submitted to Energy Systems Research Unit, Department of Mechanical Engineering, University of Strathclyde, Glasgow, United Kingdom.

Amraoui, M.A and Aliane K (2015) Numerical Study of the Three-dimensional Flow in a Flat Plate Solar Collector with Baffles, 22ème Congrès Français de Mécanique Lyon, 24 au 28 Août 2015.

Anyanwu E.E. and Iwuagu C.J. (1995) Wind Characteristics and Energy Potentials for Owerri, Nigeria, International Journal of Renewable Energy Volume 6, No 2, Pp 125-128.

Aouf A. A and Amer A. M (2014) Experimental Investigation of an Evacuated-Tube Solar Water Collector With Serpentine Through-Flow Pipe, Journal of Engineering and Development, Vol. 18, No.2, Pp 122-132.

Asere A. A., Dasin D. Y., and Habou, D. (2011) "Development of Convective Heat Transfer Correlations in The Cooking Pot of a Parabolic Concentrator Solar Cooker" Nigeria Journal of Solar Energy, Vol. 22, Pp 1-6.

ASHRAE (1997) ASHRAE Handbook of Fundamentals

ASHRAE (2000) ASHRAE Fundamentals Handbook

ASHRAE (2005) ASHRAE Fundamentals Handbook

ASHRAE (2011) ASHRAE Fundamentals Handbook

Ayoola, O. A (2014) Effect of Tank Size on the Temperature Distributions for Solar Water Heaters, M.Sc Thesis submitted to Mechanical Engineering Department, Eastern Mediterranean University, Gazimağusa, North Cyprus.

Balen, I., Soldo, V., and Kennedy, D. (2003) Analysis of cooling and heating of water with flat-plate solar radiators, Conference on Sustainable Developments of Energy, Water and Environmental Systems, Dubrovnik, Croatia.

Bathe, K (1982) Finite Element Procedures in Engineering Analysis Original US Edition Prentice-Hall Inc., USA.

BP (2015) BP Energy Outlook 2035 2015 Edition [www] Available from bp.com/statisticalreview [Accessed 24/04/2016].

BP (2016) BP Energy Outlook 2035 2016 Edition [www] Available from bp.com/statisticalreview [Accessed 24/04/2016].

Budihardjo, I. and Morrison, G.L. (n.d) Performance of Water-in-Glass Evacuated Tube Solar Water Heaters, School of Mechanical and Manufacturing Engineering University of New South Wales, Sydney 2052, AUSTRALIA.

Capellán-Péreza, I., Margarita, M., Carlos de C, Óscar C., and Luis, J. M (2014) Fossil Fuel Depletion and Socio-Economic Scenarios: An Integrated Approach, Energy, DOI:10.1016/j.energy.2014.09.063.

Garnier, Celine (2019) Performance Measurement and Mathematical Modelling of Integrated Solar Water Heaters, PhD Thesis submitted to the Department of Energy and Environmental Engineering, Edinburgh Napier University.

Chaabane, M., Mhiri, H., Le Palec, G., and Bournot, P (2010) Numerical Study of An Integrated Collector Storage Solar Water Heater, 2nd International Conference on Engineering Optimization September 6 - 9, Lisbon, Portugal.

Dobson, R T (2005) Thermal modelling of a night sky radiation cooling system, Journal of Energy in Southern Africa, Volume 16 No 2, pp 20-31.

Duffie, J. A. and Beckman W.A (2006) "Solar Engineering of Thermal Processes" New York, 4th edition.

Eduardo F. C., Manuel B., Ignacio A. and Daniel, L. (2010) Control of Solar Power Systems: A survey Proceedings of the 9th International Symposium on Dynamics and Control of Process Systems, Leuven, Belgium.

Energy Information Administration (2012) Annual Energy Review 2011 [www] Energy Information Administration Available from http://www.eia.gov [Accessed 18/04/2016].

Energy Information Administration (2013) International Energy Outlook 2013 [www] Energy Information Administration Available from http://www.eia.gov [Accessed 17/04/2016].

Energy Information Administration (2015) Country Analysis Brief: Nigeria [www] Energy Information Administration Available from http://www.eia.gov [Accessed 22/04/2016].

Eswaran S., Chandru M., Vairavel M. and Girimurugan, R. (2014) Numerical Study on Solar Water Heater using CFD Analysis, International Journal of Engineering Sciences & Research Technology, Volume 3 (3), Pp 1485-1489.

Farschad, T. and Mohammad, S. (2014) Improvement of thermal performance of a solar chimney based on a passive solar heating system with phase-change materials, Energy equipment and systems, energyequipsys/ Vol 2/No2/ Pp 141-154.

Feng G., Xiaolong X., and Runping N. (2015) An Experimental and Analytical Study of a Radiative Cooling System with Flat Plate Collectors, 9th International Symposium on Heating, Ventilation and Air Conditioning (ISHVAC) and the 3rd International Conference on Building Energy and Environment (COBEE).

Freegah, B., Asim, T. and Mishra, R. (2013) Computational Fluid Dynamics based Analysis of a Closed Thermo-Siphon Hot Water Solar System. In: 26th International Congress of Condition Monitoring and Diagnostic Engineering Management, Helsinki, Finland.

Ghassem H., Moien, F. F. and Shahram, D. (2010) Investigation of a hybrid system of nocturnal radiative cooling and direct evaporative cooling, Building and Environment 45 (2010) Pp 1521–1528.

Haghshenasfard, M., Ekramian, E., and Etemad, S.Gh. (2014) Numerical Analysis of Heat Transfer Performance of Flat Plate Solar Collectors, Journal of Fluid Flow, Heat and Mass Transfer Volume 1, DOI: 10.11159/jffhmt.2014.006, Pp 38-42.

Hammadi, H. S. (2008) Natural Circulation Solar Water Heating System in Basrah Mechanical Engineering Department-Engineering College University of Basrah.

Hutton, D. (2004) Fundamentals of Finite Element Analysis, First Edition, McGraw Hill Higher Education.

Balen, I and Vladimir, S. (2005) Radiative water-cooling in maritime and moderate continental climatic conditions, Journal of Mechanical Engineering 51, 7-8, Pp 399-404.

Ijemaru G.K, Adamu M. Z., Obatoke E. A., Hussaini, H. and Ajayi, F.O. (2014) Design and Modelling of a Solar Water Heating System, Industrial Engineering Letters, Vol.4, No.12, Pp 70-79.

International Energy Agency (2011) Solar Energy Perspectives [www] International Energy Agency Available from http://www.iea.org [Accessed 09/06/2016].

International Energy Agency (2015) 2015 Key World Energy STATISTICS [www] International Energy Agency Available from http://www.iea.org [Accessed 18/04/2016].

Iordanou, G. (2009) Flat-Plate Solar Collectors for Water Heating with Improved Heat Transfer for Application in Climatic Conditions of the Mediterranean Region, Durham theses, Durham University. Available at Durham E-Theses Online: http://etheses.dur.ac.uk/174/.

Ivette, R. P. (2006) Unsteady Laminar Convection in Cylindrical Domains: Numerical Studies and Application to Solar Water Storage Tanks, Doctoral thesis, Centre Tecnològic de Transferència de Calor, Departament de Màquines i Motors Tèrmics Universitat Politècnica de Catalunya.

Jung-Sik, C., Jae-Sub, K. and Dong-Hwa, C. (2010) "Development of a Novel Tracking System for Photovoltaic Efficiency in Low Level Radiation", Journal of Power Electronics, Vol. 10, No. 4.

Kalogirou, A. S. (2004) Solar thermal collectors and applications, Progress in Energy and Combustion Science 30, Pp 231–295.

Kalogirou, A. S. (2009) Solar Energy Engineering: Processes and Systems, Academic Press
Publications, USA, 1st Edition.

Khan, N., Abas, N., and Kalair, A (2015) Review of fossil fuels and future energy technologies, Futures 69, Pp 31-49

Kreith, F. and Bohn, M. S. (1993) Principles of Heat Transfer, Fifth Edition, West Publishing Company USA.

Kumavat, M. M. (2016) Design, CFD Analysis and Fabrication of Solar Flat Plate Collector, International Research Journal of Engineering and Technology, Volume: 03 Issue: 01, Pp 1000-1004.

Leonardo-energy (n.d) "Solar Water Heating in The World: Strong Diffusion due to The Large Impact of Incentives" Leonardo-energy [www] Available from www.leornado-energy.org.

Liu, B. Y. H. and Jordan, R. C (1963) The Long-Term Average Performance of Flat-Plate Solar Energy Collectors, Solar Energy, Volume **7**, 53.

Manikandan, J and Sivaraman, B (2016) Experimental Analysis of Double Glazed Flat Plate Solar Water Heater with Various Absorber Plate Geometries, International Energy Journal 16, Pp 151-156.

Manjunath, M. S., Vasudeva K. K., and Yagnesh Sharma, (2011) Three Dimensional Numerical Analysis of Conjugate Heat Transfer for Enhancement of Thermal Performance using Finned Tubes in an Economical Unglazed Solar Flat Plate Collector, Proceedings of the World Congress on Engineering Volume III, London, U.K.

Matsuta, M., Terada, S., and Ixo, H (1987) Solar Heating and Radiative Cooling using a Solar Collector-Sky Radiator with a Spectrally Selective Surface, Solar Energy Vol. 39. No. 3, Pp. 183-186.

Meir, M. G., Rekstad, J. B., and Løvvik, O. M. (2003) A Study Of A Polymer-Based Radiative Cooling System, Solar Energy Vol. 73, No. 6, pp. 403–417.

Mills, A. F. (2000) Heat Transfer, Prentice Hall, Upper Saddle River, New Jersey, USA

Mingke, H., Gang, P., Lei, L., Renchun, Z., Junfei, L., and Jie, J. (2015) Theoretical and Experimental Study of Spectral Selectivity Surface for Both Solar Heating and Radiative Cooling, International Journal of Photoenergy Volume 2015, DOI: 10.1155/2015/807875, Pp 1-9.

Mirzabozorg, H., Hariri-Ardebili, M. A., Shirkhan, M., and Seyed-Kolbadi, S.M. (2014) Mathematical Modeling and Numerical Analysis of Thermal Distribution in Arch Dams considering Solar Radiation Effect, The Scientific World Journal, Volume 2014, DOI: 10.1155/2014/597393, Pp 1-15.

Naveena, k. R. R. and Sharath, D (2014) Three dimensional numerical analysis of unglazed solar water heater for enhancement in thermal performance, International Journal of Latest Trends in Engineering and Technology (IJLTET) Vol. 4 Issue 2, Pp 94-102.

Nwaigwe K.N., Okoronkwo C.A., Ogueke N.V., Ugwuoke, P.E and Anyanwu E.E. (2012) Transient Analysis of a Nocturnal Radiative Cooling of a Building in Owerri, Nigeria, Research Journal of Applied Sciences, Engineering and Technology 4(15), Pp 2496-2506.

Nwaigwe, K. N. (2011) Transient Analysis and Performance Prediction of Passive Cooling of a Building using Long Wave Nocturnal Radiation, PhD Thesis, Department of Mechanical Engineering, Federal University of Technology Owerri, Nigeria.

Nwosu, P.N. and Onyegegbu, S.O. (2012) Numerical Study of Models for Estimating Edge Loss in Solar Absorbers, Journal of Thermal Science and Engineering Applications, Volume 4, DOI: 10.1115/1.4006870, Pp 1-11.

Ogueke N. V. (2005) Transient Analysis and Performance Prediction of a Solid Adsorption Solar Refrigerator, PhD Thesis, Department of Mechanical Engineering, Federal University of Technology Owerri, Nigeria.

Ogueke, N. V., Anyanwu, E. E., and Ekechukwu, O.V., (2009) A review of solar water heating systems, Journal of Renewable and Sustainable Energy **1**, 043106, Pp 1-21.

Ogueke, N. V., Onwuachu, C. C. and Anyanwu, E. E. (2011) Experimental Study of Long-Wave Night Sky Radiation in Owerri, Nigeria for Passive Cooling Application, World Renewable Energy Congress, Linkoping, Sweden, Pp 8-13.

Okoronkwo C.A (2011) Experimental study of passive cooling of a building using long-wave night sky radiation in Owerri, Nigeria, PhD thesis, Department of Mechanical Engineering, Federal University of Technology, Owerri, Imo State, Nigeria.

Olusola, B., Mustafa, D., Akinola, B. and Oluwaseun, A. (2017) A review of renewable energy potential in Nigeria; solar power development over the years, Engineering and Applied Science Research 44(4), Pp 242-248.

Parimal S. Bhambare and Parishwad, G. V., (2013) " Study of Medium Temperature Solar Thermal Applications" International Journal of Applied Research and Studies, Volume 2, Issue 5, Pp 1-11.

Partridge, L.E. and Coulstock, A.D (2003) Solar Heating and Cooling In Commercial Buildings, Destination Renewables – ANZSES, Pp 36-41.

PDE Solutions Inc. (2018) FlexPDE 7.12 Professional Trial Version Win64 16:26:47 August 16, 2018.

Rao, S. A. (1989) The Finite Element Method in Engineering, Second Edition, Pergamon Press, New York.

REN21 (2014) ECOWAS Renewable Energy and Energy Efficiency Status Report, REN21 publications

REN21 (2017) Renewables 2017 Global Status Report, REN21 publications

Renewable Energy World (2004) Solar thermal water heating: Technology Fundamentals [www] Renewable Energy World 02/2004 pp. 95-99. Available from www.renewableenergyworldw.com. [Accessed: 06/06/2016].

Riahi, A. and Taherian, H. (2011) Experimental investigation on the performance of thermosyphon solar water heater in the south Caspian Sea, Thermal science, vol. 15, no. 2, pp. 447-456.

Rostamzadeh, A., Adim, M., and Sabzi, S (2011) Experimental and Numerical Study of Forced Circulation Solar Water Heaters (SWHs), Proceedings of the Global Conference on Global Warming, Lisbon, Portugal.

Sako, M. K., et al., (2007) Economical and Technical Viability of a Thermosyphon Solar Water Heater in Côte D' Ivoire, Journal of Applied Sciences, 7 (24), Pp. 3977-3982.

Samuel, S., Edwin, M, and Jorge, R. (2016) Numerical Analysis of Thermosyphon Solar Water Heaters, International Journal of Sustainable and Green Energy. Vol. 5, No. 1, DOI: 10.11648/j.ijrse.20160501.11, Pp. 1-7.

Sen, Z (2008) Solar Energy Fundamentals and Modeling Techniques: Atmosphere, Environment, Climate Change and Renewable Energy, Springer-Verlag London Limited, Accessed 4/7/2017, DOI 10.1007/978-1-84800-134-3.

Shonhiwa, C., Yang, S. and Baokuan, L. (2015) Numerical Simulation and Measurement of Temperature Distribution in Water-in-Glass Evacuated Solar Water Heater, Physical Science International Journal 6(3): Pp 169-184.

Sinan, K., Mustafa, G., and Furkan, D (2012) "Theoretical and Experimental Performance Investigation of a Two-axis Solar Tracker under the Climatic Condition of Denizli, Turkey" PRZEGLĄD ELEKTROTECHNICZNY, Volume 88 (2), Pp 332-336.

Sumathy, K., Ruchi, S., Phillip, E. and Jiawei, G. (2013) Recent advances in the solar water heating systems: A review, Renewable and Sustainable Energy Reviews 19, Pp 173–190.

Thibault, Q. P., Luca, G., Ongun, B. K., Eleftherios, B., and Bjarne, W. O. (2016) Influence of the environmental parameters on nocturnal radiative cooling capacity of solar collectors, proceedings of the 12th REHVA World Congress: volume 3, Aalborg: Aalborg University, Department of Civil Engineering.

TimeandDate (2017) "Past Weather in Owerri, Nigeria" [www] TimeandDate Available from https://www.timeanddate.com/weather/nigeria/owerri/historic?month=9&year=2017 [Accessed 12/09/2018]

Toress, J.L., Lakpa, P., Damanski, R. and Francisco, S.C (2013) Numerical Simulation of the Solar Thermal Energy Storage System for Domestic Hot Water Supply located in South Spain, THERMAL SCIENCE: Vol. 17, No. 2, pp. 431-442.

Trane (2011) Cooling and Heating Load Estimation: One of the Fundamental Series, A publication of Trane, a business of Ingersoll Rand [www] Trane, Available from http://www.trane.com [Accessed 5/5/2017].

US Army Corps of Engineers (2011) “Central Solar Hot Water Systems Design Guide” [www] US Army Corps of Engineers

Vasudeva, K. K., Madhwesh, N., Shiva, K. and Manjunath, M. (2015) Numerical and Experimental Study of A Solar Water Heater for Enhancement in Thermal Performance, International Journal of Research in Engineering and Technology, Vol 4 (3), Pp 548-553.

Veeraboina, P and Yesuratnam, G (2014) Optimal Design & Analysis of Solar Water Heating System using Solar Factors for Energy Efficiency & Thermal Performance, Universal Journal of Renewable Energy 2, Pp 112-125.

Vettrivel, H and Mathiazhagan, P (2013) Thermal Performance Optimization Of A Flat Plate Solar Water Heater Collector Using Matlab, International Journal of Mechanical and Production Engineering, Volume- 1, Issue- 5, Pp 14-18.

Wenfeng, G., Tao, L., Wenxian, L., and Chuanxu, L. (2011) Numerical Study on Mixing Characteristics of hot Water inside the Storage Tank of a Solar System with Different Inlet Velocities of the Supply Cold Water, Procedia Environmental Sciences 11, Pp 1153-1163.

World Energy Council (2013) “World Energy Council Resources” [www] World Energy Council Available from https://www.worldenergy.org/news-and-media/press-releases/world-energy-council-report, [Accessed 18/04/2016].

World Energy Council (2015) “World Energy Council report confirms global abundance of energy resources and exposes myth of peak oil” [www] Available from https://www.worldenergy.org/news-and-media/press-releases/world-energy-council-report [Accessed 27/04/2016].

Yarshi, M and Benny, P (2015) Analysis of Heat Transfer Performance of Flat Plate Solar Collector using CFD, International Journal of Science, Engineering and Technology Research (IJSETR), Volume 4, Issue 10, Pp 3576-3580.

Zeghib, I and Chaker, A (2015) Modeling and Simulation of a Solar Thermal System for Domestic Space Heating Using Radiators Low Temperature, International Journal of Renewable Energy Research, Vol.5, No.1, Pp 266-276.

Zerrouki, A., Boumedien, A., Bouhadef, K., (2002) The Natural Circulation Solar Water Heater Model with Linear Temperature Distribution, Renewable Energy, 26, 4, pp. 549-559.

Appendix I: Numerical Data for location studies

Time	Tss_Owerri	Tb_Owerri	Tt_Owerri	Tw_Owerri	Ta_Owerri	Tsky_Owerri
6	23.1109127	23.110913	23.1109127	23.1109127	23.1109127	6.13288362
6.5	23.5682885	23.505619	23.4076174	23.2544242	23.6518121	6.349444173
7	25.3765002	25.176993	24.8636161	24.0659874	24.25	6.591840527
7.5	28.4216763	28.044541	27.4563035	25.6252033	24.8952411	6.85667529
8	32.5438491	31.958664	31.0542371	27.9009545	25.5764953	7.140039707
8.5	37.5867131	36.771087	35.5222344	30.8334931	26.2821059	7.437540098
9	43.3972303	42.335963	40.725549	34.3481795	27	7.744345571
9.5	49.815476	48.500436	46.5219044	38.3572001	27.7178941	8.055257417
10	56.6761509	55.106144	52.7630946	42.7635696	28.4235047	8.364799177
10.5	63.8018463	61.982691	59.2888293	47.4583694	29.1047589	8.667325091
11	71.0111668	68.955474	65.9341399	52.3263599	29.75	8.957143517
11.5	78.1168501	75.843837	72.5275952	57.2450993	30.3481879	9.228651016
12	84.9438492	82.478591	78.9080749	62.0974164	30.8890873	9.476472176
12.5	91.3112499	88.684451	84.9078895	66.759155	31.3634434	9.695599866
13	97.0504071	94.297595	90.3695625	71.1113268	31.7631397	9.881530494
13.5	102.00614	99.166817	95.1469324	75.0410127	32.0813374	10.03038898
14	106.035273	103.15207	99.1036691	78.4399031	32.312592	10.13903854
14.5	109.013694	106.13134	102.119903	81.2092842	32.4529467	10.20517093
15	110.862229	108.026	104.11707	83.2806951	32.5	10.22737356
15.5	111.519438	108.77427	105.032043	84.5949699	32.4529467	10.20517093
16	110.949067	108.33852	104.824373	85.1081873	32.312592	10.13903854
16.5	109.142787	106.70803	103.479092	84.7942509	32.0813374	10.03038898
17	106.120677	103.89957	101.007396	83.6458918	31.7631397	9.881530494
17.5	101.93036	99.956626	97.4460693	81.674732	31.3634434	9.695599866
18	96.9585206	95.228042	93.0872254	79.0276476	30.8890873	9.476472176
18.5	43.905536	43.805036	43.7523754	43.4602492	30.3481879	9.228651016
19	35.1557622	35.025849	34.8459538	34.4780253	29.75	8.957143517
19.5	32.4398117	32.319524	32.139995	31.8029591	29.1047589	8.667325091
20	31.0712954	30.962328	30.797296	30.4916426	28.4235047	8.364799177
20.5	26.4770155	26.550898	26.6623938	27.2806931	27.7178941	8.055257417
21	25.4345062	25.505685	25.6086985	26.1906171	27	7.744345571
21.5	24.6483006	24.717774	24.8169242	25.380113	26.2821059	7.437540098
22	23.9415048	24.009358	24.1055866	24.6533859	25.5764953	7.140039707
22.5	23.2731917	23.33938	23.4327911	23.9655299	24.8952411	6.85667529
23	22.6381962	22.702721	22.7932998	23.3110856	24.25	6.591840527
23.5	22.0418989	22.104838	22.1926291	22.6959884	23.6518121	6.349444173
24	21.4921232	21.553619	21.6387476	22.1286778	23.1109127	6.13288362
24.5	20.9965937	21.056836	21.1394937	21.6173619	22.6365566	5.945037859
25	20.5630735	20.622296	20.7027426	21.1702728	22.2368603	5.788276632
25.5	20.1985777	20.257048	20.3356049	20.7948254	21.9186626	5.664481387
26	19.9090331	19.967045	20.044083	20.497263	21.687408	5.575072907
26.5	19.6991233	19.756987	19.8329164	20.2825054	21.5470533	5.521040151
27	19.5722042	19.630241	19.7054999	20.154067	21.5	5.502965215
27.5	19.5302499	19.588783	19.6638293	20.1140089	21.5470533	5.521040151
28	19.5738201	19.633169	19.7084693	20.1629023	21.687408	5.575072907
28.5	19.7020485	19.762522	19.8385425	20.2998248	21.9186626	5.664481387
29	19.9126537	19.974542	20.0517409	20.522369	22.2368603	5.788276632
29.5	20.2019726	20.265545	20.3443596	20.8266839	22.6365566	5.945037859
30	20.5650159	20.630513	20.7113549	21.2075317	23.1109127	6.13288362

Time	Tss_PH	Tb_PH	Tt_PH	Tw_PH	Ta_PH	Tsky_PH
6	22.5	22.5	22.5	22.5	22.5	5.89132328
6.5	22.9167814	22.8578274	22.7670042	22.6223749	22.8519497	6.0300924
7	24.593912	24.4052925	24.1120104	23.3563868	23.2235429	6.17777076
7.5	27.4158607	27.0593305	26.5079355	24.7734646	23.6084214	6.33197951
8	31.2218001	30.6694038	29.8221118	26.8392854	24	6.49016802
8.5	35.8550101	35.0867496	33.9186462	29.4923509	24.3915786	6.64965234
9	41.1636325	40.1665551	38.6635236	32.6578129	24.7764571	6.80766045
9.5	46.9931252	45.7610361	43.9189941	36.2504951	25.1480503	6.96138348
10	53.1803742	51.713794	49.5384056	40.174253	25.5	7.10803158
10.5	59.5631373	57.8689238	55.3749035	44.329142	25.8262843	7.24489288
11	65.9727872	64.0640062	61.2747897	48.6077188	26.1213203	7.36939382
11.5	72.2312958	70.1271384	67.074605	52.8928536	26.38006	7.47915867
12	78.1725141	75.8975365	72.6208181	57.0721318	26.5980762	7.57206646
12.5	83.6558812	81.2388942	77.7827705	61.0481909	26.7716386	7.64630308
13	88.5424285	86.0161176	82.4303625	64.7222392	26.8977775	7.70040686
13.5	92.7039223	90.1041432	86.4424601	68.0004487	26.9743346	7.73330587
14	96.0276425	93.3926116	89.7114145	70.7969665	27	7.74434557
14.5	98.4196656	95.7890703	92.1461638	73.0365166	26.9743346	7.73330587
15	99.807184	97.2212606	93.6744972	74.6562417	26.8977775	7.70040686
15.5	100.140114	97.6387299	94.2446872	75.6071514	26.7716386	7.64630308
16	99.3920169	97.0137831	93.8264992	75.855168	26.5980762	7.57206646
16.5	97.5603445	95.3417794	92.4115834	75.3817426	26.38006	7.47915867
17	94.6660175	92.6407884	90.013254	74.1840389	26.1213203	7.36939382
17.5	90.7523993	88.9506529	86.6656974	72.2746913	25.8262843	7.24489288
18	86.1668907	84.584865	82.6316073	69.7868879	25.5	7.10803158
18.5	39.8785071	39.7677133	39.7072136	39.3835915	25.1480503	6.96138348
19	30.4879664	30.3454516	30.1456408	29.7405101	24.7764571	6.80766045
19.5	27.785267	27.6540525	27.4555369	27.0864786	24.3915786	6.64965234
20	26.6034342	26.4854107	26.3038315	25.9714707	24	6.49016802
20.5	23.734917	23.7953986	23.8999172	24.4490565	23.6084214	6.33197951
21	22.1469746	22.20307	22.2857715	22.7508227	23.2235429	6.17777076
21.5	21.4015103	21.4573791	21.5350998	21.9832906	22.8519497	6.0300924
22	20.9183006	20.9744528	21.0509429	21.4957308	22.5	5.89132328
22.5	20.5343553	20.5906205	20.666497	21.1093752	22.1737157	5.76363925
23	20.2041336	20.2603264	20.33557	20.7760118	21.8786797	5.64898917
23.5	19.9147745	19.9708095	20.0453492	20.4829754	21.61994	5.54907767
24	19.6648951	19.7207767	19.7946208	20.2295761	21.4019238	5.465354
24.5	19.4557233	19.5115207	19.584757	20.017645	21.2283614	5.39900571
25	19.2891528	19.3449733	19.4177382	19.8494289	21.1022225	5.35095594
25.5	19.1670711	19.2230486	19.2955203	19.7270976	21.0256654	5.32186314
26	19.0909615	19.1472468	19.2196338	19.6523276	21	5.31212175
26.5	19.061704	19.1184568	19.190987	19.6261123	21.0256654	5.32186314
27	19.0794805	19.1368629	19.209775	19.6486824	21.1022225	5.35095594
27.5	19.1437343	19.2019049	19.2754408	19.7194771	21.2283614	5.39900571
28	19.2531574	19.3122675	19.3866666	19.837139	21.4019238	5.465354
28.5	19.4057002	19.4658902	19.5413842	19.9995314	21.61994	5.54907767
29	19.598597	19.6599937	19.7368008	20.2037676	21.8786797	5.64898917
29.5	19.8284072	19.8911206	19.9694426	20.4462561	22.1737157	5.76363925
30	20.0910689	20.1551904	20.2352076	20.7227579	22.5	5.89132328

Time	Tss_Ikeja	Tb_Ikeja	Tt_Ikeja	Tw_Ikeja	Ta_Ikeja	Tsky_Ikeja
6	23.66987298	23.66987298	23.66987298	23.66987298	23.669873	6.356718342
6.5	24.11754884	24.05448375	23.95770635	23.80504118	24.0332333	6.503653294
7	25.92188852	25.71935739	25.40456154	24.59594394	24.4644661	6.679480574
7.5	28.97026022	28.58656585	27.99261351	26.13012575	24.9561929	6.881871789
8	33.10130293	32.5055436	31.59017649	28.37959996	25.5	7.108031576
8.5	38.1578558	37.32740069	36.061848	31.28681377	26.0865828	7.354698394
9	43.98701511	42.90655217	41.27335134	34.77906837	26.7059048	7.618158811
9.5	50.42983013	49.09118308	47.08354759	38.77054782	27.347369	7.89427779
10	57.32263218	55.72457735	53.34591086	43.16634884	28	8.178546453
10.5	64.49019238	62.63851523	59.90232258	47.85982859	28.652631	8.466147625
11	71.75345486	69.6607187	66.59012977	52.73800764	29.2940952	8.752038334
11.5	78.92740844	76.61277805	73.24015642	57.68061442	29.9134172	9.031047344
12	85.83853428	83.32705678	79.69288735	62.57212707	30.5	9.297984904
12.5	92.30683849	89.62924656	85.7817199	67.28969514	31.0438071	9.547761082
13	98.16341465	95.3553658	91.34919752	71.7148593	31.5355339	9.77550855
13.5	103.2451398	100.3465684	96.24194931	75.72957484	31.9667667	9.976705326
14	107.4017304	104.4559766	100.3172186	79.22095	32.330127	10.14729285
14.5	110.5273144	107.5795213	103.4728506	82.10523163	32.6193977	10.28378489
15	112.5289114	109.625211	105.6175071	84.30441146	32.8296291	10.38336313
15.5	113.3356817	110.5221781	106.6794652	85.75306611	32.9572243	10.44395566
16	112.9031565	110.2248524	106.6107411	86.4017591	33	10.46429532
16.5	111.2151233	108.7148712	105.3890549	86.21888319	32.9572243	10.44395566
17	108.284104	106.0016226	103.0184913	85.19159665	32.8296291	10.38336313
17.5	104.1507804	102.1217702	99.5291892	83.32605433	32.6193977	10.28378489
18	99.20934792	97.4303065	95.21734907	80.76903491	32.330127	10.14729285
18.5	45.09390004	44.99614809	44.94448021	44.66089494	31.9667667	9.976705326
19	36.71069041	36.58466902	36.40965385	36.0533752	31.5355339	9.77550855
19.5	34.20296362	34.08665299	33.91260923	33.5874099	31.0438071	9.547761082
20	32.99605391	32.89103247	32.73163818	32.43777786	30.5	9.297984904
20.5	27.87656595	27.95697307	28.07037172	28.7190522	29.9134172	9.031047344
21	27.28843863	27.36787868	27.48002184	28.12106408	29.2940952	8.752038334
21.5	26.69742208	26.77541438	26.88557289	27.51462363	28.652631	8.466147625
22	26.09344533	26.16978487	26.27758864	26.89292391	28	8.178546453
22.5	25.48379447	25.55838716	25.66361477	26.2643613	27.347369	7.89427779
23	24.8777096	24.95053499	25.05306616	25.63888289	26.7059048	7.618158811
23.5	24.28476242	24.35585768	24.45565369	25.02663952	26.0865828	7.354698394
24	23.71390487	23.78335169	23.88043086	24.43701772	25.5	7.108031576
24.5	23.17446857	23.24239338	23.33684017	23.87980807	24.9561929	6.881871789
25	22.67544106	22.74200625	22.83396794	23.36442535	24.4644661	6.679480574
25.5	22.22513269	22.2905353	22.38021657	22.89956834	24.0332333	6.503653294
26	21.83101144	21.89547721	21.98313386	22.49304504	23.669873	6.356718342
26.5	21.49958268	21.56336125	21.64929412	22.15165255	23.3806023	6.24054646
27	21.23628987	21.2996494	21.38419812	21.88107755	23.1703709	6.156566227
27.5	21.04543	21.10865205	21.19218794	21.68580572	23.0427757	6.105781605
28	20.93008433	20.99345817	21.07637689	21.56904894	23	6.088787702
28.5	20.89206843	20.95588513	21.03859866	21.53269555	23.0427757	6.105781605
29	20.931902	20.99644871	21.07937718	21.57727386	23.1703709	6.156566227
29.5	21.04879937	21.11435345	21.1979168	21.70194699	23.3806023	6.24054646
30	21.24068085	21.30750437	21.39211412	21.90452495	23.669873	6.356718342

Time	Tss_Maiduguri	Tb_Maiduguri	Tt_Maiduguri	Tw_Maiduguri	Ta_Maiduguri	Tsky_Maiduguri
6	23	23	23	23	23	6.088787702
6.5	23.503518	23.43582879	23.3288215	23.16284781	23.70389941	6.370430337
7	25.46691215	25.25257855	24.91393349	24.05676979	24.44708573	6.672363853
7.5	28.76424249	28.35958982	27.72596101	25.76133915	25.21684285	6.989967324
8	33.22089199	32.59323005	31.62049804	28.23893078	26	7.318112806
8.5	38.66789305	37.79304956	36.45096071	31.42253762	26.78315715	7.651238366
9	44.93555749	43.797208	42.06760498	35.22776117	27.55291427	7.983445946
9.5	51.84851654	50.43801055	48.31418818	39.55700502	28.29610059	8.308621285
10	59.22422848	57.5405071	55.02685844	44.30228133	29	8.620571823
10.5	66.86719633	64.91687494	62.02882029	49.34290137	29.65256857	8.913177517
11	74.57409935	72.37132752	69.13493565	54.54903307	30.24264069	9.180548773
11.5	82.15095185	79.71672704	76.16761313	59.793664	30.76012004	9.417185314
12	89.39524477	86.7572505	82.9401836	64.9408344	31.19615242	9.618129676
12.5	96.11440433	93.30623948	89.2739157	69.85781148	31.5432772	9.779109214
13	102.1275868	99.18792875	94.99966193	74.41642559	31.79555496	9.896660951
13.5	107.2629854	104.2347792	99.95520008	78.49070956	31.94866917	9.968234269
14	111.3681996	108.2975552	103.9949303	81.96416628	32	9.992267346
14.5	114.3394925	111.2739396	107.0177718	84.75238991	31.94866917	9.968234269
15	116.0904471	113.0779821	108.9375436	86.77965553	31.79555496	9.896660951
15.5	116.5610456	113.6490098	109.6916979	87.98587116	31.5432772	9.779109214
16	115.7213067	112.9552529	109.2449613	88.32976831	31.19615242	9.618129676
16.5	113.5722988	110.9949281	107.5905461	87.79031598	30.76012004	9.417185314
17	110.1455676	107.795784	104.7498879	86.36706604	30.24264069	9.180548773
17.5	105.5014303	103.4135317	100.7713049	84.07970634	29.65256857	8.913177517
18	100.0518866	98.22064109	95.96800467	81.08847532	29	8.620571823
18.5	42.38252858	42.27838039	42.22400705	41.92059937	28.29610059	8.308621285
19	33.21434089	33.07942306	32.89287835	32.51004272	27.55291427	7.983445946
19.5	30.29624519	30.17099915	29.98426274	29.63255672	26.78315715	7.651238366
20	28.79048708	28.67675436	28.50455372	28.18474187	26	7.318112806
20.5	30	30	30	30	25.21684285	6.989967324
21	24.36942777	24.43314486	24.54079947	25.10979683	24.44708573	6.672363853
21.5	22.72207814	22.78084542	22.86925262	23.36018436	23.70389941	6.370430337
22	21.74541943	21.80255588	21.88476582	22.35007154	23	6.088787702
22.5	20.99788722	21.05393742	21.13298992	21.5840909	22.34743143	5.831502923
23	20.36081887	20.41581742	20.49237019	20.93162625	21.75735931	5.60206771
23.5	19.80372172	19.85770146	19.93192753	20.36019378	21.23987996	5.403400574
24	19.32243816	19.37552733	19.44760172	19.86604165	20.80384758	5.237868277
24.5	18.92038116	18.9727933	19.04298259	19.45330744	20.45672281	5.107321162
25	18.60215813	18.65416606	18.72282566	19.12722183	20.20444504	5.013135773
25.5	18.37160373	18.42351677	18.49105527	18.89198831	20.05133083	4.956257725
26	18.23190352	18.28405449	18.35092819	18.75108555	20	4.937238094
26.5	18.18502134	18.23775583	18.3044537	18.70665629	20.05133083	4.956257725
27	18.23147697	18.28514107	18.35216929	18.759284	20.20444504	5.013135773
27.5	18.3702752	18.42520529	18.49307306	18.90793604	20.45672281	5.107321162
28	18.59890114	18.6554162	18.7246235	19.14997036	20.80384758	5.237868277
28.5	18.91335063	18.97174484	19.04277163	19.48117761	21.23987996	5.403400574
29	19.3081866	19.36872276	19.4420198	19.89584727	21.75735931	5.60206771
29.5	19.77661877	19.83952473	19.9155034	20.38685805	22.34743143	5.831502923
30	20.31061595	20.37607113	20.45509731	20.94579058	23	6.088787702

Time	Tss_Sokoto	Tb_Sokoto	Tt_Sokoto	Tw_Sokoto	Ta_Sokoto	Tsky_Sokoto
6	24.05025253	24.05025253	24.05025253	24.05025253	24.05025253	6.5105629
6.5	24.55325417	24.48496846	24.37705111	24.20837718	24.73867	6.792092608
7	26.53208134	26.31547689	25.9731391	25.10590086	25.5	7.108031576
7.5	29.86739006	29.45797503	28.81636009	26.82841928	26.32121597	7.45414782
8	34.39024612	33.75447799	32.76797707	29.34390079	27.18826668	7.825486733
8.5	39.9374553	39.0502127	37.68700001	32.59041781	28.08631665	8.216394054
9	46.3443429	45.18826729	43.42854456	36.48789211	29	8.620571823
9.5	53.43996933	52.00530833	49.84068588	40.94242536	29.91368335	9.031167888
10	61.04503753	59.32961483	56.76283779	45.84890114	30.81173332	9.440897296
10.5	68.96542701	66.97480433	64.01980059	51.08830672	31.67878403	9.842191987
11	76.99683581	74.74426441	71.4258997	56.5309429	32.5	10.22737356
11.5	84.94245727	82.44826361	78.80134399	62.04871132	33.26133	10.58884264
12	92.59372935	89.88526252	85.95429653	67.50243017	33.94974747	10.91927742
12.5	99.74962602	96.8605574	92.69862539	72.75446971	34.55347338	11.21183358
13	106.2184639	103.1880097	98.85553038	77.67002735	35.06217783	11.46033756
13.5	111.8226881	108.6946641	104.2579363	82.12033756	35.46715673	11.65946542
14	116.397477	113.2193361	108.749023	85.98109818	35.76148078	11.80490015
14.5	119.8003457	116.6219607	112.1912433	89.13925906	35.94011403	11.89346103
15	121.9397878	118.8116785	114.4938353	91.51587489	36	11.9232
15.5	122.7449484	119.7172191	115.5839944	93.04278059	35.94011403	11.89346103
16	122.1742625	119.2954148	115.415283	93.66948979	35.76148078	11.80490015
16.5	120.2186274	117.534392	113.9708854	93.36621558	35.46715673	11.65946542
17	116.9018732	114.4541389	111.2643431	92.12502469	35.06217783	11.46033756
17.5	112.2796044	110.1054827	107.3387632	89.95985327	34.55347338	11.21183358
18	106.7820177	104.8767296	102.5195991	87.03454592	33.94974747	10.91927742
18.5	46.17296093	46.07829109	46.03024571	45.75594039	33.26133	10.58884264
19	37.75559105	37.63271382	37.4641352	37.11697025	32.5	10.22737356
19.5	35.00256177	34.88826848	34.71935616	34.39988693	31.67878403	9.842191987
20	33.50366381	33.39956452	33.24362117	32.95233371	30.81173332	9.440897296
20.5	30	30	30	30	29.91368335	9.031167888
21	27.36138003	27.4394937	27.55358443	28.19447047	29	8.620571823
21.5	26.43346486	26.50913448	26.61887538	27.23724917	28.08631665	8.216394054
22	25.56742205	25.64061726	25.74637043	26.3429312	27.18826668	7.825486733
22.5	24.73307357	24.80381978	24.90563818	25.48080104	26.32121597	7.45414782
23	23.93439373	24.00277672	24.10069643	24.65505083	25.5	7.108031576
23.5	23.18159927	23.2477713	23.34189659	23.87644859	24.73867	6.792092608
24	22.48658564	22.55076441	22.64129591	23.15755147	24.05025253	6.5105629
24.5	21.86054288	21.92299703	22.01022003	22.5101289	23.44652662	6.266958958
25	21.3129255	21.37396604	21.45822757	21.94408056	22.93782217	6.064113902
25.5	20.85272163	20.91269706	20.99441343	21.46884237	22.53284327	5.904227343
26	20.48761464	20.54690376	20.62655265	21.09248097	22.23851922	5.788924378
26.5	20.22367166	20.2826744	20.36078247	20.8213554	22.05988597	5.719314419
27	20.06522527	20.12435328	20.20148335	20.65999696	22	5.696040899
27.5	20.01482263	20.07449055	20.15122885	20.61105631	22.05988597	5.719314419
28	20.07320031	20.13381683	20.21076049	20.67527979	22.23851922	5.788924378
28.5	20.2392791	20.30123835	20.37898306	20.85150707	22.53284327	5.904227343
29	20.51018136	20.57385479	20.65298256	21.13669397	22.93782217	6.064113902
29.5	20.88127373	20.94700269	21.02807077	21.52595479	23.44652662	6.266958958
30	21.34623688	21.41432548	21.49785624	22.01264543	24.05025253	6.5105629

Appendix II: Numerical Data for Surface Coatings

Time	Tss@CS_PET	Tb@CS_PET	Tt@CS_PET	Tw@CS_PET	Tss@Al_PET	Tb@Al_PET	Tt@Al_PET	Tw@Al_PET	Tss@T_PET	Tb@T_PET	Tt@T_PET	Tw@T_PET
6	23.1109127	23.1109127	23.110913	23.1109127	23.1109127	23.1109127	23.110913	23.1109127	23.11091	23.110913	23.11091	23.11091
6.5	23.5115489	23.4510319	23.360719	23.2233116	23.8006152	23.6902957	23.529335	23.2878217	23.49142	23.434443	23.34902	23.21874
7	25.0914899	24.8989843	24.600625	23.8918936	26.6241651	26.2672272	25.720408	24.4254591	24.97278	24.793665	24.51502	23.85157
7.5	27.8038428	27.4422305	26.873349	25.2301925	31.3405136	30.6917206	29.67845	26.7082889	27.50302	27.167162	26.63727	25.10726
8	31.5360768	30.9786457	30.094913	27.2372638	37.5101264	36.5541767	35.046157	30.0250959	30.98797	30.469767	29.64636	26.98848
8.5	36.1597846	35.3875542	34.157988	29.8738997	44.7298263	43.4676362	41.465226	34.1982084	35.31614	34.597063	33.45002	29.46321
9	41.5392933	40.5400982	38.945183	33.0797029	52.6390956	51.0827193	48.605545	39.0299151	40.36498	39.432835	37.9427	32.47797
9.5	47.5323101	46.3004566	44.331381	36.7805232	60.9138062	59.0839901	56.166272	44.3199333	46.00249	44.851151	43.00848	35.96442
10	53.9807023	52.5170822	50.175801	40.8864861	69.264117	67.1888459	63.876651	49.8763181	52.08685	50.71618	48.52132	39.84238
10.5	60.7232058	59.0349834	56.333631	45.3007409	77.4190342	75.1326466	71.482276	55.5117675	58.46217	56.878117	54.3413	44.01847
11	67.5871939	65.687765	62.648535	49.9153723	85.1325686	82.6748333	78.751224	61.0509172	64.97229	63.186553	60.32728	48.39543
11.5	74.39804	72.3066699	68.961198	54.6175655	92.1713523	89.5866769	85.462076	66.3223891	71.45064	69.480612	66.32753	52.86621
12	80.96932	78.7110158	75.100137	59.2829697	98.3173286	95.6538049	91.406196	71.1604361	77.73089	75.599287	72.18957	57.32085
12.5	87.1249071	84.7296447	80.902114	63.7905842	103.384663	100.692854	96.403968	75.418139	83.64909	81.383433	77.76192	61.64799
13	92.7169237	90.2184656	86.229054	68.0359641	107.237528	104.569223	100.32257	78.9833857	89.03801	86.670233	82.8888	65.73049
13.5	97.5996446	95.0350224	90.943685	71.9131608	109.757727	107.164916	103.04417	81.752697	93.74436	91.309926	87.42597	69.45725
14	101.639544	99.0482529	94.91882	75.3214422	110.855751	108.389417	104.47646	83.6394263	97.64957	95.186102	91.26045	72.73865
14.5	104.720978	102.144035	98.042681	78.1692824	110.475865	108.184739	104.5577	84.5777986	100.6445	98.191065	94.28673	75.48834
15	106.750001	104.228936	100.22256	80.3772324	108.598434	106.527792	103.25909	84.5251245	102.6388	100.23491	96.41558	77.62984
15.5	107.657122	105.232958	101.38752	81.8801709	105.240624	103.431163	100.58572	83.462986	103.5655	101.25017	97.57858	79.10022
16	107.399114	105.11136	101.49029	82.6290526	100.455846	98.9426964	96.576376	81.3976223	103.3835	101.19427	97.73061	79.85228
16.5	105.960024	103.845733	100.50837	82.5921371	94.332126	93.1440066	91.302255	78.359607	102.0785	100.0505	96.85098	79.8559
17	103.351241	101.444149	98.444387	81.7556857	86.9894485	86.1480202	84.864847	74.4028394	99.66273	97.827831	94.94343	79.09855
17.5	99.610806	97.940579	95.32565	80.1240968	78.5761904	78.0956088	77.392883	69.6028831	96.17346	94.559795	92.0352	77.58521
18	95.0767287	93.6363323	91.39878	77.8129115	69.4490612	69.2969033	69.131645	64.0828277	91.93538	90.536037	88.3637	75.42744
18.5	44.1710479	44.048605	43.889956	43.5077369	39.5418215	39.4568173	39.368334	39.1882878	44.23649	44.14785	44.05733	43.78445
19	35.2989206	35.1600808	34.93056	34.4779611	34.0875074	33.9552267	33.74633	33.3375443	34.36977	34.280808	34.13732	33.83537
19.5	32.5664249	32.4404297	32.227944	31.8188244	31.9184284	31.8127287	31.641655	31.2977761	31.48003	31.400663	31.26476	30.99222
20	31.1875643	31.073824	30.882289	30.5130045	30.4733143	30.3910263	30.256507	29.9790404	30.1359	30.064663	29.94161	29.69574
20.5	24.1209967	24.2541311	24.439015	25.4959796	19.2652341	19.5975761	20.067109	22.7011844	26.4804	26.554148	26.66545	27.28271
21	23.4693003	23.5996306	23.780326	24.8125355	18.1306965	18.4529599	18.898344	21.3730778	25.43989	25.510881	25.61363	26.19405
21.5	22.8325258	22.9597144	23.135856	24.1415283	17.3892574	17.7065133	18.142535	20.5607306	24.65526	24.7245	24.82333	25.38466
22	22.2075293	22.3314266	22.502771	23.4808657	16.7722231	17.0843049	17.512344	19.8861889	23.94978	24.017363	24.11322	24.65885
22.5	21.599315	21.7199321	21.886417	22.8369	16.2179242	16.5242097	16.943733	19.2712126	23.28262	23.348509	23.44151	23.97181
23	21.0157184	21.1331841	21.294902	22.2185916	15.7097187	16.0099103	16.420543	18.6997305	22.64868	22.712873	22.803	23.3181
23.5	20.4648421	20.5793709	20.736526	21.6348795	15.2440221	15.5381688	15.939945	18.1710115	22.05337	22.115944	22.20325	22.70368
24	19.9551934	20.0670794	20.21999	21.0951028	14.8220386	15.1104735	15.503803	17.6890151	21.50452	21.565627	21.65024	22.13702
24.5	19.4948908	19.6044975	19.75359	20.6081331	14.4467604	14.7300233	15.115598	17.2588636	21.00987	21.069703	21.15181	21.62631
25	19.0913043	19.1990536	19.344845	20.1819934	14.1217143	14.4004959	14.779215	16.8856236	20.5772	20.635983	20.71585	21.17981
25.5	18.7508728	18.857235	19.000322	19.8236726	13.8504742	14.1255981	14.498549	16.5742838	20.21351	20.271518	20.34947	20.80492
26	18.4789923	18.5844747	18.725518	19.5390129	13.6362218	13.9086171	14.277045	16.3291811	19.92473	19.982263	20.05867	20.5079
26.5	18.2799297	18.385068	18.52478	19.3326221	13.4815308	13.752203	14.117468	16.1537496	19.71555	19.772921	19.84819	20.29365
27	18.1567637	18.2621072	18.401235	19.2078028	13.3882454	13.6582497	14.021793	16.0504216	19.58933	19.646855	19.72143	20.1657
27.5	18.1113317	18.2174357	18.356747	19.1665023	13.3573995	13.6278151	13.991123	16.0205543	19.54804	19.606043	19.68038	20.12611
28	18.1442059	18.2516177	18.391884	19.2092812	13.3891649	13.6610701	14.02564	16.0643869	19.59224	19.651041	19.72561	20.17544
28.5	18.2546795	18.3639279	18.50591	19.3353021	13.4828184	13.7572669	14.124574	16.1810194	19.72106	19.780972	19.85625	20.31278
29	18.4407746	18.5523587	18.69679	19.5423428	13.6367254	13.9147238	14.286192	16.3684082	19.93223	19.993537	20.06997	20.53571
29.5	18.6992679	18.8136467	18.961217	19.8268273	13.8483374	14.1308244	14.507795	16.6233813	20.22207	20.28505	20.36308	20.8404
30	19.0257339	19.1433179	19.294665	20.1838812	14.1142028	14.4020313	14.785738	16.9416701	20.5856	20.650493	20.73054	21.22159

Appendix III: Numerical Data for Result Benchmarking

SOLAR HEATING		
Time	Riahi et al (Exp)_Iran	Present Model_Nigeria
6	22	23
6.5	22	24
7	30	25
7.5	36	28
8	42	33
8.5	50	38
9	58	43
9.5	58	50
10	60	57
10.5	62	64
11	68	71
11.5	70	78
12	75	85
12.5	79	91
13	83	97
13.5	83	102
14	84	106
14.5	84	109
15	85	111
15.5	90	112
16	85	111
16.5	84	109
17	75	106
17.5	70	102
18	65	97
18.5	50	44
19	45	35
19.5	40	32
20	35	31
20.5	28	26
21	27	25
NOCTURNAL COOLING		
Time	Mingke et al (Exp)_China	Present Model_Nigeria
22	17	24
22.5	16	23
23	17	23
23.5	17.5	22
24	17	21
24.5	16	21
25	16	21
25.5	14	20
26	13	20
26.5	12	20
27	13	20
27.5	13	20
28	13	20
28.5	13	20
29	12	20
29.5	15	20
30	17	21
STORAGE TANK_Diurnal		
Time	Riahi et al (Exp)_Iran	Present Model_Nigeria
6	23	24
7	30	27
8	32	31
9	33	35
10	38	40
11	46	45
12	52	49
13	60	53
14	64	56
15	67	57
16	64	58
17	62	57
18	62	54
19	62	51
20	62	46
STORAGE TANK_Nocturnal		
Time	Ali et al (Exp)_Iran	Present Model_Nigeria
21	15	27
22	13	25
23	14	24
24	11	23
25	10	22
26	9	21
27	5	21
28	4	21
29	2	22
30	2	22

Time	Anyanwu (Exp_plate)_NSK_Nigeria	Anyanwu (Exp_tube)_NSK_Nigeria	Present Model_Plate_OW_Nigeria	Present Model_Tube_OW_Nigeria	Present Model_Plate_PH_Nigeria	Present Model_Tube_PH_Nigeria
8	32.4	19.9	32.5	31.05423714	31.2	29.82211177
8.5	32.4	19.9	37.6	35.52223441	35.9	33.91864622
9	36.9	28.3	43.4	40.72554901	41.2	38.6635236
9.5	45.3	39.9	49.8	46.52190442	47.0	43.91899407
10	59.1	45.1	56.7	52.7630946	53.2	49.53840564
10.5	71.9	53.7	63.8	59.28882933	59.6	55.37490353
11	81.7	63.1	71.0	65.93413992	66.0	61.27478965
11.5	91.1	71.7	78.1	72.52759522	72.2	67.07460496
12	99.8	81.6	84.9	78.90807485	78.2	72.62081811
12.5	93.8	83.7	91.3	84.90788947	83.7	77.78277054
13	102.5	85	97.1	90.36956249	88.5	82.43036252
13.5	108.8	92.7	102.0	95.1469324	92.7	86.44246012
14	107.2	93.5	106.0	99.1036691	96.0	89.71141452
14.5	101.2	95.5	109.0	102.1199034	98.4	92.14616382
15	98.7	95.3	110.9	104.1170704	99.8	93.67449724
15.5	98.4	90	111.5	105.0320427	100.1	94.24468721
16	81	82.6	110.9	104.8243728	99.4	93.82649918
16.5	57	60.9	109.1	103.4790921	97.6	92.41158345
17	49.1	51.6	106.1	101.0073955	94.7	90.01325398
17.5	45.1	45.8	101.9	97.44606934	90.8	86.66569739
18	40.9	41.8	97.0	93.08722544	86.2	82.6316073
18.5	35.8	37	43.9	43.75237537	39.9	39.70721355
19	31.2	33.6	35.2	34.84595385	30.5	30.14564081
19.5	25.8	27.7	32.4	32.13999502	27.8	27.45553687
20	23.4	24.2	31.1	30.79729603	26.6	26.30383154
20.5	23	24	26.5	26.66239376	23.7	23.89991717
21	22.3	23	25.4	25.60869849	22.1	22.28577149
21.5	22.3	22.3	24.6	24.81692422	21.4	21.53509985
22	22.3	22	23.9	24.10558657	20.9	21.0509429
22.5	22	20	23.3	23.43279106	20.5	20.66649698
23	22	20	22.6	22.79329982	20.2	20.33557001
23.5	20.2	20	22.0	22.19262913	19.9	20.04534923
24	20.2	20	21.5	21.6387476	19.7	19.79462082
24.5	20.2	20	21.0	21.13949366	19.5	19.58475696
25	20.2	20	20.6	20.7027426	19.3	19.41773819
25.5	20.2	20	20.2	20.33560495	19.2	19.29552026
26	20.2	20	19.9	20.04408297	19.1	19.21963381
26.5	20.2	20	19.7	19.83291639	19.1	19.19098702
27	20.3	20	19.6	19.70549993	19.1	19.20977498
27.5	20.4	20	19.5	19.66382926	19.1	19.27544077

Appendix IV: Model Input Parameters

Location:	**Owerri**	**PH**	**Ikeja**	**Maiduguri**	**Sokoto**
Latitude (^{o}N):	5.49	4.67	6.42	12	13.03
Longitude (^{o}E):	8.67	7.17	3.45	13.33	5.27

Polyethylene windscreen:	
Thickness	20*10^(-6)m
Transmissivity	0.92
Emissivity	0.9
Refractive index	1.54

SCONOR:	**CS**	**AL**	**Ti**
Thermal conductivity	54W/mK	220W/mK	26W/mK
Density	7833kg/m^3	2707kg/m^3	4510W/mK
Specific heat capacity	465J/kgK	896J/kgK	544J/kgK
Thickness	0.00103m		
Length	1.42m		
centre-to-centre distance	0.1m		
Tilt angle	Latitude+15^{o}		
TPET:			
Absorptivity	0.92/0.55		
Emissivity	0.88/0.55		

BOND:	
Specific heat capacity	465
Density	7850
Thickness	0.003m
Width	0.026m
Thermal conductivity	0.33

TUBE:	
Thermal conductivity	386W/mK
Density	8954kg/m^3
Specific heat capacity	380J/kgK
No of riser tubes	12
Tube inner diameter	0.012m
Tube outer diameter	0.015m

WATER	
Thermal conductivity	0.608W/mK
Density	998.2kg/m^3
Specific heat capacity	4186J/kgK
Mass flow rate	0.0833kg/s

Ground Albeido	0.2
Refractive index of air	1.0

STORAGE TANKS

Mass of water	300kg-wt
Height of tank	1m
Diameter of tank	1m
Number of zone	5

INSULATION

Thickness	0.1
Thermal conductivity	0.038W/mK

MODEL ROOM

Number of people	1
Length	9.9
Breadth	5.2
Height	2.77
Wall thickness	0.1
Wall material conductivity	0.1
Density of air in room	1.180kg/m^3
Specific heat of air	1005J/kgK
Number of Air Changes per day (ACPD)	0.3